KLYSTRON-MODULATOR SYSTEM AVAILABILITY OF PLS 2 GEV ELECTRON LINAC

M.H. Cho, S.S. Park, J.S. Oh, and W. Namkung
Pohang Accelerator Laboratory
Pohang University of Science and Technology(POSTECH)
San 31, Hyoja-dong, Pohang, Kyungbuk 790-784 KOREA

Abstract

PLS Linac has been injecting 2 GeV electron beams to the Pohang Light Source(PLS) storage ring since September 1994. PLS 2 GeV linac employs 11 sets of high power klystron-modulator(K&M) system for the main RF source for the beam acceleration. The klystron has rated output peak power of 80 MW at 4 microsec pulse width and at 60 pps. The matching modulator has 200 MW peak output power. The total accumulated high voltage run time of the oldest unit has reached beyond 23,000 hour and the sum of all the high voltage run time is approximately 230,000 hour as of May 1996. In this paper, we review overall system performance of the high-power K&M system. A special attention is paid on the analysis of all failures and troubles of the K&M system which affected the linac high power RF operations as well as beam injection operations for the period of 1994 to May 1996.

Introduction

The PLS 2 GeV linac employs 11 units of high power pulsed klystrons(80 MW) as the main RF sources. The matching modulators of 200 MW(400 kV, 500 A) can provide a flat-top pulse width of 4.4 sec with a maximum pulse repetition rate of 120 Hz at the full power level. For the good stability of electron beams, the pulse-to-pulse flat-top voltage variation of a modulator requires to be less than 0.5%. In order to achieve this goal, we stabilized high voltage charging power supplies well within requirement by a phase controlled SCR voltage regulator(both AC and DC feedbacks). The K&M system are normally operating in 70% to 80% of the rated peak power level to avoid the multipactoring phenomena occasionally occurring in a random fashion inside the waveguide networks and accelerating structures of the linac system. The sum of all high voltage run time for total 11 K&M systems installed in the PLS linac, is approximately 230,000 hours.

In this paper, we analyzed the overall system availability and the system fault statistics during the PLS commissioning operation. During this period the availability was ~90% for the case of 24 hr maintenance mode with 2-shift works and the availability drooped down to ~75% for the case of day-time only(44 hr per week) maintenance mode. The most frequent type of static fault which requires the attendance of a maintenance crew has been identified as main circuit breaker(CB) trips due to the abnormal behavior of thyratron switches. For the improvement of the system availability the SCR gate hold interlock and the slow start of the DC high voltage together with the automatic remote reset of the static faults using the computer control are adapted.

K&M System Performance

The key features of the K&M system design include the 3-phase SCR controlled AC-line power control, resonant charging of the PFN, resistive De-Qing, end-of-line clipper with thyrite disks, pulse transformer with 1:17 step-up turn ratio, and high power thyratron tube switching. The major operational parameters of the PLS-200-MW K&M system are listed in Table 1.

For the fault free stable operation of the system, the thyratron tube is one of the most important active components which require continuous maintenance and adjustments.

Table 1. Operational parameters of K&M systems.

Peak beam power	~150 MW(200 MW max.)
Pulse width	ESW 7.5μs, 4.4μs flat-top
Pulse rep. rate	30 pps(120 pps *max.*)
PFN impedance	2.64Ω(5% positive mismatch)
Voltage stabilization	SCR, DC feedback & 5% De-Q'ing
Pulse transformer	1:17(turn ratio), L_{lk}:1.3μH,C_{st}:69nF
Thyratron switching loading	Heating factor: 46.8×10^9, 8.5 kA peak anode current
Klystron tube	Drive power:~300 W, gain:~53dB, peak power:80/65 MW (currently running at 50 to 65MW)

The thyratron tubes which meet the PLS-200-MW system specifications are listed in Table 2 together with their specifications. Three types of thyratron tubes, ITT/F-303, Litton/L-4888, and EEV/CX-1836A are installed in our system, and the performance evaluations are underway. This effort is initiated to improve the system from the frequent occurring faults(see Fig.3) caused by the irregular recovery action of the thyratrons, which strongly depends upon the reservoir control.

There are three types of system interlocks, namely dynamic, static, and personal protection interlocks. All the static fault activation is initiated by the relay logic circuit, and the dynamic faults which require a fast action response are activated using the electronic comparator circuit. When the system operation is interrupted by the static fault, it can be recovered either by the remote control computer or manual reset. However, we have been performing all manual resets till July 1995 for the purpose of the experience accumulation,

such as to find the type of troubles and system bugs which could provide ideas of the system improvement.

Table 2. Comparison of the thyratron tubes.

ITEM	ITT F-303	Litton L-4888	EEV CX-1836A
Heater(V_{ac}/A) *max*	6.6 / 80	6.7 / 90	6.6 / 90
Reservoir(V_{dc}/A) *max*	6.0 / 20	5.5 / 40	6.6 / 7
Peak anode(kV/kA) *for*	50 / 15	50 / 10	50 / 10
Peak anode vol.(kV) *inv*	50	*n/c*	50
Avg. anode cur.(A) *max*	8	8	10
min DC anode vol.(kV)	2	10	5
Heating factor($x10^9$) *max*	300	400	*n/c*
dI/dt(kA/μs) *max*	50	16	10
Anode delay(μs) *max*	0.3	0.4	0.35
Trigger jitter(ns) *max*	2	10	10

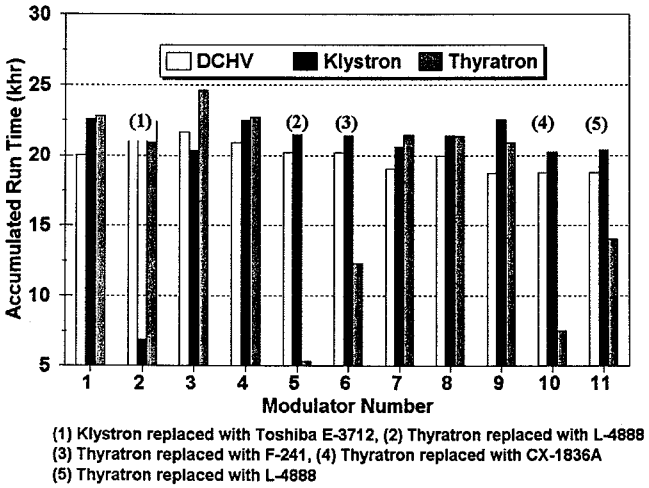

Fig. 1. Accumulated run times of the K&M systems.

The statistical analysis of the machine availability presented in this paper is applied to two different periods. One period is based on the operational method of the manual reset mode by the maintenance crew only for the period of September 1994 to May 1995. The other is based on automatic reset mode by the remote computer control for the period of May 1995 to May 1996. The major circuit change for the computer controlled reset mode is the CB trip interlock modification ; instead of CB trip activates SCR gate hold and the soft start of the DC high voltage.

System Availability Statistics

Since the completion of the PLS 2 GeV linac installation in December 1993, all the K&M systems have been in operation continuously except scheduled short-term shut downs. Fig.1 shows the total accumulated times of klystron and thyratron heater operation, and the high voltage run. Sum of the high voltage run time of each modulator has reached over 230,000 hour, and the experience accumulated so far provides the valuable information for the stable operation. Fig. 2 shows the monthly failure and down time statistics for the period of September 1994 to May 1995(manual reset) and the period of May 1995 to May 1996(auto reset).

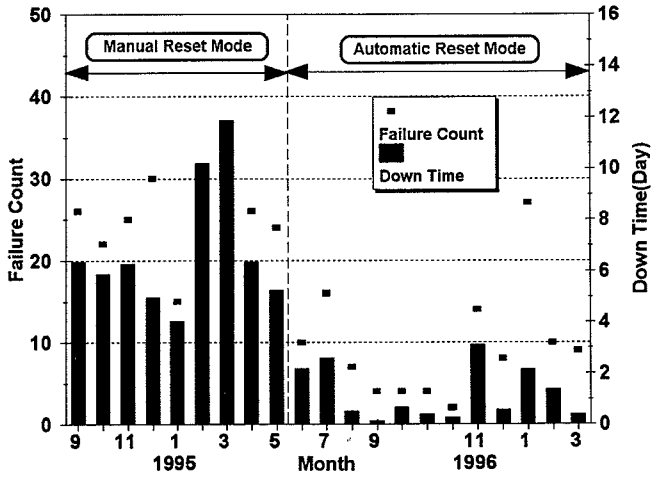

Fig. 2. Monthly failure and down time status of klystron-modulator system.

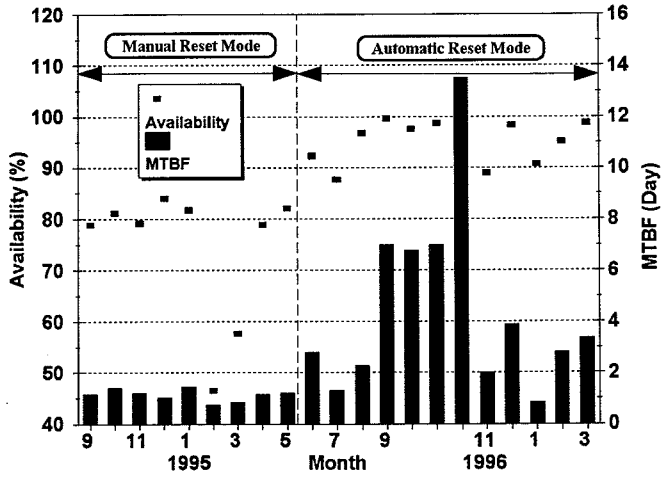

Fig. 3. Monthly availability and MTBF status of klystron-modulator.

Machine availability analysis has been performed based on the data using the techniques described in detail in reference[3]. Fig.3 is the monthly availability and MTBF (mean time between failure) statistics of klystron-modulator system. The table 3. is the summary of the average fault analysis data. The MTBF calculated by dividing the sum of the accumulated modulator run time with the total fault count(MTBF=N*TO/FC). The MTTR(mean time to repair) is equal to the total down time divided by total fault counts (MTTR=TD/FC).

One can see in table 3, approximately 76% of the machine availability(A=1-MTTR*FC/TO) has been improved to approximately 96% by applying auto reset mode operation

with the simple CB trip modification, which is also shown in Fig 2 & 3. It indicates most of the system troubles are not so serious, and in many cases they are easily recoverable.

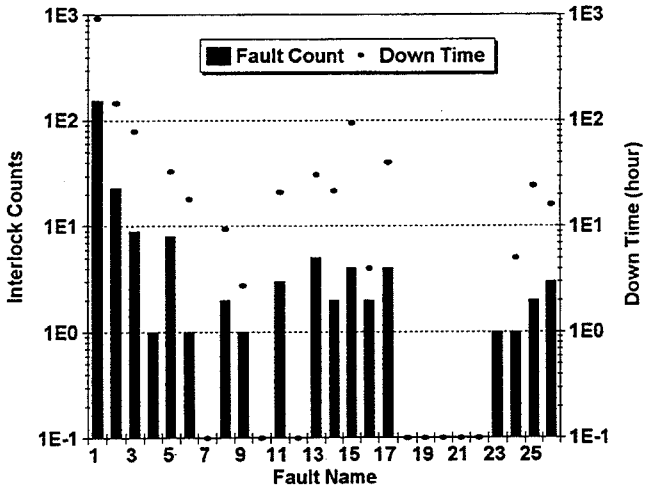

Fig. 4. Interlock status of klystron-modulator system for the period of September 1994 to May 1995.

Table 3. Fault analysis of klystron-modulator system for PLS.

Item	94.9-95.5	95.5-96.5
Number of modulators, N	11	11
Spare no. of modulators	0	0
Operation time(hr)*1, TO	6000	7560
Total failure counts, FC	226	115
Total down time(hr)	1468	344
MTBF(hr)	26.5	65.7
MTTR(hr/failure count)	6.5	2.998
System availability, A	0.76	0.96

*1) Operation time for the statistical analysis.

Fig. 4 shows the total systems static fault count data collected during the period of September 1994 to May 1995. Fig. 5 is the total system static fault count data collected for the period of Jun 1995 to May 1996. From Fig. 4 & 5 one can see the significant decrease in CB trip count by the CB trip modification and the apparent relative increase in klystron troubles as the accumulated run time increases.

Summary

It is approximately 2 years since the PLS 2 GeV linac has started its operation. We have analyzed the klystron-modulator systems performance record for the period. It is observed that the reliability of klystron is well over our expectations compared with other components in the modulators. The life time of thyratron tubes appears to be reasonable except the occurrence of infant failures. However, the major improvement is necessary for the reservoir control which is the main source of system troubles. The machine availability statistics of the K&M system for the manual reset mode is calculated to be approximately 76%. It appears to us that there are still lots of rooms for the improvement toward the availability more than 96% with proper choices of the protection circuits and the automatic reset mode. During the period of Jun 1995 to May 1996 we have modified our OCR (over current relay) interlock not to interrupt main CB but SCR gate(with static fault action) as an attempt to reduce major source of static fault. During the period no system damage has been occurred, and we have activated remote reset control in the case of static fault. Just one year old statistics shows an excellent system's availability of approximately 96%.

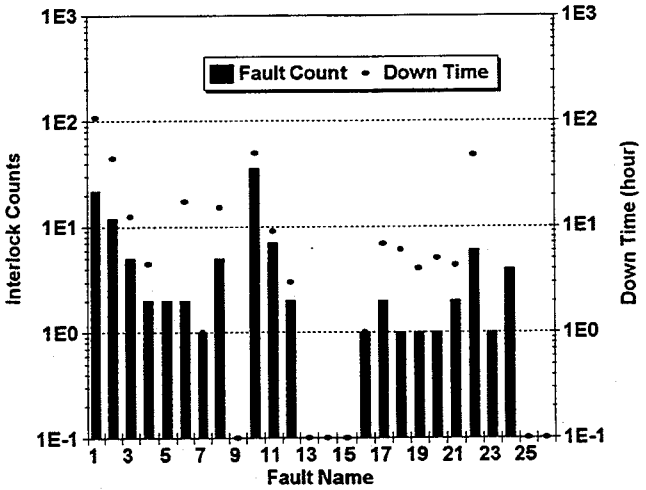

Fig. 5. Interlock status of klystron-modulator system for the period of Jun 1995 to May 1996. (1)CB trip, (2)klystron vacuum, (3)fan, (4)magnet flow low, (5)SCR ac over current, (6)magnet temp. high, (7)cooling temp., (8)thyratron heater, (9) triaxial cable, (10)klystron heater, (11)magnet current low, (12)EOLC, (13)core bias current low, (14)core bias current high, (15)key switch, (16)thyratron driver, (17)thyratron grid circuit, (18)replaced charging inductor, (19)replaced klystron, (20)replaced thyratron, (21)replaced MPS, (22)replaced ion pump controller, (23)PFN RC snubber, (24)De-Q'ing fault.

Acknowledgments

This work is partially supported by POSCO (Pohang Steel and Iron Co.) and Korea Ministry of Science and Technology.

References

[1] W. Namkung, "PLS 2 GeV Linac," Proc. 1994 Int'l Linac Conf., Tsukuba, Japan, Aug.21-26, pp.14-18(1994).
[2] M. H. Cho et. al, "High Power Microwave System for PLS 2 GeV Linac," Proc. 1994 Int'l Linac Conf., Tsukuba, Japan, Aug. 21-26, pp.418-420 (1994), M. H. Cho et. al, "Design of 200 MW Pulse Modulator for PLS 2 GeV Electron Linac," Proc. 3rd European Particle Accelerator Conf., Berlin, Germany, Vol.2,pp. 1591-1593 (1992).
[3] A. R. Donaldson and J. R. Ashton, "SLAC Modulator Operation and Reliability in the SLAC Era," IEEE Conf. Proc. 20th Power Modulator Symposium, pp.152-156 (1992).

CONCLUSIONS FROM THE LISA SUPERCONDUCTING LINAC EXPERIENCE

M. Castellano, @L. Catani,M. Ferrario, M.Minestrini,
P. Patteri, F, Tazzioli, @S. Tazzari
INFN, Laboratori Nazionali, C.P. 13, 00044 Frascati
@ INFN andUniversity of Rome II- Tor Vergata

Abstract

The commissioning of the experimental superconducting (SC) RF linac LISA (working at 4 K) has been completed and conclusions can be drawn regarding the performance of this low energy (25 MeV), high average power machine.

The illustration of the difficulties encountered in commissioning and operating this rather compact accelerator with few people can give suggestions for improvements to those interested in the application of such machines (as FEL drivers, gamma and neutron generators, etc) in a non specializaed environment.

1.Introduction

The INFN Frascati National Laboratories (LNF) started the LISA project, concerning the construction of an SC-RF linac in 1988, in the mainframe of an effort to promote activities in the field of SC-RF technology applied to accelerators.

At the beginning of the '90s however INFN decided the construction of the DAFNE Phi-factory to become the first priority of the Laboratories, thereby moving RF-SC activities and the LISA project to a lower priority level. The construction of the machine, started at the end of 1989, was nevertheless completed in 1993.

Lisa has been described in various conferences [1]. For ease of the reader we recall that the SC linac is composed of four independent cryostats, each housing a 4-cell 500 MHz cavity of the Desy-Hera design. We report the parameters of the machine in Table 1, where achieved and design values are shown. Question marks regard parameters that could not be measured for lack of specific instruments .

Table 1 - Parameter list of the LISA accelerator .

	Achieved	Goal
Energy(MeV)	20	25
Bunch length(mm)	(?)	2
Peak current(A)	(?)	5
Duty cycle(%)	2	2
Macropulse current(mA)	1	2
Invariant emittance(πmrads)	10^-5	10^-5
Energy spread	2x10^-3	2x10^-3
Micropulse frequency(MHz)	50	50
Macropulse frequency(Hz)	3	10

In the following two years the commissioning of LISA has been concluded with the limited forces of our small group (6 graduates and 3 technicians) and the support of external industries for maintenance and repairing of apparatus.

This has been possible thanks to the high degree of automation of the whole machine and to the easy use of the Apple MacIntosh man-machine interface. This experience should encourage those who are doubtful about installing a SC linac in University or research Lab environment that cannot afford a numerous team of specialized personnel.

On the other hand, a limited number of operators implies a careful organization of shifts in order to keep the machine running for long periods, as is necessary for an efficient use. In fact, as it takes about three days to cool-down the cavities and one day to warm-up, to which are possibly to be added a couple of days to recover the cold state in case of a transient electrical power failure, it is evident that the running period should not be less than one month. This can be achieved if an efficient automatic system of He gas recovery is provided, so that permanent presence of experienced personnel on the site is not requirted. In our case, in the absence of such a system, the compressor had to be restarted by an operator in a few tens of minutes, otherwise the gas was lost in air through the exhaust valves. This fact limited the running periods of Lisa to about two weeks, which resulted in a very lengthy and unefficient commissioning.

2. Commisioning of the linac

The most difficult problem we had to face during commissioning, and which ultimately limited the performance of the machine, was the presence of cavity vibrations in the cold machine, due to thermo-acoustic oscillations in the refrigerator-cryostat system. They seem to be mainly due to the close interconnection of the gas circuits of the cryostats through the common return line between valve box and refrigerator. In fact a relevant reduction of vibrations has been achieved by closing partially the gas return lines from the cryostats to the valve box, thus decoupling somehow the circuits [2]. In other similar structures (JAERI, Japan,) where each cryostat carries on top its small refrigerator, no such vibrations have been detected. A centralized scheme like ours is therefore not to be recommended. One should at least decouple each cryostat from the system by a local phase separator.

Two of the cavities show much stronger vibrations than the others. This may be due to some internal defect of insulation between the 4 K body and the 70 k shield. When ultimately we succeeeded in limiting the vibrations of these cavities so that the corresponding frequency deviation was within the loaded bandwidth, it was evident that the voltage and phase stabilizing systems have to work at their best in order to keep the beam energy fluctuations below 1%.

The phase feedback is the more critical as it has to cope with ±45 degrees deviations. The corrections require supplementary power from the klystrons, setting a limit to the voltage obtainable from these two cavities and therefore on the maximum stable beam energy (15 MeV, well below the 20 MeV peak achieved).

All cavities show structure deformations and consequent field unflatness as deduced from the measurements of their dispersion curves [3]. The maximum deviations of the inter-cell coupling factors $K\theta$ from their average are shown in

Table 2 for the two worst Lisa cavities in comparison with a not well tuned Desy cavity of which the field unflatness has been measured. It is therefore to be expected thast in our cavities the field unflatness is of the same order (i.e.70%).

Table II

	CAV-1	CAV-4	DESY NOT TUNED
$K_{\pi/4}$	1.91 %	1.91 %	2 %
$K_{\pi/2}$	2.32 %	2.27 %	2.17 %
$K_{3\pi/4}$	3.27 %	3.16 %	2.89 %
<K>	2.5 %	2.45 %	2.35 %
∂K/<K>	54 %	51 %	38 %
E_{max}/E_{min}			1.7

All cavities show also Q degradation with respect to the values originally measured at the factory in horizontal tests on the cavity fully assembled in the cryostat. As shown in Fig.1, there is a decrease of the low field Q by about a factor 2, and a decrease of the field emission threshold by about 30%.

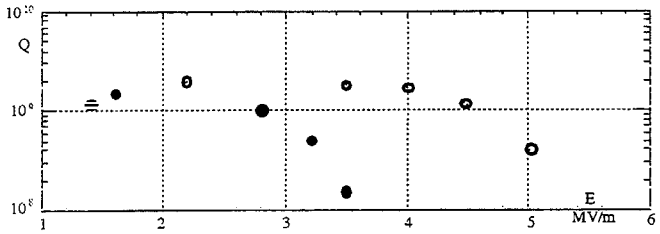

Fig.1- Typical Q vs E curve(empty dots are factory values).

This however has not been the ultimate energy limiting factor, as the pulsed regime (with several % duty cycle) is widely compatible with the cooling power of the refrigerator. Quench has rarely occurred for gradients well above 5 MV/m.

After the original degradation following the installation on the accelerator, the cavities have suffered no apparent further deterioration even though their inner walls have been hit frequently by the beam and moreover no laminar flow clean air has been employed during the frequent disassembly operations on the vacuum chamber. The machine has shown to be much sturdier in handling than feared at first.

3.Diagnostics issues.

Beam diagnostics have played an important role in the commissioning of the accelerator. The types of devices used are: toroids for average macropulse current, strip-lines for transverse position and beam time structure, fluorescent and OTR targets for both transverse position and shape.

Strip-lines are essential for a good beam transport through the 1 MeV arc where no fluorescent targets are available. The data acquisition system allows to display a trajectory on line (see Fig. 2), so that manual corrections can be made to minimize the distance of the trajectory from the axis. The automation of this process has not been implemented due to lack of control software manpower.

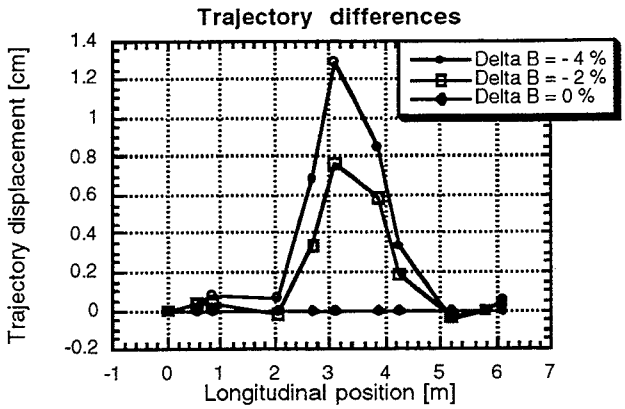

Fig. 2 - BPM measurement of the relative beam displacement in the arc varying the bending field of -2% (square points) and -4% (dot points)

The drawbacks found in the strip-lines system are scarce sensitivity, so that the readings are reliable only above 1 mA beam current, and thermal drifts that oblige to perform frequent offset calibrations. The experienced acquired in Lisa has however allowed us to design better electronics for the Desy-TTF experiment [4].

Strip-lines have also been employed in an unusual way as broadband detectors to obtain information on the time structure of the beam. The shape of the envelope of the 50 MHz lines spectrum of the signal induced by the beam on the strips gives information on the proper settings of inflector, chopper and prebuncher parameters (see Fig. 3) [5]. A proper time structure is essential for a good capture of the beam by the SC cavities.

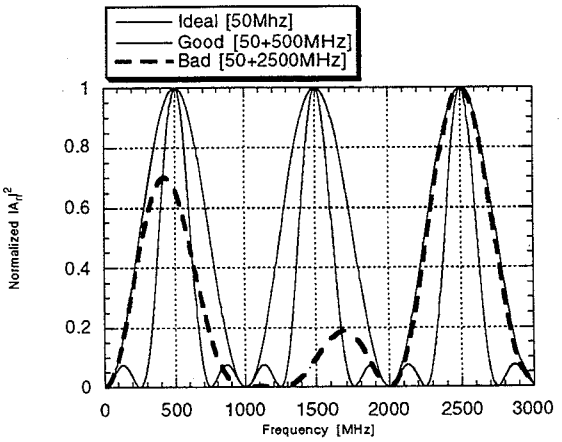

Fig.3- Normalized square amplitude of spectrum envelopes vs frequency. The outer full line is the ideal one(only 500 MHz buckets evenly filled), the inner full line is a good one(mainly 500 MHz buckets filled. The dashed line is a bad one, with many 2500 MHz side buckets filled.

As to fluorescent targets, in order to avoid saturation, it was found very useful to use simple oxidized Aluminium ones in the lower energy part of the injector. Optical Transition Radiation foils, originally planned only to test the prototypes for the Desy-TTF experiment, have shown to be a very effective instrument for the beam transverse charge distribution measurement at higher energies.

Measurement of bunch length, which is expected to be a few ps, was not possible because of lack of specific

instruments. A tentative to use the traditional indirect method consisting in detecting energy spectrum variations vs the RF phase of one of the cavities [6] failed because the beam after the SC cavities was not stable enough over long periods. We have however prepared the hardware for a measurement on the 1 MeV injector beam, which is sufficiently stable, based on coherent transition radiation spectrum [7] and we hope to perform it in the near future.

4- Reliability.

A question that is often posed by potential users of SC linacs is about the reliability of operation of such a machine. Only the non traditional parts will be discussed here. It must be stated first that the operation has been too discontinuous to allow for statistics and that this machine was not intended for users. The various sectors have worked for about two months per year (in 4 shifts of two wees each) from 1992 to 1995. Only in the last two years the machine has been commissioned as a whole.

The hardware of the SC cavities has behaved well. No discarges were detected in the main couplers, due to their large oversizing, and we did not need to use the antenna cooling system. No troubles came from the HOM suppressors, which were left unterminated, due to the negligible interaction of the beam with HOMs.

The refrigeration system has performed well. We had only to substitute, after the first two years, the gas exhaust valves on the cavity LHe container, which had lost their tightness due to frequent blowing in preliminary manoeuvres. Occasional interruption of operation during the shifts was mainly caused by electrical power failure due to thunderstorms.

Another peculiar accident connected with the high charge of the beam pulse regards the glass windows through which the cameras look at the fluorescent targets. Several of these windows were broken due to charge accumulating on the surface. We solved the problem by a metalization of the surface itself.

5. Conclusions

Regarding general features of the accelerator, it is to be remarked that the 1 MeV injection energy is too low for a good beam capture efficiency by the SC cavities. A few more MeV would be advisable. It would also be better to place the injector on axis with the cavities, to avoid beam position fluctuations due to imperfections in the achromaticity of the arc in connection with injector beam energy variations (in our design the arc was required by the planned recirculating beam transport after the FEL interaction for energy recovering).

In conclusion, the correction of the defects of two of the cavities and some modifications of the LHe distribution system would allow LISA to attain the design goals. It is the priority given to other projects that has stopped the work on this machine. In fact many potential uses of this machine have been proposed besides the original FEL application.

The intense, high quality beam of this machine, that has allowed us to detect OTR radiation without difficulty even at 1 MeV [8], is a precious source, and many experiments have been proposed, among which the generation of high brillance monochromatic X rays through channelling in crystals, a medium intensity cold neutron source, and the test of coherent inverse Compton scattering .

References.

[1] - Proceedings of the 1990 Linac Conference-Los Alamos - . 635.

[2]- Proc. RF SC Workshop - Saclay 1995.

[3]- Proc. PAC 1993- CEBAF-573.

[4] - P. Patteri et al- EPAC 96 Proceedings.

[5] - M.Ferrario et al.EPAC 96 Proceedeings.

[6] - M.Jablonka et al-Beam performance of MACSE-EPAC 94, London- 713.

[7]- H. Wiedemann et al.
Physical Review Letters **73**, 1994, N.7

[8]- M. Castellano et al.
Nuc. Inst. Meth. in Physics Res.- **A357** (1995) 231.

A High Current Proton Linac with 352 MHz SC Cavities

C. Pagani, G. Bellomo, P. Pierini
INFN - Sezione di Milano - LASA, Via Fratelli Cervi 201, 20090 Segrate (MI) Italy

Abstract

A proposal for a 10–120 mA proton linac employing superconducting beta-graded, CERN type, four cell cavities at 352 MHz is presented.

The high energy part (100 MeV-1 GeV) of the machine is split in three β-graded sections, and transverse focusing is provided via a periodic doublet array. All the parameters, like power in the couplers and accelerating fields in the cavities, are within the state of the art, achieved in operating machines.

A first stage of operation at 30 mA beam current is proposed, while the upgrade of the machine to 120 mA operation can be obtained increasing the number of klystrons and couplers per cavity. The additional coupler ports, up to four, will be integrated in the cavity design. Preliminary calculations indicate that beam transport is feasible, given the wide aperture of the 352 MHz structures.

A capital cost of less than 100 M$ at 10 mA, reaching up to 280 M$ for the 120 mA extension, has been estimated for the superconducting high energy section (100 MeV-1 GeV).

The high efficiency of the proposed machine, reaching 50% at 15 mA, makes it a good candidate for proposed nuclear waste incineration facilities and Energy Amplifier studies [1, 2].

Choice of the 352 MHz Frequency

Our design is based mainly on the choice of a low RF frequency for the SC linac. A wide experience in the design, construction and operation of 352 MHz cavities and RF systems is available at CERN [3]. The 352 MHz frequency at moderate gradient operation (around 5 MV/m) allows for large geometrical irises and lower beam current densities. A critical issue for such a machine will be the control of the beam halo growth [4], and the choice of a low frequency allows to lower both the space charge tune depression and the ratio of the beam (core) size with respect to the beam line aperture.

Another important issue, the future availability of several 1.3 MW CW klystrons of the CERN LEP RF system, that will be decommissioned before year 2000, gives an economical impulse for the investigation of a scheme based on the LEP 352 MHz frequency. Moreover, we have also to take into account the experience of several European companies for cavities production and the cavity tooling machines already available at the companies [3].

In our view the developement of new β-graded structures [5, 2], with up to four coupler ports, at 352 MHz could allow to reach a beam current of 120 mA employing present technological RF components (simply by incrementing the number of klystrons and couplers/cavity, limiting the power per coupler to approximately 200 kW).

In the following we present a preliminary parameter set for the high energy part (100 MeV-1 GeV) of the machine, as presented to C. Rubbia in the framework of a possible INFN collaboration to the Energy Amplifier and waste transmutation project. The low energy part should be composed of two sections: an RFQ [2] (up to ≈ 7 MeV) and a conventional DTL linac (up to ≈ 100 MeV). This design has been recently included as the candidate for the high energy accelerator section of the Energy Amplifier proposal [6], and work is in progress for a full optimization of the optics and for the development of the RF cavities.

The β-graded structures for the high energy section

We have chosen to cover the energy range from 100 MeV to 1 GeV with three different families of β-graded four cell cavities at 352 MHz, with cell length defined as $L_{\mathrm{cell}} = \bar{\beta}\lambda_{\mathrm{RF}}/2$. Four cell cavities have been chosen in order to reduce the number of cavities and the physical structure length, that has to include cut-off tubes, coupler and HOM ports.

This choice of three energy ranges (and consequently of three $\bar{\beta}$ values for the different sections) allows to keep the transit time factor of a particle in each cavity always greater than 0.9, along the whole machine. The main characteristics of the cavities in each section are given in Table 1.

Table 1: Energy range, design $\bar{\beta}$, active length and length of the focussing period, for the three families of 4 cell cavities.

Energy (MeV)	$\bar{\beta}$	L_{active} (m)	L_{FIDO} (m)
100–185	0.47	0.800	7.5
185–360	0.60	1.022	8.4
360–1000	0.76	1.294	9.5

The energy gain in each cavity is given by:

$$\Delta T_{\mathrm{cav}}(MeV) = L_{\mathrm{active}}(m) E_{\mathrm{acc}}(MV/m) g\left(\frac{\bar{\beta}}{\beta}\right)\cos(\phi_{\mathrm{RF}})$$

where $L_{\mathrm{active}} = NL_{\mathrm{cell}}$ is the active cavity length (in Table 1), E_{acc} is the accelerating field in the cavity, $g(\bar{\beta}/\beta)$ is the transit time factor of the cavity, depending on the design $\bar{\beta}$ and the actual beam β, and ϕ_{RF} is the operating RF phase.

In our design, considering the requirement of phase stability, we have chosen $\phi_{\mathrm{RF}} = -30°$, and $g > 0.9$ all over the machine.

The role of the transit time factor g can be seen in Figure 1, where we plot the energy gain of each cavity along the machine. Here we chose a constant E_{acc} in each section (the values are given in Table 2); as an alternative approach one can individually set the cavity gradients to provide a constant energy gain in the sections.

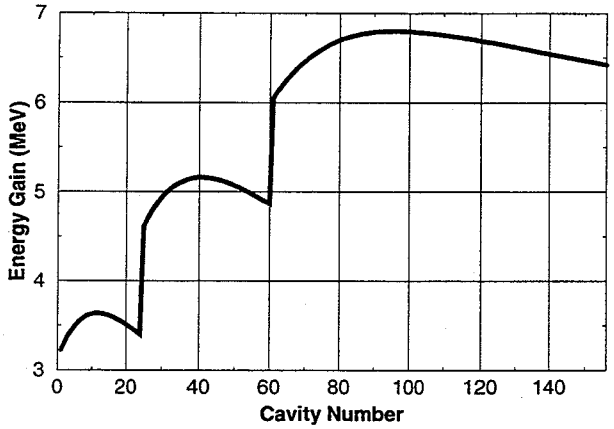

Figure 1: Energy gain along the three linac sections, as a function of the cavity number, keeping the nominal accelerating gradient fixed in each section (see text for details).

The basic accelerating cell of each linac section consists of one cryomodule containing four cavities, transverse focusing is provided by quadrupole doublets every cryomodule.

Focusing Structure

The focusing structure is a FIDA cell, where the beam acceleration is provided by four RF cavities, in one cryomodule, between successive quadrupole doublets, as seen in Figure 2. The possible use of quadrupole triplets to allow for 'rounder' beams will also be considered.

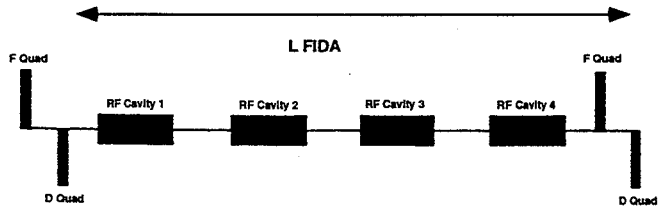

Figure 2: Focusing structure of the linac.

The three sections of the linac have different cell lengths. The active cavity length and the corresponding lattice periodicity in the three sections are indicated in Table 1.

The quadrupole integrated field Gl ranges from 1 to 3.5 T along the machine, hence it is possible to place warm normal conducting quadrupoles between the cryomodules.

For this reference design the zero current maximal phase advance per cell has been set to 90°, although a value close to 60° or 72° should be more appropriate. In the first unit of the first section there is a strong longitudinal phase advance and a reduction of E_{acc} will be investigated.

Preliminary calculations with the linear space charge code TRACE-3D [7] in the current range of 10-120 mA show that beam transport with a beam radius/aperture ratio in the range 10–50 along the machine is possible.

Section details

In Table 2 we report the main characteristics of the three sections of the high energy part of the linac, including RF power distribution. The maximum RF power in the couplers is approximately 200 kW, the current upgrade would require the insertion of additional couplers (up to four) in each cavity. The four coupler ports should be integrated from the beginning in the cavity design.

Table 2: Section details.

	S. 1	S. 2	S. 3
N. of structures	24	36	96
$\bar{\beta}$	0.47	0.60	0.76
E_{acc} (MV/m)	5.2	5.8	6.0
Section length (m)	45	76	226
10 mA beam current			
RF Power/section (MW)	0.85	1.81	6.35
RF Power/cavity (kW)	35.4	50.3	66.1
couplers/cavity	1	1	1
Klystron/section	1	2	6
120 mA beam current			
RF Power/section (MW)	10.2	21.72	76.2
RF Power/coupler (kW)	212	201	198
couplers/cavity	2	3	4
Klystron/section	≈10	≈20	≈80

A total of 156 cavities and 350 m of physical length are required for the three sections of the superconducting linac, in this reference design. These two numbers could slightly increase in the final design, in order to: decrease the cavity gradient, employ quadrupole triplets focusing, include beam diagnostic elements inside the cryomodules or matching elements between sections.

Cost of the linac, and efficiency considerations

The capital cost of the superconducting linac, excluding the RF power costs, is approximately 72.5 M$, and the cost breakdown is indicated in Table 3.

Estimated RF Capital Cost

Assuming, 1.5 M$ per klystron (1.3 MW, CW with power supplies) and 50 k$ per coupler (including the RF distribution), in Figure 3 we plot the total capital cost of the linac (including the RF system), and the total capital cost per MW of beam power, as a function of the beam current (in mA).

Table 3: Capital cost of the SC linac.

Item	Number	M$
Cavities (with tuners)	156	39.0
Quadrupoles	78	3.1
RF Controls	156	4.2
Vacuum Pums	40	1.0
Vacuum Valves	78	1.0
Cryostats	39	8.0
Beam Monitors	80	0.8
Controls	1	3.0
Cryoplant Cost (8 kW @ 4.2 K)	1	8.9
Ancillary Equip. (350 m)		3.5
Total Cost		72.5

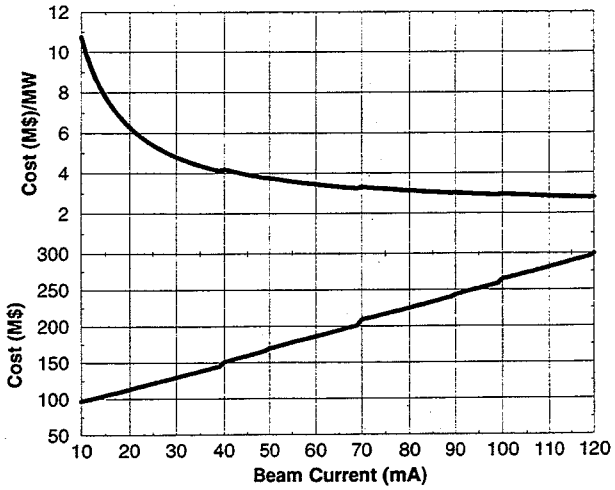

Figure 3: Lower curve: Linac total capital cost (in M$, including RF system). Upper curve: Total cost per MW of beam power vs. beam current (mA).

Overall Linac Efficiency vs. Beam Current

Assuming a klystron efficiency of 58%, a refrigeration power of approximately 2.5 MW and a contingency power of 1 MW dedicated to the ancillary components of the linac, the overall efficiency of the machine as a function of the beam current is presented in Figure 4. Note that 50% plug efficiency is reached at 15 mA operation. The operation at the full 120 mA current would allow to reach nearly the nominal klystron efficiency.

Conclusions

A preliminary study for a low frequency, high current superconducting proton linac for nuclear waste incineration and energy amplifier applications has been proposed. The machine operates at the 352 MHz of the LEP RF system with three sections of β-graded superconducting cavities.

Preliminary calculations indicate that beam transport at high current is possible, and further studies to address cavity design, both from the electromagnetic and the engineering point of view, and beam halo formation are in the starting phase.

The choice of the RF frequency and of the machine parameters provides a very good plug efficiency at high beam current, a crucial issue for the proposed applications.

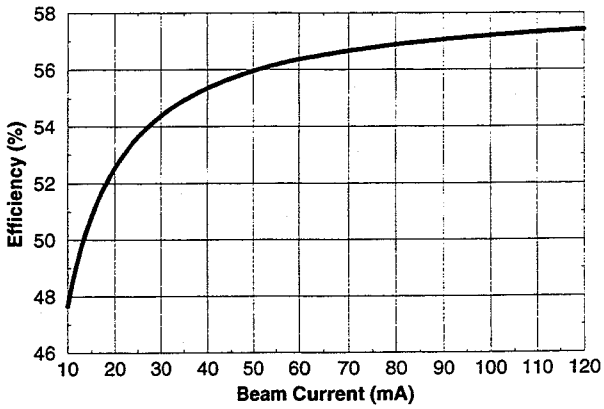

Figure 4: Overall linac plug efficiency vs. beam current (mA)

Acknowledgements

We are grateful to Carlo Rubbia who stimulated this work.

References

[1] C. Rubbia et al., 'Conceptual Design of a Fast Neutron Operated High Power Energy Amplifier', CERN/AT/95–44 (ET);
F. Carminati et al., 'An Energy Amplifier For Cleaner and Inexhaustible Nuclear Energy Production Driven By a Particle Beam Accelerator', CERN/AT/93–47 (ET).

[2] G. Lawrence, 'Transmutation and Energy Production with High Power Accelerators', Proceedings of the 1995 Int. Part. Accel. Conf., p. 35, (1996), and references therein;
K. Chan et al., 'Superconducting High Intensity RF Proton Linac for Transmutation Technologies', Proceedings of the 7th Workshop on RF Superconductivity, p. 623, (1996).

[3] E. Chiaveri, 'Production by Industry of a Large Number of Superconducting cavities: Status and Future', Proceedings of the 7th Workshop on RF Superconductivity, p. 181;
G. Geschonke, 'Experience with Superconducting RF Cavities in LEP', ibidem, p. 143, (1996).

[4] R. Ryne, S. Habib, T. Wangler, 'Halos of Intense Proton Beams', Proceedings of the 1995 Int. Part. Accel. Conf., p. 3149, (1996), and references therein.

[5] J. Delayen et al., 'Design Considerations for High-Current Superconducting Ion Linacs', Proceedings of the 1992 Linac Conference, p. 1715, (1993).

[6] C. Rubbia and J. Rubio, 'A Tentative Programme Towards a Full Scale Energy Amplifier', CERN/LHC/96–11 (EET), Geneva, 15th July 1996.

[7] K.R. Crandall and D.P. Rushtoi, 'TRACE-3D Documentation', LA-UR-90-4146.

PRELIMINARY RESULTS ON NIOBIUM SPUTTERED FILMS INSIDE TESLA TYPE CAVITIES

M.Minestrini, M.Ferrario, @W.DeMasi, @V.Merlo, @S.Tazzari
INFN, LNF, P.O. Box. 13, 00044 Frascati, Italy
@University of Tor Vergata and INFN Sez. Roma II - Via della Ricerca Scientifica 1, 00133 Roma, Italy

Abstract

In the framework of the ARES project and as a possible application for TESLA [1] we realized a test set-up to study the deposition of Nb films inside a single-cell TESLA type cavity. The plasma confinement was obtained with two external coils centered on the cavity axis in a magnetic bottle configuration. The system is operational and optimization of the discharge parameters is in progress: samples are been produced to test the film quality.

This paper covers a brief description of the test set- up and preliminary results on samples (thickness, RRR, and XRD measurements).

Introduction

The Nb coated copper cavities provide higher stability against quench respect to cavities traditionally made of Nb sheet. This is a very important characteristics for high acceleration field application, because quenching is still a field limitation above 10MV/m for high frequency cavities [2].

Sputtering is a well known [3] and useful technique for coating copper RF cavities with superconducting thin films [4], [5].

Magnetron sputtering to coat accelerating cavities with superconducting film was developed at CERN for 500 MHz cavities, and is at present used in industry to coat 350 MHz copper cavities for LEP with Nb films [6]: the magnetic field is produced by a coil placed inside the cylindrical cathode and displaced in steps along the cavity axis to achieve a uniform coating.

Because our setup is designed to coat 1.3 GHz cavities for TESLA that are 3 times smaller than the CERN ones, external coils placed on the outside of the cavity cut-off pipes (see Fig.1) and producing a magnetic mirror field configuration have been adopted, so as to preserve full control over the field shape and intensity.

The two coils are contained in a soft iron shield (low carbon contents) 4 mm thick realized so as to be taken down completely and changed according to needs. This configuration has the aim to obtain a magnetic field concentrated along the axis of cavity with a minimum at center of about 200 Gauss and a mirror ratio ($B_{min.}/B_{max.}$) of about 2.

The field simulation has been obtained with Poisson-Superfish program, on which is based the whole coil design.

The Sputtering System

The sputtering system is schematically shown in Fig.1; we have different stainless steel TESLA type cavities [7] in the inner walls of which, along all cavity profile, we can place small copper and sapphire (Al_2O_3) samples that allow us to make a complete film diagnostic. We can characterize the Nb film through RRR (Residual Resistivity Ratio), T_c thickness and XRD (X Ray Diffraction) measurements.

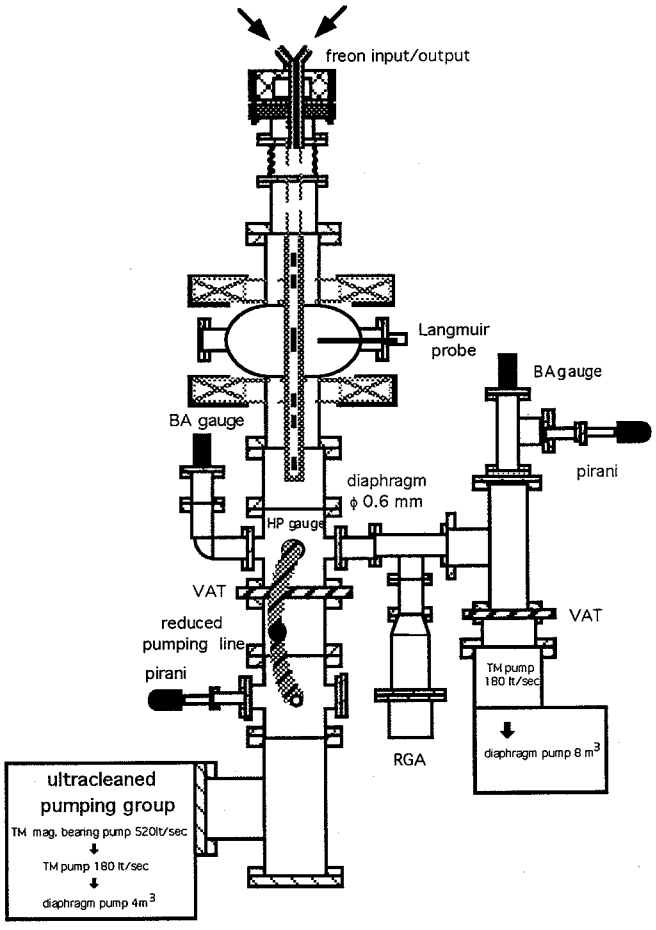

Fig.1 Sputtering system scheme

The vacuum on the system is performed by an ultracleaned pumping group consisting in a 4 m^3/h diaphragm pump for the primary vacuum and two on fall turbo molecular pumps (nominal pumping speed respectively 180

l/sec and 300 l/sec) one of which is provided with magnetic bearing, in this way we have a very good compression ratio for hydrogen besides a good ultimate pressure (~10^{-10} mbar) and total absence of hydrocarbons.

The system is provided of a residual gas analyzer (RGA) which besides finding the ultimate pressure gas composition, permits to check, during sputtering process, the percentage of gas produced, as for instance hydrogen, that damages the film structure if it is over a certain threshold. To use the RGA during sputtering process, due to relatively high operating pressure (~10^{-3} mbar), we need a differential pumping, i.e. the RGA communicates with cavity through a diaphragm of .6 mm and it is provided with another pumping system in such way as to decrease the pressure of 3 order of magnitude respect to the pressure of the cavity vacuum chamber.

The cathode consists of a vacuum tight stainless steel tube (17 mm inner diameter) surrounded by a niobium liner (20/24 mm inner/outer diameters). The liner is an high purity Nb tube (RRR value better than 150) without welding. The stainless steel tube is provided of an inner support that holds and centers 7 SamCo permanent magnets (small cylinders 8 mm diameter 16 mm long) along all the cavity length that will be cooled through a liquid freon circuit to take away about 2 KW of power. We have performed the preliminary tests to optimize discharge parameters; in those preliminary tests we used magnetic bottle configuration without permanent magnets inside cathode.

Discharge parameters optimization

To characterize our system we produced I versus V curves for different pressures, typical curves are shown in Fig. 2.

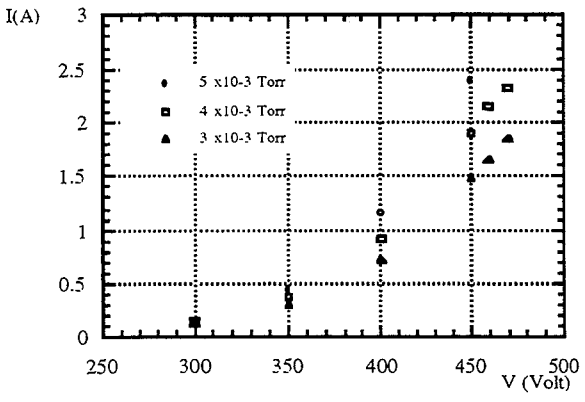

Fig.2. Discharge characteristics at different pressures

The current in our coils was 80 A and the distance between the coils 17.5cm. After a coil shields optimization and coils distance reduction (10.8cm) to increase plasma confinement, we could work at lower pressure (3x10^{-3} Torr) and higher current (1.5 A) with same voltage; we obtained the I versus V curves showed on Fig. 3.

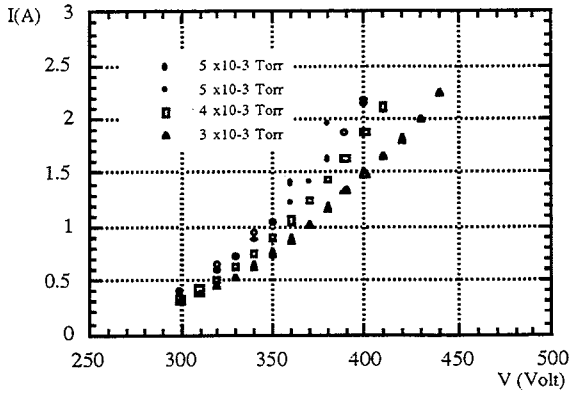

Fig.3. Discharge characteristics at different pressures with new magnetic shields configuration

We produced 4 samples, the discharge parameters for each sample are listed on table 1. The sample 4* is produced with new magnetic shield configuration.

Sample	Current [A]	Power [W]	Pressure [mTorr]	t
1	1.0	400	4.5	60'
2	1.0	400	4.5	60'
3	1.2	480	5.1	60'
4*	1.5	600	3.0	50'

Table 1
Discharge parameters

As one can observe the discharge current for last sample was increased at lower pressure due to a better plasma confinement with new magnetic field configuration.

Measurements on samples

The crystalline quality of the samples has been investigated by means of x-ray diffraction in the θ-2θ mode using Cu $K\alpha_1$ radiation. Diffraction data from sample 4* are shown in Fig 4.

Indexing of the lines allowed the identification of three different orientations, namely (110), (211), (321), the latter being barely discernible as a bump in the experimental data. The lattice constant d_o has been estimated by careful extrapolation in order to minimize systematic errors (see

Tab.2), a comparison can be made with the value d_o=3.30 Å quoted for bulk Nb crystals. The samples have thus the same lattice parameter within the experimental uncertainties (± 0.006 Å).

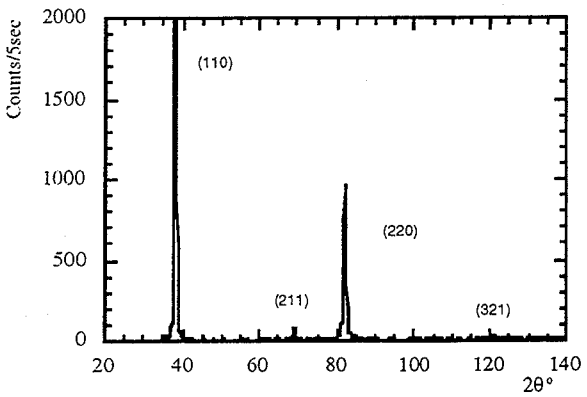

Fig.4 Diffraction data for sample 4*

Other conclusions can be drawn from an analysis of the relative intensities of the diffraction peaks from the (110), (211) orientations. For a polycrystalline sample the ratio of the intensities can be calculated using standard crystallography packages (including temperature factor corrections), yielding the value I_{211}/I_{110} = 0.305. The same ratio has been estimated from the experimental data (see Tab.2). From these results it is readily seen that the films have a tendency to grow along a preferred orientation, in this case the (110). The effect is particularly evident in samples 3 and 4*, where the intensity from the (211) orientation is depressed by a factor of 30 compared to the predicted intensity from a polycrystal.

Sample	Depos.rate [Å/sec]	d_o [Å]	I_{211}/I_{110}	Thickness [μm]	RRR
1	4.4			1.6	9
2	4.4	3.312	9.2×10^{-2}	1.6	10.5
3	6.1	3.314	9.7×10^{-3}	2.2	12.5
4*	8.7	3.316	1.1×10^{-2}	2.6	16

Table 2
Results on samples measurements

An analysis of RRR shows that the values increase with the deposition rate and with the thikness; for sample 4* a lower deposition pressure works together producing a further increase.

Conclusions

We need more statistics, but preliminary results on RRR measurements show that this new magnetron sputtering configuration is competitive with the CERN one [8].

In the near future we plan to optimize the magnetic field in order to further improve the discharge confinement.

Surface resistance measurements are also foreseen to obtain a more complete diagnostic picture of film quality.

References.

[1] TESLA Collaboration, TESLA TEST FACILITY LINAC - Design Report, ed. D.A.Eduards (DESY Print March 1995, TESLA 95-01).

[2] H.Padamsee, Proc 6th workshop on RF superconductivity, ed. R.M.Sundelin, CEBAF 93, vol.1

[3] J.A.Thornton, A.S.Penfold, Thin film processes, ed. J.L.Vossen (Academic Press, New York 1978).

[4] C.Benvenuti, N.Circelli, M.Hauer and W.Weingarten, IEEE Trans. Mag. MAG-21 (1985) 153 .

[5] C.Benvenuti, N.Circelli, M.Hauer, Appl. Phys. Lett. 45 (1984) 5.

[6] C.Benvenuti, D.Bloess, E.Chiaveri, N.Hilleret, M.Minestrini, W.Weingarten, Proc. 3rd workshop on RF superconductivity, ANL-PHI-88-1, vol. 2.

[7] M.Ferrario, S.Kulinski, M.Minestrini, S.Tazzari, Nucl. Intr. & Meth. in Phys. Res. A 343 (1994) 655-662.

[8] G.Orlandi, C.Benvenuti, S.Calatroni, M.Hauer, F.Scalambrin, Proc 6th workshop on RF superconductivity, ed. R.M.Sundelin, CEBAF 93, vol.2

PROGRESS UPDATE ON THE DEVELOPMENT OF THE ^{3}He LINAC FOR PET ISOTOPE PRODUCTION

P. Young, D. Sun, D. Larson of Science Applications International Corporation,
R. Pasquinelli, K. Anderson, F Bieniosek, C. W. Schmidt, M. Popovic, E. McCrory, R. Webber of Fermilab*,
J. Link, K. Krohn, of the University of Washington, and J. Bida of the Biomedical Research Foundation of Northwest Louisiana

Abstract

In 1995, Fermilab and SAIC formed a collaboration with partners from the University of Washington (UW) and the Biomedical Research Foundation of Northwest Louisiana (BRF) to explore an innovative approach to the production of radioisotopes. The accelerator system that is being developed accelerates ^{3}He to 10.5 MeV and then delivers this beam to the target to produce the short lived radioisotopes of interest to the PET community (^{18}F, ^{15}O, ^{13}N, ^{11}C). Research is being conducted to investigate the contribution that this promising approach can make to clinical and research PET.

The accelerator system has several very interesting aspects. These innovations include multiple RFQ accelerators configured in series, a gas stripper jet to doubly charge the low energy (1 MeV) ^{3}He beam, and an isochronous matching section to manipulate the transverse and maintain the longitudinal profile of the beam (without the use of an RF buncher) in the charge doubler transition section between RFQ's. This paper updates the progress of the PET ^{3}He RFQ accelerator, the current status of the design, and some of the interesting ongoing research.

Introduction

The idea of using ^{3}He for the production of radioisotopes for PET is not new. Development work on this concept was conducted by SAIC and the University of Washington in the early 1990's.[1] When the original program was being formulated, the PET environment in which it could make a contribution was significantly different than it is today. The original development was based on the belief that ^{18}F labeled compounds would be favored by the PET community. Also important was a global shortage of ^{18}O which made the standard approach of producing ^{18}F using $H_2{}^{18}O$ expensive and potentially unpredictable.

Since that time things within the PET community have changed significantly. There is no longer a significant shortage of $H_2{}^{18}O$. Also, FDA policy has changed regarding regulation of PET radiopharmaceuticals (Federal Register, February 27, 1995). The new policy no longer gives an advantage to ^{18}F labeled compounds. This means that ^{11}C agents are now no more trouble than ^{18}F. Carbon opens up a much larger array of molecules to label. Furthermore, recent developments in radiochemistry for preparing the important precursor, $^{11}CH_3I$, avoid the use of liquid solvents and $LiAlH_4$ which are very air and moisture sensitive, and make the precursor directly in the gas phase and at substantially higher specific activity. This leads to a smaller yield (mCi) requirement of $^{11}CO_2$. But, to take full advantage of this new technology, higher specific activity is necessary (i.e. new PET machines must be good producers of ^{11}C as well as ^{18}F). In these several ways the environment in which ^{3}He RFQ technology can make a significant and meaningful contribution to the advance of PET has changed.

While there have been interesting developments of several new low energy accelerators over the last 2-3 years - the Cyclone 3D (IBA), the TR13 (EBCO), PETtrace (GE), the tandem cascades from SRI or the new deep valley machines (CTI Siemens) - all of these machines use essentially the same nuclear reactions and target chemistry. The RFQ using ^{3}He, on the other hand, is a different approach and thus holds significant potential and research opportunities for advancing the state of the art in PET isotope generation.

System Description

Before the radiochemistry and targetry for ^{3}He could be investigated, an accelerator was needed that would supply a beam with the desired characteristics and parameters. The accelerator that had been developed by SAIC and the University of Washington in the early 1990's was a good starting point but needed to be upgraded to provide a more powerful tool for researching ^{3}He in light of current information. Analysis and a series of discussions resulted in the baselining of new operating parameters as indicated in Table 1.

Table 1 Accelerator Design Parameters

	Energy (MeV)	I_e (μA) average	Rep. Rate (Hz)	PW (μsec)
Existing Sys	8	300	360	55
New Sys.	10.5	200	360	70

Since the radiochemistry and targetry associated with pulsed high intensity ^{3}He beams was to a large extent unknown, it was decided that the system being developed needed to follow a conservative approach, i.e. it needed to be flexible and powerful enough to accommodate a wide range of targetry options. In particular it needed to be able to produce large quantities of ^{11}C since this isotope is likely to be used increasingly in PET. Table 2 indicates the beam required as a

Table 2: ^{3}He Current Required for PET RFQ

Radionuclide	mCi EOB in target	μA_e 8MeV*	μA_e 9.5MeV**	μA_e 10MeV**
^{18}F	600	333	207	177
^{11}C (low SA)	1000	202	140	125
^{11}C (high SA)	440	298	195	163
^{13}N	100	266	168	104
^{15}O (low SA)	800	517	360	318
^{15}O (high SA)	200	899	559	460

* 1 MeV energy loss in target window
** 1.5 MeV energy loss in target window

*Operated by the Universities Research Association under contract with the U. S. Department of Energy.

function of the final energy for the target quantities of the various PET isotopes. The requirements of Table 2 led to the accelerator current and energy requirements stated in Table 1. With this baseline information from our radiochemistry collaborators at UW and BRF, the existing 8 MeV ^{3}He accelerator was redesigned to meet the new requirements. The results of this redesign are shown in Figure 1. This layout makes the most efficient use of the existing equipment while solving some of the more challenging technical problems. Some interesting aspects of this accelerator system are:

Ion Source

Since one can achieve a much more efficient acceleration (length and power) with a doubly charged beam, a very attractive approach would be to make use of a doubly charged ion source. Unfortunately, nature works against this goal. With the second electron being bound with an energy of about 54.4 eV, common ion sources do not produce sufficient quantities of the doubly charged ion (15 mA required). As an alternative, the singly charged beam can be accelerated to an energy where it can be efficiently stripped (1 MeV). It is this approach that has been taken.

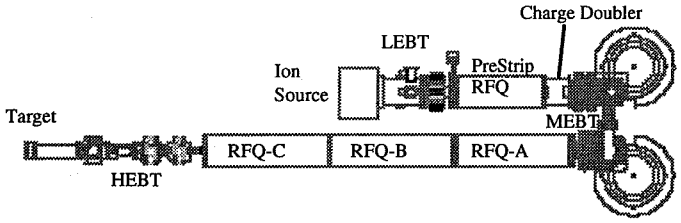

Figure 1. Layout of the BRF PET Accelerator.

Charge Doubler

At an energy of 1 MeV and a current of 400 μA_{avg} (20 mA_{peak}), carbon foil strippers could not survive the high power density. Both gas cells and gas jet strippers have been investigated. A jet stripper has been developed and tested with very promising results.

Medium Energy Beam Transport (MEBT)

The most difficult aspect of this accelerator system is the matching element between the prestripper and the post stripper RFQ's. This transition section needs to accomplish several things. It must provide sufficient space to accommodate the gas stripper (gas containment) while maintaining the longitudinal bunching of the beam and transversely matching the beam into the second RFQ. To overcome experimental realities, tunable components are desired. The longitudinal phase space of the beam must be maintained in order to eliminate the buncher/shaper section from the second RFQ (which at this beam energy would add about 1.5 m to the length of the second RFQ). Previous attempts to utilize an RF buncher to contain the beam longitudinally had been unsuccessful due to the very tight space constraints and the large number of free electrons (due to the proximity of the charge doubler). Based on this, it was decided to build an isochronous beam transport system that maintains the longitudinal and manipulates the transverse phase space of the beam.

Radio Frequency Quadrupole

The accelerator that had been developed under the earlier program had been designed for a final energy of 8 MeV. In order to achieve the higher energy requirements of the new system, it was decided that the most direct approach would be to add a third RFQ (manufactured by SAIC) to the high energy section to go from 8 MeV to the final energy of 10.5 MeV. This resulted in three RFQ's operating in series. The RFQ cavities are not resonantly coupled. Each cavity must be synchronized to and resonant at the same frequency. To accomplish this the resonant frequency of each cavity is controlled through adjustment of the temperature of the cavity cooling water. No mechanical tuners are used. Tests on this tuning system at full (2.5%) duty factor have been successful.

Status

The development of this system has taken place in two phases. A 1 MeV test stand was assembled from the accelerator components of the old system. Using this test stand, a number of the more difficult aspects of the system were addressed. Among the things that were studied are: low energy and medium energy beam characterization, ion source operation with He, charge doubler stripping efficiency, and charge doubler gas containment. The results of these tests have been incorporated into the design of the new components. Some of the information gained in the 1 MeV tests are summarized below.

Ion Source

He^+ ions are obtained from a fairly standard duoplasmatron ion source. The source operates at 360 Hz with a pulse length of 70 μs. It requires a gas consumption of 2-4 std cm^3/min (~ 1 liter / day of operation). Since ^{3}He is relatively expensive all attempts are made to minimize loss by reducing the source button (aperture) and pressure. Also the source is started and operated on ^{4}He except when ^{3}He is necessary. Because of the heavier ion and high duty factor, filament shielding is critical to prevent overheating and fast erosion. The filament is enclosed in a cylindrical shield with a sufficient opening to extract electrons while minimizing back-streaming ions. Several weeks of reliable and stable source operation have been obtained. A 25 mA beam is extracted at 20 kV from an ~ 1 cm plasma cup through a 0.8 cm grounded extraction electrode with an electron suppression electrode. Slightly after extraction the ~90% normalized beam emittance was measured to be 0.5 - 0.7 π mm mrad. One magnetic solenoid is used to focus the 20 keV beam into the RFQ. At the entrance of the RFQ, 0.7 m beyond the source, 75% of the beam is within ~0.5 π mm mrad emittance (normalized)[2].

Measured Emittance of the 1 MeV beam

After the Prestripper RFQ, at 1 MeV, the rms emittance has been measured to be 0.2 mm mrad (or ~34 π mm mrad unnormalized for 90% of the beam)[2]. This was measured with 5.5 - 7 mA at 1 MeV from the RFQ. Better matching and understanding of the RFQ transmission is needed. A maximum beam of 11 - 13 mA has been observed from the RFQ and appears to have similar characteristics. This was achieved with a larger solenoid in the 20 keV transport line.

Charge Doubler tests

A prototype stripper cell based on a pulsed gas jet was built to determine efficiency and gas flow in a realistic geometry. A mechanical injector (Nissan fuel injector) provided gas pulses to a converging-diverging nozzle. A directed gas jet of line density approximately 3-6x10^{16} cm^{-2} was created at the nozzle. It passed across the beam and was directed into a vacuum pump. The flow rate of the gas jet was sufficient to prevent excessive heating of the gas by the beam, and the injected gas was pumped out between beam pulses.

A magnetic spectrometer that bends the 1-MeV He^{+} and He^{++} beam ions into Faraday collectors at bend angles of 11.5° and 23.6° respectively, was used to test operation of the gas jet. Stripping efficiency was determined by measuring the relative distribution of beam current on the two collectors. Stripping efficiency for several gases is shown in Figure 2 as a function of back pressure on the injector.

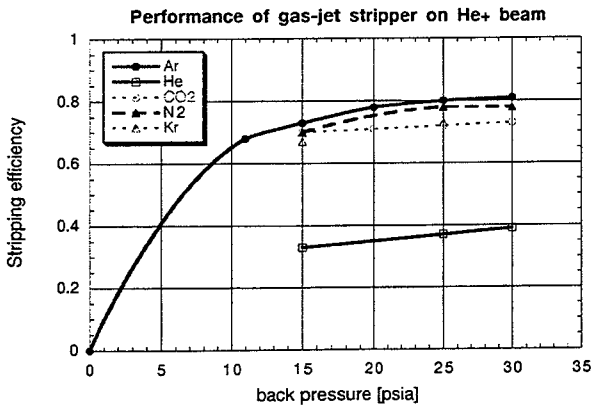

Figure 2 Performance of gas-jet stripper on He^{+} beam

The best performance was obtained with argon gas, which reached 80% stripping efficiency at a pressure of 25 psia. Pressure measured at the RFQ was 2.8x10^{-6} Torr for this operating point, at a repetition rate of 60 Hz. We expect to be able to operate at no less than 70% stripping efficiency at the design rate of 360 Hz by increasing pumping capacity. An operational version of the stripper cell is now in fabrication.

Medium Energy Beam Optics

As part of the design effort for the new MEBT (Figure 3), a number of options were investigated. It was recognized that folding the machine would accomplish the goal of keeping the length of the system manageable and could also do the longitudinal dynamics. Designs were investigated that included 180 degree bends, two 90 degree bends, three 60 degree bends, four 45 degree bends, and 30-60-60-30 degree combinations. In each case where multiple dipole designs were tried, quadrupoles were placed between the dipoles and varied in strength and position. Various internal gradients and edge angles were also tried. While it is possible to make a 180 degree bend which has the proper transition energy, it has not yet been possible to have a 180 degree bend design which is isochronous. For this and other reasons it was decided to use 2 x 270 degree bending MEBT which could be made isochronous.

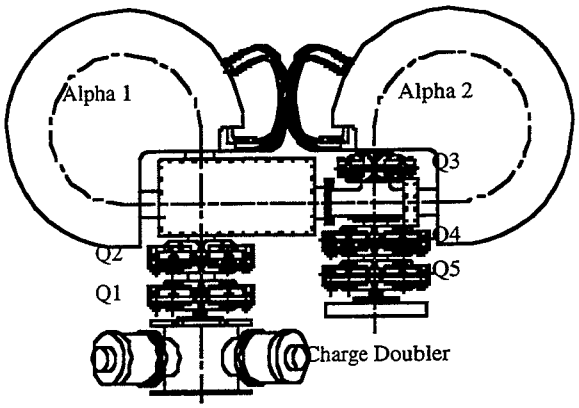

Figure 3 MEBT Mechanical Layout

The beam optics of the MEBT are shown in figure 4. The major magnets for this transport system have been fabricated and are being tested. The installation and commissioning of the transport system is scheduled to take place over the next two months.

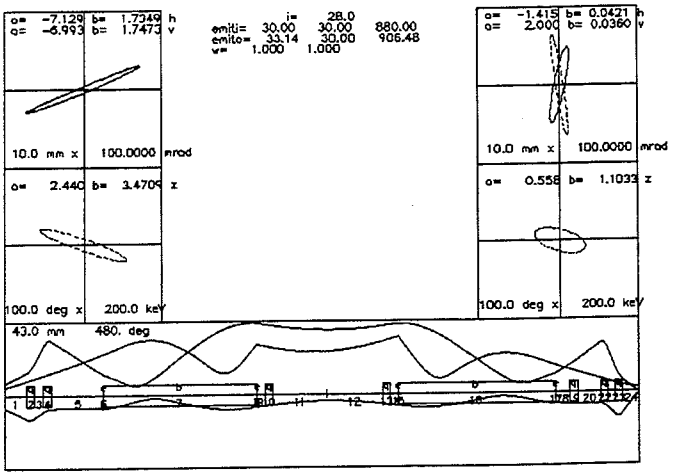

Figure 4 MEBT optics

Schedule

The modifications to the accelerator system are scheduled to be completed and tested in late 1996. Once completed, the accelerator will be run at Fermilab for 6 to 8 weeks in order to test shielding and do some initial targetry development. Following this run, the machine will be disassembled and shipped to the Biomedical Research Foundation. The accelerator system has been built in a modular fashion in order to facilitate moving. We anticipate that the move and commissioning will take about 8 weeks, after which the in-depth targetry and radiochemistry research will begin.

Reference

1. W. Hagan, et.al., "A Helium-3 RFQ Accelerator for PET Tracer Production", Proceedings of the Ivth International Workshop on Targetry and Target Chemistry, 1991, Pp 19

2. "Elliott McCrory, et.al. "Emittance Measurement Techniques Used in the 1 MeV RFQ for the PET Isotope Project at Fermilab". This Conference.

OPERATING PERFORMANCES AND CURRENT STATUS OF THE LASER INJECTOR COMPLEX FACILITY (LIC)

M.I. Ayzatsky, E.Z. Biller, A.N. Dovbnya,V.A. Kushnir, V.V. Mitrochenko,L.V. Reprintzev, and D.L. Stepin
National Science Center, Kharkov Institute of Physics&Technology(KIPT),
310108, Kharkov, Ukraine

Abstract

Paper is dedicated to description of the operating performances and current status of the Laser Injector Complex Facility (LIC). This linac was constructed for investigation of physics of the high-brightness electron beam forming and acceleration. The linac consists of a multipurpose RF gun and a novel acceleration structure. LIC can be operated with microsecond (thermionic emission) and nanosecond (laser stimulated emission) duration of current pulse and energy of electrons 13-20 MeV. In thermionic regime we have obtained electron beam duration 0.5-1 μs, beam current about 1 A and normalized rms emittance about 20 π mm mrad. The results of experimental measurements of beam performances are given..

Introduction

LIC, (Linear Injector Complex), facility was developed and constructed in view of forming and acceleration of high - brightness electron beams. This R&D was to be followed by beam research in the following arias:

- ultra - short wave generation;
- wake-field generation in plasmas and other systems;
- relativistic electron beam focusing in plasmas;
- testing of the diagnostic equipment developed within the framework of the VLEPP program.

The electron energy at the accelerator output was to be 15 to 20 MeV which is sufficient to carry out the above programs. One of the major factors taken into account during development of the facility was limitation of the RF - power (20 - 25 MW) obtainable using the available klystron KIU-12. LIC accelerator complex was commissioned during 2 years (1991 - 1992). In 1994, the facility was shut down in order to reconstruct the injector and assemble experimental devices in the area of plasma physics. The work was renewed in 1995.

Its basic components are an RF-gun [2,3], the accelerating section, beam steering and its focusing elements, beam diagnostics, cooling water system and control elements. The RF system includes a klystron with the maximum power operation up to 25 MW, a set of waveguides, controllable phase shifter and attenuator.

Having in view the multipurposeness of the facility under development, we brought out the following major criteria which were taken into account while choosing the necessary type of the accelerating structure:

- the feasibility of acceleration of beams with high charge in the stored energy mode at moderate values of RF-power input ($P \approx 20$ MW);
- reduction of amplitudes of TEM waves which are exited by high-intensity electron beam and lead to emittance enhancement or even to shortening of pulse length (BBU instability);
- the feasibility of intense electron beam acceleration with small radial dimensions with the minimum number, or even absence, of external focusing elements.

Table 1

Operating mode	$4\pi/3$ ($2\pi/3$)
Length (m)	2.31
Disk hole diameter, $2a$ (cm)	5
Disk thickness, t (cm)	5
Periodic length, D (cm)	7.145
Attenuation, α (1/cm)	$2.44\ 10^{-3}$
Group velocity	$0.01c$
Freguency, f (MHz)	2797
Shunt impedance (for fundamental space harmonic amplitude/for synchronous space harmonic amplitude), (Megohms/m)	31.3/11.3

The most attractive was the accelerating structure STRAM-90 (the abbreviation standing for STRucture Accelerating Modified) developed at NSC KIPT which has been designed to accelerate intense short -pulsed electron beams in the stored energy mode at moderate values of RF power input values ($P \approx 15 \div 20$ MW) [4,5]. This structure represents a disk-loaded waveguide with the period being two times higher than that in the disk-loaded waveguide with $2\pi/3$ mode. Particle acceleration in such structure is made by the first spatial mode of the electromagnetic wave propagating in the opposite direction to the electron beam. Beside increasing the charge value, which can be accelerated in the stored energy mode, the STRAM-type structure has the RF-focusing owing to the presence of a large non-synchronous spatial mode [6,7].

The period increase also leads to a considerable reduction in the TEM-wave generation, since the particles are synchronous with higher spatial modes of these oscillations.

However, employment of such a structure in the linac under development was hampered by two factors. The first one being in the fact that due to a small shunt impedance at the first spatial mode there was the necessity to make use of the traveling wave resonant ring in order to increase the

acceleration gradient. The second one was the structure losing its advantages during transition to the single-bunch acceleration mode [4]. We have developed a new version STRAM-91, producing acceleration at the first spatial mode, but having both an increased value of the accelerating field and a low level of higher mode amplitudes irradiated by particles [4]. This was achieved by making use of unusually thick disks with large values of the coupling hole.

Major parameters of this section, developed and fabricated at NSC KIPT, are given in Table 1. The dispersion characteristics measured at a six-cavity assembly are given in Fig.1.

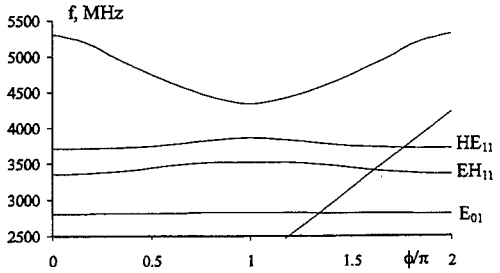

Fig.1. Dispersion characteristics of STRAM-91

The beam characteristics measurement system consists of two pulsed beam current monitors, a magnetic particle energy analyzer, a unit of movable slot collimators, a Al_2O_3 screen with a TV camera and a multi-sectional Faraday cap. Beam emittance measurements at the linac exit are performed by the three gradient technique. A quadruple lens is used for this purpose together with the particle spatial distribution monitor, placed at a distance of 2 m from the lens, and consisting of a set of moving slots 0.3 mm wide. In order to make estimations of the transverse dimensions a Al_2O_3 screen with TV-camera as well as a sectional Faraday cap consisting of several coaxial ones are employed.

Calculation Results

At all stages of the accelerator development calculations were performed both analytically and as computer simulations. In this way, during development of the acceleration section its geometrical dimensions were calculated, as well as basic RF-characteristics for operation at $4\pi/3$ mode. Besides, the calculations were done of the particle dynamics in the sections allowing to evaluate the degree of RF- focusing and peculiarities of wake-field generation.

During designing of the gun, in order to optimize its resonators and determine the beam characteristics a set of calculations and simulations (the SUPERFISH and PARMELA codes were used) was performed. In a more detail, the calculation results are given in [3]. From the calculations it follows that the gun can be used successfully both in photo- and thermionic emission modes.

In order to study the particle dynamics in the accelerator using the numeric simulations within the PARMELA code, a model of the entire accelerator was constructed including the RF gun, beam-forming elements and the accelerator section. At first stage we began to study the thermoemission regime with long pulse duration. Preliminary results show that despite of the high injection energy (W_0≈1 MeV) there is a strong phase movement of the particles at the initial part of acceleration process. We connect this fact with the smallness of accelerating field amplitude at the entries of our section. Under such conditions a strong phase movement can take place at sufficiently high energy of the injected electrons. Under optimum conditions the length of bunches can be strongly reduced (from 50° at the exit of the RF-gun to 4°- 7°- at the exit of the accelerating structure).

Very interesting are the results of radial motion. As it have been mentioned in previous papers [5,6], in the accelerating structure under consideration there is RF-focusing and at the accelerator exit we should have converging electron beam. Besides, we modeled various accelerator operation modes and beam relationship vs. different parameters in order to compare them with experimental results.

Experimental Results

Experimental studies in the operation mode of forming and acceleration of single picosecond pulses require utilization of very complicated and costly laser system. Over and above, studies on wake-field generation in plasmas in 1995 called for beams of microsecond duration. In this connection, research into accelerator characteristics during the initial stage was done at a microsecond beam current pulse. With this in mind, the gun had been outfitted with a thermionic emission cathode 5 mm in diameter [2]. The RF-tuning provided for the equal field strength in the first and second cavities which is optimum in case of the thermionic emission cathode at field strength inside the cavity of 25 to 30 MV/m.

In stable accelerator operation regimes (pulse repetition rate ≤6.25 PPS, current pulse duration 2 μs, RF-power input ~1.8 MW) the typical current pulse amplitude at the exit was 1.5 - 2.0 A. With an optimum phasing of the acceleration section the output pulsed current was 1- 1.1 A making the capture rate near 70% which is in accordance with the calculated data. Experimentally shown is the possibility of current pulse reduction at the linac exit from 2 to 0.25 μs by way of decreasing of RF-power input or increasing of cathode heating. This is accompanied by particle energy decrease at the gun exit due to beam loading, and only the most energetic electrons become involved in the acceleration process.

In the experiments was observed a ramp in pulse current of RF-gun and a drop of field strength in the cavities on account of the electron back bombardment of the cathode surface. This phenomena was studied during the experiments. It was found that at a pulse repetition rate exceeding 6.25 PPS the overall average cathode surface temperature

went up above 90° C which called for a decrease of the heating, leading under certain RF-power input conditions to an unstable gun operation.

An analysis of the particle energetic distribution at the linac exit showed that at a pulsed current ~1 A and pulse duration 1.4 μs the energy spectrum possesses an additional maximum in the high-energy region. The shape of the energy spectrum is determined by particle energy coherent losses (beam current loading). In this way, at I=1.05 A the mean energy was 13.5 MeV, the width of the integral energy spectrum 7% (Fig.2-1), while the width of particle spectrum distribution, as they were injected into the section after ~1 μs from the beginning of the pulse, did not exceed 3% (Fig.2-2).

For the same accelerator operation regime a three gradients method was used to measure beam emittance. From this measurements it follows that in the vertical plane the integral (during the entire pulse) normalized emittance was 26 π·mm·mrad. During emittance measurements in the vicinity of the temporal point corresponding to the current maximum (~1 μs after the beginning of the pulse) this value did not exceed 16 π·mm·mrad.

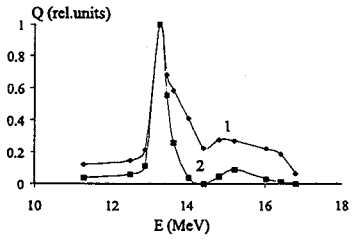

Fig.2. Energy spectrums.

Experimental results show that at the accelerator exit we have converging electron beam. As there is a dependence of beam dimensions on the beam injection phase into the accelerating section (Fig.3), we can make a conclusion that this phenomena is determined RF-focusing.

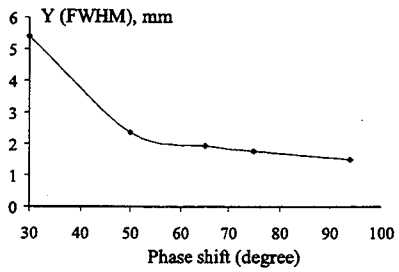

Fig.3. Beam dimension (Y) vs. injection phase.

During the tests after upgrading the beam characteristics were also studied in the photo-emission operation mode. At the first stage, BaNi cathode was used as a photocathode at such a temperature that practically excluded operation in the thermionic emission mode. During cathode irradiation at the wavelength 355 nm the gun produced pulsed current 2 - 2.5 A, with the pulse width 6 - 7 ns. At the accelerator output the pulsed current value was 1.3 - 1.6 A. Beam current measurements were done relative to cathode temperature and field strength in the gun cavity.

At present, an experimental research on wake-field excitation in plasmas of various density is carried out at the accelerator. Having this in view, an experimental device was assembled at the accelerator exit, including a coaxial plasma gun (plasma density being 10^{10} - 10^{16} cm^{-3}) and a diagnostic set for plasmas and the wake-field. During the assembly, the problem was solved of in-vacuum separation between the accelerator part of facility and its plasma-relation portion. Taking into account the fact that the beam has small dimensions, an extended collimator was placed at the accelerator exit (4 cm long, 4 mm in diameter), as well as auxiliary vacuum pump. Such a set up allowed to maintain the necessary vacuum condition in accelerator during plasma gun operation. Particle losses in the collimator do not exceed 10%.

Conclusions

Thus, NSC KIPT has built and put into operation a multipurpose accelerator facility for R&D purposes. Our simulations and experimental data allow to state that combination of an RF gun with the accelerating section operating at the 1-st spatial harmonic makes it possible to create injector accelerators with a high beam brightness. The subsequent research on particle dynamics in the accelerator should be continued in the direction of studies on the radial dynamics and clearing out the conditions to provide at the linac exit for intense beam production with the minimum emittance. Over above viewing to employ LIC as an FEL driver, we are planing to increase the current pulse duration to 8 - 10 μs.

Acknowledgments

We express our gratitude to the staff of "Accelerator" R&D Production Establishment of NSC KIPT for their invaluable help to the experiments. We are indebted to the AOT-1 group of LANL (USA) for their contribution to our successful work on the particle dynamics simulations.

References

[1] M.I. Ayzatsky et al. "High Brightness Electron Linac with RF Gun and Accelerating Structure on Backward Wave", Proc. EPAC96, will be published.

[2] M.I. Ayzatsky et al. "Two-cell RF Gun for a High Brightness Linac", Proc. EPAC96, will be published.

[3] V.A. Kushnir and V.V. Mitrochenko "Simulation of Beam Performances of the Two-cell RF Gun", Proc. EPAC96, will be published.

[4] M.I. Ayzatsky. ZhTF, 1995, Vol. 65, 6, p.153, (in russian).

[5] M.I. Ayzatsky, E.Z. Biller, E.V Bulyak et al. Voprosy attomnoi Nauki i Tekniki, VANT: series, Nuclear Physics Research (Theory and Experiment), 1991, 3(21), pp. 16-18, (in russian)

[6] L.A. Makhnenko, V.L. Parhomov, K.N. Stepanov. ZhTF, 1965, Vol. 35, 4, p.618, (in russian)

[7] M.I. Ayzatsky, E.V Bulyak, V.I. Kurilko. Proc. 12 th AU-Union Seminar on Charged Particle Accelerators, Dubna, 1992, vol. 1, p. 412, (in russian)

DEVELOPMENT OF INHOMOGENEOUS DISK-LOADED ACCELERATING WAVEGUIDES AND RF-COUPLING

M.I. Ayzatsky and E.Z. Biller
National Science Center, Kharkov Institute of Physics&Technology(KIPT),
310108, Kharkov, Ukraine

Abstract

A description of different types of the accelerating structures that have been studied and constructed in NSC KIPT for electron linacs during last years is given in this paper. The accelerating structures consist of the inhomogeneous disk-loaded waveguides and input and output couplers. The disc-loaded waveguides operate at f = 2797 MHz in $2\pi/3$ mode and have different laws of variation of the disk apertures. Before brazing cups were tuned with using special method. This method is discussed in this paper.

Introduction

During development and tuning of linac accelerating sections, based on homogeneous disk-loaded waveguides, widely used are various cavity stacks, shorted at each end or at only one (plunger method) (see, for example, [1]). In case of homogeneous structures, the possibility of their employment for E-modes is based on the fact that in the infinite periodic waveguide there exists for E-modes an infinite number of symmetry planes whose replacement with metal planes does not affect the field structure. For such short-circuiting, despite the fact that only the finite number of cavities are involved in the cavity stack, the characteristics of the both traveling waves (into which the standing wave of the stack can be expanded) are completely identical to those of the wave propagating through infinite (or matched at the ends) waveguide.

A more complicated is the case of inhomogeneous disk-loaded waveguides for which the periodicity condition is violated and, strictly speaking, the grounds disappear not only for utilization of cavity stacks, but for existence of traveling waves which are synchronous with charged particles. If the disk-loaded waveguide parameters vary slowly along the waveguide, then, the amplitudes of reflected waves are small, and in the system there is a traveling wave with slow-varying parameters. Tuning of such waveguides, using cavity sets, is performed with a low systematic error which is proportional to the inhomogeneity value. As far as the possibility of using for acceleration (generation, amplification) purposes disk-loaded waveguides with highly variable parameters, in each specific case, there is necessity to analyze the types and structures of waveguide fields and, then, develop techniques for tuning the components of this slow-wave structure. In general case, there are no stringent laws which could guarantee one or another property of the inhomogeneous structure, as different from homogeneous ones.

One more requirement imposed on the cavity stacks is the possibility of a consecutive tuning (i.e., a selection the geometrical dimensions one way or another) of waveguide cells. In case of cavity stacks, which model the homogeneous disk-loaded waveguides, this requirement is fulfilled automatically: when one has tuned K cells he can tune (K+1)-cell. In case of inhomogeneous structures, such condition becomes realizable depending upon the degree of coupling between different resonators that form the disk-loaded waveguide.

The calculations performed by us on the base of a new disk-loaded waveguide model (coupled cavity chain) [2] indicate that for waveguides with the period $D \geq \lambda/3$, where λ is the free-space wavelength, the "remote" coupling influences weakly on the phase-shift per cell. For $\varphi = 2\pi/3$, taking into account the "cross-cavity coupling" ((i, i-1), (i, i+1), (i-1, i+1), i - is the cavity number) at $a/\lambda < 0.14$ (a - is the coupling hole radius), one can expect to achieve an accuracy of forming a phase-shift per cell of the order of $\Delta\varphi \leq 0.05°$. If one restricts oneself only "paired coupling" ((i, i-1), (i, i+1)), then, the accuracy of phase-shift per cell is getting worse - $\Delta\varphi \leq 0.5°$. Development of the techniques of disk-loaded waveguide cell tuning that should allow to make feasible the cross-cavity coupling is a difficult task, since during tuning of the i-th resonator one has to take into account, somehow, the effect from the (i+1)-th resonator which has not yet been tuned.

This paper presents the results of our research on the technique of cell-tuning in a strongly inhomogeneous disk-loaded waveguides which realizes paired coupling.

Underlying Theory

From the paper [2] it follows that an infinite chain of cylindrical cavities of the length d and the radii b_i, coupled through co-axial cylindrical holes with the radii a_i in the cavity dividing walls with the thickness t (inhomogeneous disk-loaded waveguide with the period $D = d + t$) at $D > \lambda/3$ can be, with a definite accuracy, described by a set of coupled equations

$$[\omega_n^2(1+\alpha_n^{(+)}+\alpha_n^{(-)})-\omega^2]\,u_n = \omega_n^2(\beta_{n,n-1}\,u_{n-1}+\beta_{n,n+1}\,u_{n+1}) \quad (1)$$

where u_n - are the amplitudes of E_{010}-modes in the n-th cavity, ω_n - is the n-th cavity eigen frequency, $\sqrt{\alpha_n^{(+)}}$, $\sqrt{\alpha_n^{(-)}}$ - are the relative n-th cavity eigen frequency shift due to coupling with (n+1) and (n-1) cavities, $\beta_{n,n+1}$, $\beta_{n,n-1}$ -are the coupling coefficients. If $\alpha_n^{(+)}$ and $\beta_{n,n+1}$ are determined by geometrical dimensions of only the n-th and (n+1)-th

cavities, as well as by the coupling hole radius a_n ($\alpha_n^{(-)}$, $\beta_{n,n-1}$ are determined by geometrical dimensions of the n-th, (n-1)-th cavities and the hole radius a_{n-1}), then we shall say that the cavity coupling is paired. If these coefficients depend on geometrical dimensions of three cavities (n-th, (n+1)-th and (n-1)-th), as well as two coupling hole radii a_i, a_{i-1}, then, such coupling we shall call "cross-cavity coupling".

Let's find the conditions, when the set (1) at $\omega=\omega_*$ (ω_* - is the operating frequency) has the solution of such form $u_n = u_{n,0}\exp(in\varphi)$, where $u_{n,0}$ - is the real value. From (1) it follows that in order to achieve this, the following conditions is to be fulfilled $\beta_{n,n-1}\,u_{n+1,0} = \beta_{n,n-1}\,u_{n-1,0}$. For the n-th cavity (1) will take on the form

$$[\omega_n^2(1+\alpha_n^{(+)}+\alpha_n^{(-)})-\omega_*^2]\,u_{n,0} = 2\,\omega_n^2\,\beta_{n,n-1}\,u_{n-1,0}\cos(\varphi), \quad (2)$$

and for the (n-1)-th cavity

$$[\omega_{n-1}^2(1+\alpha_{n-1}^{(+)}+\alpha_{n-1}^{(-)})-\omega_*^2]\,u_{n-1,0} = 2\,\omega_{n-1}^2\beta_{n-1,n}\,u_{n,0}\cos(\varphi). \quad (3)$$

From (2) and (3) it follows that, if $\alpha_n^{(+)}$ is independent from the parameters of the (n+1)-th cavity, $\alpha_{n-1}^{(-)}$ - from the parameters of the (n-2)-th cavity and $\beta_{n-1,n}$, $\beta_{n,n-1}$ depend only upon the parameters of the n-th and (n-1)-th cavities, then, two equations (2) and (3) become closed and determine fully the relation of geometrical dimensions of the n-th and (n-1)-th cavity. In this case, having tuned the (n-1)-th cavity, one can find the conditions which must satisfy the geometrical dimensions of the n-th cavity, and, consequently, allow to consecutively tune all waveguides cavities. It can be shown that at the paired coupling $\beta_{n-1,n} = \beta_{n,n-1}$ and these coefficients are determined by the geometrical dimensions of the n-th and (n-1)-th cavities, only. Things are more complicated with the dependence of coefficients $\alpha_n^{(+)}$ on the parameters of the (n+1)-th cavity and $\alpha_{n-1}^{(-)}$ on the parameters of the (n-2)-th cavity. Even under the assumption of paired coupling such dependence exists. However, our calculations shown that this dependence is considerably weaker than the dependence on the parameters of the n-th ((n-1)-th) cavity, and can be neglected, as a result.

Cavity stacks for tuning inhomogeneous waveguides with $\varphi = 2\pi/3$

From the equations (2) and (3) it follows that in order to achieve the traveling wave mode in an inhomogeneous disk-loaded waveguides with the mode type $\varphi = 2\pi/3$ it is necessary that the parameters of the (n-1)-th and the n-th cavities be connected via the relationship

$$[\omega_{n-1}^2(1+\alpha_{n-1}^{(+)}+\alpha_{n-1}^{(-)})-\omega_*^2][\omega_n^2(1+\alpha_n^{(+)}+\alpha_n^{(-)})-\omega_*^2] = \omega_n^2\,\omega_{n-1}^2\beta_{n,n-1}\,\beta_{n-1,n}. \quad (4)$$

Suppose we have placed the n-th and (n-1)-th cavity into some sort of a cavity stack. It can be shown that the conditions (4) is fulfilled in the case, when in the cavities A and B (see Fig.1),adjoining the cells under consideration, the amplitudes of E_{010}-modes equal to zero. For cavity stacks, shorted at both ends, this condition can be accomplished by coupling the cavities A and B to terminal cavities, resonance-tuned at the frequency $\omega=\omega_*$ with taking into account the frequency shift due to the hole effect. Such cavity stacks have already been used for tuning separate parts of quasi-constant impedance sections for LIL accelerator [3]. However, there the cells were tuned not consecutively , i.e. beginning from the entrance (or exit), but in different stacks being then simply joined one-to-one.

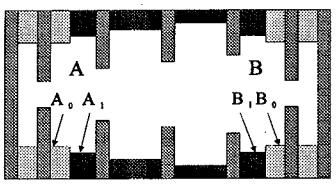

Fig.1. Cavity stack.

The above results indicate that it is possible to use a consecutive tuning of all cells for disk-loaded waveguides with an arbitrary law of the coupling hole radius variation. With that, at the operating frequency $\omega=\omega_*$ the traveling wave mode with the phase shift on the order of $2\pi/3$ with a certain accuracy is guaranteed in a waveguide. However, a quite natural question arises about the characteristics of such traveling wave, since the inhomogeneity in a disk-loaded waveguides is created with the purpose of optimizing its characteristics. Let's consider, for instance, a quasi-constant impedance section. Such a waveguide is supposed to consist of several homogeneous ($a_i = const$) segments with different radii of the coupling holes and transition sells which provide the matching of these segments. Our analysis indicates that fulfillment of such a requirement is realizable only under a certain law (unknown a priory) of hole radius variation. If one use the disks in the transition sells with some law of the hole radius variation (for instance, the linear one) and consecutive tune all cavities following the above technique, he can obtain a waveguide which will operate in a traveling mode at $\omega=\omega_*$, but its segments which are homogeneous relatively the hole radius will not be homogeneous relatively the waveguide inside diameter. Thus, under application of the above technique to the consecutive cell tuning in the case of the linear law of hole radius variation in the transition sells, the waveguide inside diameter will be periodically change within the second segment, i.e. the second segment of the section will be bi-periodic. For the subsequent "homogeneous" segments the law of the waveguide inside diameter variation will be more complicated. In the case of the linear law of hole radius variation in the transition sells two homogeneous segments cannot be matched together without violation of the condition $\varphi = 2\pi/3$. and the precise matching is impossible and from the transition there occur certain reflection with a small phase jump. What is more expedient for the accelerating section: the traveling wave mode with cavity frequency variation along the length of the structure, and, consequently, with the acceleration amplitude variation causing a certain decrease in the energy gain or a

joining of segments with a small phase jump and reflection that, also, leads to a certain decrease in the energy gain? There is no unambiguous answer to this question. In each case one will have to analyze the energy gain (or other characteristics) with taking into account the above factors. Our calculations indicate, for instance, that in the case of a structure with two homogeneous segments and for the linear law of hole radius variation in the transition sells more preferable would be the situation with the periodic cavity frequency variation in the second segment from the standpoint of energy gain.

Consecutive tuning feasibility is determined by stability of the technique, as well. The numerical analysis indicates that small errors in the tuning of individual cells should not lead to the exponential growth of subsequent deviations, i.e. the technique must be stable.

Inhomogeneous accelerating sections

The National Science Center "Kharkov Institute of Physics&Technology" (NSC KIPT) has created a technological base for building accelerating structures on the base of disk-loaded waveguides. The basic elements of a disk-loaded waveguides is asymmetric cell (disk and cup). The high-precision copper cups and disks are made on diamond tool lathers. Prior to brazing, the cups are tuned using different cavity stacks. Brazing a segment of cups and irises, segments and couplers are made in a vacuum RF-furnace at 779°C using the KIPT technology.

We have developed and manufactured four short inhomogeneous accelerating sections with $\beta_{ph}=1$ and $\varphi=2\pi/3$, three of which (S1, S2, S3) have quasi-constant law of coupling hole radius variation with a linear decrease of radii in transition cells, while in the fourth one (S4) the coupling hole radii decrease linearly from entrance to exit. Calculated characteristics of the first three sections are given in Table 1.

Prior to brazing the first section sells were tuned using the method completely coinciding with the one presented in [3]. Cavities in the second, third and fourth sections were consecutively tuned in the cavity stack using the above described method. While doing so, as compare with [3], the number of auxiliary cells was reduced to the minimum - we used only four auxiliary cells (see Fig.1). Cells A and B were composite ones ($A=A_1+A_0$, $B=B_1+B_0$, $A_0=B_0$) and during tuning process cells A_0 and B_0 were unchanged while the radii of cells A_1 and B_1 were changed according to a certain law. For sections S2 and S3 the radii of cells A_1 and B_1 were changed after tuning the transition sells, for section S4 - they were consecutively tuned together with the main sells. After brazing the sections cells were tuned by way of a small external deformation of the cups until the needed phase shift was achieved ($\delta\varphi=4\pi/3$) during the shorting plunger movement. Since such a tuning cleaned away all the errors of the first tuning (before brazing) we did not see the difference in the characteristics between sections S1, S2 and S3.

Table 1
Calculated characteristics of the S1, S2, S3 sections

	I=0 A	I=1.2A
Frequency, MHz	2797.2	2797.2
Input Power, MW	13	13
Energy Gain, MeV	17.8	9.5
Beam Power, MW		11.4
Gradient, Mev/m	14.3	7.6
Section Length, m	1.227	1.227
Filling Time, μsec	0.31	0.31
Field Attenuation, Nep/sect.	0.24	4.2
Output Power, MW	8	0.03
Number of Homogeneous Segments (Iris Diameters, mm)	4 (25.441, 23,630, 21.821, 19.620)	

During measurements of the after-brazing phase shifts it was found that the operating frequency of all sections was 150 to 200 kHz lower than the calculated one. It can be explained as errors of used cavity stack. Indeed, the above stacks are just for paired cavity coupling. According to the results of our calculations [2] the negligence of the "remote" coupling can produce errors during tuning about $\Delta\varphi\leq+0.5^{\circ}$ which agrees in value and sign with the obtained deviation of the operating frequency.

The section S1 was installed on KUT accelerator [4]. The results of beam characteristics measurements agreed with simulations.

Thus, our R&D has shown that the feasibility is there to tune (with a certain error) of disk-loaded waveguides with arbitrary law of hole radius variation. In order to achieve the necessary characteristics the choice of such law must be made with taking into account both the properties of inhomogeneous waveguides as the feasibility of tuning such waveguides. In view of all the above-said, a procedure should be worked out to optimize the structures considered. At present, based on the approach [2] we have begun to investigate this problem.

Acknowledgments

The authors wish to thank A.N.Dovbnya, V.A.Kushnir and V.V.Mitrochenko for discussions relating results of this work.

References

[1] O.A. Valdner, N.P. Sobenin, I.S. Zverev et al. Disk Loaded Waveguides. Reference Book. Moscow, Energoatomizdat, 1991.

[2] M.I.Ayzatsky. New Mathematical Model of an Infinite Cavity Chain, Proc. EPAC96, will be published.

[3] Bienvenu G., Bourdon JC, Brunet P. et al. Accelerating Structure Developments for the LEP Injector Linac. Proceedings of the 1984 Linear Aceelerator Conference. GSI-84-11. p. (1984)

[4] M.I.Ayzatsky, Yu.I.Akchurin, V.I.Beloglazov et al. KYT - Industrial Technological Accelerator, Proc.XIV Particle Accelerator Workshop, Protvino, v.4, p.259 (1994)

OPTIMIZATION OF ION SOURCE EXTRACTION AND TRANSPORT WITH SYMBOLIC MANIPULATION PROGRAMS: ELECTROSTATIC LENSES FORMULAS

M. Cavenago
INFN-LNL, via Romea n 4 I-35020 Legnaro (PD) Italy

Abstract

The partly built line of the ECR ion source Alice, mainly based on electrostatic elements, needs several optimizations for different ion beam (A/q ranges from 2 to 9). Numerical codes easy to maintain and fast to execute were in demand. Beam optics codes are usually implemented as a kind of object oriented programs followed by a purposely written high level interpreter. This level was here replaced by general programs, combining symbolic and numerical capability, which therefore support different programming styles and a much finer physical description. Highly efficient linear tracking of electrostatic elements was obtained combining piecewise analytical solutions for quadratic and linear elements; some basic formulas and a sample result for Alice line are shown. Extension of elements to nonlinear case is given here, with detail for the anode lens.

Introduction

The beam transport system of the ECR [1] ion source Alice is mainly constituted by electrostatic elements (extractor, three einzel lens and the accelerating column), with one magnetic dipole for charge selection (Fig. 1). Due to the relative importance of fringing fields, our need for a flexible and easily adaptable matrix tracking code was apparent; nonlinear effects were also considered a second goal. We wrote some application programs, executed (interactively) by Mathematica [2]. Usual formulas for sources, drifts, thin lens and dipoles were easily implemented, as well as graphic capabilities. This paper describes the nontrivial approximations and equations that we used in simulating round electrostatic elements in some detail.

Paraxial analysis of einzel lens was indeed possible, by decomposing the lens in seven regions (or elements), where the axial field E_z is assumed either constant (linear elements) or linearly increasing (quadratic elements) [3]. Use of more than three regions allows a closer fit to actual fields. A noteworthy nonlinear approximation (nonlinear means applicable to nonparaxial rays), namely the Piecewise Quadratic Approximation (PQA) is first introduced and briefly discussed; matching between linear and quadratic element is extended off-axis, allowing region boundaries to make a arctg$\sqrt{2}$ angle with z axis and introducing fictitious charges on element boundaries. We apply this general concept to anode lens effect.

We follow SI units in the code (generally) and use nonrelativistic mechanics, as suitable for ion sources. Since orbits do not depend on mass and charge in electrostatic fields, in section 2 and 3 we set unit mass and charge $e = m = 1$ for brevity.

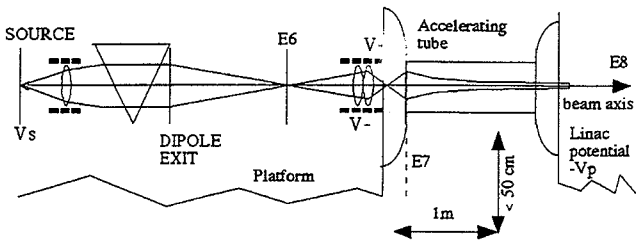

Figure 1: Beam line from platform (scale is approximated; transverse dimension exaggerated).

Einzel Lens Paraxial Model

Let E be the total particle energy, a constant of motion, valid for every element of our beamline. First, we review the quadratic element. Consider a vacuum region where the electrostatic potential $\phi(r,z)$ is exactly:

$$\phi(r,z) = A + Bz + C(\tfrac{1}{4}r^2 - \tfrac{1}{2}z^2) \qquad (1)$$

Hamiltonian separates as $H = H_z + H_r$ with $H_r = (2p_r^2 + Cr^2)/4$, whose value H_r^c is a constant of motion; also the value of H_z is the constant of motion $H_z^c = E - H_r^c$. Solving motion equations and eliminating t in favour of z we write the motion from z_i to z_o as

$$\begin{pmatrix} r \\ p_r \end{pmatrix}_o = \begin{pmatrix} \cos\psi & \sqrt{2/C}\sin\psi \\ -\sqrt{C/2}\sin\psi & \cos\psi \end{pmatrix} \begin{pmatrix} r \\ p_r \end{pmatrix}_i \qquad (2)$$

$$\psi(z_o,z_i) = \frac{1}{\sqrt{2}}\mathrm{Arsh}\frac{Cz-B}{\sqrt{2H_z^cC - 2AC - B^2}}\Bigg]_{z_i}^{z_o} \qquad (3)$$

with $2H_z^c = 2E - p_r^2(z_i) - Cr^2(z_i)/2$. From these nonlinear formulas a linear approximation in (r,p_r) is obtained by putting $H_z^c = E$ in eq. (3). In case $C < 0$ analytic continuation is taken. Case $C = 0$ is the linear element.

The potential of einzel lens $\Phi(r,z)$ can be fitted by elements like eq. (1) on intervals of z axis $r = 0$; interval borders z_n are called breaking points here. In present code, we find convenient to use the well-known approximation for symmetrical einzel lenses [3] :

$$\Phi(0,z) = \frac{V_2}{2\omega(z_b - z_a)}\log\frac{\mathrm{ch}[\omega(z+z_b)]\mathrm{ch}[\omega(z-z_b)]}{\mathrm{ch}[\omega(z+z_a)]\mathrm{ch}[\omega(z-z_a)]} \qquad (4)$$

with $\omega = 1.318/R$ where R is the radius of electrodes and $z = z_a$, $z = z_b$ their faces; in perspective, also the potential

$\Phi(0,z)$ numerically computed (by POISSON) and adequately interpolated can be fitted by the same elements.

Elements are easily counted by plotting (see Fig. 2a) the second derivative $\Phi_{,zz}$ and associating a $C > 0$ element to some maximum (region III) and a $C < 0$ element to some minimum (region I) or low plateau. Between these elements, a $C = 0$ element (region II) will certainly improve matching. At $z = 0$ we can include a $C = B = 0$ element (region 0) or not, depending on lens dimension z_a. In these regions, potential elements on axis are better written:

$$\begin{array}{lll} \phi = & a & 0 < z < z_0 \\ \phi = & a + \frac{1}{2}b(z - z_0)^2 & z_0 < z < z_1 \\ \phi = & c + d(z - z_0) & z_1 < z < z_2 \\ \phi = & \frac{1}{2}e(z - z_3)^2 & z_2 < z < z_3 \end{array} \quad (5)$$

and $\phi = 0$ for $z > z_3$. Imposing continuity of $\phi(0,z)$ and $\phi_{,z}(0,z)$ everywhere, we get $c = a - \frac{1}{2}d(z_1 - z_0)$, $e = d/(z_2 - z_3)$ and $z_3 = -2(a/d) + z_0 + z_1 - z_2$.

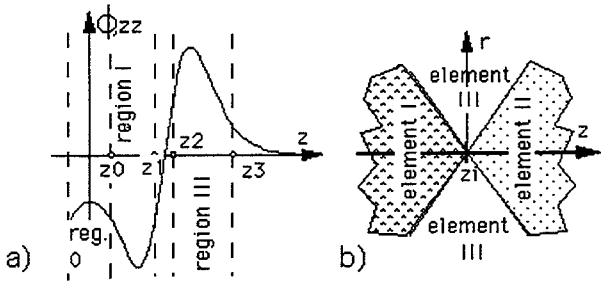

Figure 2: a) Breaking point determination from potential derivatives on z axis; 2b) Regions at a breaking point.

We choose $a = \Phi(0,0)$ to exactly reproduce the field at lens middle . The remaining parameter z_0, z_1, z_2 (breaking points) and d can be determined by fitting ϕ to the actual potential Φ, that is by minimizing the norm

$$\sum_{z^{(j)}} w_0(\phi - \Phi)^2 + w_1(\phi_{,z} - \Phi_{,z})^2 + w_2(\phi_{,zz} - \Phi_{,zz})^2 \quad (6)$$

where $z^{(j)} = j(L/N)$ and L is long enough ($L = z_b + 3R$ suffices). Considering also the second derivative is essential for sound results of the fit, even if weights w_0, w_1 and $w_2 \neq 0$ may be varied; we choose $w_n = R^n$. Note that $x_0 \leq 0$ is our criterion to drop region 0, which case leaves five intervals in total instead of seven.

In the paraxial approximation we can take region boundaries as $z = z_n$ planes, and extend potential off-axis according to (1). Indeed, at any z_n, $\phi_{,zz}$ is discontinuous, so that a r^2 discontinuity in potential arise; this term may be neglected in paraxial approximation.

Piecewise Quadratic Approximation

To apply the quadratic elements in nonparaxial case, imagine to have matched the potential ϕ and field E_z on axis at breaking point z_n between two element intervals; to fix ideas, let $z_n = 0$. The two elements are $\phi_I = A + Bz + C_I(r^2/2 - z^2/4)$ and $\phi_{II} = A + Bz + C_{II}(r^2/2 - z^2/4)$, with A and B equal because of matching for $r = 0$. Requiring potential continuity $\phi_I = \phi_{II}$ implies

$$r = \sqrt{2}(z - z_n) \text{ or } r = \sqrt{2}(z_n - z) \quad (7)$$

These two lines (in fact cones) are the element boundaries and separate three regions; in region III we may have another element as eq. (1) with a different C_{III} if desired.

Matching $\phi_{,z}$ off-axis is not possible. Discontinuity of E_z is equivalent to a charge (say positive), which implies a balancing charge (negative) to be located at lines (7). More quantitatively, Φ_t be the true potential ($\mathbf{E}_t$ the true field), ϕ our collection of elements (so that $\mathbf{E} = -\text{grad}\phi$ is a part of the electric field) and $\Phi_c = \Phi_t - \phi$ the correction (localized near eq. (7) lines) that restores matching between elements. From Laplace eq. $\triangle\Phi_t = 0$ we indeed get:

$$\triangle\Phi_c = \text{div}\mathbf{E} \quad (8)$$

From eq. (7), boundaries associated to different z_n may intersect at $r = (z_n - z_{i+1})/\sqrt{2}$, which determines the maximum radius of validity of our element decomposition.

Non paraxial analysis is more easily applied to the remarkable case of the anode lens [4], a hole of radius R in a conducting metal sheet (at $\Phi_t = 0$) separating a semispace $z < 0$ with field $E_z = E_1 \equiv E_s - E_d$ for $z \to -\infty$ from a semispace $z > 0$ with field $E_z = E_2 \equiv E_s + E_d$ for $z \to +\infty$. Our field elements are explicitly

$$\begin{array}{ll} \phi_T = -E_s z + E_d z & \text{for } r - \sqrt{2}z - R_\text{p} > 0 > z \\ \phi_V = -E_s z - E_d z & \text{for } r + \sqrt{2}z - R_\text{p} > 0 < z \\ \phi_U = -E_s z + (E_d/Z_\text{p})(\frac{1}{4}r^2 - \frac{1}{2}z^2 - \frac{1}{2}Z_\text{p}{}^2) & \end{array} \quad (9)$$

elsewhere, with $Z_\text{p} = R_\text{p}/\sqrt{2}$. Here R_p is a parameter; breaking points are at $\pm Z_\text{p}$. Choosing $R_\text{p} = 4\sqrt{2}/\pi$ gives the exact values for $\phi_U(0,0)$, similarly to einzel lens [4].

From (9) we can compute the fictitious charge of (8):

$$\triangle\Phi_c = \frac{3E_d r}{2^{3/2}Z_\text{p}}[\delta(z - Z_\text{p} + (r/\sqrt{2})) + \delta(z + Z_\text{p} - (r/\sqrt{2}))] \quad (10)$$

The effect of Φ_c on particle motion can be approximately described by a (small) transverse kick $\mathbf{K}$ when passing boundaries; for example crossing T-U boundary gives

$$K_r = -\frac{E_d r_i^2}{2\sqrt{2}Z_\text{p}v_i}(1 + 2^{-5/2}\alpha_i - 0.75\alpha_i^2 + O[\alpha_i]^3) \quad (11)$$

where r_i, z_i are r, z at the crossing; v_i is v_z at this time; α_i is p_r/p_z at this time. Component K_z is such to maintain energy unchanged. This kick does not contribute to linear focusing, but to aberations.

We can now formulate a fast tracking for the anode lens. For convenience we project initial and final states on $z = 0$. The initial motion:

$$r(z) = r_0 + p_0[\sqrt{f + 2(E_s - E_d)z} - \sqrt{f}]/(E_s - E_d) \quad (12)$$

with $f = 2E - p_0^2$ is therefore parameterized by (r_0, p_0), which would be the values of (r, p_r) at $z = 0$, if our particle would propagate in a constant field $E_z = E_1$ up to there. From (12) and boundary eq. $r - \sqrt{2}z = Z_\mathrm{p}$ crossing values r_i, z_i can be easily determined. After crossing we have $p_i \equiv p_r(z_i) = p_0 + K_r$ with the kick (11). Motion follows eq. (2) up to crossing with U-V boundary, at $z = z_o$; z_o is determined by

$$z_o = Z_\mathrm{p} - \left[\frac{r_i}{\sqrt{2}}\cos\psi(z_o, z_i) + \frac{p_i}{\sqrt{C}}\sin\psi(z_o, z_i)\right] \qquad (13)$$

which can be solved iteratively. A good starting value for ψ is $\psi(Z_\mathrm{p}, -Z_\mathrm{p}) =$

$$\frac{1}{\sqrt{2}}\left[\mathrm{Arsh}\,\frac{E_d + E_s}{\sqrt{g + E_d^2 - E_s^2}} - \mathrm{Arsh}\,\frac{E_s - E_d}{\sqrt{g + E_d^2 - E_s^2}}\right] \qquad (14)$$

with $g = 2H_z^c E_d / Z_\mathrm{p}$. Final value of p_r is $p_r(z_o^+) = p_o + K_r$ where the second kick is given by eq. (11), with r_i replaced by r_o (and similar replacement for $z_i\ p_i\ \alpha_i$).

Remarks on Programming

As a general remark, programs become more involved with their size; in our opinion, no recipe can guarantee order and clarity (and absence of error). It is then natural to break a program into several parts, mainly a "physics part" [5], where formula as (1)-(14) are coded as plainly as possible, and an "interpreter", ultimately relating with numbers and graphics; for example, as COSY and FOXY (interpreting COSY to Fortran [5]). Our try in this direction is the use of an external interpreter, at present Mathematica [2]; advantages of this approach are more evident at the beginning (as now), when the physics code is small enough to make errors unlikely; and reformulation is possible.

A Mathematica applicative program (code in brief) consists of definition of transformation of symbols, with possibility of delaying or conditioning their execution: almost any kind of programming style is possible. It is probable that object programming, implemented by "UpSetDelayed" [2], will be a fairly good recipe to order information about the several treated objects: dipoles, regions of einzel lenses or of accelerating tubes, drifts. At present, a traditional style was used: an element is a list, including the element name, kind of approximation used, and parameters. For example, {dipolex,fringe,$R, \phi, \alpha, \beta, n, D, I_2$(in), I_2(out)} represents H.Enge's model of dipole [4]. Simbols "matrix2" and "matrix3" represent actions on (x, p_x) phase-space and (x, p_x, δ) space respectively. An einzel lens is converted into a sequence of seven lists. A beamline is a list of lists, on which a traditional loop distributes the action of "matrix3". Operation on lists may be more concisely done with in-built symbols "Thread" and "Map", in an advanced style. Graphics rendering was very flexible and satisfying. We plan to merge fitting of elements to einzel into some post-processor of Poisson equation numerical solvers.

Simulation Results

Let (V_2, V_3, V_4) be the voltages of the three einzel lenses, V_1 be the source voltage and $-V_p$ be the linac voltage, referenced to platform. Fig. 3a) was computed for a beam of He^{2+}, setting $V_1 = 9$ kV, (i.e. $E = eV_1 = 18$ keV), $V_2 = 3.45$ kV for the first einzel and optimizing $(V_3, V_4, V_p) = (7, 5.65, 67)$ kV; a $\delta V_1 = 10$ V perturbation was added. Simulation for Ar^{14+} and U^{28+} beams proved even better transport, provided that latter voltages (and intermediate waists) are changed: $(V_3, V_4, V_p) = (0, 0, 99.6)$ kV and $(0, 6.3, 314)$ kV respectively . Fig 3b) shows that also aberration can be reproduced by PQA, in fairly good agreement with RungeKutta computations.

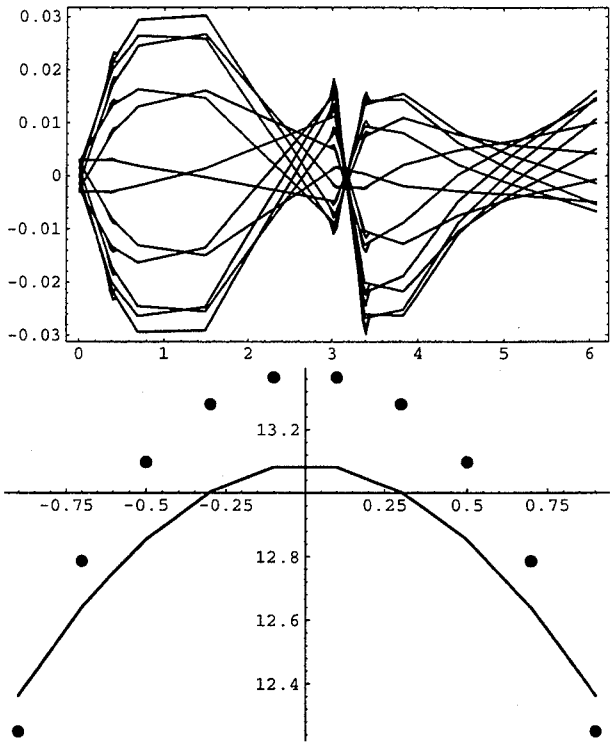

Figure 3: a) Paraxial ray r versus z (in m) for the ECR line; 3b) Focal distance/R versus r_0/R for anode lens (dots: RungeKutta), when $E_1 = 0$ and $E_2 = 0.4E/(eR)$.

References

[1] R. Geller, P. Ludwig, G. Melin, *Rev. Sci. Instr.*, 63, 2795 (1992).

[2] S. Wolfram, *Mathematica*, Addison-Wesley, Redwood City, 1988; Mathematica is a trademark of Wolfram Research Inc.

[3] P. Grivet, *Electron Optics*, Pergamon, Oxford, 1972, p. 215 (see references to R.J. Rudenberg (1948) and E. Regenstreif (1951a) there) and p. 575ff.

[4] M.Y. Bernard, p. 14 in *Focusing of charged particles*, (A. Septier, ed.), Academic, Orlando, 1967; also E. Durand, Electrostatique, tome II, Masson et C., Paris, 1966; also p. 38 in Ref. [3].

[5] M. Berz, NIM A298, 473, 1990 and A298, 426, 1990.

The New Superconducting Positive Ion Injector for the Legnaro ALPI Booster.

A. Lombardi, G. Bassato, A. Battistella, M. Bellato, G. Bezzon, G. Bisoffi, S. Canella, M. Cavenago, F. Cervellera, F. Chiurlotto, M. Comunian, R. Cortese, A. Facco, P. Favaron, G. Fortuna, M.F. Moisio, V. Palmieri, R. Pengo, A. Pisent, M. Poggi, A.M. Porcellato, L. Ziomi
INFN-LNL, via Romea 4, I35020 Legnaro (PD), ITALY
I. Kulik, ILTPE Kharkuv, Russia; A. Kolomiets, S. Yaramishev, ITEP, Moscow, Russia

Abstract

Following the demand of very heavy ion beams at the Laboratori Nazionali di Legnaro a new injector for ALPI is foreseen. At present ALPI is fed by a 16 MV XTU Tandem providing, routinely, beams up to masses of the order of 90 amu. In order to upgrade the possibilities of the complex and accelerate masses up to 200 amu the novel injector has been designed. The new machine consists of an ECR source on a high voltage platform, capable of 350 kV, followed by two superconducting RFQ resonators operating at 80 MHz and boosting the beam energy up to about 570 keV/amu. Downstream the SRFQ's eight Quarter Wave Resonators similar to the ALPI bulk niobium cavities are foreseen, to reach a proper ALPI injection energy of about 950 keV/amu. This paper describes the project.

Introduction

The new positive ion injector for the Legnaro heavy ion facility PIAVE (Positive Ion Accelerator for Very-low Energy) will increase the capability of the complex in delivering very heavy ion beams to the experiments. The user request, after more than a decade of operation of the XTU tandem, is to have very heavy ion beams with intensities of few particle-nA onto the target. The new machine will allow the simultaneous operation of the two main accelerators operating at Legnaro, the XTU tandem and the post accelerator ALPI, that are forced to work in alternative, at present, being the tandem the only injector for ALPI [1,2,3]. Figure 1 shows the PIAVE technical layout from the ion source to the injection in ALPI.

The beam is formed in the ECR source Alice [4] which is located on a high voltage platform and accelerated by the 350 kV applied voltage. As shown in figure 1 the HV platform is placed 4 m higher than the ALPI vault floor on a concrete support. This solution, dictated by the dimension of the platform and the required distances from the wall, calls for a transport line which displaces the beam by about 5 m in the vertical direction and about 2 m in the horizontal one [5].

The transport line contains the double-drift double-frequency bunching system operating at 40÷80 MHz for the proper injection into the SRFQ.

The first accelerating section of PIAVE which consists of two superconducting RFQ cavities housed in the same cryostat (see fig. 1.). The output energy of the RFQ section has been optimized with respect of the acceleration efficiency of the structure. Following the SRFQ's there are eight accelerating Quarter Wave cavities of the same type of the bulk niobium low-β section of ALPI[6], with some minor modifications in order to decrease the β_{opt} value from 0.055 to 0.05. The QWR's are housed in two cryostats and in between there is a quadrupole doublet for transverse focusing.

Downstream the accelerating sections of PIAVE there is the transport and matching line to ALPI which includes two room temperature bunchers (in fig. 1. only one of them is shown being the second one hidden in the chosen view).

The choice of using superconducting structure has been driven by the fact that ALPI is capable of running in CW mode, being itself a superconducting machine. This follows the traditional use of electrostatic machines in nuclear physics and fulfill the request of the high efficiency multi-array γ-spectroscopy detectors which need a beam intensity of some pnA with 100% duty cycle.

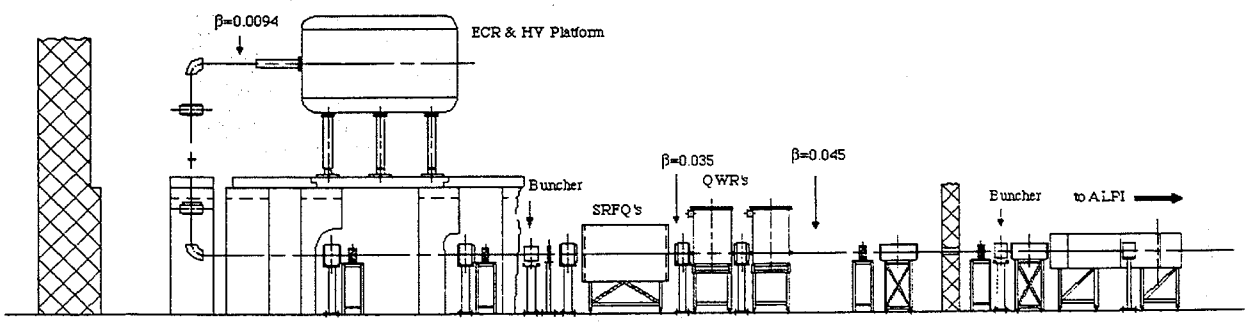

Fig. 1. The PIAVE layout

Table 1
Injector parameters

Source and LEBT			
Ion source	ECR	14 GHz	
Mass to charge ratio	8.5÷1		
Platform voltage*	350	kV	
Energy	41.2	keV/u	(β=.0094)
Beam emittance	0.5	mm mrad	(norm.)
Bunching system	DDDF	40÷80	MHz
$\Delta\varphi$	±6	deg	(80 MHz)
ΔW	±0.55	keV/u	
RFQ Accelerator			
Radio Frequency	80	MHz	
Input Energy	41.2	keV/u	(β=.0094)
Output Energy	578	keV/u	(β=.0352)
Average acceleration*	2.16	MV/m	
Max. Surface E field*	25	MV/m	
Max. stored energy/RFQ*	≤4	J	
Acceptance	≥0.9	mm mrad	(norm.)
Output emittance	0.5	mm mrad	(norm.)
	≤0.7	ns keV/u	
	SRFQ1	SRFQ2	
Vanes length	134.7	76.3	cm
Output energy	341.7	578.3	keV/u
Voltage *	150	280	kV
Number of cells	41	13	
Average aperture R_0	0.8	1.53	cm
Modulation factor m	1.2-3	3	
Synchronous Phase φ_s	-40÷-18	-8	deg
Tank diameter	46	62	cm
Max. surface B field*	280	295	G
Shunt impedance Rsh/Q	22.7	23.7	Ωm
Quality factor Q	7e8	9e8	
Power dissipation (4K)*	≤7	≤7	W
QWR Section			
Number of resonators	8		
Output energy*	948	keV/u	(β=.045)
Radio Frequency	80	MHz	
Optimum β	0.05		
Accelerating Field	3	MV/m	
Shunt impedance Rsh/Q	3.2	kΩ/m	
Quality factor Q	10^9		
Power per cavity (4K)	≤7	W	
Synchronous Phase $\lvert\varphi_s\rvert$	20	deg	
Matching Line to ALPI			
Number of bunchers	2	(room temperature)	
Buncher Eff. Voltage VT	≤100	kV	

* The values are referred to a mass to charge of ratio 8.5, ($^{+28}U^{238}$).

Beam Dynamics

The new injector has to provide the very heavy ion beam for ALPI replacing the tandem, which means that the beam quality of the machine has to compete with the very good transverse emittance of an electrostatic machine. Moreover the longitudinal structure of the beam has to be acceptable for the injection into ALPI. These requests have to be combined with the optimization of the acceleration efficiency due to the very high costs of the superconducting structure and ancillary.

The main features of this design are the bunching of the beam outside the RFQ, the optimization of the acceleration efficiency with proper choice of voltages and apertures and the minimization of the output longitudinal emittance, that determines the modulation law[3,5,7].

The ion velocity for the transition between the RFQ structure and the QWR has been chosen balancing the acceleration efficiency of the two structures. Indeed at higher beam energy the rf stored energy in the RFQ becomes prohibitive, at lower beam energy the transit time factor in the two gaps QWR's is too low.

The result of the design study is summarized in table 1.

The Superconducting Structures

The project foresees two different resonators for the RFQ section for a total structure length of ~ 2.5 m, housed in a single cryostat mainly to reduce the unavoidable drift space between the cavities. We are forced to split the RFQ into two resonators otherwise the rf energy stored in the cavities would make the phase lock with a reasonable rf power amplifier impossible [3].

The first of the two cavities to be built is the second RFQ, named SRFQ2, because it is the most critical one concerning the rf electronics demands. The drawing of the cavity is shown in figure 2.

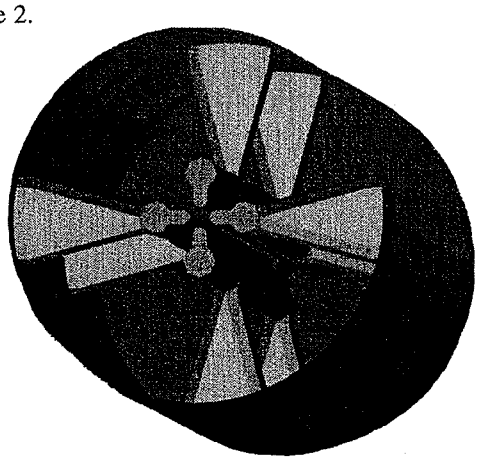

Fig. 2. The SRFQ2 resonator

The SRFQ's are made of e-b welded niobium sheets. The choice of this construction technology is advised by the tightness of the time schedule of the project, but a parallel research experiment on the feasibility of this kind of structure in OFHC copper with a sputtered niobium film is in progress.

From the mechanical point of view, effort has been put in the calculation and modification of the eigenfrequencies of the mechanical vibrations of the cavities to minimize the effect on the rf operation[3,8]. The stiffening ribs and the bars push the mechanical resonant frequency to ~150 Hz, whereas the frequency without any stiffening but with the already optimized shape of the supports is ~50 Hz; this is more convenient considering the environment mechanical noise.

The SRFQ resonators will work in a self-excited loop mode and one needs a rf amplifier power of at least 500 W [3,9] in order to have a dynamic range of ±10 Hz, considering the quite high stored energy. This high rf power needed for the feed back control loop puts both rf and thermal constraints on the rf feed lines and on the cryostat.

The slow tuner range is of ±100 kHz, through elastic deformation of the two end plates by ±2.5 mm. A tuning system to compensate the ±50 mbar pressure variation of the liquid helium bath is under investigation.

As mentioned above, the second part of the accelerator is made of eight superconducting QW resonators operating at 80 MHz similar to the low energy section cavities of ALPI [6]. The only modification we foresee is the variation of the β_{opt} through modification of the beam port geometry. This minor change will not require a new study of the structure, that has been constructed and successfully tested.

Infrastructures

The most demanding ancillary system of the whole project is the liquid helium production and distribution system. PIAVE requires a cooling power of 130 W at 4.5 K and 600 W at 80 K and it is connected with the ALPI cryogenic complex. To avoid the overloading of the 80 K circuit the use of a separated liquid nitrogen refrigeration system is foreseen.

Another important constraint on the cryogenic system is the quietness concerning the mechanical noise because of the sensitivity of the SRFQ cavities to the vibrations. Different solutions are now under investigation ranging from an inexpensive system made of a dewar for the phase separation of the liquid helium to the use of superfluid helium.

All the other accelerator systems are an upgraded replica of the well proven ALPI systems [2].

The main novelty, concerning the beam diagnostics, is the design and construction of a beam emittance measuring box essential for the tuning of the transfer lines.

Status of the Project

PIAVE has been approved as a "Special Project" by the executive committee of INFN in its meeting of July 1996. It is a three years project with a cost of ~7.7 Billion Lit.

The feasibility studies of the project are going on since the middle of 1995 and in March 1996, before presenting officially the project to the INFN, an international committee reviewed the design in all aspects, giving scientific approval.

The SRFQ cavities are in a prototyping stage and the internal parts of the stainless steel full scale model of SRFQ have been e-b welded. The model is meant to check all the construction details of the cavities and to construct the proper mechanical jigs because the construction of the niobium cavity will immediately follow.

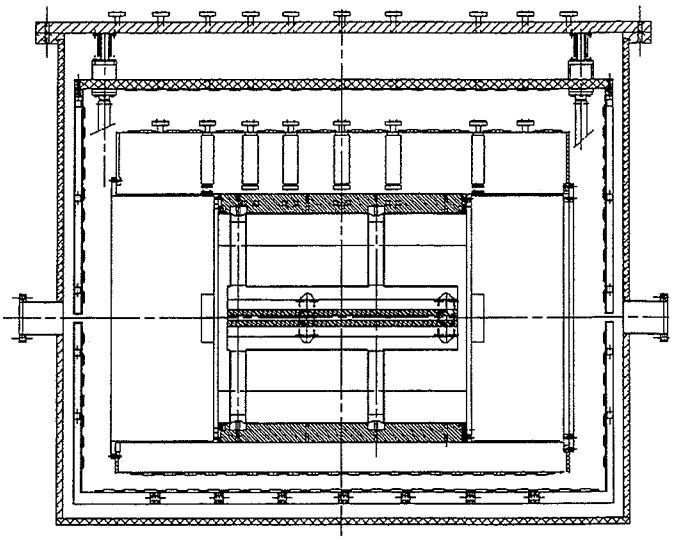

Fig. 3. The test cryostat and the SRFQ2 cavity

A test cryostat, able to house both the different SRFQ cavities, is under construction. The main feature of the design is the use of titanium for the liquid helium reservoir to avoid the stresses due to the different thermal contraction between the cavity, made of niobium, and the reservoir which contains it in a helium bath (see fig. 3.).

References

[1] G. Fortuna "Status of ALPI and Related Development of Superconducting Structure " this conference proceedings.

[2] G.Bisoffi et al "The Positive Ion Injector for ALPI", presented to the 7th International Conference on Heavy Ion Acceleration Technology, Canberra

[3] A. Pisent et al. "Status of the Superconducting RFQ project for the Legnaro New Positive Ion Injector", to be published in the EPAC 1996 conference proceedings

[4] M. Cavenago and G.Bisoffi "Commissioning of the ECR source Alice" NIM A328(193) p.262-265, and M.Cavenago "Selection of charge from the ECR Alice without forming a Waist", NIM, A328(1993),266-269

[5] A. Pisent "Beam Dynamics of the new LNL injector", LNL-INFN (REP) 107/96

[6] A. Facco et al. " Experience with the bulk niobium low β resonators at LNL" presented to the 7th International Conference on Heavy Ion Acceleration Technology, Canberra

[7] I.Ben-Zvi et al "Design of a Superconducting RFQ resonator" Particle Accelerators 35 (1991) 177.

[8] G. Bisoffi et al. "Superconducting RFQ cavities of the new heavy ion injector at Legnaro", to be published in the proceedings of the "Seventh Workshop on RF Superconductivity", Paris, October 1995.

[9] I Ben-Zvi et al " The control and electronics of the superconducting booster module", NIM A245 (1986) 1-12

A NEW MATCHER TYPE BETWEEN RFQ AND IH-DTL FOR THE GSI HIGH CURRENT HEAVY ION PRESTRIPPER LINAC

U.Ratzinger and R.Tiede
GSI
Darmstadt, Germany

Abstract

The adaptation of a RFQ beam to the typical requirements at the entrance of a drift tube linac is rather difficult at high intensities and high A/q values. The high focusing power needed for such a matcher can be provided by a conventional array with rather large quadrupoles and rebuncher cavities only. Many problems arising from such a design can be avoided by using an element which is focusing in transverse and longitudinal direction at the same time, that is a short RFQ ('Super Lens') with 10 cells typically and a larger aperture as compared to the main RFQ. A xy-steerer and a short quadrupole doublet with small aperture were added to gain flexibility with regard to beam mismatch and misalignment corrections. This new concept is realised for the GSI 15 mA U^{4+} injector, which is under construction.

Beam dynamics calculations are presented and compared with results for a conventional solution consisting of a rebuncher and a quadrupole triplet.

Introduction

At present a new UNILAC prestripper LINAC is under construction in order to fill the Heavy Ion Synchrotron SIS up to the space charge limit [1],[2].

The new LINAC consists of a RFQ cavity up to 120 keV/u and a IH-DTL section up to 1.4 MeV/u.

So far, for the beam matching from a RFQ into an IH-DTL the conventional array consisting of the elements quadrupole triplet (doublet) - rebuncher cavity - quadrupole doublet was used [3] [4] . These accelerators however were zero current designs with A/q values below 9.5 .

For the new GSI High Current Injector with $A/q \leq 65$ the use of similar matching designs would lead to considerable difficulties: very powerful and long conventional quadrupole lenses with big apertures are necessary, as well as a powerful rebunching cavity. According to the separation of longitudinal and transverse focusing within such a system, it is rather sensitive with respect to beam intensity fluctuations.

These problems led to the idea of using a short adapter RFQ ('Super Lens') focusing in all three dimensions and located directly in front of the first IH-DTL [5]. A short, small aperture quadrupole doublet placed behind the main RFQ adds the needed flexibility to that system.

Parameters of the Matching Section Components

The main parameters of the matching section are summarized in Table 1. The geometric arrangement is shown in Fig. 1. Between accelerator RFQ output and adapter RFQ input a distance of about 560 mm is taken by a xy-steerer, a quadrupole doublet, a vacuum valve and a diagnostic box. Along that distance the beam radius is increased to around 5 mm. A 'Super Lens' minimum aperture radius of a = 6.8 mm (compared to a = 4.1 mm at the main RFQ output) was chosen, which allows to get the needed emittance shapes at the entrance of the IH-DTL. The adapter RFQ is designed for $\phi_{s.p.} = -90°$ in order to get maximum longitudinal focusing power and to reduce the vane-vane voltage. This leads to a rather simple structure with 11 identical cells.

Table 1
Characteristic Matching Section Parameters

Total Length	/ m	1.4
Magnetic Quadrupole Doublet		
Effective Length	/ mm	139 ; 115
Effective Gradient	/ T/m	153 ; 153
Aperture Diameter	/ mm	16.0 ; 16.0
Adapter - RFQ		
Cell Number		11
Electrode Length	/ mm	748
Frequency	/ MHz	36.136
Peak Vane Voltage	/ kV	212
Min. Aperture Radius	/ mm	6.8
Modulation Factor		1.64
Synchr. rf Phase	/ deg	- 90

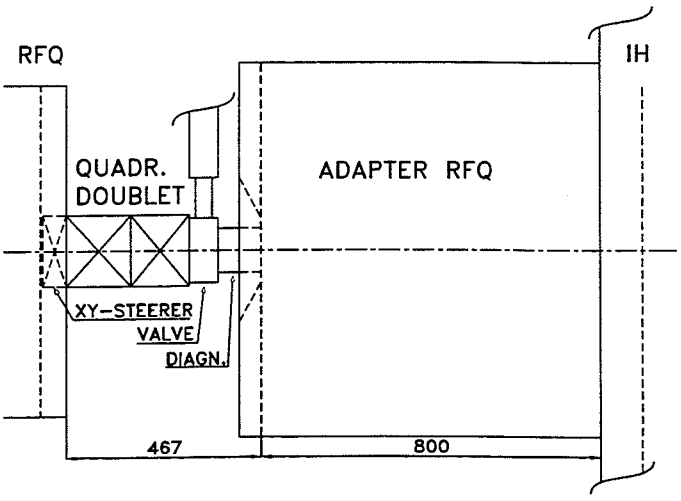

Fig. 1 Schematic of the Matching Section Components

Beam Dynamics Code Extensions

For beam dynamics calculations along the IH-DTL the LORASR code has been developed during several years. It is particularly well adapted to the beam dynamics concept of 'Combined Zero Degree Synchronous Particle Sections' [6]. With the standard routines drift tube accelerating sections as well as quadrupole lens sections can be calculated. A space charge routine is included. For the new matcher, the LORASR code had to be extended in order to calculate the matcher and the IH-DTL in one step. The aim was to have an aditional tool for investigating short RFQ sections.
From a data set containing the maximum vane-vane voltage V , the longitudinally effective voltage $AV\pi/4$, the cell number, the minimum aperture a and the synchronous phase for each cell, the code calculates the cell lengths $\beta\lambda/2$ and modulation factors m and simulates the RFQ fields based on the 2-term-potential description from ref. [7].

At $\phi_{s.p.}$= -90, the entrance and exit regions of the adapter RFQ are very sensitive with respect to fringe field disturbances, because the electrodes are on maximum potential at bunch passage. For that reason fringe field calculations are included, based on the analytical potential expansion as proposed in ref. [8] . Unfortunately it was not very well suited in the present case with matching in and out sections relatively short compared to the cell lengths and high modulation factors, so careful fitting of boundary conditions was necessary. To get rid of the disturbing higher order potential expansion modes along the real geometric distance from electrode end to the resonator end wall, the calculated space was extended by 80% beyond the end wall. This led to a remaining potential on the end wall of 5 % of the max. electrode potential, the equipotential surface fitting rather well to the end wall geometry.

The main result on fringe field calculations was that beam quality deteriorations are kept small if the matching in and out region is short. Therefore it was decided to have a distance of 7 mm only between electrode ends and end walls.

Beam Dynamics Calculations

Calculations were performed with 4 different beam intensities of 0, 5, 10 and 16.5 emA respectively and with corresponding input particle distributions as derived from the main RFQ calculations. A optimum parameter set for each intensity was defined [9]. Additionally, the sensitivity of a given parameter set with respect to beam intensity changes was investigated.

In routine operation, the new LINAC will have to assure good beam quality at the full range of intensities and should be independent of beam intensity fluctuations.

Fig. 2 and 3 illustrate the calculation results for the entire matching section at 16.5 emA. The main characteristics are : the transverse beam envelope is rather smooth ; the longitudinal focusing into the IH-DTL is done in a controlled way and is stable against moderate shifts of rf operation parameters at the RFQ and at the 'Super Lens'. The complete array is also resistant to the different beam parameter requirements described above.

Emittance growth is essentially due to space charge effects, because at low beam current values it is negligible.

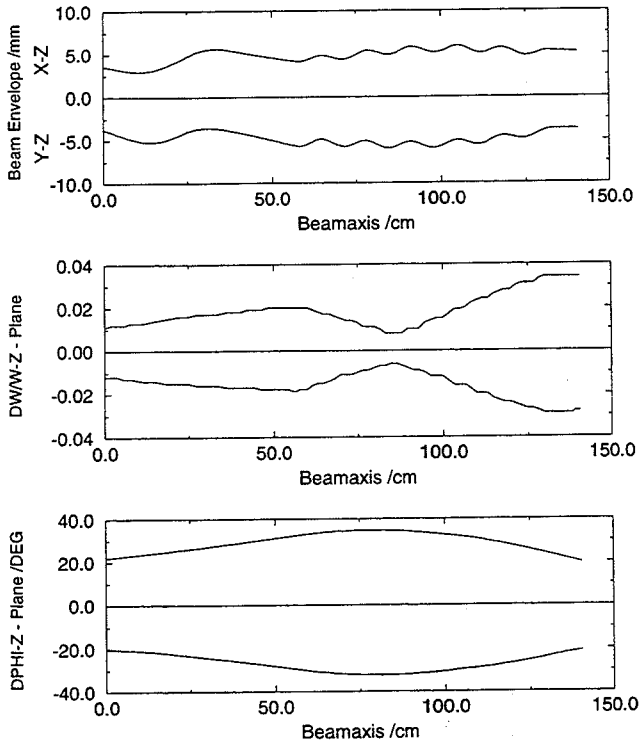

Fig. 2. Transverse and longitudinal 100 % beam envelopes.

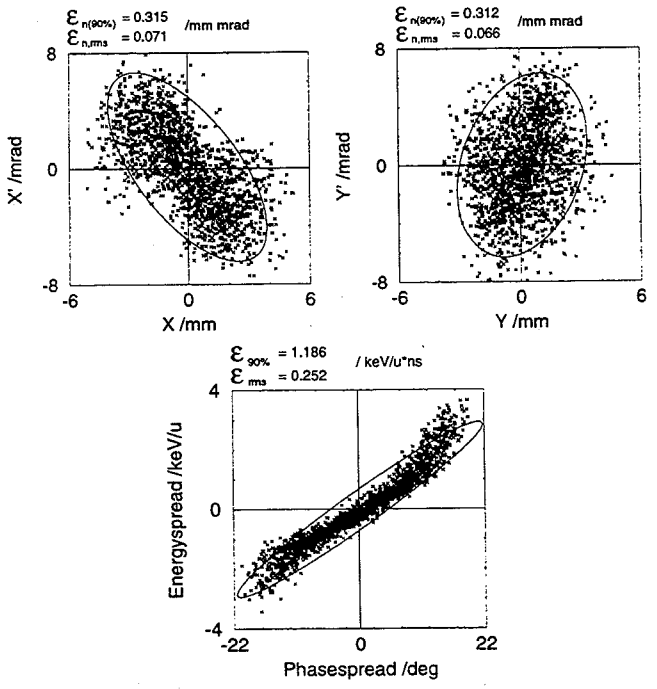

Fig. 3. Matcher Output Emittance Plots (16.5mA ; A/q=65).

Comparison with a Conventional Matching Array

In early design studies the possibility of using a conventional matching section was checked. The beam dynamics calculations result for a 16.5 emA beam with A/q = 65 is shown in Fig. 4 and 5. The corresponding parameters of the components are summarised in Table 2.

Table 2
Parameters of the Conventional Matching Array Components

Total Length	/ m	1.3
Magnetic Quadrupole Triplet		
Effective Length	/ mm	230 ; 320 ; 190
Effective Gradient	/ T/m	65 ; 63 ; 65
Aperture Diameter	/ mm	36 ; 36 ; 36
Rebuncher Cavity		
Gap Number		2
Total Length	/ mm	≅ 200
Peak Gap Voltage	/ kV	240

As the design presented in Fig. 4 has some disadvantages which will be mentioned below, it was decided early not to investigate this alternative further on, so that detailed calculations for different beam currents are missing. However from the experience with the 16.5 emA optimisation the design is expected to be much more sensitive to beam current and rf level variation.

From Fig. 4 it can be seen that before transverse focusing first becomes evident, a big beam radius of around 10 mm in one space is already reached, which makes refocusing by a long and powerfull quadrupole triplet necessary. Placing the triplet in front of the rebuncher would have made the beam focusing into the IH-DTL even more complicated.

On the other hand, placing the rebuncher in front makes the longitudinal focusing difficult and sensitive to beam intensity fluctuations (Fig.5). One can see that a compact beam with small phase extension cannot be properly focused into the DTL. In fact it had to be enlarged in phase space at the main RFQ output, which needed additional matching out gymnastics at the main RFQ.

The emittance growth values for the investigated case were comparable to those of the new matcher.

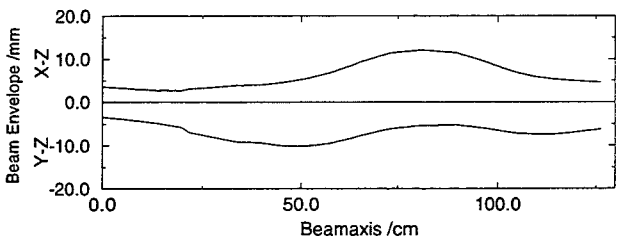

Fig. 4. Transverse 100 % beam envelopes for the rebuncher cavity - quadrupole triplet configuration.

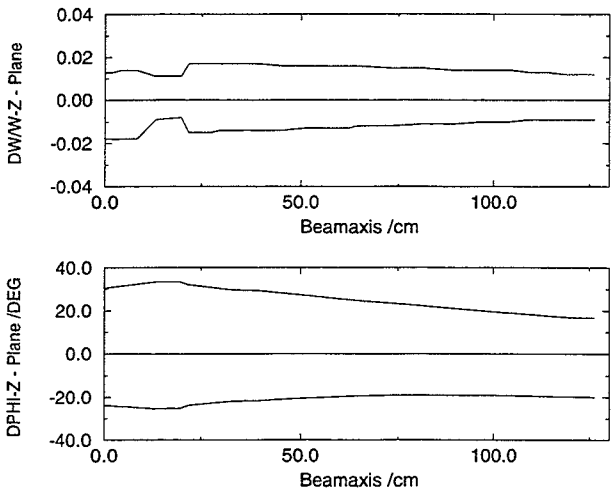

Fig. 5. Longitudinal 100 % beam envelopes for the rebuncher cavity - quadrupole triplet configuration.

Acknowledgments

Many thanks to all members of IAP - Universty Frankfurt engaged in this project - especially to A. Schempp - for the close collaboration in finding out the optimum beam parameters at the matcher input, and to J.Klabunde for the discussions on this subject.

References

[1] "Beam Intensity Upgade of the GSI Accelerator Facility", GSI-95-05 Report.

[2] U.Ratzinger, "The New GSI Injector Linac for High Current Heavy Ion Beams", these Proceedings.

[3] J.Klabunde, "The High Charge State Injector for GSI", Proc. of the 1992 Linac Conf. Ottawa, AECL-10728,Vol.1,p.570-574.

[4] H.Haseroth, "The CERN Heavy Ion Facility", Proc. of the 1994 EPAC, London, p.138-142.

[5] U.Ratzinger, "High Current IH Structures", Proc. of the 1994 EPAC, London, p.264-266.

[6] U.Ratzinger, "The IH Structure and its Capability to Accelerate High Current Beams", Conf. Record of the 1991 IEEE PAC, San Francisco, 91 CH 3038-7, p.567.

[7] I.M.Kapchinsky, "Theory of Resonance Linear Accelerators", Harwood Academic Publishers, New York 1985, Sect. 2.10.

[8] K.R.Crandall, "RFQ Radial Matching Sections and Fringe Fields", Proc. of the 1984 Linac Conf. Darmstadt, GSI-84-11, p.109-111.

[9] A.Schempp, "Design of Compact RFQ's", these Proceedings.

SPACE CHARGE DOMINATED BEAM TRANSPORT IN THE 1.4 MeV/u-UNILAC-STRIPPER SECTION

W. Barth, J. Glatz, J. Klabunde and U. Ratzinger
GSI, Planckstraße 1, 64291 Darmstadt, Germany

Abstract

The intensity upgrading program for the GSI accelerator facility comprises major modifications of the UNILAC for its operation as a high current injector into the heavy-ion synchrotron SIS. This paper focuses on space charge effects arising in the stripper section at 1.4 MeV/u between a new 36 MHz preaccelerator (under construction) and the existing Alvarez structures.
In this section the charge states of incoming ions, having a mass-to-charge ratio of A/q ≤ 65, are increased by stripping in a nitrogen jet to allow further acceleration at A/q ≤ 8.5. The anticipated high current beam of e.g. 4 pmA uranium will experience considerable space charge forces, most severely after the charge state jump in the stripper (from 4^+ to an average charge state of 28^+ for uranium).
The associated emittance growth has been studied for the present transport section, it was found to depend strongly on the underlaying particle density distribution. The amount of ‚useful' beam remaining within given emittance limits will be discussed.

Introduction

The goal to fill the SIS up to the space charge limit requires beam intensities of up to 15 emA ($^{238}U^{4+}$) in the UNILAC prestripper section. [1] The necessary replacement of the present Wideröe accelerator by a high current RFQ and two IH-type cavities will be realized in 1998. The beam transport at 1.4 MeV/u and matching from the exit of the IH-tank to the gas stripper, charge state separation after stripping and matching to the existing Alvarez poststripper linac, all under space charge conditions, have been studied.

Table 1: Parameters of stripper section for uranium

	Exit of IH	Stripper to charge separation	Entrance of Alvarez
Mass	238		
Charge state	4	28 (mean)	28
Current	15 emA	105 ... 12.5 emA	12.5 emA
Energy (v/c)	1.4 MeV/u (β=0.054)		
Bunch frequency	36 MHz	36 MHz	36 MHz
Phase width	±6° (a)	±25° (b)	±6° (c)
Energy spread	±0.2% (a)	±1.7%	±1.8% (c)
Horizontal emittance	11 π·mm·mrad (90%) (a)		15 π·mm·mrad (c)
Vertical emittance	11 π·mm·mrad (90%) (a)		22.5 π·mm·mrad (c)
Relative space charge force (d)	1	50	6

(a) Present result of particle dynamics calculations in RFQ and IH
(b) Chosen for low emittance growth
(c) Upper limit, defined by the acceptance of SIS
(d) For identical bunch dimensions

As the present length of the stripper section may be maintained in the future, the study has to resolve if the existing installation, modified as shown in Fig. 1, is capable of high current operation. Emphasis is given to the study of emittance growth as the SIS poses limits; the acceptance of the poststripper Alvarez section is uncritical. Table 1 summarizes the beam parameters at the IH exit, at the gas stripper and at the entrance of the Alvarez structure.

UNILAC stripper section as studied for high current beam transport

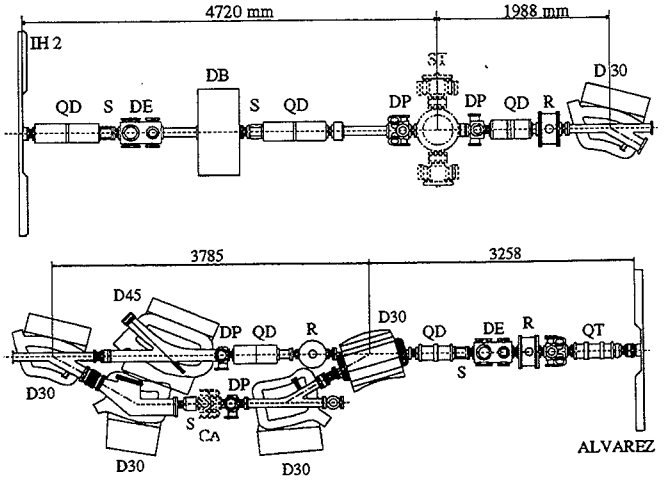

D30	30° bending magnet	QD	Quadrupole doublet
D45	45° bending magnet	QT	Quadrupole triplet
DB	Six gap debuncher (108 MHz)	R	Rebuncher (36 MHz)
DE	Emittance measurement device	S	Steerer
DP	Diagnostics	ST	Gas stripper
CA	Charge analysis		

Fig. 1. Optical elements and beam diagnostic devices in the stripper section between IH2 exit and the Alvarez accelerator, including the gas stripper ST and the charge analysing system of four dipoles D30.

The mechanical layout of the stripper section is shown in Fig. 1. Two quadrupole doublets and a six gap rebuncher (operating frequency 108 MHz) are provided to match the beam to the gas stripper. The charge separator is composed of four 30° bending magnets, charge separation is required between the second and third dipole at maximum dispersion. Transverse and longitudinal matching to the poststripper linac is done with a quadrupole doublet, a triplet and two 36 MHz rebunching cavities.

Matching to the gas stripper

Due to the beam current jump in the stripper (e.g. 12 mA to 105 mA) the downstream section up to the charge analysis is heavely space charge loaded (see Table 1). By iterative

calculations reasonable beam properties at the gas stripper were found, which allow the beam passage through a 9 mm aperture, minimize emittance growth and account a larger growth value to the vertical plane as allowed by the SIS acceptances (Table 1). As a consequence a bunch width of ±25° (36 MHz) at the stripper is demanded and beam waists are to be located before resp. after the stripper in the vertical resp. horizontal plane.

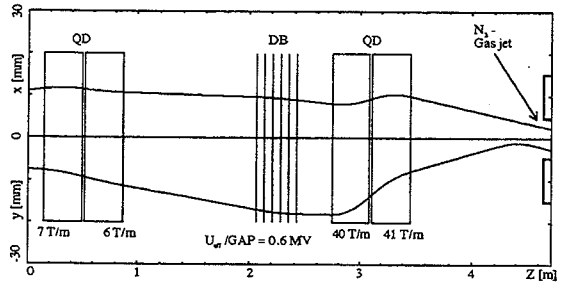

Fig. 2. Transverse matching to the gas stripper, calculated with the code MIRKO. [2] Notations see Fig. 1.

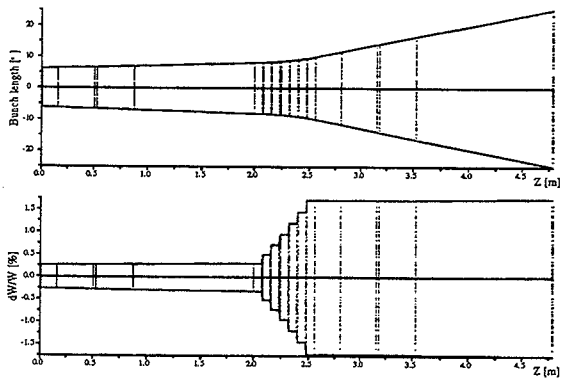

Fig. 3. Long. matching to the gas stripper, calculated for a KV-distribution with PARMT.

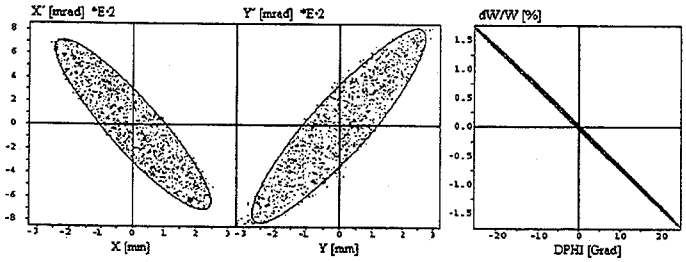

Fig. 4. Transverse KV- and longitudinal homogenous phase space distribution at the stripper position corresponding to the in- and output beam parameters of Table 1.

The envelope matching to the gas stripper including space charge forces is shown in Fig. 2. The required bunch length is obtained by transforming the beam to an energy spread of ±1.7% in the six gap structure with gap voltages of 0.6 MV. Quadrupole strength up to 12 T are required due to the magnetic rigidity of the beam of 10 Tm.

Emittance growth in this section is below 10 % for all planes and different particle distributions. A KV distribution remains virtually undistorted (Fig. 4).

Charge separation and matching to the poststripper linac

In the section from the stripper to the entrance of the Alvarez accelerator the electrical beam current is reduced by the charge state separation (from 105 mA ^{238}U of average charge state 28 to 12.5 mA $^{238}U^{28+}$). An exact modeling of the space charge effect in the separation process, not yet possible with existing tools, was approximated by a current jump before the second dipole magnet. The transverse and longitudinal beam envelopes are given in Fig. 5 and Fig. 6.

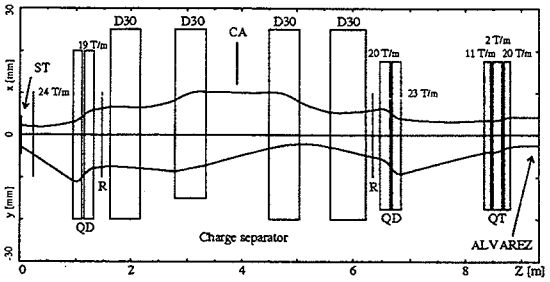

Fig. 5. Transverse beam dynamics between the stripper and the entrance of the poststripper linac (notations as in Fig. 1).

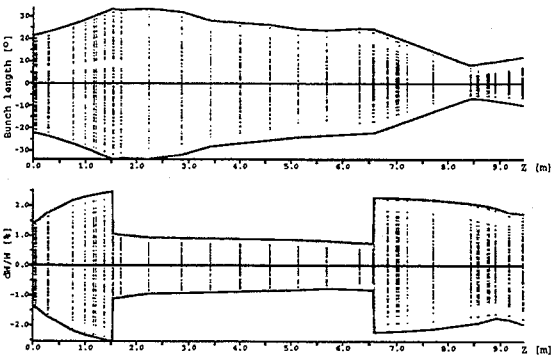

Fig. 6. Longitudinal beam dynamics between the stripper and the entrance of the poststripper linac.

Growth of energy spread by space charge force after the stripper is obvious in the plot of the particle dynamics calculation. The bunchers are required to limit the initially large phase width growth and to produce short bunches at the Alvarez entrance.

Emittance growth effects

The charge separator is an achromatic system and the stripper gas jet density of 4µg/cm^2 is too low to induce significant energy or angular straggling. Therefore the emittance growth is dominated by space charge forces.

As an example the horizontal rms-emittance growth along the beamline is shown in Fig. 7, calculated with a KV-distribution and a more peaked distribution (homogenous in a six dimensional hyperellipsoid folded with a Gaussian and cut at 3σ) on the basis of particle-particle interaction. The apparent emittance growth by dispersion is compensated behind the magnet system, leaving the current and distribution dependent space charge effect. For low intensities the net emittance growth is zero.

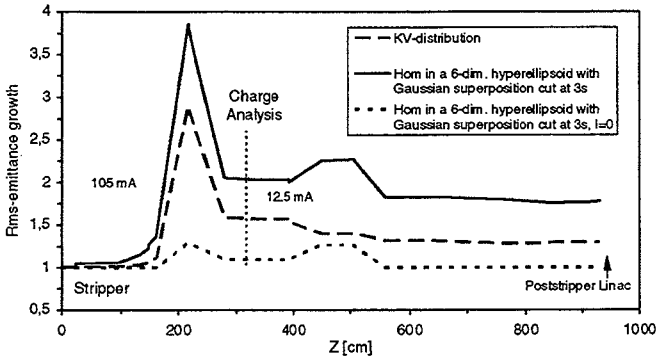

Fig. 7 The rms-emittance growth after stripping for three different distributions calculated by PARMT.

Starting with different particle distributions, which all hold 90 % of the intensity in emittance areas as given in Table 1, the rms emittance values at the end of the stripper section have been calculated for the three phase planes.

Fig. 8 is a summary of the results. Type 2 is a homogenous distribution in a six dimensional hyperellipsoid. The distributions 12 to 42 have increasingly intensified cores, which result in increasing emittance growths by up to a factor of 2 compared to the homogenous distribution.

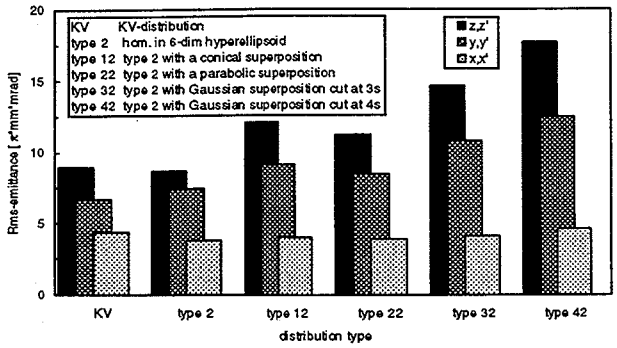

Fig. 8. Rms-emittance for different input particle distributions.

In such a „peaked" distribution the electric field rises more steeply near the center than at the edge; this deviation from linearity causes „ears" of the distribution (Fig. 9), which increase the emittance areas.

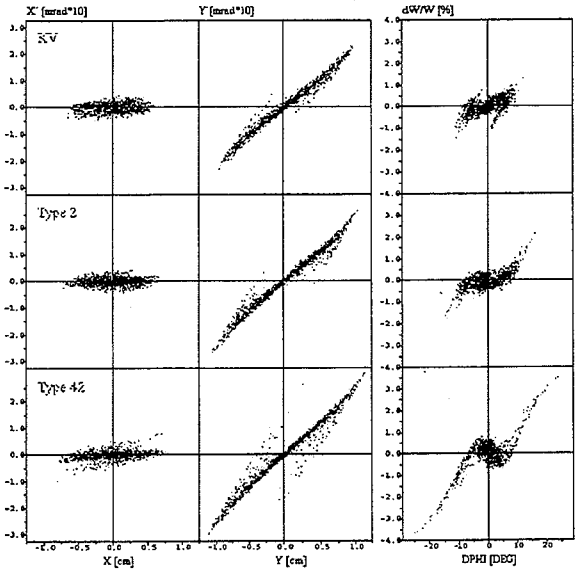

Fig. 9. Results of multiparticle calculations for three different input distributions.

More relevant for the injection into the SIS than the rms emittances is the intensity fraction remaining within the acceptances of the SIS listed in Table 1. Table 2 shows the fraction of beam intensities matching the requirements in the three phase space planes. For the not unrealistic distributions of type 42 the more prominent peaking of the particle density leads to less acceptability; however the loss of useful intensity is less than might be expected from the rms-emittance growth.

Table 2 Fraction of beam intensities corresponding to the design emittances (see Table 1)

Distribution	KV	Type 2	Type 42
Horizontal	0.81	0.90	0.80
Vertical	0.82	0.78	0.72
Longitudinal	1.00	1.00	0.96

Conclusion

With respect to emittance growth a rather homogenous particle density in the bunch is favourable. Aside from attempting to achieve flatter distributions from the IH-accelerator the activities concerning emittance growth will also cover a rigorous shortening of the very-high-current section, an increase of transverse beam size at the stripper position, analysis and optimization of the charge separation process and beam neutralisation in drift spaces.

References

[1] U. Ratzinger, The new GSI Injector linac for high current heavy ion beams, these proceedings.

[2] B. Franczak, MIRKO, Proc. of the Europhysics Conf. Computing in Accelerator Design and Operation, Berlin, 1983

HIGH-INTENSITY LOW ENERGY BEAM TRANSPORT DESIGN STUDIES FOR THE NEW INJECTOR LINAC OF THE UNILAC

W. Barth, L. Dahl, J. Klabunde, C. Mühle, P. Spädtke
GSI, Planckstraße 1, 64291 Darmstadt, Germany

Abstract

GSI will replace the Wideröe prestripper linac by an RFQ and IH-type accelerator presently under construction. The new prestripper linac should deliver beam intensities to fill up the heavy ion synchrotron SIS to the space charge limits for all ions. In case of uranium the new injector has to deliver 15 emA U^{4+}. One of the two existing ion-source terminals has already been rebuilt for installation of the high current sources of CHORDIS- and MEVVA-type. Therefore, investigations of high-current beam transport have been made in the existing LEBT. For that, additional beam diagnostic elements have been installed: beam transformers, emittance measurement devices, residual gas ion spectrometer. The measured beam properties, e.g. transverse emittance, degree of space charge compensation, support the design of the future LEBT. According to the various requirements two layouts of the new LEBT have been studied so far.

Introduction

To improve the high-current performance of the UNILAC for injection in the SIS the Wideröe prestripper accelerator will be replaced by an RFQ and an IH-type accelerator [1]. This requires also a redesign of the LEBT from the ion source to the RFQ entrance. For that, the following basic requirements on the beam dynamics have to be considered: High transmission for the high-current beam, preservation of the brilliance along the beam line, isotope seperation even for the heaviest elements, achromatic image and slope at the end of LEBT, transverse phase space matching to the RFQ, and insensitivity to space charge and energy fluctuations of the beam.

The study of the future LEBT profits greatly from beam investigations at the present beam transport system. Measurements of beam transmissions, transverse emittances, degree of space charge compensation, comparison of beam simulations with experimental data, etc. support the LEBT design considerably.

In the first part measurements on high-intensity beams will be reported. Afterwards different layouts of a new LEBT will be discussed.

Measurements on High-Intensity Beams

The existing injection beam line between the high current ion source and the switching magnet has been equipped with additional beam diagnostic instruments as shown in Fig. 1.

The beam transmission has been measured by Faraday cups and calibrated beam transformers. The transverse emittances have been measured by slit-collector systems. These measurements give information about the brilliance of the beam. Emittance growth along the beam line can be detected. Also profile measurements at different positions will support the evaluation of the beam simulation model.

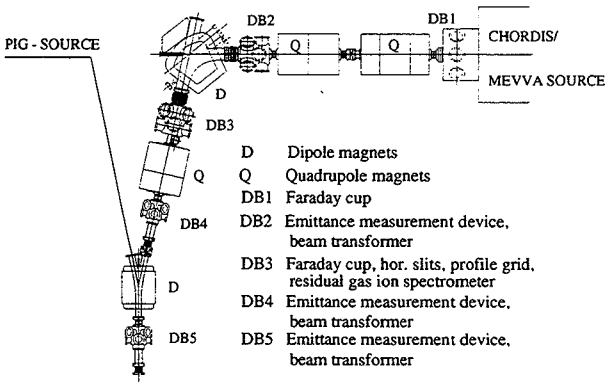

Fig. 1. Present low energy beam transport line.

Space charge potential and build-up time of beam neutraliziation can be measured by a new residual gas ion spectrometer. Description of this system and first measurements will be reported in a separate contribution of these proceedings [2].

In Table 1 some representative results of emittance measurements are given for different ion species delivered from the high-current sources CHORDIS and MEVVA, the beam energy was 11.7 keV/u. The beam transfer from DB2 to DB4 (see Fig. 1) was simulated with the ellipse transformation code MIRKO and the Monte Carlo code PARMT.

Table 1
Results of Emittance Measurements

Ion species/ current (mA)	Source type	Locus	ε_x (95%) (π·mm·mrad)	ε_y (95%) (π·mm·mrad)
$^{20}Ne^{+}$ / 16	CHORDIS	DB 2	56	54
		DB 4	56	57
$^{40}Ar^{+}$ / 10	CHORDIS	DB 2	58	67
		DB 4	59	59
He^{+} /14	CHORDIS	DB 2	77	74
		DB 4	84	70
He^{+} /16	CHORDIS	DB 2	80	74
		DB 4	84	70
$^{58}Ni^{2+}$ / 4	MEVVA	DB 2	97	90
		DB 4	92	88
$^{27}Al^{2+}$ / 3	MEVVA	DB 2	52	52
		DB 4	46	54

Figure 2 shows results of beam dynamics calculations at different current levels. Measured emittances and computed

phase space ellipses at zero current coincide each other. Therefore, a high degree of space charge compensation can be stated. This result was also confirmed by beam width measurements behind the bending magnet where a very small horizontal beam size was adjusted at the mass separator slits. Figure 3 illustrates the big increase of beam width if the beam simulation includes space charge forces. The measured beam width agrees very well with the zero-current simulation.

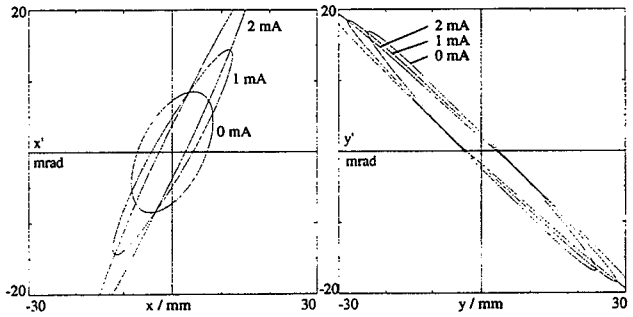

Fig. 2. Transverse emittances at DB4 calculated for different effective currents.

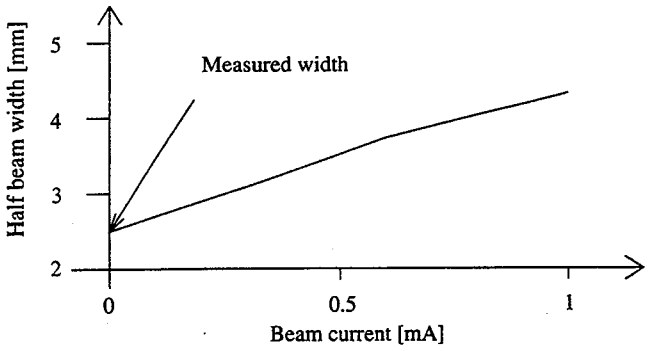

Fig. 3. Computed beam width at the spectrometer slits.

The comparison of emittance areas listed in Table 1 indicates that there is no evident growth between the diagnostic stations DB2 and DB4. This result is in full agreement with PARMT simulations (at I = 0), higher order effects are included.

Properties of the Existing LEBT

The existing LEBT as shown in Fig. 1 has been studied for the use of high-intensity beam transport for the new injector. To match the beam to the RFQ acceptance it has to be partly rebuilt. Figure 4 shows the transverse beam envelope matched by four quadrupole magnets to the RFQ acceptance. The envelope is based on an emittance of 138 π·mm·mrad in both planes, corresponding to the RFQ acceptance.

The high current sources deliver beam pulses of 1–2 ms length and a repetition rate ≤ 5 Hz for the heavy ion synchrotron. The PIG sources serve the low energy experimental area with a second beam of up to 6 ms length and a repetition rate of 50 Hz. For future time sharing operation laminated magnets are planned.

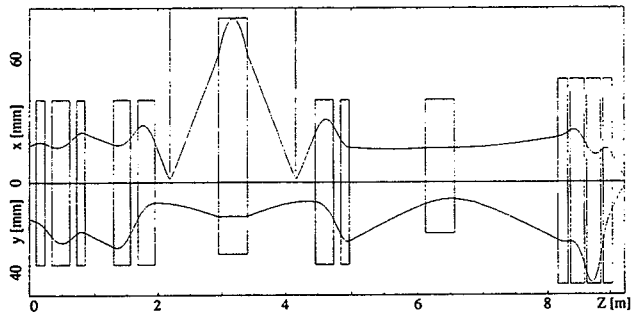

Fig. 4. Transverse beam envelope calculations for the existing mass spectrometer and a matching quadruplet in front of the RFQ.

The layout of the complete LEBT including also the PIG source beam line is presented in Fig. 5.

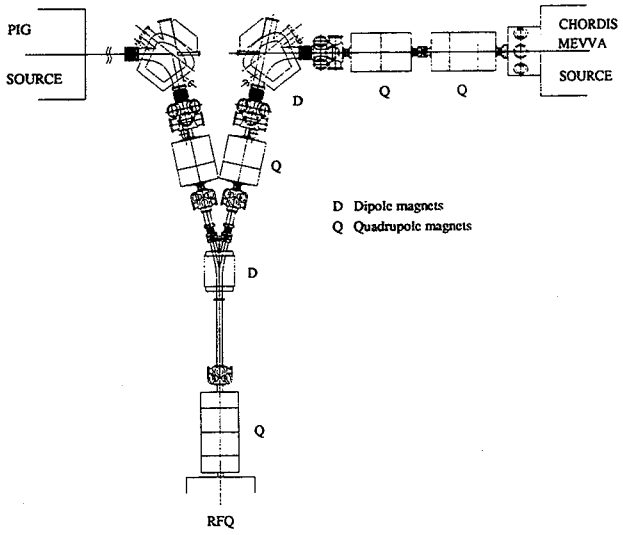

Fig. 5. Mechanical layout of the studied LEBT, a shortened version of the existing LEBT.

The 77.5^0 spectrometer magnet performs a mass resolution $m/\Delta m = 220$. This allows the isotope separation of all elements which is necessary for many experiments and reduces the space charge forces in the following transport and accelerator sections.

This LEBT is achromatic only in the way that particles of different energies coincide in a focus at the RFQ entrance but unfortunately with different angles. This is shown in Fig. 6.

Emittance measurements directly behind the variable high voltage gap (DB1 in Fig. 1) turned out that the emittance areas are in the range of 70–90 π·mm·mrad at the new energy of 2.2 keV/u and have constant orientation. The acceptance of the LEBT and the RFQ of 138 π·mm·mrad allows therefore a certain emittance growth due to momentum spread or space charge of the beam. Investigations carried out with PARMT prove a possible momentum spread $\Delta p/p \leq 5 \cdot 10^{-4}$ which is higher than the specified stability of the high voltage power supplies. Space charge forces at a current of 0.5 mA would

cause an emittance growths of about 70%, which would fill the RFQ acceptance completely.

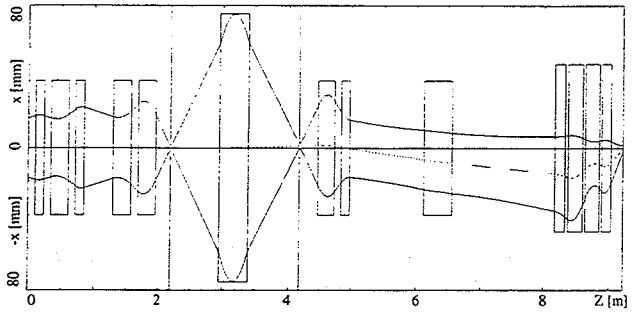

Fig. 6. Horizontal envelope for a beam with a momentum deviation of $\Delta p/p = 0.001$.

Study of an Achromatic LEBT

A new LEBT design was studied which should be doubly achromatic to prevent beam loss due to instabilities of the extraction and preacceleration voltage of the order of 10^{-3} due to current fluctuations. Furthermore, it should be capable to transport space charge dominated beam.

The envelopes of the new transport system are presented in Fig. 7. A magnetic quadrupole triplet adapts the beam onto the achromatic deflector consisting of two 45° sector field dipole magnets with an intermediate quadrupole singlet. The dipole edges are vertically focusing. Two quadrupole triplets match the transverse emittances to the RFQ acceptance.

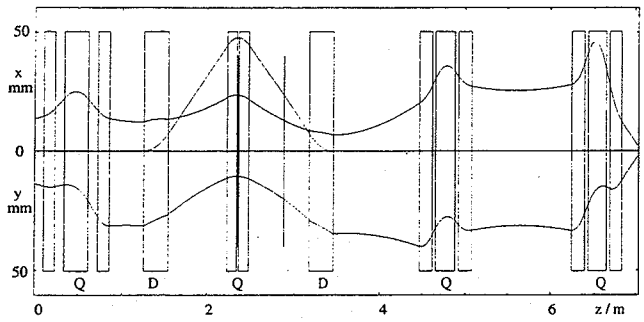

Fig. 7. Beam envelope in a double achromatic system for a space charge force of 4 mA and dispersion trajectory for an energy deviation of 14%.
Q: magnetic quadrupoles, D: dipole magnets.

Mass separation was given up to the benefit of an effective space charge increase to 4 mA, equvivalent to a compensation degree of 75%.

Multi-particle calculations for this LEBT were done with the PARMT code considering higher order effects. At an effective beam current of 4 mA a transmission of 100% is obtained with an emittance growths of 35% for the horizontal and respectively 31% for the vertical plane. So only 80% of the RFQ acceptance of 138 π·mm·mrad is occupied by the calculated phase space distribution.

Investigations of the sensitivity for energy fluctuations show an effective emittance growth caused by chromatic aberrations of the magnetic quadrupoles.

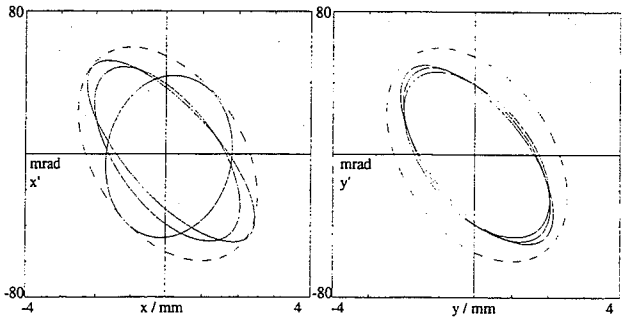

Fig. 8. RFQ acceptance (dotted) and beam emittances for three energy deviations: 0, + 2.8%, - 2.8%.

Figure 8 shows the transversal beam emittances for an energy spread of ± 2.8%. This value is by far higher than assumptions of the order of 10^{-3} for high-intensity beams. Fast intensity fluctuations which partly convert into energy spread are therefore not critical.

Also fluctuations within a macropuls of ± 14% of the effective space charge current of 4 mA do not exceed the RFQ acceptance for fixed quadrupole settings.

Conclusion

The existing LEBT modified for high-current injection performs high mass resolution, is compact, and enables a low cost modification for high-current operation. The sensitivity for dispersion limits the energy spread to $\leq \pm 10^{-3}$. The space charge sensitivity needs a space charge compensation degree ≥ 90%.

The alternative LEBT design is doubly achromatic, and therefore insensitive to energy spread or fluctuation up to ± 2.8%. Current fluctuations of ± 14% will be accepted by the LEBT and the RFQ. Even at a space charge compensation of only 75 % complete transmission can be reached.

The low momentum resolution of this LEBT design allows only the separation of charge states. Further studies are going on to achieve the high mass resolution additionally.

References

[1] U. Ratzinger, The New GSI Injection Linac for High-Current Heavy Ion Beams, these Proceedings.

[2] R. Dölling, et al., Investigations of Space Charge Compensation with Residual Gas Ion Energy Analyser, these Proceedings.

Design and Wakefield Performance of the New SLC Collimators

F.-J. Decker, K. Bane, P. Emma, E. Hoyt, C. Ng, G. Stupakov, J. Turner, T. Usher, S. Virostek, D. Walz
SLAC*, California, USA

Abstract

The very small transverse beam sizes of the flat SLC bunches are 100–170 μm in the horizontal and 30–50 μm in the vertical near the end of the SLAC linac. Unexpectedly large transverse wakefield kicks were observed from the collimators in this region during 1995. Upon inspection, it was found that the 20 μm gold plating had melted and formed a line of spherules along the beam path. To refurbish the collimators, an improved design was required. The challenging task was to find a surface material with better conductivity than the titanium core to reduce resistive wakefields. The material must also be able to sustain the mechanical stress and heating from beam losses without damage. Vanadium was first chosen for ease of coating, but later TiN was used because it is more chemically inert. Recent beam tests measured expected values for geometric wakefield kicks, but the resistive wall wakefield kicks were four times larger than calculated.

1 Introduction

To suppress background in the detector, collimators are used at the end of the SLC linac. The surface of these collimators were inspected in 1995 and the gold coating on the titanium jaws was found to be severely damaged. A dark 1 mm wide stripe along the beam path was visible, which consisted of gold flakes and spherules of ≈250 μm diameter (Fig. 1). They were responsible for a 25–50 times larger than expected wakefield kick [1]. A new durable surface material for the coating was necessary with high conductivity to reduce resistive wakefields.

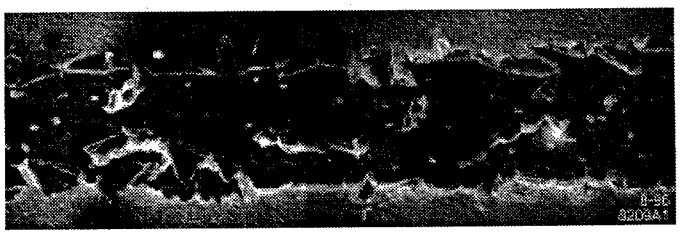

Fig. 1: Damaged collimator surface (stripe width ≈1 mm). The beam enters at the left, creating gold flakes and spherules.

2 Coating Material for Collimators

The core material for the collimator jaws is a titanium alloy Ti-6Al-4V, which best survives beam impact. The coating material requires a higher conductivity (Table 1, [2]).

2.1 Background Issues

The surface material chosen initially was gold to give the particles scattered out of the core material additional *dE/dx* loss. This was a compromise between the desire to reduce background to the detector as well as resistive wakefields contributions and the known hazards of higher single bunch temperature spikes and resulting thermal shock waves. Since the linac collimators are 1.5 km from the interaction point and additional downstream clean up collimation exists, the high *Z* surface requirement has now been eliminated.

2.2 Survivability

With respect to survivability of the surface coating, no material is an obvious choice. But since the resistivity of Ti-6Al-4V is about 70 times larger than gold (the resistive

Table 1
Potential conductive surface coatings for titanium collimators. Ti# stands for Ti-6Al-4V.

Material	Z	X_0/ρ cm	T_{melt} °C	R μΩ-cm	E 10^{-6} psi	α 10^6 $°C^{-1}$	Eα psi $°C^{-1}$	Eα/σ_{UT} 10^3 $°C^{-1}$	k W/ cm °C
Ti#	16.3	3.77	1650	175	16.5	11	182	1.3	0.07
Cu	29	1.45	1083	1.67	17	16.6	282	8.8	3.9
Al	13	9.03	659	2.83	10	25	250	19.2	2.39
Cr	24	1.7	1860	12.8	36	6.2	223	18.6	0.92
V	23	2.05	1735	24.8	18.2	8.3	150	2.2	0.31
Mn	25	1.6	1244	28	23	22.8	524	7.3	
Ni	28	1.35	1728	7.0	30	13.3	400	8.7	0.84
Ti	22	3.35	1680	42	15.5	8.7	135	1.5	0.17
Au	79	0.35	1063	2.44	11.3	14.3	161	10.8	2.95
TiN	14.8	3.87	2930	22	36	8.3	300		0.29
TiC	14.3	3.84	3140	60	8.0	7.4			0.21

* Work supported by DOE, contract DE-AC03-76SF00515.

wakefield kick would be $\sqrt{70}$ times larger), a material with less sensitivity (up to 10 times of gold) was needed. Nickel, vanadium, and TiN fall into that range.

Nickel is somewhat ferromagnetic at the high frequencies of the short bunch, it is difficult to coat and its figure of merit ($E\alpha/\sigma_{UT}$) is marginal, but it has the best resistivity (7 μΩ-cm). Vanadium has a larger resistivity but sputters more easily onto Ti. Some collimator jaws were coated with vanadium, which is fine for dry air or vacuum. Unfortunately, it chemically reacts with water and presents handling problems. The final choice was TiN, a golden looking coating (e.g. on drill bits) with a resistivity of 22 μΩ-cm. Not all of the material properties are understood (blank in Tab. 1), but a test with an electron arc welding torch showed good survivability for TiN. The hard coating might allow the phonon shock wave to penetrate to the Ti, while at a gold-Ti boundary it would be reflected [3].

3 Collimator Wakefields

The close proximity of the jaws to the beam (0.8–1.2 mm gap) will lead to wakefields. The following discusses different types due to their origin: geometric, resistive, and "granularity" wakefields with their linear and quadratic effects.

3.1 Geometric wakefield

The peak dipole component of the geometric wakefield for a round collimator (flat: $\pi^2/8$ larger) is [4]

$$\Delta y' = 4\frac{r_e N}{\sqrt{2\pi}\,\gamma\,\sigma_z^{3/2}}\left(\frac{y}{a}\right)$$

which is 2 μrad for $N = 5\cdot10^{10}$ particles, a bunch length σ_z = 1.25 mm, energy factor γ = 90000, classical electron radius r_e, and a beam offset y equal to the pipe radius a. This has to be compared to a beam size σ_y = 50 μm, and an angular divergence $\sigma_{y'}$ = 1.0 μrad for an emittance $\gamma\varepsilon_y$ = $0.45\cdot10^{-5}$ m-rad and a betatron function value β = 50 m. These beam parameters are assumed throughout the paper. The effect of the kick is illustrated in Fig. 2.

By rounding the edges (r = 9 mm) the geometric wakefield component of the tapered collimator (R = 10 m) is reduced by a factor of 2. This then gives an expected maximum dipole kick for our flat jaws of $\Delta y'$= 1.3 μrad. A $3\sigma_{y'}$ kick gives an emittance growth of about 30% and $5\sigma_{y'}$ about 60%.

The higher order component of the geometric wakefield was calculated with MAFIA [4] and the result divided by 2 for the rounded edges. This simulation agrees well with a round collimator scaling estimate for y'

$$\sum_{m=1}^{\infty}\frac{1}{m}r_1^m r_2^{m-1} = \frac{-\ln(1-r^2)}{r}$$

when r_1=r_2=r=y/a (see Fig. 3 dashed curve).

The quadrupole wakefield near the axis of a round collimator is zero (for a round beam), but for a flat collimator it is about 1/3 of the dipole kick [5]:

$$\Delta y'_2 = 1/3\ \Delta y'\ y_2/a$$

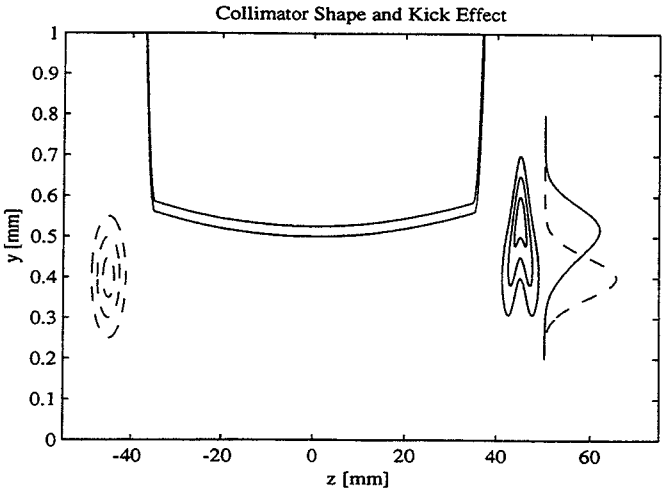

Fig. 2: Tapered collimator and a resultant wakefield kick of $3\cdot\sigma_y$. The contour lines and projections of the incoming (dashed), and outgoing beam (solid) are shown.

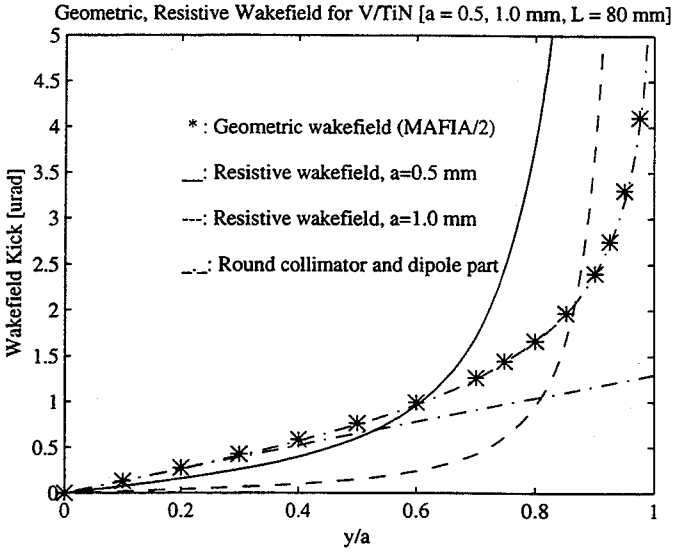

Fig. 3: Geometric and resistive wakefield estimates.

where y_2 is the offset of a second (test) particle within the centered bunch. For a half-gap of a = 0.5 mm and a $\Delta y'$ = 1.3 μrad this results in a differential quadrupole kick over the bunch with a maximum which is about 20% of a typical magnetic quadrupole strength at the end of the linac. This effect is somewhat reduced since the x and y collimator jaws are close together and have usually similar gaps ($5\sigma_x$ = 800 μm, $10\sigma_y$ = 500 μm), and therefore cancel each other.

3.2 Resistive wakefield

The resistive dipole wakefield kick due to parallel resistive plates of length L is [6]

$$\Delta y' = \frac{\pi r_e N L}{4a^2\gamma}\left(\frac{c}{\sigma\sigma_z}\right)^{1/2} f(s/\sigma_z)\left(\frac{y}{a}\right)$$

with a maximum kick of 0.95 μrad (a = 0.5 mm, f = 1, and a conductivity $\sigma = 4.1\cdot10^{17}$ s^{-1} for TiN.

To get the higher order components, the term y/a has to be replaced by the following (with $r = y/a$):

$$\frac{1}{\pi}\left(\frac{\pi r+\sin\pi r}{1+\cos\pi r}\right).$$

3.3"Granularity" wakefield

The wakefield due to the spherules was roughly estimated to be [7]:

$$\Delta y' = \frac{r_e N L}{4\sqrt{\pi a^2 \gamma \sigma_z}} g\left(\frac{y}{a}\right)$$

where 25% of the surface is covered with spherules and g is the granularity (or corn size). Comparison to the resistive wakefield yields:

$$g = \pi^{3/2}\sqrt{\frac{c\sigma_z}{\sigma}}.$$

For g = 250 μm the resultant kick is about 50 times the resistivity kick from gold. This explained the large wakefields of the damaged parts.

4 Experimental Results

The collimators were set to a specific gap size $2a$, and moved across the beam. The beam position monitor signals up- and down-stream were recorded to measure the kick, the beam loss and the incoming offset (Fig. 4).

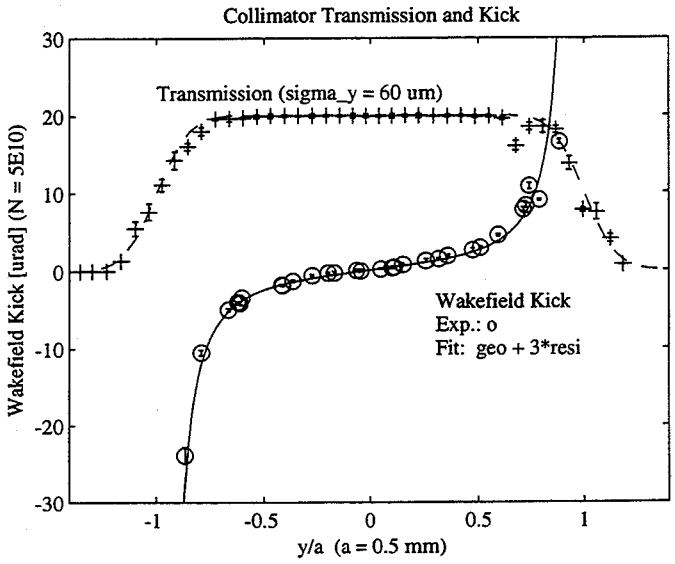

Fig. 4: Beam transmission (+) and measured kicks (o). The solid curve shows the expected behavior including 3 times the expected resistive kick.

Scanning with different collimator gap sizes allows distinction between the geometric and resistive wakefields. At wide gaps the geometric wake dominates, while at small gaps the resistive wakefield is bigger. By plotting the linear slope at $|y/a|<<1$ versus $1/a$ (a = half gap size) the geometric part should be independent of a, while the resistive part should grow quadratically (see Fig. 5).

The expected and measured kicks for a = 0.5 mm are summarized in Table 2. The average kick over the beam from the form factor f is 0.71 (geometric) and 0.78 (resistive). The 40% bigger kick for the geometric part might be due to the uncertainty of the rounded edges. But the factor of 4 difference in the resistive part is so far unexplained.

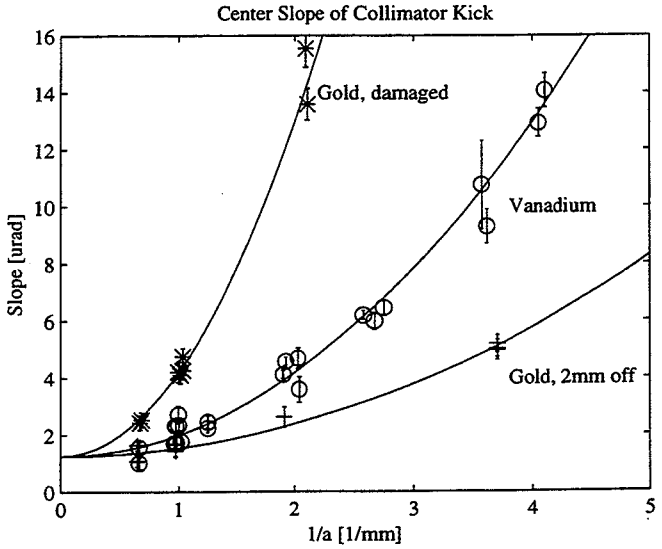

Fig. 5: Slope of the linear part of the wakefield kick versus $1/a$. The fit (solid) shows a kick about a factor of 4 higher than expected for the resistive wakefield.

Table 2
Collimator wakefield kicks in μrad.

	Expected	Measured	Factor
Geometric	0.92	1.29±0.10	1.4
Au	0.26	1.12±0.06	4.3
V	0.74	2.88±0.10	3.9
Au, damaged	---	11.6±0.4	--

5 Summary

The new collimators with TiN (and V) coatings have survived beam impacts. The wakefield kicks were reduced by a factor of four. The measured resistive wall wakefield kick is a factor of 3-4 larger than expected.

References

[1] K.L.F. Bane et al., "Measurement of the Effect of Collimator Generated Wakefields on the Beams in the SLC", PAC95, Dallas, May 1995, p. 3031.

[2] D. Walz et al., PAC89, Chicago, SLAC-Pub-4965.

[3] W. Stoeffle, LLNL, private communication.

[4] K. Bane and P. Morton, Linac 86, SLAC, p. 490.

[5] A. Piwinski, DESY-HERA-92-04, Jan. 92.

[6] A. Chao, "Physics of Collective Beam Instabilities In High Energy Accelerators", J. Wiley&Sons, New York, 1993, chap. 2.

[7] A. Chao, private communication.

Long-Range Wakefields and Split-Tune Lattice at the SLC

F.-J. Decker, C.E. Adolphsen, R. Assmann, K. Bane, K. Kubo#,
M. Minty, P. Raimondi, T. Raubenheimer , R. Ruth, W.L. Spence

SLAC*, Stanford CA 94309, USA

Abstract

At the SLC, a train consisting of one positron bunch followed by two electron bunches is accelerated in the linac, each separated by about 60 ns. Long-range transverse wakefields from the leading bunch were found to cause up to a factor of three increase in beam jitter for the trailing bunches. Incoming jitter is efficiently damped by BNS damping, but excitations in the middle of the linac from sources such as long-range wakefields can grow in amplitude. To measure the wake function, the time difference between the positron and electron bunches was changed, determining the frequency and strength of the dominant mode contributing to the dipole wakefield. By splitting the horizontal and vertical phase advance, or 'tune', of the magnetic lattice, it was possible to decrease the resonant excitation from these wakefields and thereby reduce the jitter of the electron beam by a factor of two.

1 Introduction

Long-range wakefields cause beam break up in multi-bunch beams [1]. The NLC design has adopted the use of damped and detuned structures to overcome these difficulties [2]. In the SLC the problem is less severe since the e^+ and e^- bunches can be individually steered due to their different beta-functions. However positron jitter translates via transverse wakefield kicks into electron jitter, and a positron orbit change (arising e.g. from orbit oscillations for emittance reduction [3]) will also change the electron orbit. The magnitude of these effects were measured by kicking the positron beam in the ring-to-linac beamline (RTL) and measuring the orbits for both beams in the linac. Observations and experiments are discussed, which led to a cure for the jitter.

2 Operational Observations

Several indirect observations indicated that the dominant beam jitter in the vertical plane for electrons was due to long-range transverse wakefields from the positrons. Large electron y jitter, amplified along the linac about 6 times more than expected from the short-range wakefields [4], e^+/e^- jitter correlation, x/y jitter correlation, and the fact that the electron jitter was reduced by a factor of two if the positrons were not present, all were noted. While beam loading changes with positron intensity was a possible explanation, the long-range transverse wakefield hypothesis was confirmed in the following experiments:

a) kick the positrons in the RTL to induce a large oscillation in the linac, measure the electron orbit shift,
b) change the positron-electron bunch separation and look for changes in the amplitude response.

3 Oscillation Experiments

Figure 1 (a) shows an example in which the positron bunch is kicked in the RTL. A large excitation of the electron bunch in the linac results (b). For a 1 mm oscillation with $3.3 \cdot 10^{10}$ particles in the positron bunch, the amplitude is 250 μm in electron x, and 500 μm in electron y. The positron oscillation is seen to decohere to 100 μm at the end of the linac.

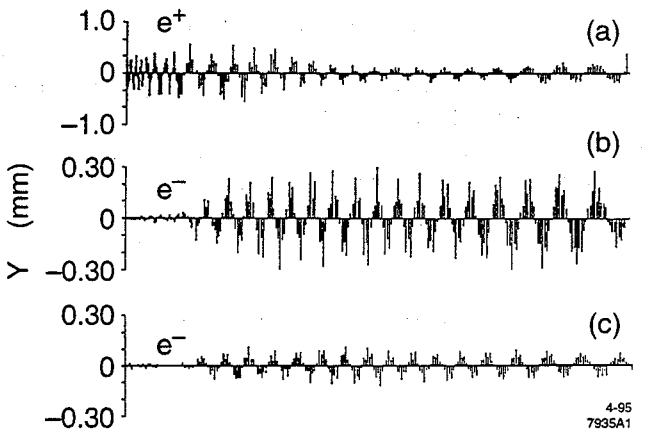

Fig. 1: (a) A positron oscillation in the SLC linac kicks the electrons via long range transverse wakefields, (b) for the design lattice, and (c) the new split-tune lattice (compare Section 6).

Orbits were also measured for different e^+ and e^- bunch spacings, necessarily adjusted in steps corresponding to –2, –1, 0, and +1 S-band buckets, or 0.35 ns intervals. The electron oscillations are locally 90° out of phase with respect to the positron oscillations, as expected if they are driven by the latter. Their amplitude varies in sign and magnitude with the positron bucket. Figure 2 shows the measured signed amplitude vs. bunch spacing fit to a single mode (see Section 5), which is thus determined to have a frequency of 4141.7 MHz and amplitude of 350 μm for a 1 mm oscillation with $3.3 \cdot 10^{10}$ positrons. Shifting the frequency to 4144.5 MHz (dashed curve) would zero the wakefield at the operation separation of 59.0 ns. Early in the history of SLAC [2], cells 3, 4, and 5 following the input couplers in selected accelerator sections were 'dimpled' to raise the modes by either

Visiting scientist from KEK.
* Work supported by DOE, contract DE-AC03-76SF00515.

2 or 4 MHz. Therefore implementing such a frequency shift appears to be feasible.

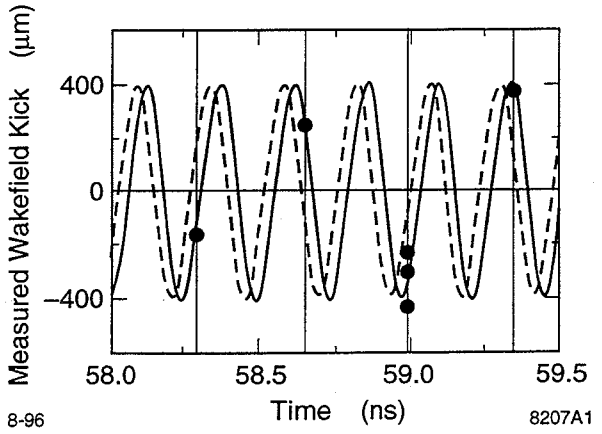

Fig. 2: The average kick in amplitude and sign is plotted versus the time for the different positron buckets. The solid curve has a frequency $f = 4142$ MHz while $f = 4144.5$ MHz for the dashed curve.

4 Static Bucket Changes

In addition to communicating jitter from the leading positron bunch to the following electron bunch, the long-range wakefield will be excited to the extent that the average steered positron trajectory is offset in the accelerator structures. This 'static' long-range wakefield effect is manifested when the distance between the positron and electron bunches is changed. Figure 3 shows the measured trajectory shift due to a shift in the positron-electron separation by one S-band bucket. The positron orbit shift reflects beam jitter and position monitor noise, while the electron shift is clearly an oscillation driven by the static positron wakefield. Its 150 μm peak amplitude is large compared to the 20 μm expected from a single 12 m long structure offset by 1 mm.

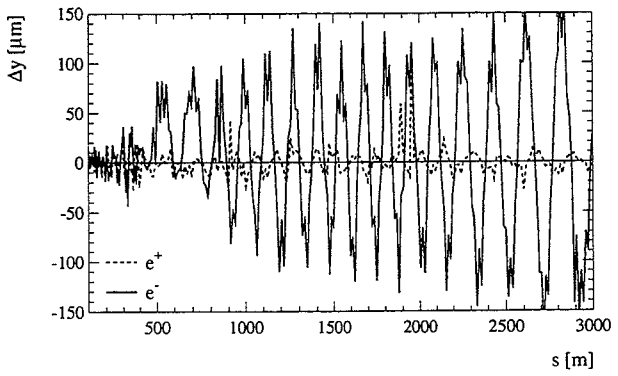

Fig. 3: Difference orbit in the electron beam by moving the leading positron bunch by one bucket.

Static long-range wakefield effects are not very important for the SLC operation, since they can be steered out. The measurements of the static e^- deflections due to bucket changes however, contain information about the offsets between the positron trajectory and the accelerating structure, including structure misalignments. Preliminary studies aimed at isolating structure misalignments from bucket shift data have demonstrated the need for further work before the technique can be applied to practical alignment problems.

5 Theoretical Estimates

Figure 4 shows the dipole wakefield for the SLAC linac structure, calculated using a two-band circuit model [5]. Although the lowest dipole mode has the strongest kick factor of the structure by at least a factor of two, there are about 50 modes of similar strength that span 4140 MHz to 4320 MHz. These modes rapidly decohere for increasing bunch separation up to 10 ns, after which they partially recohere, exhibiting various beating patterns.

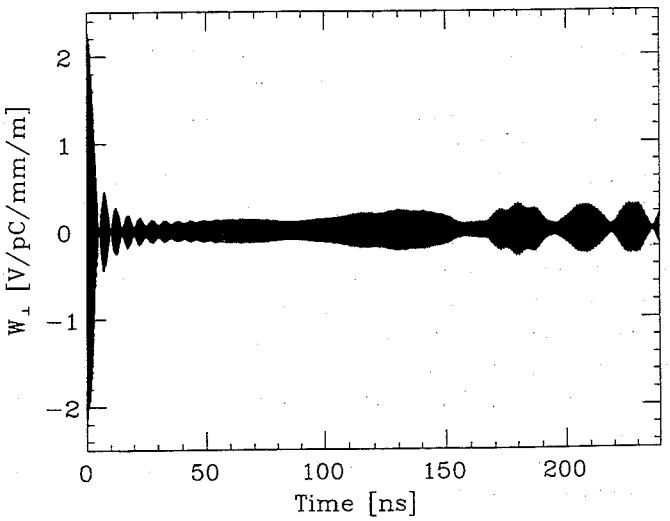

Fig. 4: Theoretical calculation of the transverse wakefield vs time for the lowest dipole modes of the SLAC structure.

In the neighborhood of 59 ns, where the SLC normally runs, a single frequency with an amplitude $W_\perp$ = 0.13 V/pC/mm/m dominates. This is relatively weak compared to the short-range wakefield which peaks at $W_\perp$ = 5 V/pC/mm/m, and averages $W_\perp$ = 0.9 V/pC/mm/m over a 1 mm (rms) bunch. In addition, non-cylindrically symmetric external loading gives a damping factor w, different in x and y. For our regime $w_y = 0.85$ and $w_x = 0.45$, since the input couplers are oriented horizontally. A 1 mm oscillation extending over 500 m of a bunch with $3.5 \cdot 10^{10}$ particles induces an oscillation with a peak transverse momentum $eV_y = 1/2\ W_y$ (500 mm-m)(5.6 nC) $w_y \cong 155$ keV/c. For a 8 GeV beam this corresponds to an angle of 20 μrad, and for $\beta = 20$ m a peak position offset Δy = 400 μm, in agreement with measurements (Fig. 2).

6 Split-Tune Lattice

In a *simple* FODO lattice, the long-range wakefield produced by coherent betatron oscillations in a leading positron

bunch will *resonantly* drive betatron oscillations in a trailing bunch. Despite their opposite electric charges, both bunches see the same magnetic lattice (offset by one quadrupole), and hence have identical free betatron frequencies. The resonance is easily alleviated, however, by using a less symmetrical 'split-tune' lattice in which 'focusing' and de-focusing' magnets are given different absolute strengths. The betatron phase advance in the x and y planes for a particular charge differ, and are interchanged for the opposite charge.

A phase advance difference $\Delta(\Delta\psi)$ between the two bunches accumulated over some length of the linac will inhibit the growth in the trailing bunch's oscillation amplitude by $\sqrt{2(1-\cos[\Delta(\Delta\psi)]}/|\Delta(\Delta\psi)|$ relative to perfect resonance. Thus $\Delta(\Delta\psi) = 218°$ is required for a factor of 2 reduction, 262° for a factor of 3, and 885° for a factor of 7.8. The corresponding F-D magnet fractional strength difference to produce a unit (small) phase advance split, $1/2\cos[(\Delta\psi + \Delta\psi)_{cell}/4]$ for thin quadrupoles, is typically 0.617%/°/cell (for an average 90°/cell lattice).

A split-tune lattice was implemented in the first half of the SLC linac—more precisely in Sectors 2 through 16, comprising 79 FODO cells. 31 cells (sector 2, 3, and 4) had had nominal 90°/cell phase advance in both planes, and the remaining 48 had had 76°/cell. The new lattice has 31 cells with average $\Delta\psi_x \cong 95°$, and $\Delta\psi_y \cong 91°$, and 48 cells with $\Delta\psi_x \cong 81°$, and $\Delta\psi_y \cong 69°$, all as seen by electrons. Thus the absolute accumulated phase advance difference between electrons and positrons, in both planes, is 680°.

The choice of 'sign' for the split, i.e., the fact that the positron y plane phase advance is the larger, was made on the basis of its implications for intra-bunch (short-range) wakefield effects. An essential component in the control of the latter in the SLC is BNS damping [6], in which a systematic energy variation along the bunch, in conjunction with phase advance chromaticity, inhibits the resonant excitation of oscillations in the tail of the bunch, and partially compensates the short-range wakefield phase shift. Since the vertical jitter sensitivity is the greater, the positron jitter has tended to be worse than the electron, and a reduction in the former leverages a reduction in the latter, the chosen split direction favors positron vertical phase advance chromaticity. The beam envelope (beta-function) is little affected by the asymmetry in 'focusing'.

Figure 1 (c) shows about a factor of 3 less e^+ to e^- coupling. This reduced the rms jitter by about 30% in y from 75% to 50% of σ_y, and 15% in x from 40% to 35% of σ_x. (see Fig. 5).

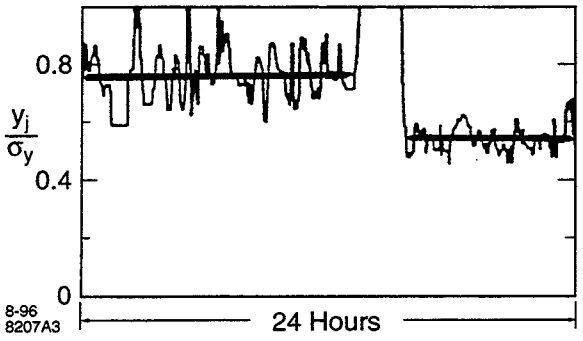

Fig. 5: Jitter reduction after the introduction of the split-tune lattice.

7 Conclusion

The static effect of long-range transverse wakefield kicks from positrons to electrons were measured, but they can be generally tuned out. However a jittery positron beam has caused an even higher electron jitter. The split-tune lattice has helped to reduce that effect below the natural jitter of the electron beam.

References

[1] R. Neal, "The Stanford Two-Mile Accelerator", W.A. Benjamin, Inc., 1968, p. 217.

[2] K.A. Thompson, et al., Part. Accel., 47 (1994) 65.

[3] J.T. Seeman, et al., "The Introduction of Trajectory Oscillations to Reduce Emittance Growth in the SLC Linac", XV Int. Conf. on High Energy Accelerators, Hamburg, July 1992, p. 879.

[4] C. Adolphsen, T. Slaton, "Beam Trajectory Jitter in the SLC Linac", PAC95, Dallas, May 1996, p. 3034.

[5] K. Bane and R. Gluckstern, Part. Accel., 42 (1993) 123.

[6] J.T. Seeman, et al., "Measured Optimum BNS Damping Configuration of theSLC Linac", PAC93, Washington, D.C., 1993, p. 3234.

Higher Order Beam Jitter in the SLC Linac

F.-J. Decker, C.E. Adolphsen, B. Podobedov, P. Raimondi

SLAC*, Stanford CA 94309, USA

Abstract

The pulse-to-pulse behavior of the beams in the SLC linac is dominated by wakefields which can amplify any other sources of jitter. A strong focusing lattice combined with BNS damping controls the amplitude of oscillations which otherwise would grow exponentially. Measurements of oscillation amplitude along the linac show beam motion that is up to six times larger than that expected from injection jitter. A search for possible sources of jitter within the linac uncovered some problems such as structure jitter at 8 to 12 Hz, pump vibrations at 59 Hz and 1 Hz aliasing by the feedback systems. These account for only a small fraction of the observed jitter which is dominantly white noise. No source has yet been fully identified but possible candidates are dark current in the linac structures (not confirmed by experiment) or subtle correlations in injection jitter. An example would be a correlated x-z jitter with no net offset visible on the beam position monitors at injection. Such a correlation would cause jitter growth along the linac as wakefields from the head of the bunch deflect the core and tail of the bunch. Estimates of the magnitude of this effect and some possible sources are discussed in this paper.

1 Introduction

After the sawtooth instability [1] in the damping rings of the Stanford Linear Collider (SLC) was fixed (reduced) by changing the impedance of the vacuum chamber [2], the current in the linac could be raised from about $3 \cdot 10^{10}$ to $3.5 \cdot 10^{10}$ particles per bunch in the 1994/95 run. This resulted in an enormous amount of transverse beam jitter of $\Delta y/\sigma_y$ = 0.6-0.8. Many correction schemes for measuring the beam properties evolved, but some reduction in e^- jitter was achieved by splitting the phase advance to generate a decoherence in the long-range wakefield excitation [3]. The jitter still remained big and besides some distinct frequency lines [4], the jitter is coming from a white noise source which grows by a factor of up to six in the linac [5]. Possible candidates were: (a) dark currents in the structure exciting transverse kicks (this could not be confirmed), and (b) higher order jitter effects. Under this term we understand, that the whole jitter is already fully developed, but hidden at the beginning of the linac. The easiest understanding would be an x-z correlation jitter, where the head and tail distribution cancels the jitter in the beginning but it develops an x jitter down the linac due to the wakefield of the offset head particles. Another type of 'hidden' injection jitter is due to bunch length variations, which would change the linac transport properties. In the sections that follow we discuss those two sources of hidden jitter after reviewing the characteristics of the linac jitter growth.

2 Correlated and Uncorrelated Jitter

By launching a betatron oscillation and looking at the amplitude and phase down the linac, one can measure the effective R_{12}'s and their determinant. Transverse wakefields and BNS-damping change the behavior compared to the model lattice.

Since the jitter could be partly visible and partly hidden, the complex correlation of (x, x') in the beginning with (x, x') at the end could uncover some of that higher order jitter. But there was still the biggest factor uncovered (see Fig. 1).

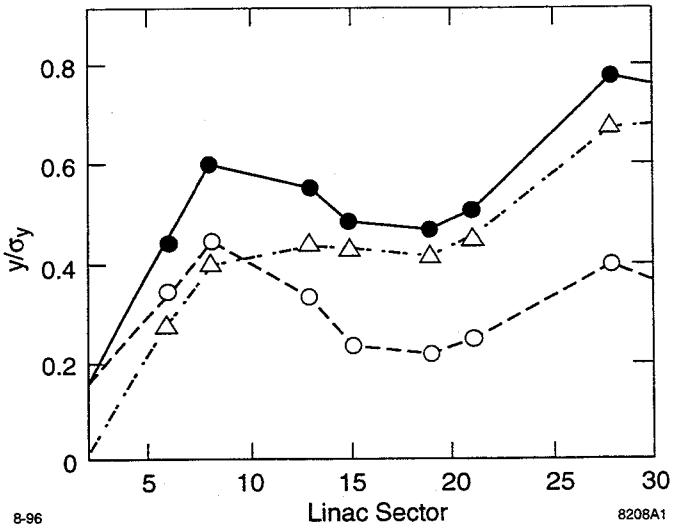

Fig. 1: Measured correlated and uncorrelated jitter development in the linac. While the correlated part (dash) shows the expected jitter profile (up and then down), the uncorrelated part (dash-dotted) grows steadily.

3 Definition and Examples of Higher Order Jitter

Under the definition of higher order jitter we would like to understand any jitter, which is fully present, but hidden at the beginning of a system (e.g. linac) and gets only altered, amplified, or uncovered in that system. No other source in that system (linac) should be counted to "higher order jitter", it is only the hidden, incoming jitter.

An example is a jittery x-z correlation at the beginning of the linac. Compared to the normal transverse jitter, which puts the whole bunch to an offset $\langle \Delta x \rangle \neq 0$, it puts the head and the tail to opposite directions $\Delta x_{head} = -\Delta x_{tail}$ so that $\langle \Delta x \rangle = 0$. The development in the linac is shown in Fig. 2.

* Work supported by DOE, contract DE-AC03-76SF00515.

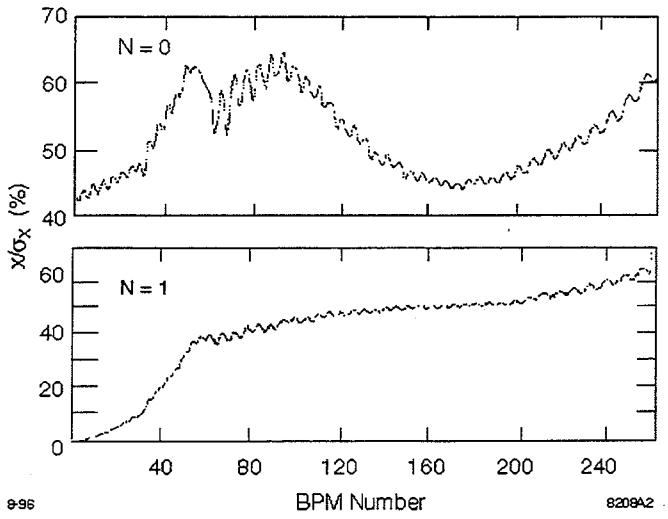

Fig. 2: The normalized jitter in the linac is not constant for high current, but can grow or damp depending on the BNS damping setup. A typical SLC behavior is shown at the top ($N = 0$), while a higher order jitter ($N = 1$, bottom) is invisible with a normal BPM at the beginning, but then grows to the same amplitude.

The jitter amplitudes at the beginning were chosen that there is a 60% jitter ($\Delta y/\sigma_y$) at the end for all cases with a normalized emittance of $3 \cdot 10^{-6}$ m-rad and $3.5 \cdot 10^{10}$ particles per bunch. The necessary initial jitter scales like

$$\sigma_{\Delta x}(z) = 20\ \mu\text{m} \cdot (z/\sigma_z)^N / 2^N.$$

One source of such a jitter is a bunch length change $\Delta\sigma_z$ in the damping ring, which creates an energy spread change $\Delta E/E$ in the bunch length compression systems. If, additionally, η, η' or their higher order terms (T_{i66}, U_{i666}) are not exactly zero, a higher order transverse offset change is introduced. A linac bunch length change is also visible as higher order jitter [6].

4 'Weak' Sawtooth Instability

Since the 1993 vacuum chamber upgrade of the damping rings, the turbulent microwave instability (called sawtooth instability in the SLC [1]) has changed its character from strong (r and φ-modes couple) to weak (only radial modes couple) [7]. The sawtooth amplitude was reduced and the diagnostic signals went down below the detectable level. Therefore it took about one year till a small correlation of the linac jitter with some sawtooth signal could be found [9]. Since then major work and considerable progress had been made on the signal processing, so that the 180 kHz signal of one bunch can be studied in amplitude and phase (Fig. 3).

Measuring the signal with a gated ADC over a short gate (ns) it is possible to correlate it with BPMs or other devices in the linac. There are two effects which reduce the correlation:
1. The timing must be right; a big correlation at one time setting of the gated ADC gives a negative correlation 2.75 μs later, and none at 1.375 μs.
2. Even the biggest correlation is suppressed due to the bursts; a medium gated ADC value can come from the crest of the 180 kHz signal of the rising or falling part of the burst, or it comes off-crest (+ or –) from the center part of the burst. Signal Splitting and two ADC at 0 and 1.375 μs would give the whole information.

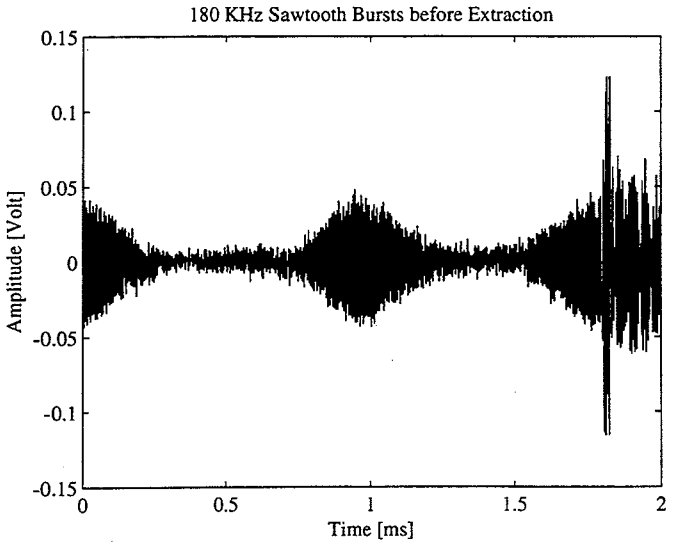

Fig. 3 Eight "sawtooth" bursts happen in about 8 ms. Here three are visible just before extraction (spike). The burst can or cannot happen at extraction time.

5 Measurements

An ensemble of 512 beam pulses at 120 BPMs (about 1/2 of the linac), the bunch length, the sawtooth signal and some other parameters was studied. The correlation factor (mean subtracted)

$$r = \frac{< xy >}{\sqrt{< x^2 >}\sqrt{< y^2 >}}$$

between the sawtooth ADC signal and y-data from a BPM at the end of the linac was measured to be $r = 0.64$, which means that at least $r^2 = 0.41$ of the whole jitter power is coming from the sawtooth. This is a much bigger single source than 30 water pumps generating 59 Hz (0.1 of power) and 8-10 Hz due to water turbulence and quad support (0.2 of power).

The correlation development down the linac is shown is Fig. 4. The x component shows a behavior of a higher order jitter, while the y is slowly decreasing. The last point with less jitter is after the collimators.

There was also a correlation of the sawtooth signal with the bunch length which jittered by 10% ($\Delta\sigma_z/\sigma_z$) with $r = 0.62$ (39% of power spectrum), see Fig. 5, and only a small correlation with the current jitter $r = 0.31$ (10% of power).

By exciting a bunch length oscillation about 1 ms before extraction, the sawtooth amplitude at extraction was much reduced and less frequent. This resulted in a reduction in linac jitter of 30%, which is somewhat more than expected if all the correlation could be reduced:

$$j_{new}/j_o = \sqrt{1-r^2}\,.$$

This suggests that some of the correlation was reduced, which could be the mentioned amplitude/phase ambiguity of the sawtooth signal or a not perfect timing setup of the gate.

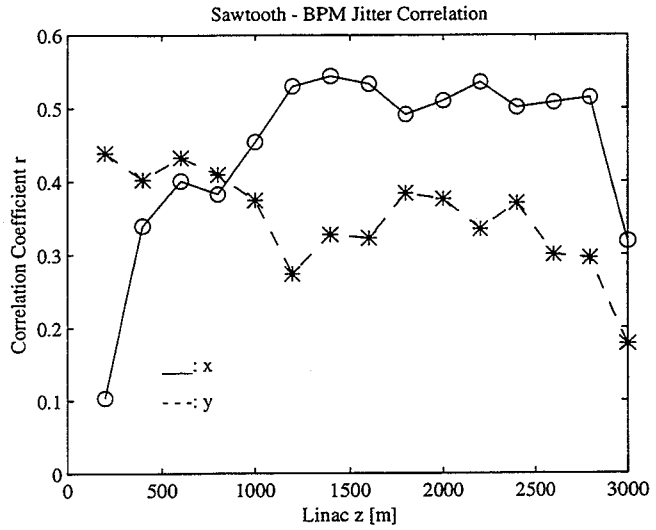

Fig. 4: Sawtooth to jitter correlation versus z in the linac (x: solid, y: dashed).

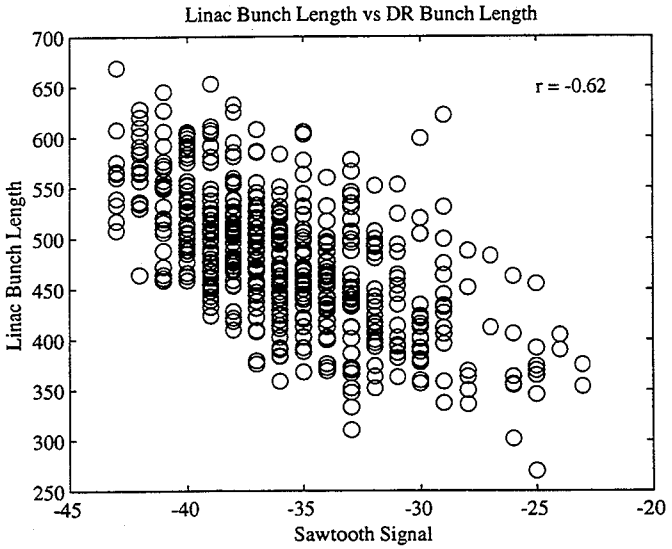

Fig. 5: Linac bunch length jitter versus sawtooth signal.

5 Summary

Hidden, incoming jitter or "higher order jitter" can have big effects in the linac due to the high currents and wakefields. A source from the damping ring (sawtooth) has been identified to be a good example of such a hidden jitter. It could be substantially reduced.

Acknowledgment

We would like to thank R. Siemann for his discussion and his instrumental and persistent support, and special thank go to M. Minty, who pointed out the usefulness of the pre-extraction bunch length excitation.

References

[1] P. Krejcik et al., "High Intensity Bunch Length Instabilities in the SLC damping Rings", PAC93, Washington, May 1993, p. 3240.

[2] K. Bane et al., "High-Intensity Single bunch Instability Behavior in the New SLC Damping Ring Vacuum Chamber", PAC95, Dallas, May 1995, p. 3109.

[3] F.-J. Decker et al., " Long-Range Wakefields and Split-Tune Lattice at the SLC", LINAC96, Geneva, Aug. 1996.

[4] J. Turner et al., "Vibration Studies of the Stanford Linear Accelerator", PAC95, Dallas, May 1996, p. 665.

[5] C. Adolphsen, T. Slaton, "Beam Trajectory Jitter in the SLC Linac", PAC95, Dallas, May 1996, p. 3034.

[6] R. Assmann and F. Zimmermann, "Possible Sources of Pulse-to-Pulse Orbit Variation in the SLAC Linac", LINAC96, Geneva, Aug. 1996.

[7] K.L.F. Bane and K. Oide, "Simulations of the longitudinal Instability in the New SLC Damping Rings", PAC95, Dallas, May 1995, p. 3105.

[8] R. Siemann, B. Podobedov, private communication.

THE BROWN-SERVRANCKX MATCHING TRANSFORMER FOR SIMULTANEOUS RFQ TO DTL H^+ AND H^- MATCHING

E. A. Wadlinger and R. W. Garnett
Accelerator Operations and Technology Division
Los Alamos National Laboratory,
Los Alamos, New Mexico, 87545, USA*

Abstract

The issue involved in the simultaneous matching of H^+ and H^- beams between an RFQ and DTL lies in the fact that both beams experience the same electric-field forces at a given position in the RFQ. Hence, the two beams are focused to the same correlation. However, matching to a DTL requires correlation of the opposite sign. The Brown-Servranckx [1] quarter-wave ($\lambda/4$) matching transformer system, which requires four quadrupoles, provides a method to simultaneously match H^+ and H^- beams between an RFQ and a DTL. The method requires the use of a special RFQ section to obtain the Twiss parameter conditions $\beta_x = \beta_y$ and $\alpha_x = \alpha_y = 0$ at the exit of the RFQ [2]. This matching between the RFQ and DTL is described below.

$\lambda/4$ Matching Transformer

Figure 1 shows the two-quadrupole-$\lambda/4$ matching transformer with an additional quadrupole placed at each end to produce the appropriate Twiss parameters to match to the FODO lattice of the downstream DTL. This 4-quadrupole transport section will transform a beam with Twiss parameters $\beta_{x1} = \beta_{y1}$ and $\alpha_{x1} = -\alpha_{y1}$ to a beam having Twiss parameters $\beta_{x2} = \beta_{y2}$ and $\alpha_{x2} = -\alpha_{y2}$. The middle two focusing elements plus the three drift lengths comprise the $\lambda/4$ - (quarter wave) transport. Quadrupole Q_1, placed where $\beta_x = \beta_y$ and $\alpha_x = -\alpha_y$, adjusts α while preserving the condition $\alpha_x = -\alpha_y$ and is used to adjust the beam size at Q_2 while the quarter wave transformer preserves the condition $\beta_x = \beta_y$ and $\alpha_x = -\alpha_y$. Quadrupole Q_2 is used to obtain the final desired α while again preserving the condition $\alpha_x = -\alpha_y$.

Because of the time varying nature of the RFQ, the H^+ and H^- beams have the relationship $\alpha_x(H^+) = \alpha_x(H^-)$, and $\alpha_y(H^+) = \alpha_y(H^-)$ at the exit of the RFQ; but, in a dc quadrupole channel, the matched beam satisfies $\alpha_x(H^+) = \alpha_y(H^-)$ and $\alpha_y(H^+) = \alpha_x(H^-)$. By setting $\alpha_x = \alpha_y = 0$, for both H^+ and H^- at the end of the RFQ, the Brown-Servranckx [1] matching transformer can be used for matching.

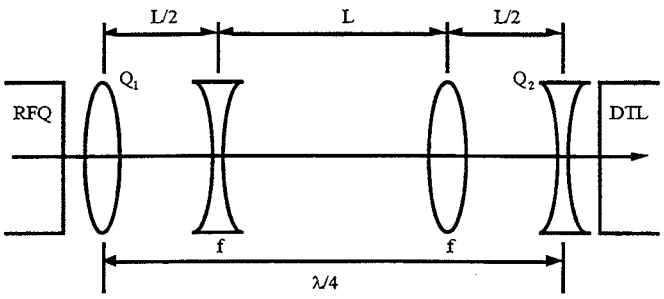

Fig. 1. The Brown-Servranckx matching transformer used to match a beam from an RFQ to a DTL.

The quarter-wave transport matrix, $R_{\lambda/4}$, is (the sign of the focal length depends on the charge of the hydrogen ion)

$$R_{\lambda/4} = \begin{bmatrix} 1 & \frac{L}{2} \\ 0 & 1 \end{bmatrix} \begin{bmatrix} 1 & 0 \\ \pm\frac{1}{f} & 1 \end{bmatrix} \begin{bmatrix} 1 & L \\ 0 & 1 \end{bmatrix} \begin{bmatrix} 1 & 0 \\ \mp\frac{1}{f} & 1 \end{bmatrix} \begin{bmatrix} 1 & \frac{L}{2} \\ 0 & 1 \end{bmatrix}$$

$$= \begin{bmatrix} \left(1 - \frac{L^2}{2f^2}\right) \mp \frac{L}{f} & 2L - \frac{L^3}{4f^2} \\ -\frac{L}{f^2} & \left(1 - \frac{L^2}{2f^2}\right) \pm \frac{L}{f} \end{bmatrix} \qquad (1)$$

which, in terms of the phase advance per period, μ, and the Twiss parameters, is

$$R_{\lambda/4} = \begin{bmatrix} \cos\mu + \alpha\sin\mu & \beta\sin\mu \\ -\gamma\sin\mu & \cos\mu - \alpha\sin\mu \end{bmatrix}. \qquad (2)$$

Equation (2) for the quarter wave transport system is

$$R_{\lambda/4} = \begin{bmatrix} \alpha & \beta \\ -\gamma & \alpha \end{bmatrix} \qquad (2a)$$

where $\mu = 90^o$. This condition is achieved in Eq. (1) when

*Work supported by the U.S. Department of Energy

$$\left(1-\frac{L^2}{2f^2}\right)=0 \qquad (3)$$

which determines the focal length, f, of the inner two quadrupole lenses given the lens separation, L.

We require a transport matrix that preserves the condition $\alpha_x=-\alpha_y$. The Twiss parameter map for any matrix R is

$$\begin{pmatrix}\beta_2\\ \alpha_2\\ \gamma_2\end{pmatrix}=\begin{bmatrix} R_{11}^2 & (-2R_{11}R_{12}) & R_{12}^2 \\ (-R_{11}R_{21}) & R_{11}R_{22}+R_{12}R_{21} & (-R_{12}R_{22}) \\ R_{21}^2 & (-2R_{21}R_{22}) & R_{22}^2 \end{bmatrix}\begin{pmatrix}\beta_1\\ \alpha_1\\ \gamma_1\end{pmatrix}. \qquad (4)$$

The matrix elements in parenthesis change sign in going from the x-plane to the y-plane. The other elements do not change sign. For $\beta_{x1}=\beta_{y1}$ and $\alpha_{x1}=-\alpha_{y1}$, then $\beta_{x2}=\beta_{y2}$ and $\alpha_{x2}=-\alpha_{y2}$. This is achievable with the quarter-wave transport system because the diagonal matrix elements R_{11} and R_{22} change signs between the x- and y-planes while the off-diagonal matrix elements R_{12} and R_{21} do not change.

The quadrupole lenses placed at the beginning and end of the quarter-wave transport preserve the condition $\alpha_x=-\alpha_y$. The transport matrix elements for a single lens,

$$R=\begin{bmatrix} 1 & 0 \\ \pm 1/f & 1 \end{bmatrix}, \qquad (5)$$

when substituted in Eq. (4), gives

$$\begin{pmatrix}\beta_2\\ \alpha_2\\ \gamma_2\end{pmatrix}=\begin{bmatrix} 1 & 0 & 0 \\ \mp 1/f & 1 & 0 \\ 1/f^2 & \mp 2/f & 1 \end{bmatrix}\begin{pmatrix}\beta_1\\ \alpha_1\\ \gamma_1\end{pmatrix}. \qquad (6)$$

When $\beta_{x1}=\beta_{y1}$ and $\alpha_{x1}=-\alpha_{y1}$, then $\beta_{x2}=\beta_{y2}$ and $\alpha_{x2}=-\alpha_{y2}$.

Discussion

The Brown-Servranckx transport system is straight forward to tune. Given a circular beam at the location of quadrupole Q_1 in Fig. 1, the focal length of the middle two quadruples is adjusted to produce a circular beam at the location of quadruple Q_2 giving a quarter wave transport between Q_1 and Q_2. Quadrupole Q_1 is then adjusted to give the proper beam size at the location of Q_2 (giving β_2). Finally, quadrupole Q_2 is adjusted so that the beam size is a constant after each FODO cell of the DTL (giving the correct α_2).

There are limitations to the degree of magnification that can be achieved by this transformer. The Twiss parameter β_2 has a minimum value equal to R_{12}^2/β_1. For details of this and other useful insights to beam transport, see Ref. 1.

If the transverse focusing per unit length is identical at the output of the RFQ and the input of the DTL, the quarter-wave transport can be eliminated. Also, if in addition to the above condition, $\alpha_x=\alpha_y=0$ at the RFQ output, a single magnetic quadrupole can be used to obtain the appropriate matching ($\alpha_x=-\alpha_y$) of both H^+ and H^- beams into the DTL.

References

[1] K. L. Brown and R. V. Servranckx, "First- and Second-Order Charged Particle Optics," SLAC-PUB-3381, July 1984.

[2] K. Crandall, "Ending the RFQ Vane Tips with Quadrupole Symmetry," 1994 Linac Conference, Tsukuba, Japan.

BEAM SELF-EXCITED RF CAVITY DRIVER FOR A DEFLECTOR OR FOCUSING SYSTEM

E. A. Wadlinger
Accelerator Operations and Technology Division
Los Alamos National Laboratory,
Los Alamos, New Mexico, 87545, USA*

Abstract

A bunched beam from an accelerator can excite and power an rf cavity which then drives either a deflecting or focusing (including nonlinear focusing) rf cavity with an amplitude related to beam current. Rf power, generated when a bunched beam loses energy to an rf field when traversing an electric field that opposes the particle's motion, is used to drive a separate (or the same) cavity to either focus or deflect the beam. The deflected beam can be stopped by an aperture or directed to a different area of a target depending on beam current. The beam-generated rf power can drive a radio-frequency quadrupole that can change the focusing properties of a beam channel as a function of beam current (space-charge-force compensation or modifying the beam distribution on a target). An rf deflector can offset a beam to a downstream sextupole, effectively producing a position-dependent quadrupole field. The combination of rf deflector plus sextupole will produce a beam current dependent quadrupole-focusing force. A static quadrupole magnet plus another rf deflector can place the beam back on the optic axis. This paper describes the concept, derives the appropriate equations for system analysis, and gives examples. A variation on this theme is to use the wake field generated in an rf cavity to cause growth in the beam emittance. The beam current would then be apertured by emittance defining slits.

Deflector System

Figure 1 shows the concept in a system designed to aperture a high current beam. The RF generator and deflector are conceptually shown as two units. The beam deflection angle is proportional to the beam current. This deflection becomes a displacement at the beam collimator. Permanent magnet non-linear focusing magnets can enhance the operation of the RF deflector.

Beam Interaction with an Rf Field

In this section, a differential equation describing the rf field generated in a cavity excited by a bunched beam is derived and solved. This differential equation depends on the energy deposited in the cavity by the beam and the energy lost in the cavity due to resistive wall losses. We consider a TM_{010} mode single-cell cavity (DTL type) where the electric field is along the beam direction and is concentrated on the axis of the cavity between the drift tube noses.

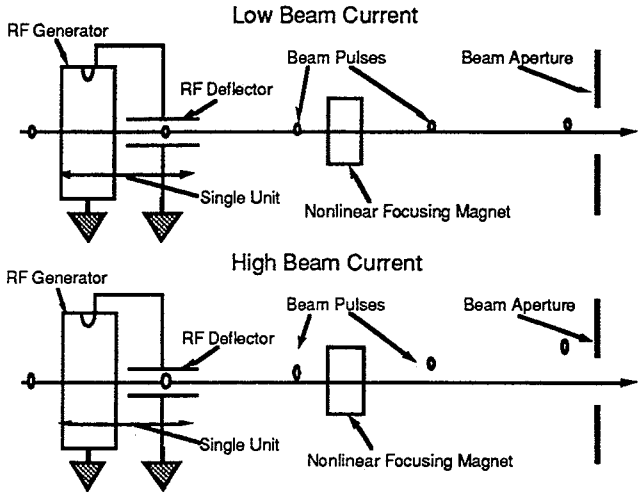

Fig. 1. RF Deflector Concept.

The bunched beam from the accelerator drives a cavity that produces rf power which then drives a beam deflecting cavity. The deflecting cavity could be followed by nonlinear magnets and then phase-space defining apertures to remove the deflected beam.

Work done against the rf electric field by particles traversing the gap adds energy to the rf field. This gain in the field energy, ΔU_P, due to one particle is

$$\Delta U_P = \int_{-Z_g/2}^{Z_g/2} eE_g \cos(\omega t + \varphi) dz \qquad (1)$$

where

$$z = vt, \quad \frac{\omega}{v} = \frac{2\pi}{\beta\lambda}, \qquad (2)$$

e is the charge on an electron, Z_g is the gap length, E_g is the gap voltage, ω is 2π times the rf frequency, β is the velocity of the particle with respect to the velocity of light, λ is the free space rf wavelength, v is the particle's velocity, t is time, and φ is the rf phase when a particle enters the gap.

Assuming that the change in particle energy in crossing the gap is small compared to the particle's kinetic energy and treating v as a constant, Eq. (1) is integrated to obtain

$$\Delta U_P = eE_0 T\beta\lambda \cos\varphi \qquad (3)$$

where, E_O is an average field strength defined by

$$E_g Z_g = E_0 \beta\lambda \ , \qquad (4)$$

and T is a transit time factor. The transit time factor is defined as

*Work supported by the U.S. Department of Energy

$$T = \sin\left(\frac{\pi Z_g}{\beta\lambda}\right)\Big/\left(\frac{\pi Z_g}{\beta\lambda}\right) . \quad (5)$$

Equation (3) gives the energy gain in the rf electric field due to one particle crossing the rf-gap.

Beam Bunch Rf Energy Gain

The individual charges in a beam bunch enter the rf-cavity at different phases φ. The phase distribution of the particles is described by the function $\rho(\varphi)$. The total charge per beam bunch is

$$q = \int_{-\pi}^{\pi} \rho(\varphi) d\varphi . \quad (6)$$

Let,

$$\Delta U_B = \frac{\text{average rf field power gain}}{\text{beam bunch}}$$

be the energy deposited in the cavity by a complete beam bunch, and use Eq. (3) to obtain

$$\Delta U_B = E_0 T\beta\lambda \int_{-\pi}^{\pi} \rho(\varphi)\cos(\varphi) d\varphi . \quad (7)$$

The integral in Eq. (7) can be defined in terms of a dimensionless charge-distribution form factor as

$$F = \frac{1}{q}\int_{-\pi}^{\pi} \rho(\varphi)\cos(\varphi) d\varphi . \quad (8)$$

The value of F is less than 1 (it is equal to 1 for a δ function distribution). This form factor is rather insensitive to beam bunch length. For example, assume that $\rho(\varphi)$ is described by the rectangular distribution

$$\rho(\varphi) = \begin{cases} q/2\varphi_0 & -\varphi_0 < \varphi < \varphi_0 \\ 0 & \text{otherwise} \end{cases} , \quad (9)$$

where φ_O is the phase extent of the distribution. Then,

$$F = \sin(\varphi_0)/\varphi_0 . \quad (10)$$

When $\varphi_O = 0$, $F = 1$, and when $\varphi_O = \pi/2$ (severe debunching), $F = 0.64$. Equations (24) and (25) (derived below) show that the maximum-generated electric field scales as F. We see that the rf-electric field is somewhat insensitive to significant beam debunching.

Let U_T equal the total rf field energy in the cavity. The rf electric field will scale as the square root of U_T. Combining Eqs. (7) and (8) and defining the constant k_1 as

$$k_1 = E_0/U_T^{1/2} \quad (11)$$

gives

$$\Delta U_B = qk_1 T\beta\lambda F U_T^{1/2} . \quad (12)$$

The constant k_1 depends on the electric field distribution in the cavity and is a function of the cavity geometry. We will later assume a model for the electric field distribution that will permit a rough calculation of k_1.

Resistive Wall Losses and Q

Equation (12) gives the rf field energy gain due to one beam bunch crossing the rf-cavity gap against the rf electric field. There are power losses in the cavity due to the finite resistance of the cavity walls. This power loss can be determined from the Q of the cavity defined as

$$Q = \omega U_T / W_L \quad (13)$$

where W_L is the average rf power loss per unit time. The rf energy loss in one rf cycle (time $\tau = 2\pi/\omega$) is then

$$W_L \frac{2\pi}{\omega} = \frac{\omega U_T}{Q}\frac{2\pi}{\omega} . \quad (14)$$

RF Time Dependent Field Equation

The change in total rf power per time is

$$\frac{\Delta U_T}{\Delta t} = \frac{\Delta U_T}{2\pi/\omega} = \frac{\Delta U_B}{2\pi/\omega} - \frac{W_L 2\pi/\omega}{2\pi/\omega} .$$

Using Eqs. (12), and (13) gives

$$\frac{dU_T}{dt} \approx \frac{\omega q k_1 T\beta\lambda F}{2\pi} U_T^{1/2} - \frac{\omega}{Q} U_T . \quad (15)$$

Equation (15) is easier to solve if E_o [from Eq. (11)] is substituted for U_T. Equation (15) becomes

$$2\frac{dE_0}{dt} = \frac{\omega q k_1^2 T\beta\lambda F}{2\pi} - \frac{\omega}{Q} E_0 . \quad (16)$$

Assuming that the rf power is zero when $t = 0$, Eq. (16) can be integrated to give

$$E_0 = \frac{Q q k_1^2 T\beta\lambda F}{2\pi}\left(1 - e^{-\omega t/2Q}\right) . \quad (17)$$

The charge per beam bunch, q, can be calculated from the instantaneous average beam current, I, and is

$$q = 2\pi I/\omega . \quad (18)$$

Substituting Eq. (18) into (17) gives

$$E_0 = E_{0_{max}}\left(1 - e^{-\omega t/2Q}\right) . \quad (19)$$

where

$$E_{0_{max}} = \frac{Q I k_1^2 T\beta\lambda F}{\omega} . \quad (20)$$

Relationship Between RF Electric Field and RF Power

A crude estimate of k_1 can be obtained by assuming that most of the rf electric field is concentrated between the drift-tube noses and is a constant. The maximum stored energy in the electric field can be calculated and related to U_T to give k_1. The value of U_T calculated from the electric field is

$$U_T = \frac{\varepsilon_0}{2}\int E^2 dV \approx \frac{\varepsilon_0}{2} E_g^2 \pi R_g^2 Z_g \,. \tag{21}$$

Solving this equation for E_g and using Eq. (4) gives

$$E_0 = \left(\frac{2Z_g}{\varepsilon_0 \pi R_g^2 \beta^2 \lambda^2}\right)^{1/2} U_T^{1/2} \,. \tag{22}$$

Comparing Eqs. (11) and (22) gives

$$k_1 = \left(\frac{2Z_g}{\varepsilon_0 \pi R_g^2 \beta^2 \lambda^2}\right)^{1/2} . \tag{23}$$

Equation Summary

Combining Eqs. (4), (11), (13), (20) and (23) give

$$E_{0_{\max}} = \frac{2QITFZ_g}{\omega \varepsilon_0 \pi R_g^2 \beta \lambda} = \text{max. average electric field,} \tag{24}$$

$$E_{g_{\max}} = \frac{2QITF}{\omega \varepsilon_0 \pi R_g^2} = \text{max. gap electric field,} \tag{25}$$

$$U_{T_{\max}} = \frac{2Q^2 I^2 T^2 F^2 Z_g}{\omega^2 \varepsilon_0 \pi R_g^2} = \text{max. total rf energy,} \tag{26}$$

and

$$W_{L_{\max}} = \frac{2QI^2 T^2 F^2 Z_g}{\omega \varepsilon_0 \pi R_g^2} = \text{max. rf power loss / time.} \tag{27}$$

Examples

We calculate $E_{g_{\max}}$ and $W_{L_{\max}}$ using Eqs. (25) and (27) for a 100 μA beam at 800 MeV. Assume a 10% beam duty factor, then I = 1.0 mA. We let $\omega/2\pi$ = 200 MHz, Q=1000, φ = 1 deg, Z_g = 1.0 cm, and R_g = 1.0 cm ($\varepsilon_0 = 10^{-9}/36\pi$). Equations (25) and (27) give $E_{g_{\max}}$ = 5.7x10^5 V/m (rf-gap voltage) and $W_{L_{\max}}$ = 5.7 watts (maximum power extracted from the beam).

We calculate the beam deflection due to a transverse rf-electric field. From,

$$\frac{dP}{dt} = eE\cos(\omega t), \tag{28}$$

we obtain

$$\Delta P_\perp = \int_{-\varphi_0}^{\varphi_0} eE\cos(\omega t)dt = \frac{2eE\sin\varphi_0}{\omega}. \tag{29}$$

The deflection angle

$$X' = \Delta P_\perp / P_{//} . \tag{30}$$

For E = 0.57 MV/m, $\phi_0 = \pi/2$ (complete rf half cycle), 5 rf deflection cavities (each of length $\beta\lambda/2$ = 0.68 m), and an 800 MeV beam, we find that X' = 10^{-3} radians. This will produce a deflection of 1 cm in 10 meters. Given this same geometry, a 10 mA beam will have a deflection angle of 10^{-2} radians and will be deflected 10 cm.

There are issues to be addressed if this system is to be used for limiting beam current for personnel safety. These include: sensitivity of the rf cavities to detuning, possible long term degradation in cavity Q due to oxidation of cavity surfaces, determining the envelope of off-nominal linac operational parameters that will cause the beam to sufficiently debunch so that the rf deflection system will no longer work, and rf cavity conditioning.

Acknowledgments

I would like to thank Paul Tallerico for several useful and interesting discussions.

BEAM-BUNCHING WITH A LINEAR-RAMP INCLUDING SPACE-CHARGE FORCE EFFECTS CYLINDER MODEL

E. A. Wadlinger
Accelerator Operations and Technology Division
Los Alamos National Laboratory,
Los Alamos, New Mexico, 87545, USA*

Abstract

The voltage-amplitude requirement of a saw-tooth waveform buncher is calculated to give a desired degree of bunching for a given beam current and particle species. This calculation includes the effect of space-charge forces with and without adjacent beam buckets. The results are compared to TRACE-3D calculations which do not include the space-charge effects of adjacent bunches. It appears that TRACE-3D calculations underestimate the bunching voltage required. The methodology and a listing of the spread sheet that performs the analytical bunching calculation are included.

Models

The beam consists of a series of uniform-density charge cylinders, see Fig. 1, that are spaced $D=\beta\lambda$ apart, with length $L=D\varphi/180$ where φ is half the total bunched-beam phase spread, β is the average beam velocity divided by the velocity of light (c), and λ is the fundamental-frequency-rf free-space wave length.

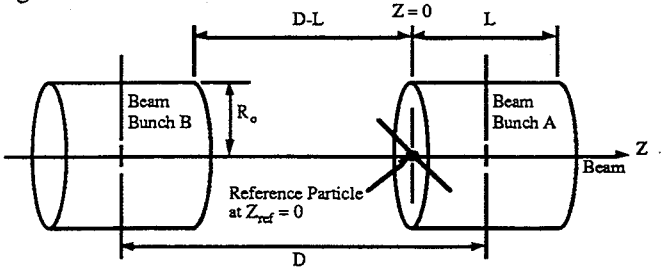

Fig. 1. Geometry for the beam bunching calculation. The motion of a reference particle at the edge of beam bunch A is determined. Two different equations of motion which include effects of space-charge forces from beam bunch A but with and without space-charge forces from beam bunch B are compared.

Space-charge forces, due to beam buckets adjacent to the reference particle, are calculated for a reference particle that is on the beam axis at a cylinder edge. The motion of this reference particle models the bunching of the entire distribution. The electrostatic potential for the reference particle is calculated from which the axial electric field seen by this particle is determined. The equation of motion for the axial motion of the reference particle is solved (the on axis reference particle experiences no transverse forces) which gives the required bunching voltage in the beam center-of-mass frame of reference. Velocities are added nonrelativistically to give the buncher voltage in the laboratory reference frame.

TRACE-3D uses a uniformly filled ellipsoidal model to estimate the space-charge forces. The equation of motion for an on-axis reference particle, using the ellipsoidal model, is integrated and the resulting bunching voltage is compared to TRACE and the cylinder model.

Derivation - Cylinder Model

Given that I is the beam current and f is the bunch frequency, the charge density of the beam in the cylinder is

$$\rho = I/\left(\pi R_0^2 L f\right) \tag{1}$$

where R_o is the beam radius (R_o is assumed to remain constant during the bunching process).

We consider only electrostatic forces in the Lorentz force equation for the time evolution of the reference particle, ignore all image-charge forces that could exist due to a beam pipe, and consider only axial motion. Therefore,

$$m\frac{dv}{dt} = eE_z\ . \tag{2}$$

where m is the particle mass, e is the electron charge, E_z is the axial electric field due to space charge, t is time, and v is the velocity of the reference particle in the beam bunch rest frame.

The on-axis axial electric field due to the two bunches can be obtained from the potential function

$$\Phi = \frac{1}{4\pi\varepsilon_o}\left(\begin{array}{l}\displaystyle\int_D^{-D+L} dZ \int_0^{R_0} \frac{\rho}{\sqrt{\left(Z-Z_{ref}\right)^2+R^2}} R\,dR \int_0^{2\pi} d\theta + \\ \displaystyle +\int_D^{L} dZ \int_0^{R_0} \frac{\rho}{\sqrt{\left(Z-Z_{ref}\right)^2+R^2}} R\,dR \int_0^{2\pi} d\theta\end{array}\right) \tag{3}$$

where ε_o is the free space permitivity. The first set of integrals is for bunch B, and the second set for bunch A. Integrating Eq. (3) for Φ, taking the derivative with respect to Z_{ref} (Z_{ref} is the Z coordinate of the reference particle), and setting Z_{ref} equal to zero to obtain E_z gives

$$E_z(\text{bunch A}) = \frac{\rho}{2\varepsilon_0}\left(\sqrt{L^2+R_0^2} - R_0 - L\right) \tag{4}$$

for the electric field seen by the reference particle due to bunch A, and

$$E_z(\text{bunch B}) = \frac{\rho}{2\varepsilon_0}\left[\sqrt{(D-L)^2+R_0^2} - \sqrt{D^2+R_0^2} + L\right] \tag{5}$$

for the electric field due to bunch B. Adding Eqs. (4) and (5) gives the total electric field seen by the reference particle

$$E_{zT} = \frac{\rho}{2\varepsilon_0}\left[\sqrt{L^2+R_0^2} - R_0 - \sqrt{D^2+R_0^2} + \sqrt{(D-L)^2+R_0^2}\right].$$

Because the electric field does not depend on velocity, Eq. (2) can be integrated to give the required reference-particle energy gain, δW_{cm}, due to bunching in the beam rest frame,

*Work supported by the U.S. Department of Energy

$$\frac{\delta W_{cm}}{e} = \frac{m}{2e}\int_{v_0}^{0} dv^2 = \frac{1}{2}\left(\frac{mc^2}{e}\right)\beta^2 = \int_{L=D}^{L_{min}} E_{zT}\, dL\,. \qquad (7)$$

The initial velocity v_O for an unbunched beam ($L = D$) gives a final bunch length L_{min} when $v = 0$. The bunch length, L, and the beam radius, R_O, are normalized to the bunch center separation distance, D, by defining $r = R_O/D$ and $s = L/D$. Using Eqs. (1), (4), (5), and (6) in Eq. (7) and integrating gives

$$\delta W_{cm} = \frac{eI}{2\pi r^2 f \varepsilon_o D}(J_A + J_B) \qquad (8)$$

where

$$J_A = \sqrt{s^2+r^2} - \sqrt{1+r^2} + r\ln\left(\frac{r+\sqrt{1+r^2}}{r+\sqrt{s^2+r^2}}\right) + 1 - s \qquad (9)$$

and

$$J_B = \begin{bmatrix} s+\sqrt{(1-s)^2+r^2} \\ -\sqrt{1+r^2}\,\ln\left(\dfrac{\sqrt{1+r^2}\sqrt{(1-s)^2+r^2}+1+r^2-s}{r\left(r+\sqrt{1+r^2}\right)}\right) \\ -\ln\left(\dfrac{\sqrt{(1-s)^2+r^2}+s-1}{r}\right) - r - 1 \end{bmatrix} \cdot \qquad (10)$$

Velocities, corresponding to the center-of-mass bunching energy-spread and the average beam velocity, are added to give the buncher voltage required in the laboratory reference-frame. The nominal beam-velocity in the laboratory reference frame is $v_0 = \sqrt{2W_0/m}$ where W_O is the nominal beam energy. The velocity of the reference particle in the beam center-of-mass reference frame is $\delta v = \sqrt{2\,\delta W_{cm}/m}$. Calculating the reference particle's energy in the laboratory reference frame and subtracting the average beam energy gives the energy gain that the buncher must supply to the reference particle which is

$$\delta W_{lab} = \delta W_{cm} + \sqrt{4 W_0\, \delta W_{cm}}\,. \qquad (11)$$

Derivation - Ellipsoidal Model

The electric field due to a uniform-charge-density-ellipsoid beam-bunch seen on axis by a reference particle at the edge of a single bunch is [1], [2], [3]

$$E_z = \frac{3IZ_{ref}}{4\pi\varepsilon_o f R_0^2 (L/2)} g(p)\,,\quad p = \frac{(L/2)}{R_0}\,, \qquad (12)$$

and g is a "form factor" which can be approximated by [1]

$$g(p) = 1/(3p). \qquad (13)$$

Substituting Eq. (13) into Eq. (12) and picking the reference particle coordinates to be on axis at the beam edge (R=0, Z_{ref}=L/2) gives for the electric field

$$E_z = \frac{I}{4\pi\varepsilon_o f R_0 Z_{ref}}. \qquad (14)$$

Carrying through the same procedure as for the cylinder model gives

$$\delta W_{cm} = \frac{eI}{4\pi\varepsilon_o r f D}\ln\left(\frac{1}{s}\right). \qquad (15)$$

Combining Eqs. (11) and (15) gives the buncher voltage required in the Lab system.

Examples and Conclusion

Figure 2 show the spread sheet used to calculate the buncher voltage. The parameters are meant to be self explanatory. Figure 3 shows a comparison of this model calculation to results obtained from TRACE-3D, which uses an ellipsoidal beam bunch model. The TRACE transport channel, used for the comparisons, consisted of a periodic series of solenoid magnets with the beam channel focusing strength set to minimize the space-charge tune depression even in the maximum bunching case. For the maximum bunching case, the initial beam size was increased 3% to keep the beam nearly matched (the solenoid magnetic field strength was not varied).

The discrepancy between the TRACE calculation and the spread sheet calculation for the ellipsoidal distribution is due to the approximation used for the form factor in Eq. (13) where this approximation overestimates the space-charge force by as much as 10%. The difference between the cylindrical model and the ellipsoidal model can be understood by comparing the ratio of the electric field calculated in Eqs. (4) and (14). Taking the ratio of these two equations and using Eq. (1) gives

$$\frac{\text{Eq. (4)}}{\text{Eq. (14)}} = 2\left(1 - \frac{R_o}{2L}\right) \qquad (16)$$

Equation (16) gives a value of close to 2 for the ratio corresponding to our examples. This ratio is also the ratio of the center-of-mass energy spread required for bunching. Using Eq. (11) to transform to the Lab frame shows that the buncher voltage required for the cylinder model should be 40% ($\sqrt{2}$) higher than the ellipsoidal model and is consistent with the result shown in Fig. (3). Also, the TRACE beam distribution for $\varphi = 180^o$ is already bunched with a pseudo-gaussian shape which causes a further underestimate of the buncher voltage required to obtain the final degree of bunching. Figure 3 shows that including adjacent bunches for calculating longitudinal space-charge effects is important only for minimal bunching ($\varphi \geq 150^o$).

BUNCHING DESIGN SPREAD SHEET 8/24/95 9:52

E. A. Wadlinger

ACHRONYM	PARAMETER	UNITS	EQUATION	VALUES
	CONSTANT PARAMTERS			
ε	Permittivity of free space	F/m	fixed constant	8.8540E-12
π	Pi	none	fixed constant	3.1416E+00
c	Velocity of light	m/s	fixed constant	2.9979E+08
	INPUT PARAMTERS			
M	Particle rest-mass energy	MeV	input	9.3800E+02
Q	Particle charge number	none	input	1.0000E+00
W	Beam energy	MeV	input	7.5000E-01
f	Fundamental bunching frequency	Hz	input	2.0125E+08
I	Beam current	A	input	2.0000E-02
R	Beam radius	m	input	3.3000E-03
φ	(+/-) final desired bunching phase spread	deg	input	4.6000E+01
	KINEMATIC PARAMETERS ETC.			
γ	Relativistic gamma	none	(M+W)/M	1.0008E+00
β	Relativistic beta	none	SQRT((γ^2-1)/γ^2)	3.9965E-02
P	Beam momentum	MeV/c	βγM	3.7517E+01
D	Length between bunch centers	m	β*c/f	5.9534E-02
r	Normalized bunch radius	none	R/D	5.5430E-02
s	Desired normalized bunch length	none	φ/180	2.5556E-01
	ALGEBRA			
J1	Integral parameter (cylinder bunch calculation)	none	SQRT(s^2 + r^2)	2.6150E-01
J2	Integral parameter (cylinder bunch calculation)	none	SQRT(1+r^2)	1.0015E+00
J3	Integral parameter (cylinder bunch calculation)	none	SQRT[(1-s)^2+r^2]	7.4651E-01
K1	Multiplication constant	none	Q*I/(2*π*r^2*f*ε*D)	9.7660E+03
JDL-part	Partial integral for E(D-L) (cylinder bunch calc.)	none	J2*ln((J2*J3+J2^2-s)/(r*(r+J2)))	3.2444E+00
JDL	Total integral for E(D-L) (cylinder bunch calc.)	none	(JDL-part)+1-s-J3+r+ln((J3+s-1)/r)	5.7658E-03
J0	Integral for E(Z0) (cylinder bunch calc.)	none	J1-J2+(1-s)+r*ln((r+J2)/(r+J1))	7.1172E-02
Wcm	Adjacent-cylinder-bunch center-of-mass energy	eV	K1*(J0-JDL)	6.3875E+02
Wsing	Single-cylinder-bunch center-of-mass energy	eV	K1*J0	6.9506E+02
Wellipse	Single-ellipse-bunch center-of-mass energy	eV	(K1*r/2)*ln(1/s)	3.6927E+02
	BUNCHER VOLTAGE TO GIVE DESIRED FINAL PHASE WITH SPACE-CH.			
	Buncher voltage for two cylinder bunches	V	Wcm + sqrt(4*W*Wcm)	4.4414E+04
	Buncher voltage for single cylinder bunch	V	Wsing + sqrt(4*W*Wsing)	4.6359E+04
	Buncher voltage for single ellipsoidal bunch	V	Wellipse + sqrt(4*W*Wellipse)	3.3653E+04

Fig. 2. Spread sheet to calculate the required buncher voltage to bunch the beam to a desired phase spread. Calculations are done for both a single bunch and for adjacent beam bunches.

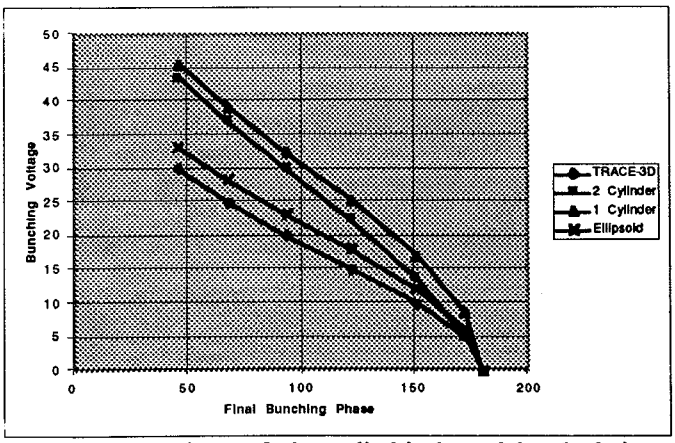

Fig. 3. Comparison of the cylindrical model calculation to results obtained from TRACE-3D for various degrees of bunching for a fixed beam radius.

References

[1] T. P. Wangler, "Space-Charge Limits in Linear Accelerators," LA-8388 (1980).

[2] K. R. Crandall, D. P. Rusthoi, "TRACE 3-D Documentation," LA-UR-90-4146.

[3] O. D. Kellogg, "Foundations of Potential Theory," (1929).

INDUCTION LINEAR ACCELERATORS FOR PHYSICS DIAGNOSTICS

Henry L. Rutkowski and William A. Barletta
Lawrence Berkeley National Laboratory
University of California - Berkeley

Abstract

The short pulse, very high current capabilities of the induction linear accelerator make it a logical candidate for certain applications to diagnosing physical properties. Two examples are fast high density explosive experiments and material science using neutron scattering. Flash x-rays are needed for imaging high density metal compression experiments. The short (50-75ns) pulse-burst capabilities of the induction linac are well suited to this. Because high x-rays doses are necessary to image the experiment and characterize density variations the multi-kiloampere capabilities of induction machines are attractive. Short neutron pulses from proton induced spallation can provide excellent energy and time resolution in material studies using neutron scattering. The induction linac simplifies spallation sources by transporting and accelerating the total beam current necessary (amperes of H^+) in a single beam with no storage. Concepts for both applications are discussed with emphasis on technical risks and costs.

Introduction

Induction linear accelerators have properties that make them valuable in physics diagnostics applications. These properties are the ability to accelerate very intense beams and the ability to generate discrete short pulses[1]. The two applications discussed here are the use of proton beams to generate spallation neutrons for material science, chemistry, and biology and the use of short high current electron pulses for fast time resolved radiography of dense rapidly moving objects. Induction linacs can accelerate any beam current that the transport system is capable of handling provided that the pulser that drives the accelerator cells can supply the required current. This is because induction accelerators do not suffer from the cavity loading effects that occur in RF machines. However, fast rep rate pulse power systems have design problems of their own, such as switch and component lifetime, and cost.

In the application of such machines to a spallation neutron source, the main advantage is that one can accelerate the entire beam current required on the spallation target in a single pass thus eliminating the need for a storage ring. Not using a ring eliminates the need for H^- ion sources which are a more complex and a lower current density technology than H^+ sources. The absence of a ring also avoids the problems associated with stripper foils and excited neutrals. By extracting the required short pulse directly in the injector one avoids the beam chopping problems of RF machines. Finally, since the physics limit placed on the beam emittance in an induction machine comes from the final focus conditions, the ion temperature of the source is not a limiting factor. The very low emittance required for injection into a ring is small compared to the emittance limit imposed by final focusing in this application.

Radiography of fast moving dense objects needs multiple pulses separated slightly in time and possibly simultaneously from more than one direction to obtain 3D imaging of the object. Such a project is underway at Los Alamos National Laboratory called DARHT[2] (Dual Axis Radiographic Hydro-Dynamic Test facility). The physics requirements for this application are quite severe: beam current of 4-6KA, beam energy up to 20MeV, focal spot < 1mm, 4 pulse burst with 50-70ns pulse length and 250ns pulse separation. Induction linac cells designed for long pulse applications may be useful for this radiography application.

Spallation Neutron Source

The first point is bunch dynamics in the machine. The simplest approach is to accelerate a bunch as a rigid body relying on acceleration to provide both current amplification and pulse shortening. One can also vary bunch lengths by varying the velocity along the bunch as a means to reduce the length of the machine. Designing for short length can reduce costs, but the limits on acceleration gradient may prevent this. Consider accelerating the head of the bunch according to a Z^2 schedule, where Z is the distance along the machine, and accelerating the tail on a linear schedule. Now assume that the output beam has an energy of 1.25 GeV, a current of 57.5A, a pulse width of 580 ns, and a rep rate of 60 Hz. These conditions correspond to a steady state output power of 2.5 MW, reflecting the initial goal of the NSNS (National Spallation Neutron Source) design team for a machine between 1 and 5MW average power. Also assume a 2MeV proton injector generating 8μs, 4.2 A pulses, parameters achievable with technology developed in the LBNL Heavy Ion Fusion Accelerator Research[3] program. The injection parameters come from imposing the condition that geometric length of the bunch is the same during its entry into the accelerator as during its exit. Inside the accelerator the bunch expands longitudinally before recompressing to its original length. Solving the relativistic equations of motion for the head and the tail with the entry and exit conditions listed above, yields a machine length of 1761m plus the length of the injector which might be 15m. There are two problems with this approach. First, the linear charge density in the bunch is 0.213μcoul/m which is very low in terms of the transport limits that can be achieved in quadruple or solenoid magnetic fields. More importantly, the peak accelerating gradient reaches 1.42MeV/m for the head and the linear gradient for the tail is 0.71MeV/m. Figures commonly used for the technologically achievable gradient range from 1Mev/m and to a more realistic 0.5MeV/m.

Assume a more practical acceleration gradient of 0.5 MeV/m and use a higher linear charge density that makes more efficient use of transport capabilities. Making the beam diameter small also reduces the mass of core material for a given number of volt-seconds (pulse voltage times pulse duration) and a given core length. In this case the beam bunch enters the accelerator completely before the acceleration cells are turned on. The entire bunch is then accelerated at the same rate and therefore the bunch length remains constant through the machine. E.P. Lee[4] has developed an envelope equation model to calculate the space charge transport limit for a given quadrupole focusing channel. This analytical model incorporates consistent expansions in KL^2 where K is the quadrupole strength and L is the lattice half period and gives errors less than 2%. From the equations one can derive an expression for the quadrupole magnetic field gradient in terms of the linear space charge density , λ, the beam maximum radius, a, the normalized emittance, ε_N, and the relativistic constants, β and γ:

$$B' = \frac{650.6\lambda}{\beta\gamma^2 a^2}\left[.9859 \pm \frac{.3043}{1 \pm \left(11.24\lambda a^2 / \gamma\varepsilon_N\right)}\right] \quad . \quad (1)$$

Using this expression one finds that it is feasible to triple the linear charge density to 0.639μcoul/m. The injection bunch length is reduced from 157m to 52.3m. The resulting higher injector current is not a problem. One can transport this bunch within a maximum radius of 1.5cm in a quad system with pole tip field .77T and bore radius of 4cm. The effects of quad length and the bore size on aberrations present no problem. The resulting accelerator is 2548m long plus the 2MeV injector and produces 200ns pulses at 60Hz with an average power of 2.5MW. The accelerating cells are 250KV each, using Metglas as the core material; there are 4992 of them in the main accelerator and 105 in the bunch entry section just after the injector.

This design was costed using scaling rules and experience from the Heavy Ion Fusion and RTA programs. The result was a total accelerator system cost of $542.7M including all design, assembly, and commissioning labor and overhead. A permanent magnet qudrupole transport system was assumed to minimize core inner radius relative to room temperature or superconducting sytems. Dropping the exit energy from 1.25GeV to 1GeV, eliminates 500m of accelerator length at the cost of dropping to 2MW average power but with a financial saving of $85.1M. The exit pulse length remains essentially the same. This cost must be viewed with considerable caution. The design was a first cut point design. Second, "rule of thumb" scaling laws based on various peoples' experience were used and the bias was toward conservatism. A more detailed design is needed to achieve reliable costs with computerized cost models. The transport system represents $87M but is based on an unoptimized constant period configuration. Substantial saving could result from better design. The cooling budget is $78.4M and probably could be reduced by better design.

In addition to the cost uncertainties there is technical risk. The issue of getting the 12.5A proton current out of the ion source with suitably low emittance for target focussing is not a problem. However fast pulse extraction preserving good beam optics from the gas source is. Recent work at LBNL on source beam chopping may provide the solution to this problem but experimental work is needed. Another risk is the lifetime and reliability of the pulse power components. Operation at 60Hz for 24 hrs/day and 80% up time implies $1.5X10^9$ pulses per year. Life tests at LBNL using FET switches have reached $2.5X10^7$ pulses at 72Hz on a nickel-iron core and $2X10^8$ pulses at 100Hz on Metglas both with convective air cooling. The systems were still operational at conclusion. Further experimental work especially on cheaper thyratron switches is needed to reduce risk and to define cooling requirements better. The beam clearances used were based on theoretical models used in the Heavy Ion Fusion program in which beam halo was not a consideration. This problem needs further study to better define the clearance requirements which in turn affect the cost of the magnets and cores. Finally, at short pulse lengths(< 0.5 μs), the power loss in Metglas cores grows quickly. Consideration should be given to ferrite materials which cost more but which would reduce cooling requirements and operational costs.

Fast X-ray Metallic Objects of Dense Radiography

Long pulse induction linac technology under development for heavy ion inertial fusion may be suitable for the radiography application. A gated cathode of some type, either electronically or laser switched, could supply a train of pulses to the accelerator. The pulse duration and separation would be governed by the cathode system while the voltage that accelerates the beam would be on throughout the burst. The two most important problems in the linac design are the accelerator cell voltage flatness and the transverse mode impedance of the cell. Other physics issues include especially the interaction between the intense beam and the bremstrahlung target, corkscrew motion of the focal spot due to beam energy variations, and emittance growth.

An induction linac cell is normally designed to operate with a pulser that is matched to a specific beam load. If the beam is not present while the voltage is on, an overvoltage condition on the acceleration gap and the cell insulator will be created. One way to deal with this problem is the use of a compensation resistor in the pulser circuit. The pulser then sees the core magnetization current, the beam current, the compensation resistor current, and the gap capacitance all in parallel. If one dominates the loading with the compensation resistor the system efficiency will be low but in a testing application like this, efficiency is not important. In this concept one is deliberately creating a beam on-beam off situation and therefore much attention needs to be devoted to this problem. Not only is it a high voltage design problem but also a beam chromaticity issue. If the accelerating voltage is not at its nominal value when a bunch arrives, the change in beam energy will contribute to transverse motion of the focal spot which reduces the geometric resolution of the radiography system.

Another approach is driving a large core, containing sufficient volt-seconds to accommodate the number of beam pulses required, with separate pulsers that are electrically

isolated from each other. There are two ways of isolating the pulsers. One is diodes and the other is to use a switch capable of holding off the acceleration gap voltage in the back direction. In the case of diodes the problem is to provide enough back voltage isolation to withstand the full acceleration gap voltage of possibly 250KV. Also the diodes must be capable of handling the full discharge power in the forward direction. It is probably easier to use high voltage switches such as thyratrons or spark gaps. This approach has the disadvantage of requiring multiple pulsers which represent extra cost, but the advantages are avoiding the load matching problem and allowing the use of less Metglas by not maintaining voltage during periods when the beam is absent. A third possibility is the use of branch magnetics[5] to drive the core without resetting between pulses.

The beam breakup (BBU) instability in linear accelerators is driven by coupling between longitudinal beam motion and the excitation of transverse modes in the acceleration cavity[6]. The BBU parameters for the existing DARHT first axis cells have been thoroughly studied. Changing to a new cell design will require detailed computer simulation to understand the precise properties of the new cavities. A code such as AMOS[7] will have to be modified to include the properties of Metglas for the calculation of the transverse impedances of the new cavities.

In the modeling of BBU the parameter[6]

$$\omega_0 \frac{Z_\perp}{Q_\perp}\left(Q_\perp\right), \qquad (2)$$

where $Z_\perp$ is the transverse mode impedance of the dominant transverse mode and $Q_\perp$ has the value for this mode, is an important quantity in the growth rate for the instability. It is therefore important to consider how this factor will change if one makes simple changes in the existing cavity by changing the feromagnetic material. Consider a simple cylindrical cavity in which one first has ferrite suitable for 70ns pulses and then replaces it with Metglas for 1μs constant voltage pulses. The total mass and therefore the cost of the core depends on the inside radius, the core length and the required cross section. If a length of the cavity has been chosen by system considerations the, core cross section is determined by $\Delta B(r_0 - r_i)d = V_p \tau$ where V_p is the gap voltage, τ is the effective pulse length, and ΔB is the total flux swing before saturation allowed by the ferromagnetic material. The question is what happens to the quantity $Z_\perp / Q_\perp$ while the outside radius r_0 is changed to accommodate the change in material and the change in τ while keeping d and r_i fixed. Therefore $r_0 = (V_p \tau / \Delta B d) + r_i$.

A single pill box model[8] of an induction cell cavity has a transverse mode impedance estimated by

$$Z_\perp = \frac{-8d}{c\omega_0 r_i^2} \mathrm{Im}\, P_1(\omega_0), \qquad (3)$$

where $P_1(\omega_0)$ is a function determined by d, r_i, and the ratio of assumed wall impedance at the outside radius r_0 to the impedance of free space. If one only increases or decreases the cavity radius then

$$\omega_0 \left(\frac{Z_\perp}{Q_\perp}\right) Q_\perp \approx \frac{8d}{r_i^2}, \qquad (4)$$

For a given current, machine length, number of cells, beam noise spectrum, acceleration gap, and pipe radius the BBU growth rate should not change. This is because it is not the cavity in which the feromagnetic material for the cell is contained that determines the $Z_\perp$ of interest but rather the cavity that contains the acceleration gap. This gap will probably not have a simple cylindrical shape and transverse mode damping structures will be included in the cavity.

The resonant frequency of a radial cavity transverse mode is

$$\omega_{1no} = \frac{c x_n}{r_0} \text{ where } x_n, \qquad (5)$$

is a constant dependent on the mode number. If the change in radius causes the resonance of the relevant mode to coincide with a portion of the beam noise spectrum that is relatively high, the BBU growth will be more severe.

Acknowledgments

This work was supported by the U.S. Department of Energy under Contract No. DEAC03-76SF00098.

References

[1] Principles of Charged Particle Acceleration, Stanley Humphries Jr., John Wiley & Sons, 1986, ch. 10.

[2] M. Burns et al., Proc. 9th Int. Conf on High-Power Particle Beams, Wash. DC, May 25-29, 1992, p. 283.

[3] S. Yu et al., Proc 1995 Particle Accel Conf and Intl. Conf on High Energy Accelerators, May 1-5, 1995, Dallas, Texas, p. 1178.

[4] E.P. Lee, Particle Accelerators, Vol. 52, 1996, p. 115 -132.

[5] H.C. Kirbie, et al., Proc. 1992 Linear Accelerator Conf. Ottowa, Canada, Aug 24-28, 1992, p. 595.

[6] G. J. Caporaso and A.G. Cole, Proc. 1990 Linear Accelerator Conf., Albuqerque, N.M., Sept. 10-14, 1990, p. 281.

[7] J.T. DeFord, et al., Proc. Conf on Computer Codes and Linear Accel Community, Los Alamos, N.M., Jan 25, 1990, p. 265.

[8] R. J. Briggs et al., Particle Accelerators, 18, 1985, p 41.

All-Electrostatic Split LEBT Test Results*

John W. Staples, Matthew D. Hoff and Chun Fai Chan
Lawrence Berkeley National Laboratory
Berkeley, California 94720, USA

Abstract

An all-electrostatic LEBT for an RFQ has been assembled and tested with beam. The LEBT includes two quasi-einzel lenses, allowing a wider range of Twiss parameters to be accommodated, and the lenses are split into quadrants, allowing electrical steering of the beam. Moreover, mechanical steering by moving the entire LEBT with a special low-friction vacuum joint was also demonstrated. The LEBT was tested with unanalyzed protons from an RF-driven bucket source by measuring the beam directly and by measuring the transmission through a subsequent RFQ as a function of LEBT electrode parameters. Agreement between calculated LEBT beam characteristics and actual measured values is excellent. This LEBT offers fully unneutralized beam transport with steering and two-knob control of exit Twiss parameters, and can be applied to negative hydrogen as well as proton beams.

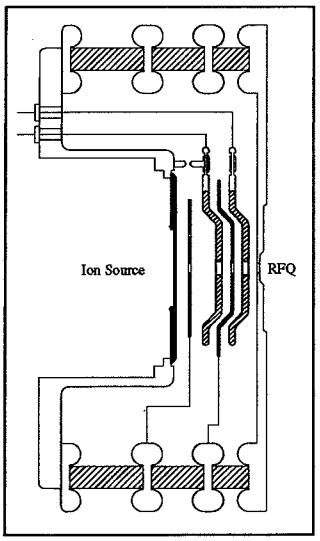

Figure 1, Electrode Arrangement

Introduction

An advanced, all-electrostatic LEBT has been built and successfully tested. This new design[1] offers several advantages over previous LEBT designs, particularly for injection into RFQ accelerators.

The strongly convergent beam required at the RFQ entrance, along with precise beam steering requirements has proven to be a formidable task as focusing and steering errors can easily reduce the performance of the RFQ. The usual method of magnetic solenoid or quadrupole transport results in space-charge neutralized transport, which may be unstable in the presence of any intensity modulation noise from the ion source, and the lack of sufficient steering or matching capability often results in betatron function mismatch at the RFQ entrance.

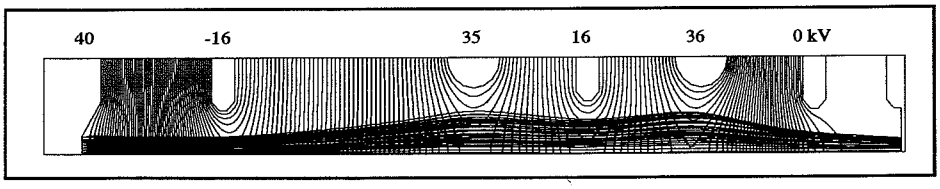

Figure 2, Beam Envelope through LEBT

The all-electrostatic LEBT designed and built by the Ion Beam Technology (IBT) group at LBNL eliminates the neutralization problem and offers several other advantages. This new design incorporates two electrostatic lenses that allow a wide range of matching conditions (Twiss parameters) to be established, insuring betatron function match to an RFQ accelerator. The design has exceptionally low aberrations, offers beam steering, in both angle and displacement, and is physically compact.

Figure 1 shows the layout of the LEBT inside the re-entrant support insulator. The ion source resides in the cylindrical cavity on the left. The total acceleration potential is 40 keV, with 59 kV across the first (extraction) gap. The two thick electrodes comprise the variable-voltage einzel lenses.

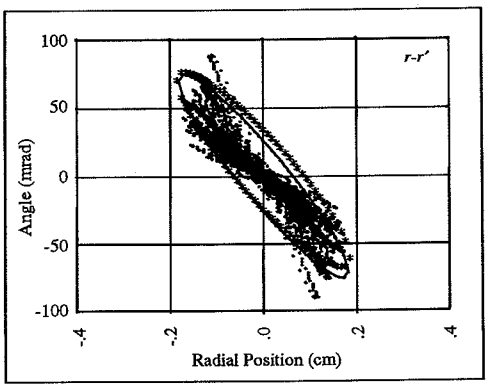

Figure 3, WOLF-Predicted r-r′ Phase Space

Beam steering is incorporated by splitting both einzel lenses into four quadrants and applying a balanced deflection voltage across opposing quadrant pairs. Up to ±7 mrad deflection is attainable from each of the two lens electrodes with 1 kV across opposing quadrants. In addition, the entire source and LEBT assembly can be moved transversely during operation in both planes by up to ±4 mm with 40 micron reproducibility. This combination of electronic and mechanical steering guarantees optimum steering of the beam into the RFQ.

Figure 2 shows the beam envelope from the ion source to the RFQ match point and Figure 3 the r-r′ phase space predicted by the WOLF ion source code (ref in [1]). The smallest lens aperture radius is 0.5 cm at the final electrodes on the right, the last one representing the beginning of the RFQ vane and the immediately preceding one the exit aperture of the LEBT itself.

Test Procedure

The LEBT performance was first measured with an Allison-

*This work was supported by the Director, Office of Energy Research, Office of High Energy Physics and Nuclear Physics Division of the U.S. Department of Energy under contract number DE-AC03-76SF00098.

type emittance scanner[2] substituted for the RFQ with the first analyzer slit located 20 cm downstream of the RFQ match point. The pulsed 30 mA beam current was measured with a toroidal current transformer at the exit of the LEBT. The nominal voltages

Ion Source Body	40	kV
Extraction Electrode	-16	kV
First Focus Electrode	35	kV (nominal)
Intermediate Electrode	16	kV
Second Focus Electrode	36	kV (nominal)
Ground End	0	kV

Table 1. Electrode Voltages

for the electrodes, referred to ground, are listed in Table 1.

The first and second focus electrodes were varied over a matrix of 33 to 37 and 33 to 38 kV, respectively, in 1 kV steps, and the Twiss parameters α, β and ε were measured. These were compared to the values predicted by the WOLF calculation for several representative values of the focus electrode voltages, the data showing good agreement between the predictions and the measurements. Figure 4 shows a typical emittance plot, with the ellipse representing the shape of the RFQ acceptance (but at a smaller emittance to emphasize the congruence of the ellipses).

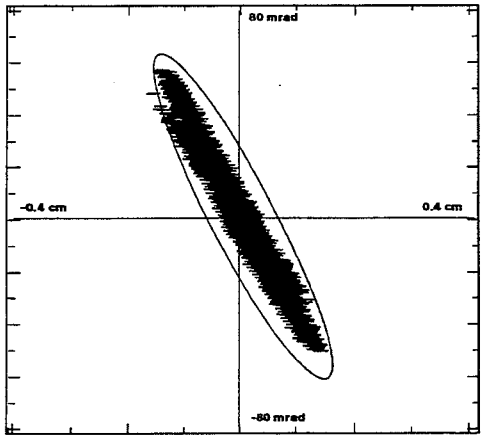

Figure 4. Measured LEBT Beam Emittance

At a total current of 30 mA, measured with the toroidal current transformer, the following emittances and Twiss parameters were measured. In this case, the electrode voltages were set to the nominal values indicated above, and the measured emittance back-projected a distance d_{back}, assuming ballistic transport, to a point 20 cm upstream of the plane of measurement, corresponding to the original WOLF calculation and to the match point of the RFQ. Table 2 lists measurements done on separate days, showing the excellent consistency of the measured values, and the results of the WOLF calculation. Also listed are measured values back projected 19.5 cm, which give better agreement to the WOLF calculation, indicating a mere 0.5 cm discrepancy of the longitudinal position of the RFQ match point between the measured and calculated values for nominal focusing electrode potentials.

Run Date	d_{back} (cm)	β (cm)	α	$\varepsilon_{rms,U}$ (cm-mrad/π)	$\varepsilon_{rms,N}$ (mm-mrad/π)
27 Sept 95	19.5	7.8	1.95	1.483	0.137
	20.0	9.9	2.26	1.483	0.137
28 Sept 95	19.5	8.9	2.11	1.454	0.134
	20.0	11.2	2.41	1.454	0.134
2 Oct 95	19.5	8.9	2.22	1.260	0.116
	20.0	11.3	2.55	1.260	0.116
WOLF		7.45	2.87	1.110	0.105

Table 2. Measured and Calculated (WOLF) Twiss Parameters

Electrical Steering

Angular beam steering is accomplished at the two focusing electrodes, split into quadrants, by applying a balanced transverse field at those points. Each pair of opposing quadrants of each of the two focusing electrodes can be operated at a voltage offset from the mean by as much as ±500 volts, or 1000 volts across an opposing pair. The angular deviation of the beam was determined by the emittance scanner, along with any variation in the Twiss parameters, including the beam emittance.

Figure 5 (next page) shows the variation in exiting beam angle, and the variation of the Twiss parameters and emittance when the voltage across an opposing pair of quadrant segments in the second focusing electrode is varied from -1000 to +1000 volts. The angular deviation is quite linear with voltage and the Twiss parameters and beam emittance are only slightly affected at large steering angles.

Coupling to an RFQ

In the second phase of the experiment, the LEBT was coupled to an 800 keV, 400 MHz RFQ[3] manufactured six years ago at LBNL designed with an injection energy of 40 keV and 50 mA beam current. The LEBT was designed to match the Twiss parameters of the RFQ with a generous margin of adjustability by varying the potentials of the two focus electrodes.

The transmission of the RFQ was calculated, using PARMTEQ, for a range of input Twiss parameters. The effect of steering, both angular and position on the RFQ transmission was measured, verifying the initial alignment of the system. The optimum transmission occurred with minimum electrical steering and with the initial mechanical alignment position.

The focusing electrode voltages were varied over the same matrix of values for which data were taken with the emittance scanner. The transmission of the RFQ over the range of Twiss parameters available from the LEBT matched very well with the predicted transmission calculated by PARMTEQ for a mismatched input beam. The maximum transmission was experimentally found at almost the exact focusing electrode voltages predicted by WOLF. We can thereby conclude that the actual acceptance of the RFQ is in agreement with the PARMTEQ prediction, and that the measured beam parameters from the LEBT show excellent agreement with the WOLF calculations over a wide range of focusing lens parameters.

Further measurement taken after the RFQ was removed from the beam line showed the species distribution from the LEBT was

approximately 64% H^+, 17% H_2^+ and 19% H_3^+. The RFQ accelerates only the H^+ component, and the expected transmission of the RFQ was expected to be only 59% for the H^+ species, due to a poor choice of geometry of the vane tips. ($A\, r_\perp = 0.75 r_0$ constant transverse radius geometry was used. Subsequent simulations with the 8-term PARMTEQ-H[4] showed that this geometry was a poor choice and a $r_\perp = 1.0 r_0$ geometry would have given much better transmission.) The total current (all species) injected into the RFQ was about 18 mA, which should result in 6.8 mA of accelerated H^+ beam. About 5.5 mA was accelerated, 81% of the expected value. This small discrepancy has not been resolved to date.

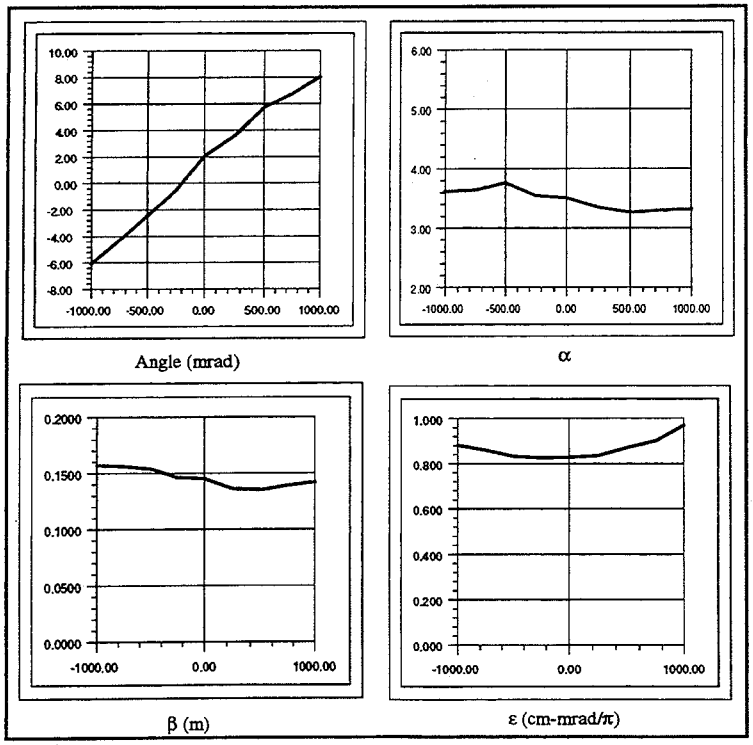

Figure 5. Steering, Twiss parameters vs. quadrant voltage unbalance

Chopping Experiment

Recently, LBNL has joined a team to develop the front end of a proposed pulsed spallation neutron source, which incorporates a 1 GeV linac and a storage ring[5]. The beam circulating in the ring requires a 35% circumference gap with a dark current of 10^{-5} of the rest of the circulating bunch. To establish this very deep gap, choppers will be placed at the ion source, in the LEBT, and a fast, 2.5 nsec chopper at the 2.5 MeV point in the linac. An experiment was prepared for this LEBT to test the feasibility of fast (1 MHz) chopping at the 40 keV level.

In the first phase of the experiment, a high-voltage pulser provided a ±1500 volt pulse, rising in 100 nsec and decaying somewhat more slowly, to opposite quadrants of the second focusing electrode to deflect the beam into a 0.6 cm diameter aperture located at the LEBT exit. With 2.7 kV across the opposite quadrants the beam was fully extinguished with a risetime comparable to the risetime of the pulse generator. Transit time in the LEBT itself limits the rise/fall time of the chop to about 15 nsec, and the 2.5 nsec risetime travelling wave chopper at the 2.5 MeV level will sharpen up the edge of the chop. The slower LEBT and ion source choppers contribute the very low dark current in the middle of the chop, and reduce the heating of the 2.5 nsec chopper beam stop.

Future Plans

The operation of this LEBT has been so successful that a minor variant of it will be used in the low-energy part of the injector for a proposed National Spallation Neutron Source[5]. Added to the basic LEBT design shown here will be the beam chopper, a segmented thin Faraday cup that pivots in from the side and a pivot-in one-way vacuum gate valve, both located between the last focusing electrode and the ground end, operated with the last focusing electrode at ground potential.

Acknowledgments

The authors thank all those who worked tirelessly on this project, including Rick Gough, Ka-Ngo Leung and his ion source group, Jim Ayers and his electronics technicians, and Bob Aita and his mechanical technicians.

References

[1] Chun Fai Chan and John Staples, *A Compact Double Einzel Lens LEBT with Steering for H+ Beams,* Proceedings of the 1994 Linear Accelerator Conference, Tsukuba, p. 594.

[2] Paul W. Allison et al, *An Emittance Scanner for Intense Low-Energy Ion Beams,* 1983 Particle Accelerator Conference, Santa Fe, p. 2204

[3] J. W. Staples et al, *A Compact Proton RFQ Injector for the Bevalac,* 1988 Linear Accelerator Conference, Newport News, 1988, p. 48

[4] N. Tokuda, private communication

[5] B. R. Appleton et al, *The National Spallation Neutron Source Collaboration: Towards a New Pulsed Neutron Source in the United States,* Fifth European Accelerator Conference, Barcelona, June 1996

THE ELECTRON GUN FOR THE DARESBURY SRS LINAC

D.M.Dykes
CLRC Daresbury Laboratory,
Warrington WA4 4AD, UK

Abstract

The electron gun for the Daresbury SRS linac injector has been modified to use the cathode-grid assembly from the Eimac planar triode 8755. The gun now has improved beam characteristics, is more reliable and the cathode assembly is quicker and easier to change. This paper describes the assembly of the electron gun, and then the re-conditioning of the cathode highlighting the vacuum environment. The action of the grid modulation system on the electron beam, which pre-bunches the electron beam, is described, and typical gun characteristics are shown.

Proposed developments to the gun system are discussed.

Introduction

Daresbury Laboratory operates the UK's national synchrotron light source, the SRS. It is operational for approximately 7000 hours a year, providing synchrotron radiation used by many varied scientific disciplines. The electron storage ring energy is 2 GeV and the beam lifetime is in excess of 30 hours at 200 mA. The storage ring is filled to 250 mA once every 24 hours.

The injection system consists of a 80 kV electron gun feeding a 10 MeV S-band electron linac, the electron beam is accelerated to 600 MeV in a 500 MHz booster synchrotron. The beam is injected into the storage ring at 600 MeV and the energy ramped to 2 GeV. The injection process takes approximately 20 minutes. Consequently the gun injection equipment is operational for less than 1 hour per day.

The electron gun has been modified to use the cathode-grid assembly from the Eimac planar triode 8755 [1]. This gives improved beam characteristics over the previous system, it is more reliable and the cathode assembly is quicker and easier to change. The paper describes the assembly of the electron gun, and the re-conditioning of the cathode, highlighting the vacuum environment. The action of the grid modulation system, which pre-bunches the electron beam, is described, and typical gun characteristics are shown. Proposed developments to the gun system are also discussed.

The Electron Gun - Mechanical Layout

The original electron gun was similar to the design by Willard [2] for the Manchester Christie Hospital Linac. It contained a 1 inch (25.4 mm) spherical oxide cathode with a separate de-mountable grid, which was modulated at 500 MHz. When the cathode failed the cathode - grid assembly was de-mounted, and the cathode sprayed with the usual carbonate mix (barium, calcium and strontium). The carbonates were converted to oxides, and when this was completed activation of the cathode took place. This process took several hours, and satisfactory conversion and activation could never be guaranteed. As this process took place while the gun was attached to the linac, the decomposition products of the carbonates could have harmful effects on the vacuum surfaces of the linac.

The gun has now been modified. Figure 1 shows the mechanical arrangement of the present gun. A miniature ceramic - metal planar triode, Eimac type 8755, has been modified to be used as the cathode grid assembly of the gun. The triode can be used up to frequencies of 3 GHz. The cathode is a conventional oxide coated cathode, but the heater power is only 10 watts, a factor of ten lower than the original.

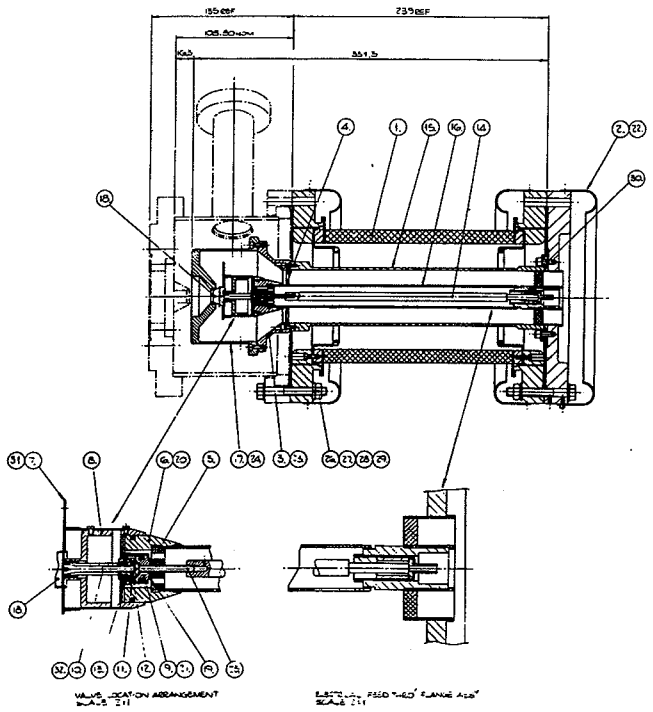

Figure 1: Mechanical Layout of the Gun

The triode is inserted in the gun assembly which is connected to a temporary heater supply, with the heater voltage set to about 2 V to keep the activated cathode temperature above 150 °C. The triode anode and body ceramic are broken off, and the beam forming electrode attached. The gun assembly is bolted to the linac and the gun evacuated, whilst maintaining the cathode temperature. Haas and Jensen [3] found that by keeping the temperature to 150 °C cathodes are not poisoned when exposed to air as the oxides are converted

to hydroxides and the hydrate is prevented. The emission capabilities are preserved.

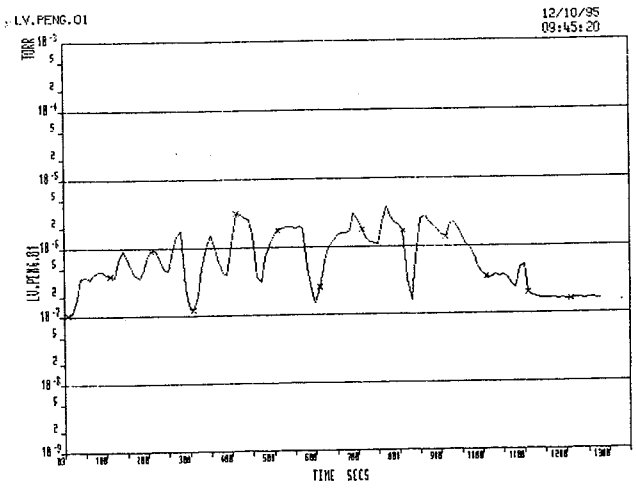

Figure 2: Plot of Gun Vacuum during Cathode Activation

When the vacuum pressure is better than 10^{-7} torr, the heater voltage is gradually increased, keeping the vacuum pressure below 10^{-5} torr. Figure 2 shows the typical vacuum pressure variation during this re-activation process, and Figure 3 the residual gas analysis at the same time. Note that the water peak increases initially, but that it is the methane peak that determines the overall pressure.

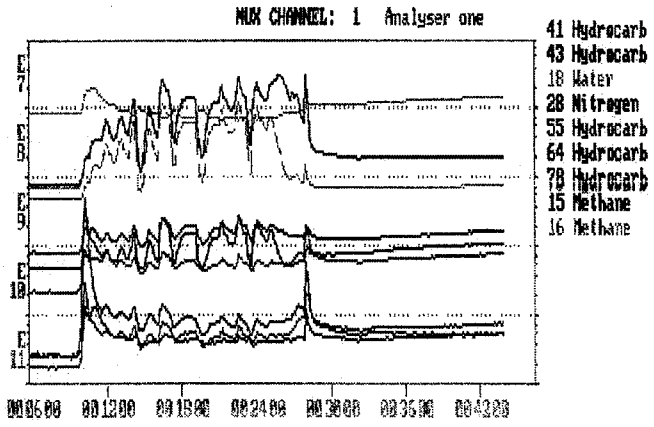

Figure 3: RGA during Cathode Activation

The installation and re-activation process is simple and quick, taking only 4 or so hours. The cathode life is typically two years, but recently improved vacuum conditions have extended that time.

The Electron Gun - Electrical Layout

Figure 4 shows the electrical layout of the gun system. The gun has to produce a 400 nS 80 keV bunch of electrons 10 times a second. The action of the triode is used to pre-bunch the beam before injection into the linac.

A three quarter wavelength coaxial cavity is connected to the gun, and sits at the gun HT, which is provided by a half sine wave pulse modulator, giving a -80 kV pulse. The heater power supply is at HT potential. There is a 0 to -200 V grid bias supply, and the 500 MHz grid modulation is fed via an 80 kV waveguide isolator.

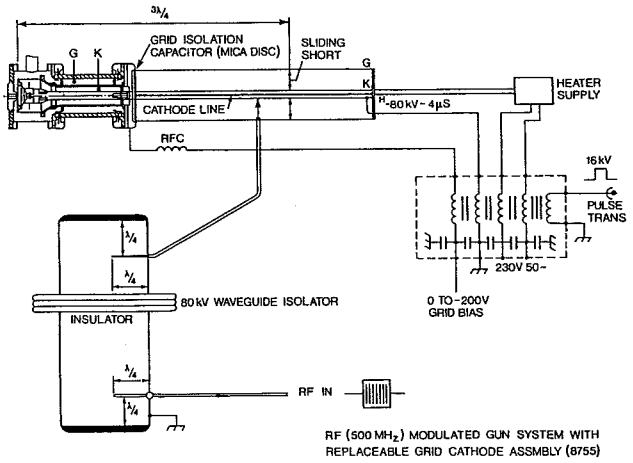

Figure 4: Electrical Layout of the Gun

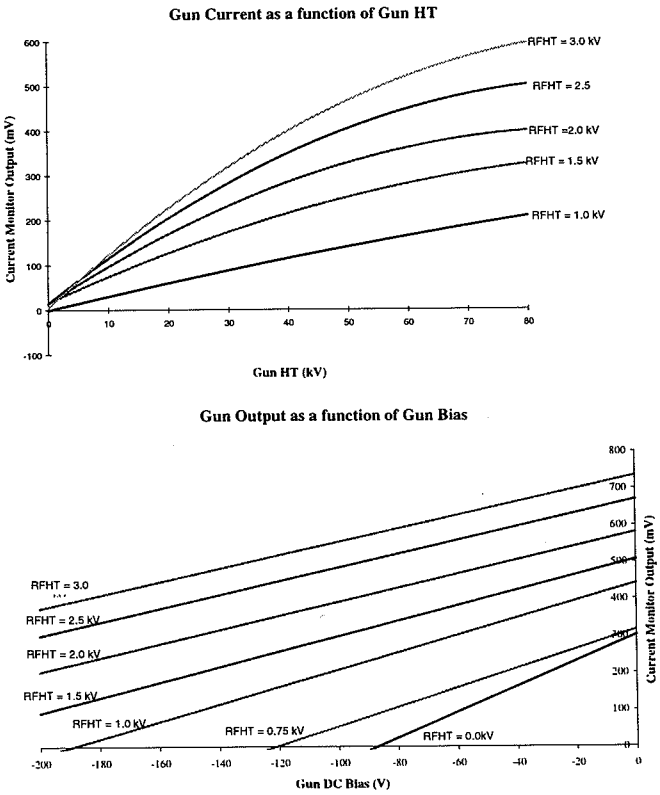

Figure 5: Gun Characteristics

Gun Characteristics

A current transformer type monitor with a bandwidth of 500 MHz, but followed by a 10 MHz filter monitors the gun current, Io. Typical gun characteristics are shown in figures 5a, the gun current as a function of gun HT for various values of grid RF modulation -dc grid bias set to -100 V, and 5b, gun current at a fixed HT at -80 kV as a function of DC grid bias for various values of grid RF modulation. These characteristics should be compared with the triode characteristics in the Eimac data sheet [1]. The differences in the slopes in figure 5b is because the output voltage of the Io monitor is proportional to average current, and the conduction angle is smaller the greater the RF amplitude.

Pre-bunching

The SRS linac does not have a pre-buncher cavity, but pre-bunching is achieved by the DC and RF biasing of the gun grid. The linac accelerating voltage is a 4 mS, 4 MW pulse at 3 GHz. The voltage is phased locked to the 500 MHz gun grid modulation. As can be seen from figure 6, by accurate phasing of either of the grid modulation or the accelerating voltage and a large grid DC offset short current micro-pulses can be injected into the linac. The more negative the DC bias the shorter the current pulse.

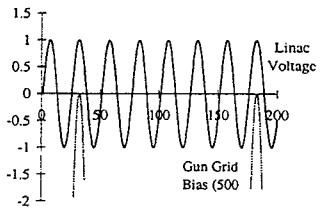

Figure 6: Linac Pre-Bunching

Future Developments

For a small but significant period, the SRS operates in single bunch mode, where only one of the 160 RF buckets in the storage ring is filled with electrons. At present this is achieved with a chopper system operating on the 10 MeV beam in the flight path between the linac and the booster synchrotron. Recently investigation has started on using the gun grid modulation system to produce the single bunch and other bunch patterns [4].

The grid modulation equipment will sit at the HT potential, whilst triggering and clock pulses will be fed via optical fibre.

Summary

The electron gun for the SRS linac injector uses the already activated cathode-grid assembly of an Eimac 8755 planar triode. The installation is simple and quick, and the cathode life is relatively long.

The measured gun characteristics are as expected and follow the original triode characteristics.

The action of the RF and DC biasing of the gun grid perform some pre-bunching for the linac.

In the future the grid modulation system will provide single bunches and any required bunch pattern.

Acknowledgements

I would like to thank Mr. Brian Taylor for the original idea of using a planar triode as the grid-cathode assembly for the SRS linac electron gun.

References

[1] Eimac Technical Data 8755, Varian EIMAC Division, 301 Industrial Way, San Carlos, California 94070.

[2] J.Willard, A High Currnt Electron Gun Suitable for use Down to 1 nanosecond Pulse Length. IEEE Trans. Nuc. Sci. June 1967.

[3] G.A.Haas and J.T.Jensen, Preconversion of Oxide Cathodes, Rev. Sci. Instr., 30, pp 562 565, July 1959.

[4] C.W.Horrabin and D.M.Dykes, DIAMOND Low Power RF System, Proceedings of the 5th European Particle Accelerator Conference (EPAC - 96), Sitges, 1996.

Ion Source Development and Operation at GSI

P. Spädtke, J. Bossler, H. Emig, K.D. Leible, M. Khaouli, C. Mühle,
S. Schennach, H. Schulte, K. Tinschert
GSI Darmstadt

At GSI different ion beams are delivered to the UNILAC, the synchrotron SIS or to the storage ring ESR. For that purpose three different injectors are in use for the UNILAC, equipped with different ion sources. The standard injector with a Penning ion source and the high current injector (with CHORDIS or MEVVA ion source) supply the Wideröe accelerator (pre-stripper section of UNILAC) with an injection energy of 11.7 keV/u. The newly built high charge state injector HLI is equipped with an ECR ion source (CAPRICE). The injection energy for the succeeding RFQ and IH accelerator is 2.5 keV/u. Both beams are further accelerated in the Alvarez accelerator (post-stripper section of UNILAC) with an injection energy of 1.4 MeV/u. For ion source tests and developments additional test benches are available. The specific advantages of each injector, recent improvements and specific operating modes are described.

1 STANDARD INJECTOR

The regular injector is equipped with a Penning ion source (fig. 1). This source is operated in a pulsed mode, typically 50 Hz with pulse length from 2 to 6 ms. Extraction voltage is between 10 and 15 kV. For SIS-operation such a high repetition rate is not necessary, and the extracted ion current within the pulse can be increased by reducing the duty cycle allowing higher peak discharge power.
Typical ion currents measured in front of the Wideröe are listed in Tab. 1. The absolute acceptance of the analyzing and transport system is about $100\,\pi$ mm mrad.

Table 1: Ion currents from the PIG source. Different operation modes are not distinguished.

Element	eμA	Element	eμA
$^{12}C^{1+}$	500 ... 680	$^{16}O^{1+}$	700 ... 890
$^{18}O^{3+}$	1000 ... 1100	$^{20}Ne^{1+}$	1000 ... 4000
$^{40}Ar^{2+}$	700 ... 820	$^{40}Ca^{3+}$	400 ... 570
$^{50}Ti^{2+}$	50 ... 81	$^{52}Cr^{3+}$	30 ... 42
$^{56}Fe^{4+}$	60 ... 72	$^{58}Ni^{3+}$	400 ... 450
$^{121}Sb^{7+}$	10 ... 12	$^{162}Dy^{7+}$	3 ... 5
$^{187}Re^{8+}$	100 ... 165	$^{197}Au^{8+}$	300 ... 410
$^{207}Pb^{9+}$	100 ... 150	$^{209}Bi^{9+}$	200 ... 240
$^{238}U^{10+}$	350 ... 400		

We hope to increase the available intensities, especially in the low repetition mode for SIS, by further development of the PIG ion source. These investigations and developments will be carried out at the newly built PIG test bench in close collaboration with the JINR in Dubna. The following modifications are planned:

- A pulsed gas feeding system should decrease the base pressure within the source and the beam line. The optimum case would be to have enough atoms to ignite the source and to decrease the pressure during the pulse to shift the charge state distribution to higher charges.
- A higher peak discharge power should yield an increased plasma density. Together with higher extraction voltages and an improvement of the extraction system higher ion currents should be achievable.
- Different cathode materials will be tested in order to improve the life time of the source.
- A splitted anode with an additional electric field perpendicular to the magnetic field will be tested to improve the extraction efficiency[1].

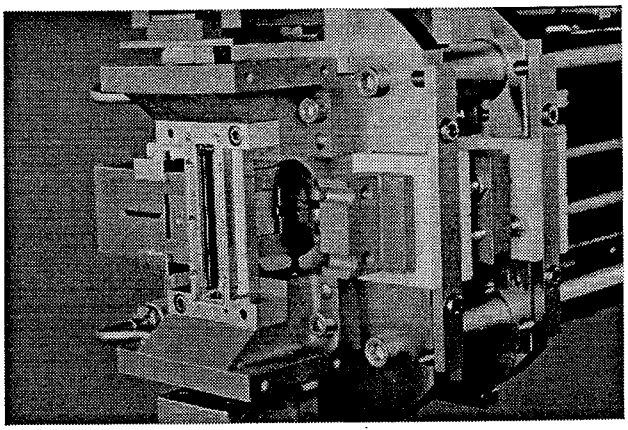

Figure 1: GSI Penning ion source.

2 HIGH CURRENT INJECTOR

To increase the available ion currents for the synchrotron the Wideröe pre-stripper section will be replaced by a RFQ/IH accelerator in the near future [2].

The injection energy will be reduced from 11.7 keV/u to 2.2 keV/u. This implies the use of lower charge states from the ion source (design ion U^{4+}, el. current 15 mA). The total extracted current from the ion source will be in the range of 100 mA. To minimize beam transport problems at low energies, there is no charge or mass separation on the high voltage platform. To preserve the beam quality during post-acceleration, the acceleration column is equipped with a movable single gap and a screening electrode[3]. The present 320 kV high voltage power supply limits the current to 40 mA. It will be replaced by a new one with a maximum voltage of 150 kV and maximum load current of 150 mA in 1997.
Like the PIG source, the CHORDIS (shown in fig. 2) is regularly operated in a pulsed mode up to 50 Hz and pulse length from 0.5 to 5 ms. Extraction voltage is between 20 and 40 kV.
Typical ion currents from the CHORDIS for D and Ne are given in table 2. The currents are measured at the same location as for the PIG source.

Table 2: Ion currents from the CHORDIS.

Element	emA	Element	emA
D_3^+	0.4 ... 0.5	$^{20}Ne^+$	4 ... 5.5

For high current investigations at the UNILAC and SIS we use the Ne-beam delivered by the CHORDIS. The molecular deuterium beam has been used instead of the atomic one for two reasons:

- The operation regime for the atomic beam is not favorable (very low rf and magnetic field level).
- Passing the gas stripper behind the Wideröe at 1.4 Mev/u the electrical current is increased by a factor of 3 by braking up the molecule and ionizing the atoms. Thus we have had a higher particle current at the experiment.

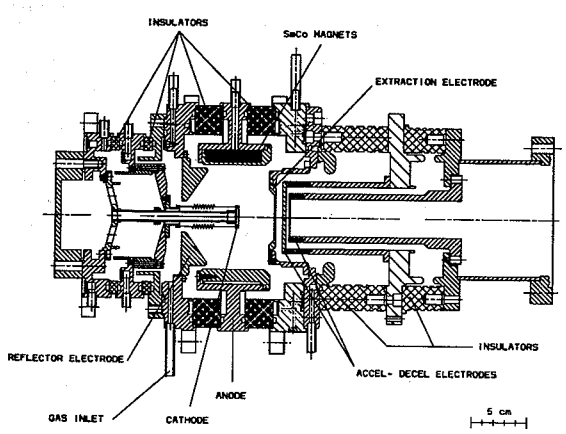

Figure 2: Gas version of CHORDIS.

For all beams from metallic elements we are using the MEVVA ion source [4]. Our version of that source type (see fig. 3) is operated in a pulsed mode with a repetition frequency of up to 5 Hz and pulse length from 0.5 to 2 ms [5],[6]. Extraction voltage is between 20 and 40 kV. The same extraction system as for the CHORDIS is used.

Typical ion currents for the MEVVA ion source are listed in table 3.

Table 3: Ion currents from the MEVVA.

Element	emA	Element	emA
$^{24}Mg^+$	15 ... 20	$^{24}Mg^{2+}$	50 ... 70
$^{48}Ti^{2+}$	25 ... 35	$^{48}Ti^{3+}$	25 ... 35
$^{58}Ni^{3+}$	25 ... 35	$^{238}U^{4+}$	20 ... 30

The Mg^+ beam has been measured at the UNILAC injector, whereas all other data have been taken at the high current test bench (analyzed current after 5 m beam transport).

For the Ti-beam the maximum of the charge state distribution is at the required charge state, for other elements special measures are necessary to get the maximum current in the desired charge state. Higher charge states can be achieved by applying a high magnetic field close to the cathode region. To decrease the charge state (1+ desired for the Mg-beam) additional gas is fed into the discharge chamber. This is shown in fig. 4.

The development of the MEVVA ion source is made in close collaboration between TASUR in Tomsk, LBL in Berkeley and GSI. After achieving the desired currents, the main activity is now to decrease the noise level on the beam as well as the pulse-to-pulse reproducibility.

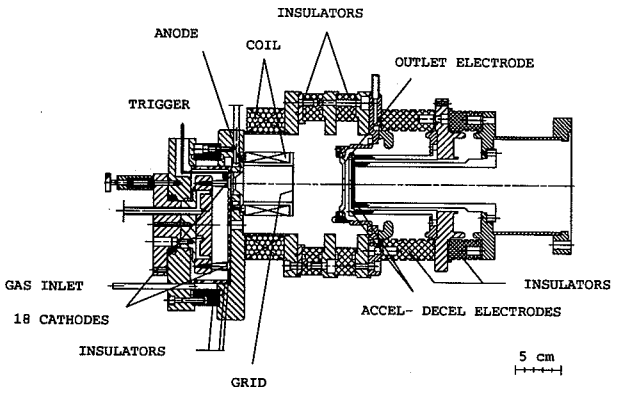

Figure 3: MEVVA ion source.

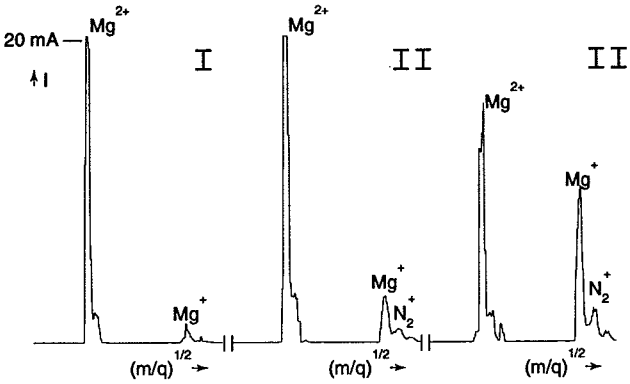

Figure 4: Mg spectra from MEVVA ion source. I: no additional gas, II: nitrogen pressure at the gas inlet is $3 \cdot 10^{-1}$ mbar, III: $7 \cdot 10^{-1}$ mbar.

3 HIGH CHARGE STATE INJECTOR

The extraction voltage from the ECR source (shown in fig. 5) is chosen to match the specific input energy of the RFQ (2.5 keV/u). Because of the high charge states available from this source no high voltage platform is necessary. The most important features of the ECR ion source are the stable production without interruptions for weeks and the low material consumption for the desired element. Typical ion currents are listed in table 4. These ion currents are not always the maximum achievable currents, but they were sufficient for the specific experiment.

Table 4: Ion currents from the ECR ion source. Enriched isotopes are marked by an asterisk.

Element	eμA	Element	eμA
$^{12}C^{2+}$	70 ... 100	$^{20}Ne^{4+}$	200 ... 250
$^{22}Ne^{4+*}$	200 ... 250	$^{40}Ar^{8+}$	200 ... 250
$^{58}Ni^{9+}$	5 ... 13	$^{62}Ni^{9+*}$	10 ... 20
$^{64}Ni^{9+*}$	10 ... 20	$^{70}Zn^{10+*}$	20 ... 50
$^{82}Se^{12+*}$	30 ... 40	$^{118}Sn^{16+}$	2 ... 5
$^{129}Xe^{18+*}$	25 ... 30	$^{136}Xe^{18+*}$	17 ... 20
$^{197}Au^{24+}$	15 ... 20	$^{208}Pb^{27+}$	5 ... 7
$^{238}U^{29+}$	2 ... 3		

The main activity for that source is to develop different techniques to create ions from solid materials [7].
Tests at the ECR test bench revealed that for Se (vapor pressure 10^{-3} mbar at $\approx$ 200°C) the regularly used oven did not yield stable operating conditions, even with some modifications to minimize the influence of the discharge on the sample temperature. For such high vapor pressure materials we built a new low temperature evaporator (fig. 6) in which the sample is placed outside the source and the vapor is guided to the standard quartz gas feeding system through a long heated quartz capillary. Thus the source operation is very similar to that for normal gases with the supplementary condition that a minimum microwave power of around 200 W should be applied to the source to avoid condensation of the material in the front part of the feeding system.

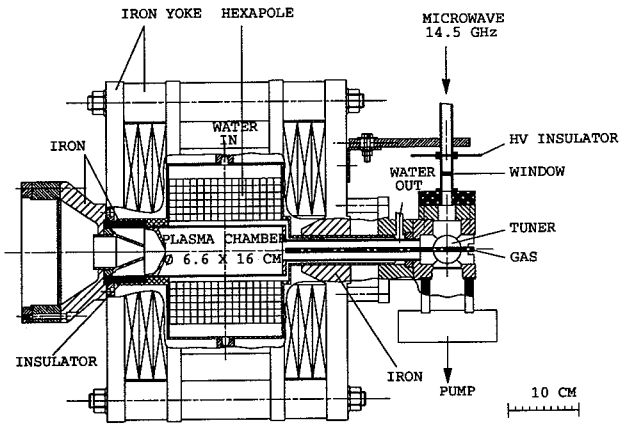

Figure 5: ECR ion source CAPRICE.

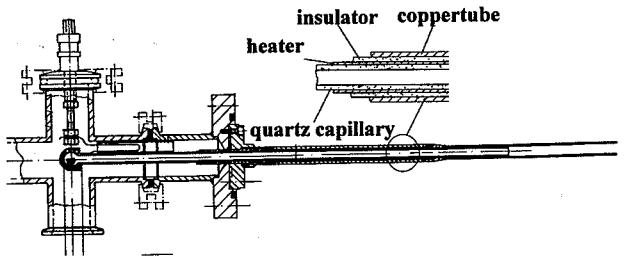

Figure 6: Evaporator for ECR ion source CAPRICE.

Comparison between test bench and injector beam line is not satisfactory. Therefore we are building an injector test bench, which will allow to transfer results to injector operation.

4 REFERENCES

[1] S.L. Bogomolov et.al., Rev. Sci. Instr., **67(3)**, 1996, 1381.

[2] U. Ratzinger, The new GSI pre-stripper LINAC for high current heavy beams, this proceedings.

[3] P. Spädtke et.al., Rev. Sci. Instr., **67(3)**, 1996, 1146.

[4] Ian G. Brown, Vacuum arc ion sources, Rev. Sci. Instrum. **65 (10)**, 1994.

[5] E. Oks et.al., Rev. Sci. Instrum. **65**, 1994, 3109.

[6] B.H. Wolf et.al., Rev. Sci. Instrum. **65**, 1994, 3091.

[7] C. Barué et.al., Rev. Sci. Instr., **67(3)**, 1996, 1368.

FEASIBILITY OF SHORT WAVELENGTH, SHORT PULSE LASER ION SOURCE FOR THE LHC INJECTOR

J. Wołowski[1], P. Parys[1], E. Woryna[1],
J. Krása[2], L. Láska[2], K. Mašek[2], K. Rohlena[2]

Abstract

Results of experimental investigations of characteristics of ion streams generated from laser plasma after focusing the laser beam either with an aspheric lens or with a parabolic mirror (allowing an observation of the ion emission in the direction of the target normal) are presented. The photodissociation iodine laser PERUN operating with $\lambda = 1.315\mu m$ and delivering energy up to $50J$ was exploited in the experiment. In this contribution we restricted ourselves to the results of ion emission measurements from $Ta-$, $Pb-$ and $Bi-$ plasma.

Introduction

Present studies of the emission of ions from the laser produced plasmas are mainly motivated by a growing interest in the physics of heavy ion accelerators. In the application of the laser plasma as a source of multiply charged heavy ions high current densities are required. From this viewpoint, as numerous experiments show, the laser plasma sources seem to be very promising. In comparison with the electron cyclotron resonance ion sources, which are employed for heavy ion injectors at present, higher current densities of highly charged ions are expected. Thus the charge state of ions, the ion velocity (or the ion energy) and the ion current density were the basic parameters of interest. However, it is evident that whilst the ECR sources are nowadays highly developed as far as their reliability and simplicity of operation is concerned, the laser sources still face major technological and even scientific problems.

PERUN Experiment and Results

Ion emission experiments were mainly performed with the photodissociation iodine laser system PERUN [1]. Ion collectors (IC), a cylindrical electrostatic energy analyzer (IEA) and a Thomson mass spectrometer (TS) were applied to monitoring the emission of the ions [2]. The ion species, their energy, abundance and/or velocity distribution were explored in dependence on the laser power density, focus setting with respect to the target surface and the changing the angle of observation. The collectors are based purely on the time-of-flight effect, the spectrometers combine time-of-flight with the action of electric or magnetic field on the ions. The collectors first separate the electron component and then they measure the ion current. The outcome is, however, influenced by the secondary emission, which is adding to the net current. Since the secondary emission coefficient, which is specific for any cathode material, may be energy and charge dependent, it introduces a certain degree of uncertainty in the results. This is the main source of error in the absolute estimates of the ion number. In the following it was assumed that for each ion charge unit impinging on the collector cathode one extra secondary electron is struck out.

The analyser devices use either an electric field alone to separate the ion species as in the IEA or the combined electric and magnetic field in the TS. The geometry of IEA is that of a cylindrical capacitor segment, where the radial electrostatic field separates the ions entering through a slit. The sensor is a vacuum windowless electron multiplier. An IEA requires a repetitive laser operation (typically 20 shots) to determine the charge energy spectrum.

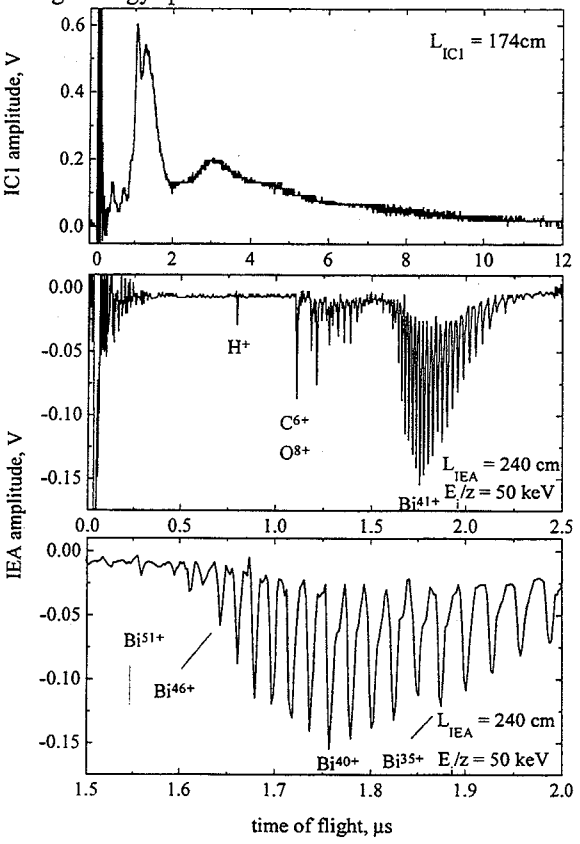

Figure 1: IC signals and IEA record of Bi.

TS renders the whole spectrum in a single shot, but the resolution power for highly charged species is poor. The output picture formed either on an ion sensitive foil or a multichannel plate is composed of a set of parabolas, each corresponding to a single value of e/m. Whereas for light elements like contaminants in the vacuum of the target chamber the parabolas are quite distinct,

the higher charges usually coalesce. In practice it is thus imperative to use an IEA to get a quantitative answer. However, if the recordings of the TA are processed numerically, in particular, a grid of precalculated parabolas is overlapped with the output the identification of ion groups is fast and convincing. Both the devices are difficult to calibrate absolutely, but placing a coaxial IC in the path of flight of an IEA makes an absolute calibration possible. Examples of ion collector signals and electrostatic analyser spectra for Bi is shown in Fig. 1. Two groups of ions (fast and thermal) are clearly discernable on the charge-integrated and time-resolved signal from an ion collector, which was located in a far expansion zone. The spectra in Fig. 1 clearly prove the existence of ions with charge states about 50+. We registered fully stripped Al, or nearly stripped Co and Ni, and ions with charge state higher than 48+ of heavy elements: Ta, W, Pt, Au, Pb and Bi. In principal, the mass-to-charge ratios, energies and abundance of the emitted ions can be determined from the spectra. The ions are not only generated, but also accelerated. The maximum energy of the ions increases with the laser power density. In our experiments with high-Z targets the highly ionized ions with energies up to several MeV were registered. Keeping in mind a two group electron model [3] the fast ion expansion velocity can be interpreted as a sound speed with the hot electron temperature.

Estimates of the ion current density and the number of ions with a given charge state produced during a single laser shot were performed by processing of the IC signal with the use of the data from IEA spectra. The total maximum ion current density attained $12mA/cm^2$ with lense and $\sim$ $22mA/cm^2$ $94cm$ from a Ta target (recalculated value according to r^2 law) using the parabolic mirror. An evaluation of the experimental data pointed out that about 30% of the ions of their total amount are in a high charge states (from 35+ to 45+). When recalculated to the number of the particles our measurements give thus at least 10^8 of ions in a single charge state within a single pulse lasting about $1\mu s$. The maximum values are observed in the direction of the normal to the target, as it follows from the measurements with the parabolic mirror. To obtain the entire ion energy distribution for a single value of the laser energy a series of measurements changing the analyzer voltage was made. As the measurements are fairly laborious and time consuming they were performed only for $Ta-$ ions, see [3].

Exploiting the theoretical considerations in [4-8] a dependence of the average charge state of ions on electron temperature was constructed, which is shown in Fig. 2. It is seen that an average charge state of Ta-ions 45 is attainable at an electron temperature of about $1.0 - 1.5keV$, while at the same temperature the average charge state of Au- and Bi-ions is 51 and 55, respectively. This corresponds to the electronic structure of the heavy ions, which unlike the neutral atoms tend to form a closed electron shell with 28 electron left (Ni-like ions). For a further ionization a fairly high potential barrier would have to be overcome. In this sense it is easier to achieve a higher ionization degree starting from heavier elements.

The generation of the ions in the laser plasma, as far as their charge states and numbers are concerned, is very sensitive to the position of the laser focus with respect to the target surface. The

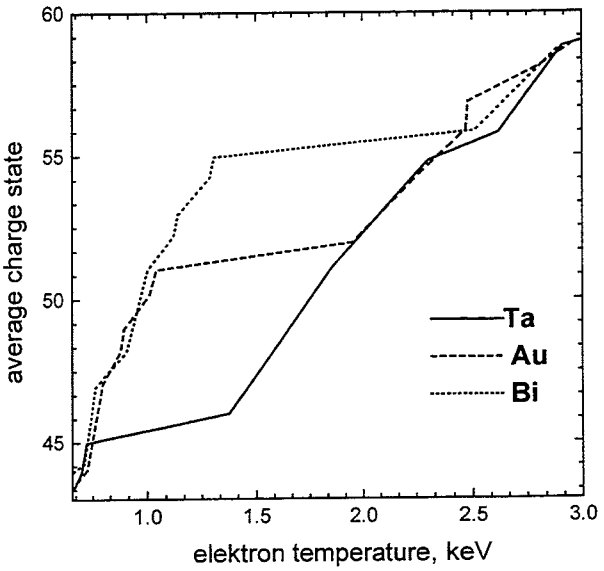

Figure 2: Calculated mean charge of Ta, Au and Bi dependent on the electron temperature

results of our studies of the effect of focus setting on the ion emission is summarized in Fig. 3. There is a position of the target lying behind the true focus (aim in front of the target surface), which is most favourable not only for generation of the highly ionized particles but also for attaining a maximum yield of the ions. Then it is most likely that the laser shots aimed repeatedly in the same point on the target surface deteriorate both the amount and the average charge state of the emitted ions. It was found that after the 3rd laser shot the plasma parameters are so changed that the energetic highly charged ions are missing and the total ion emission is much weaker.

Discussion and Conclusions

It is interesting to compare the requirements of an ideal LHC injection at CERN with the performance of the short pulsed lasers as potential ion source drivers. Since these lasers appear to be more costly and less practical then the CO_2 these drawbacks must be balanced by specific advantages offered by them. A principle advantage might well be skipping of the first stripper in the Linac line. Also the number of ions and the timing of their arrival should be such, as to allow for a single turn booster operation and possibly to avoid the use of LEAR (which would, however, be the purpose of any laser source). The requirements of CERN are summarized as follows:

For the lead ions experiment an ideal source should yield

$Pb45+$	$3.6mA$	$6\mu s$	$(= 3 \times 10^9$ ions)	$17.3keV/u$
$Pb54+$	$4.3mA$	$6\mu s$	$(= 3 \times 10^9$ ions)	$20.8keV/u$

In deriving these numbers it was assumed that the extraction voltage is set to $80kV$ and no stripper. This compares with the numbers obtained e.g. with the iodine laser using a Ta target

$Ta42+$	$22.8mAcm^{-2}$	$1\mu s$	$(= 10^8$ ions)	$12.7keV/u$

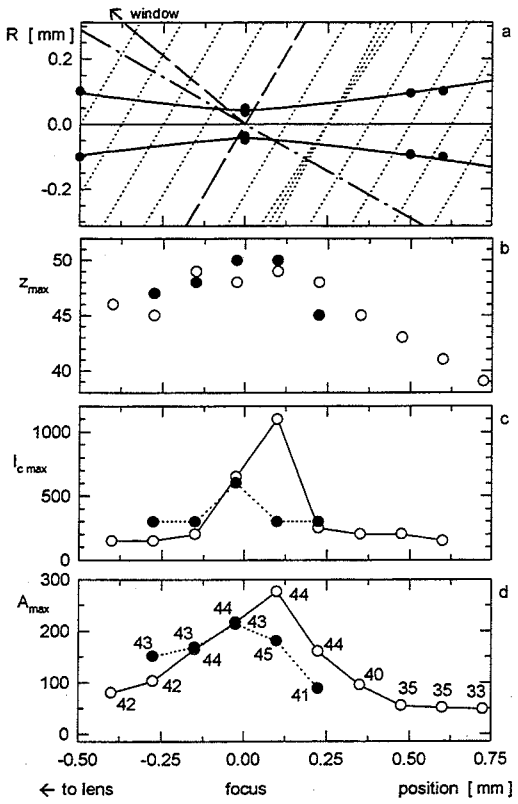

Figure 3: Dependence of the ion current and of the mean charge on the focus setting

In the last line the second number is the current density in the collector current maximum of the fast ion group (about 30% of the total) obtained with the mirror focus measured in reality by a coaxial IC $174cm$ from the target, but transformed using a quadratic law to a distance of $94cm$ (to make it compatible with the lens focusing). The fast group involves about 10 ion species and the pulse is short. Although the estimate of 10^8 ions available for the extraction is fairly conservative, it is difficult to see, how especially the pulse timing could be extended to the required $6\mu s$ tempering just at the laser. Looking at the charge-energy spectra a natural spreading of the pulse by the time-of-flight would dictate an intolerably long flying path.

A certain improvement might be expected resorting still to shorter wavelenght laser. Then there is a less acceleration and the energy spectrum is narrower. Equally a larger focus, while keeping the power density constant, might supply more ions, but at the cost of a disproportionate increase in the pulse energy, since not only the focus area grows, but also the pulse should be prolonged, see [1]. But it is unlikely that the timing of the pulse might be reconciled with the LHC injection demands without a major change in the subsequent acceleration regime,

Acknowledgements

This work was performed in a partial fullfilment of the grant *No A1010525* of the Grant Agency of Academy of Sciences of the Czech Republic and of the Czech Ministry of Education grant *KONTAKT ES008(1996)*.

References

[1] K. Rohlena et al., the preceding paper of this volume and the references ibid.

[2] S. Denus et al., J.Tech.Phys. 1825 (1977)

[3] L. Láska et al., Rev.Sci.Instrum. 67 950 (1996)

[4] M. E. Glinsky, Phys.Rev. 2(7) 2796 (1995)

[5] L. M. Wickens, J. E. Allen, J.Plasma Phys. 22 167 (1979)

[6] J. Farny, PhD Thesis, MUT Warsaw 1985

[7] I. V. Roudskoy, PhD Thesis, ITEP Moscow 1993

[8] M. Busquet, Phys.Rev.B52 2302 (1982)

ION EMISSION FROM HIGH-Z LASER PLASMAS

K. Rohlena[1], B. Králiková[1], L. Láska[1], K. Masek[1], M. Pfeifer[1], J. Skála[1], P. Straka[1],
J. Farny[2], J. Wolowski[2], E. Woryna[2], W. Mroz[3],
A. Golubev[4], B. Sharkov[4], A. Shumshurov[4],
H. Haseroth[5], H. Kugler[5], K. Langbein[5] and J. Tambini[5]
[1] Inst. Physics, Acad. Sci. Czech Rep., Prague;
[2] Inst. Plasma Physics and Laser Microfusion, Warsaw;
[3] Inst. Optoelectronics, MUT, Warsaw;
[4] Inst. Theoretical and Experimental Physics, Moscow;
[5] PS Division, CERN, Geneva

Abstract

The results of systematic studies of ion emission from plasmas generated in the focus of laser beams of short wavelengths, short pulse lasers (Nd:glass, 1 *ns*, 1060 *nm*; iodine, 0.5 *ns*, 1st harm.- 1315 *nm* 2nd harm.- 675 *nm*, 3rd harm.- 483 *nm*) are presented. The corpuscular diagnostics were based on (i) Thomson parabola spectrometer to display a general view of the ion spectra, (ii) cylindrical electrostatic ion energy analyzer to determine the detailed charge-energy ion spectra (iii) ion collectors to estimate the current density of the ion fluxes far from the focus. The ion current densities about 1 *m* from the focus are typically mA/cm^2. Fairly high charge state (>50+) and simultaneously energetic (>8 *MeV*) ions were registered. The results are interpreted either in term of a two-temperature model of the expanding plasma or by an ion emission from a dual focal spot including a hot primary focus and a colder peripheral zone.

Introduction

An expanding laser plasma is an efficient source of highly charged ions [1]. It is formed by focusing a nanosecond laser beam on a target. In the plasma corona an intense collisional ionization is going on. If the plasma is left to expand the phenomenon of charge freezing sets in. Due to the fast expansion the plasma is diluted before the recombination eradicates all the highly ionized ion species. Hence, at least part of the ions has a chance to conserve the charge state acquired in the hot plasma core and carry it at a considerable distance away from the focus. There, the ions can then be either registered by various sensors of particle diagnostics, such as ion collectors and ion analyzers (Thomson or electrostatic), or after a separation of electrons they can be transformed in an ion beam and introduced in a beam line of an accelerating system. In the following we shall concentrate, in particular, on the subnanosecond pulse laser in the near infrared region.

Laser drivers

The photodissociation iodine laser PERUN [2] in the Institute of Physics of AS CR in Prague is operating at the wavelength 1.315 μm, producing pulses of ~ 50 J, which are roughly 350-500 *ps* long and can be focused in a spot size (lens optics) of 80 μm . The average power density attainable on the target is thus ~ 10^{15} Wcm^{-2}. Frequency conversion by DKDP crystals to 2ω and 3ω is available with about 50% efficiency. The target chamber was fitted either with an aspherical f/2 (f = 20 *cm*) lens or alternatively, with a mirror (f = 28.5 *cm*) having a 12 *mm* hole in the centre to allow access to the part of the plasma expanding directly against the laser beam. The mirror focal spot is somewhat larger (~ 100 μm) than with the lens focus.

The Nd:glass laser in the Institute of Plasma Physics and Laser Microfusion in Warsaw gives at maximum 15 *J* at 1.06 μm in 1 *ns* pulses. The spot size with lens optics is about 100 μm with a power density on the target < 6 x 10^{13} Wcm^{-2}. Besides the aspherical focusing lens a combination of a lens with an ellipsoidal mirror with a central hole was used.

The CO_2 Lumonics TEA 601 laser [3] gives 50 *J* in a 50 - 70 *ns* pulse. The power density on the target is ~ 2 x 10^{12} Wcm^{-2}. Focusing is with a parabolic mirror f = 30 *cm* with a hole of 30 *mm*.

The CO_2 TIR-1 system at Troitsk [4] delivers about 100 *J* in either 25 *ns* or 2.5 *ns* pulses. The focusing system using a parabolic mirror f = 60 *cm* with a hole of 25 *mm* achieves the power density on the target either ~ 4 x 10^{13} Wcm^{-2} or ~ 6 x 10^{14} Wcm^{-2}.

At this stage of development the potential performance of laser ion source is synonymous with the results of particle diagnostics of the expanding laser plasma. None of the near infrared lasers used has an adjoint LEBT line or an RFQ to assess directly the quality of the preaccelerated ion beam. Nevertheless, the charge-energy spectra of the expanding laser plasma allow for qualified estimates of at least some properties of the ion beam derived from such a plasma.

Results

The collector signal usually indicates several ion groups, which are separated by the time-of-flight effect. The highest charge is carried by the fastest group, to which the following table relates. It presents the results obtained with the first

harmonics of the iodine PERUN system for various elements. The geometry of the measurements was either a coaxial one using a mirror (M) or the measurements were off the axis using a lens (L) focus.

Table 1. was compiled by uniting the data of IC measurements in two different distances from the focus. In the case of lens focus the IC collector was 94 *cm* from the focus, with the mirror the distance of a coaxial IC was 174 *cm*. The current densities are the peak values of the fast ion signal, recalculated in each case to the shorter distance of 94 *cm* using a quadratic law. The values for the mirror case are thus estimated fairly conservatively, [5].

Table 1

Elem.	$< z_{fast} >$	$< E_{fast} >$ [*keV/u*]	$j[mAcm^{-2}]$
Co (M)	22 (25)	32.7	14.2
Ni (M)	20 (26)	15.7	18.5
Cu (L)	(25)		
Ta (L)	(55)		12.8
Ta (M)	42 (48)	12.7	22.8
W (M)	45 (49)	10.9	22.8
Pt (M)	45 (50)	15.9	12.8
Au (M)	38 (49)	15.7	7.0
Pb (M)	40 (51)	15.9	8.5
Bi (M)	40 (51)	12.9	10.0

It would seem that the sharper focus for the lens case yields higher maximum charge numbers (values in parentheses second column) and that the higher currents are emitted from the larger mirror foci. In reality, the dependence of the ion current as well as of the maximum charge number on the power density and on the size of the focal spot are not trivial and are different in character. It is more likely that the differences between the mirror and lens geometry are given by the directional characteristics of the ion emission. When defocusing the dependence of the current has a sharp peak for the maximum power density, whilst the maximum charge number changes just slowly. This has implications, for instance, for the quality of the target surface, in particular, when placing several shots in the same spot and a crater is formed, [6].

The results are to be understood in the following way: the plasma is formed by a short intense pulse, in its hot core the electron temperature is exceeding 1 *keV* and the system is essentially in a thermal equilibrium. The highly charged ions are born in the core by an intense collisional ionization. During the expansion stage the electron temperature is falling fast, because also the laser power in the case of the short pulse goes down quickly. Not even the recombination heating can maintain the temperature on a steady level. The temperature is decreasing when the ions are still passing through a comparatively dense region. Owing to the temperature drop, the recombination sets in. The high charge states will thus be destroyed before the system is (due to the fast expansion) out of the thermodynamic equilibrium and the high charge states have been "frozen in". Especially vulnerable are the high z ions. This scenario applies to the thermal ion group, which follows the fast group and is carrying charge states, which are generally lower.

The existence of the fast group is pointing to an accelerated expansion mechanism. Such a mechanism is triggered by a group of superthermal (hot) electrons which originate from a non-dissipative laser energy deposition in the plasma. A part of the primary laser energy is transformed in electrostatic plasma waves, which accelerate the plasma electrons by the mechanism of inverted Landau damping. The resulting hot electron population is guiding the fast plasma expansion contributing thus to a survival of highly charged species.

From what has been said it is clear that an ideal laser driver should provide both the fast plasma ionization to attain as high charge state as possible and also a fast expansion to conserve the charge once formed in the core by suppressing the recombination during the expansion stage. These two requirements are difficult to meet at once. The ionization rate is mainly controlled by the electron density in the vicinity of the critical surface in the plasma, i.e. the density surface where the electron plasma frequency equals the laser frequency, $\omega_L = \omega_{ec}$,

$$n_{ec} = \omega_L^2 \frac{m}{4\pi e^2} \qquad (1)$$

beyond which the laser radiation cannot penetrate (n_{ec} is the critical electron number density, e is the elementary charge and m is the electron mass). Another factor determining the maximum attainable ionization degree is the time available for the ionization process. It is either equal to the characteristic hydrodynamic build-up time τ_{hydr} of the plasma plume, which is also the residence time of an ion inside the hot plasma core

$$\tau_{hydr} = R_{spot} / C_s \,, \quad C_s = \sqrt{\frac{< z > (n_{th} + n_h)}{M(n_{th} / T_{th} + n_h / T_h)}} \,, \qquad (2)$$

or to the laser pulse time, τ_L , which one happens to be shorter (n_{th}, n_h, $n_e = n_{th} + n_h$, and T_{th}, T_h are the number densities and temperatures of thermal and hot electron population, R_{spot} is the focal radius, M is the ion mass, C_s is the ion acoustic velocity and $< z >$ is the mean charge).
For a well tuned laser the hydrodynamic time should thus be shorter or equal to the laser pulse duration,

$$\tau_{hydr} \leq \tau_L \qquad (3)$$

to use the ionization process to a full advantage [7].

Conclusion - comparison of various lasers

In the previous sections mainly the performance of the iodine laser was being assessed, in the following we shall use the same criteria for the other types of laser driver. Since the frequency conversion changes the wavelength, the iodine

laser with a beam converted to higher harmonics (2ω and 3ω) will be considered as separate cases.

CO_2 drivers: The CO_2 lasers are an obvious choice for their high repetition rate and commercial availability. They also have usually a long pulse, meeting thus the criterion (3). However, owing to a long wavelengths (10.6 μm) the critical density (1) is too low and the ionization is slow. The highest attainable ionization degree is thus lower than that of the short wavelength lasers. Moreover, the focusability of the beam is usually bad, which reduces the power density on the target. Also, the pulse tends to have a fairly long "ramp", containing a non-negligible portion of the total energy, which induces low temperature phenomena on the target like digging an outsized crater and a splutter of the target material.

Nd:glass laser performance is not, in principle, different from that of iodine, it has a slightly longer pulse, which is a favourable feature, the energy is less controllable. A repetitive action is more difficult to implement, because of a heat build-up in the glass, but a future diode pumping might solve the problem.

Converted iodine 2ω, 3ω is giving about the same results as 1ω , but with less acceleration. Clearly, the fast expansion phase is missing, the hot electrons are absent. This means that in the hot plasma core, which is considerably more dense than in the case of 1ω , see (1), much higher charge states are formed, which only partially recombine during the expansion. A second maximum of very slow ions, which sometimes appears on the collector signal, is likely caused by an emission from a peripheral part of the focus, which is heated by an intense x-ray radiation of the primary plasma. A direct experimental prove of the existence of very highly ionized species in the focal spot created by the blue 3ω beam is, unfortunately, still missing, though the calculations seem to point in this direction.

An extrapolation towards still shorter wavelength points out that the use of excimer lasers (such as *KrF*) in the ultraviolet range should be given a serious thought. These lasers are technically related to CO_2 , are easy to operate in a repetitive regime and the deposition of laser energy in the plasma is very high. There are however difficulties with controlling the pulse shape, especially in the nanosecond range, but at least in a single pulse regime the ways of circumventing them are known.

A repetitive action is neither easy to implement in the case of iodine lasers. Though the sealed-off systems are known to operate with the frequency nearly 1 *Hz* at about 70 *J* of energy [8], the operation is in the free running regime and the pulse is thus far from being in the nanosecond range. There should be, in principle, no difficulties in changing the generation regime to obtain a subnanosecond pulse with the same rep rate, but this would mean to sacrifice a part of the energy. A serious obstacle is also the cost of such a would-be instrument, which might lie anywhere between 300 and 1000 k$ (US) .

Acknowledgements

This work was performed in a partial fullfilment of the grant *No 202/95/0039* of the Grant Agency of the Czech Republic and of the Czech Ministry of Education grant *KONTAKT ES008(1996).*

References

[1] H.Haseroth, H.Hora in "New Methods and Technologies", Chapter IV, Advances of Accelerator Physics and Technologies, Singapore, World Scientific, Singapore, Ed. E. Schopper, 466 (1993)
[2] M. Chvojka et al., Czech. J. Phys., 42, 899 (1992)
[3] R. Sherwood et al., "CERN Laser Ion Source Technical Meeting", CERN, 25th May 1994: J. Tambini, 4th WILA'95, Trest Castle, Proc. SPIE, Vol. 2762, 70 (1995)
[4] S.M. Kozikhin et al., Kurchatov Inst. Rep. IAE-5635/7, Moscow (1993)
[5] K. Roklena et al., BEAMS '96, Prague, (1996)
[6] J. Wolowski et al., "Feasability of short wavelength, short pulse laser ion source for the LHC injector", the following paper of this volume, see further citations, ibid
[7] J. Farny et al., to be published
[8] L.A. Schlie, 4th WILA'95, Trest Castle, Proc. SPIE, Vol. 2762, 28 (1995)

SMOOTH ION ENERGY TUNING IN LINEAR ACCELERATOR

A.Shalnov, B.Bogdanovich, A.Nesterovich
MEPhI, Moscow, Russia

Abstract

This paper presents the results of experimental research of energy variable proton linac, which consists of independently driven one-gap accelerating cavities. Cavity design proposed by authors seems to be optimal for high values of energy gain and beam current. A multichanel accelerating structure allows to accelerate several ion beams. Beam focusing is accomplished by means of electrostatic quadruples with variable potential, which is chosen from the viewpoint of maximum beam transit factor for each operation mode, determined by output energy. The other energy variable accelerating structures with operating frequency changing are also under consideration.

The modern stage of accelerator engineering development in Russia is characterized by a peculiar combination of the requirements to expansion function opportunities radiation installations and their efficiency increase with decrease of material inputs on their creation and exploitation. In the ion accelerators area to number of such problems it is possible to relate creation of complexes, capable to receive beams with any by given energy from a zero up to maximum and ensuring thus transfer to ions reasonably large (up to several tens percent) part of RF energy from a generator.

This problem not decided so far due to problems of practical realization. The last were connected mainly to absence of the constructive decisions enabling to supply high energy gain in a meter range (i.e. ions accelerators range), that is significant longitudinal sizes of resonators at a limited potential gradient, stipulated with breakdown significance on a small accelerating gap.

The accelerator block diagram of which is indicated on fig.1. By the authors was offered as the main accelerating element of installation to use a polyaxial resonator (PR). Ones formed from a known cylindrical resonator with wide aperture drift tube by its installation on the end face of a disk with a diameter close to size of a resonator cylindrical wall. On fig. 1 are entered following reviews: 1 - ions injector, 2 - PR, 3 - RF feed system specifying generator, 4 - phase shifters, 5 - RF amplifiers, 6 - electrodes of a electrostatic focusing system, 7 - magnetic analyzer, 8, 9 - ions beam collectors, 10 - variable resistance of a power supply system of the electrodes 6, 11 - beam slot-hole collimating system. Given scheme has basic character and does not exclude a opportunity of phase adjustment in a most specifying generator, or directly in accelerating cascades. As well as variant of discrete phase change at the expense of replacement wave cable with fixed electric length. The length determine the phases difference on the generator 3 output and each particular resonator.

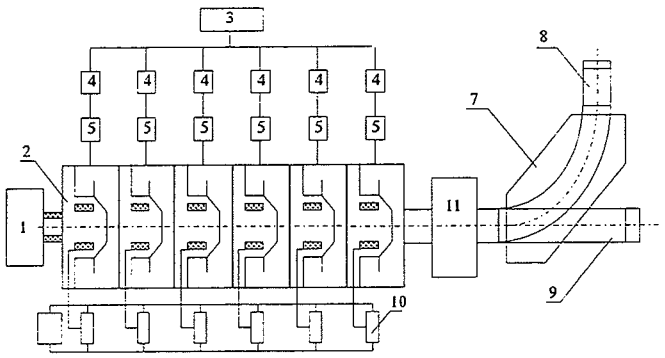

Fig.1. The accelerator block diagram.

The schematic drawing of a structure in two projections is shown on fig. 2. On a drawing are indicated: 1 - resonator cylindrical wall, forming a vacuum chamber, 2, 3 - resonator face wall, 4 - drift tube, 5 - disk, 6 - drift tube face cover, 7 - dielectric electrodes 8 holders of electrostatic focusing system, 9 - electrodes 8 potentials input, 10 - loop of a RF capacity level measurer, 11 - power input from a generator, 12 - pump system vacuum collector, 13 - frequency adjustment element, 14 - drift aperture. The drift tube cover 6 and disk 5 are replaceable, that permits by a way on selection of these elements with the various sizes to adjust resonant frequency of resonators in small limits, that it is convenient on stage of accelerator start. The focusing system electrodes fix on a plate with a opportunity them tuning on mandrils. The diametrical sizes of a drift tube internal cavity admit accommodation of a focusing system for several channels located on circles by some centimeters diameter. Accelerating structure pump carried out through cylindrical collectors, connected to nonoil pumps. Ones provided vacuum in a structure better then $3 \cdot 10^{-6}$ Torr. Tuning is executed with help of the laser beam and mandrils.

Diameter of a sicumference channels centers circle in spent experiments makes 6 sm. The resonator loaded quality equals ~700, coupling factor ~2, own quality ~2000. Arriving to the resonator power was defined as differences by the dropping and reflected waves power. The shunt resistance significance was determined by the power spectrum comparison of a simulating electron beam (instead of ions were injected electrons with energy ~40 keV). Dependence based on the accelerated electrons energy maximum and appropriate entered power level in view of the previous changes allowed to estimate shunt resistance significance. Within the measurements accuracy limits of 10% it has made 80 kOm.

The proton acceleration in an energy adjustment mode for the account of appropriate resonators phasing was executed after preliminary selection of transportation optimum conditions in a electrostatic quadruple lenses system. Thus in each of quadruples one electrodes pair of

opposite transportation channel was ground and second was under positive or negative potential.

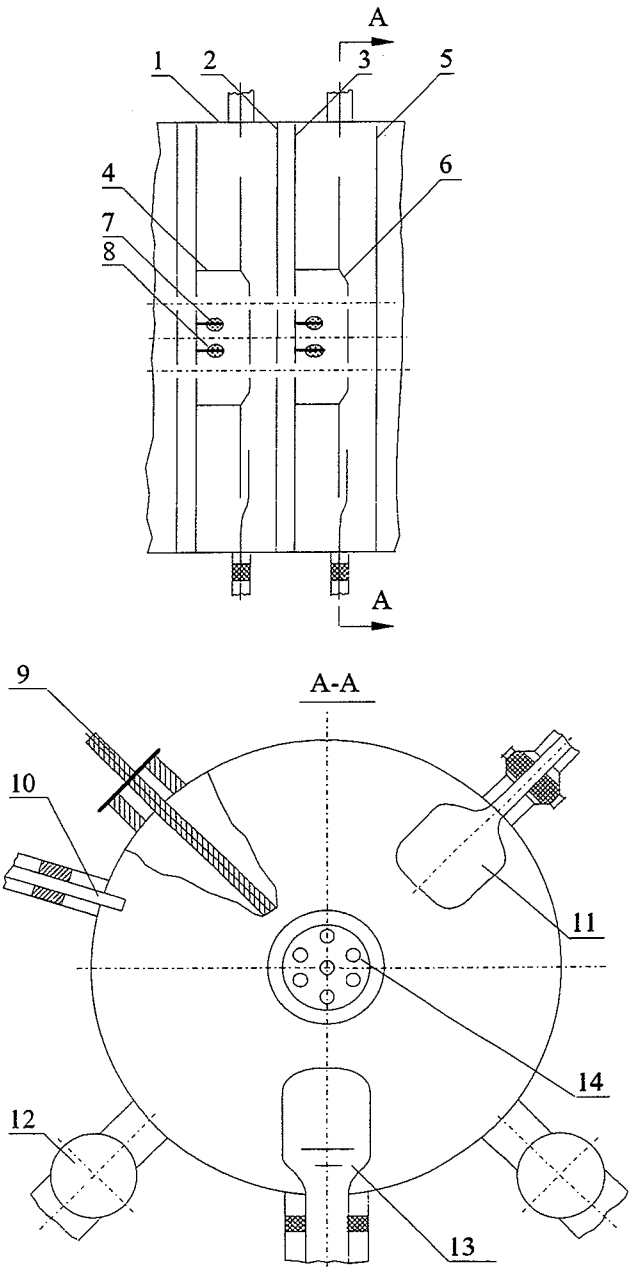

Fig.2. The accelerator structure schematic drawing.

At the power level in one resonator 40 kW the energy gain in it reached up to 56 keV. On fig. 3, 4 experimental dependencies of a current in magnet winds (power spectra analogue) are submitted. Ones removed for various RF fields phases significance in first and third resonators (in second - the RF power was not entered). As well as for a various RF power level at its division equally on the general accelerator cascade output by means of phase shifter bridge scheme. As it is visible from these drawings given regime of proton output energy smooth adjustment is realized in complete volume.

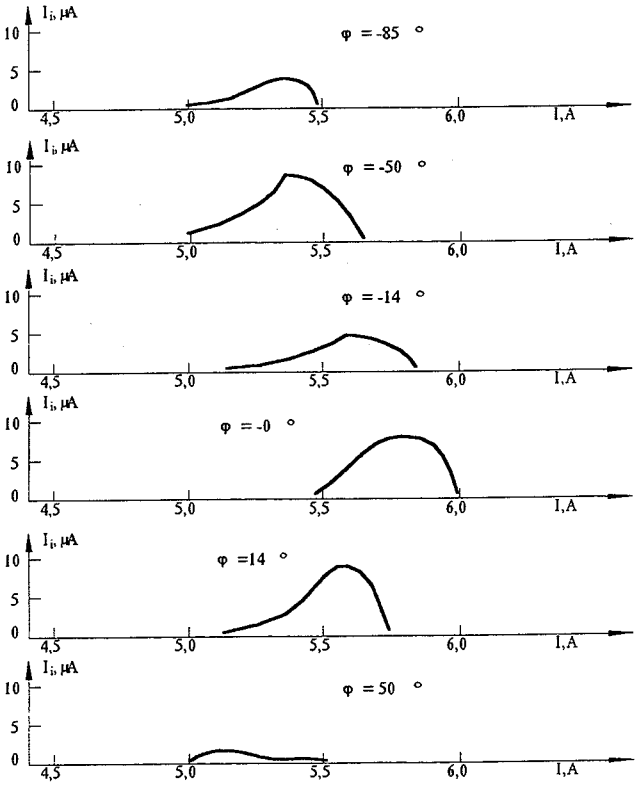

Fig.3. The dependencies of proton current from the current in magnet winds for various RF fields phases significance (P/2=17 kW).

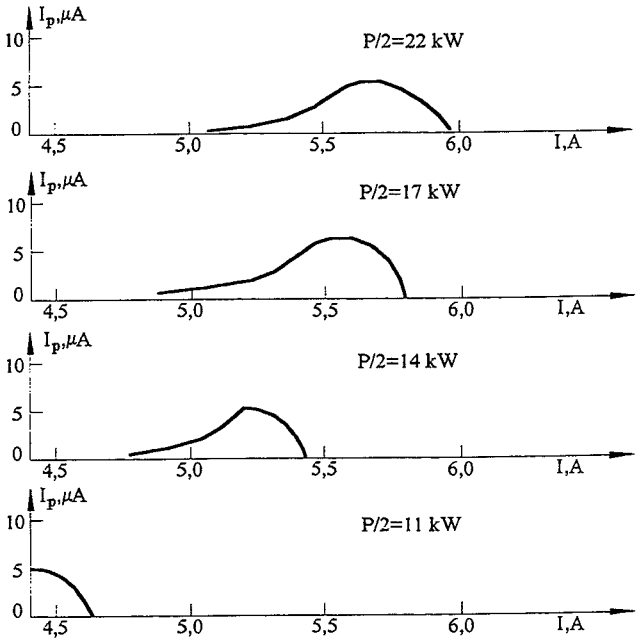

Fig.4. The dependencies of proton current from the current in magnet winds for various RF power levels (φ=-40°).

The realization simultaneous phase and peak regulation provides the task opportunity of any change law of

RF fields accelerating harmonic phase speed along system length. That it is necessary for particles acceleration in the high energy fields. It means that the accelerators on all energy (up to relative) can be executed on the basis of identical single gap resonators optimized under the form and sizes from a point of view of power walls losses minimization, that is efficiency increase. Besides fall away necessity of transition to higher frequencies. That is increase a ions capture factor at the expense of losses absence on transition sites. As well as simplifies RF system as a whole. Besides a new functional opportunity of acceleration in the same acceleration complex of a various type ions is opened. In particular, in a considered structure it is possible deuterons acceleration. For transition to heavier ions can be recommended PR with several disks installed on drift tube and external wall.

Use of a double gap resonators sequence in the kind quarter wave vibrator with drift tube is represented reasonably effective also. Thus the each resonator frequency is determined by a situation relocatable short piston in the vibrator basis. The ions flight time between backlashes can be adjusted in potential of electrode, located in each tube.

BEAM LOADING EFFECTS IN LINACS WITH RESONANT LOADED RF-POWER UPGRADE SYSTEM.

A.Shalnov, B.Bogdanovich, A.Ignatyev and V.Senyukov
MEPhI, Moscow, Russia

Abstract

The RF power upgrade systems with microwave energy compression are using for accelerating wave power increase [1-3]. The energy compression systems (ECS) with a resonant loading present the certain interest for practical use because of their specific properties [4]. They are capable to increase an accelerating wave power up to 50...100 times (up to 20 dB) and keeps this wave in accelerating structure for a longer time then conventional ECS. The resonant load is an essential part of the system and renders influence significantly on its parameters. The system consists of two connected resonators, one of which is using as a storing element and the second — as a load. Load may be a standing or a traveling wave resonator (TWR) formed by accelerating structure. Beam loading effects would change the properties of RF field in the load resonator. ECS characteristics and the accelerated beam parameters are discussed.

Introduction

The main principle of the system with resonant loading operation is based on using connected resonators [4]. Wave emitted from storing cavities (SC) pass through TWR (see Fig. 1) and becomes incident wave for SC. The resultant wave amplitude at the accelerator structure is equal sum amplitudes of those waves. This process continues while all energy primarily stored in SC passes by terns to TWR. So it causes significant field increase at accelerating structure.

Schematic drawing of the ECS with resonant load is submitted on Fig.1. Accelerating structure input and output

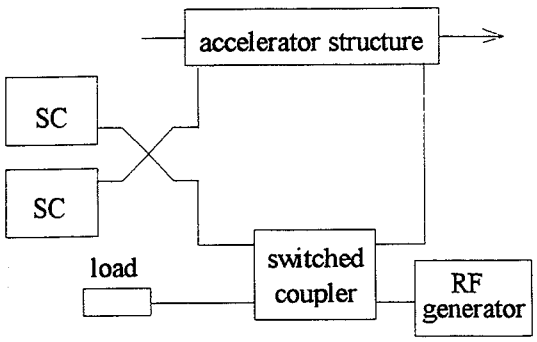

Fig. 1. Microwave energy compression system with a resonant load.

connect through switched coupler and SC and form the TWR. The switched coupler transfers the system operation mode from storing energy to its use. During the energy storing period (state A) the coupler connects generator output to storing cavities and the acceleration structure output — to an absorbing load. To use the stored energy (state B) the coupler is switched in such way that the acceleration structure output becomes connected to storing cavities, forming TWR.

At state A (see Fig. 2) energy storage occurs in SC. The wave, reflected from storing resonators, passes through a TWR and arrives in a load. When the energy storing process ends the coupler transformed in state B. The wave coming to SC is a wave leaving from accelerating structure. A wave phase shift in a TWR is chosen so that the wave coming on SC has the same phase as the wave emitted from it. Amplitude of a wave circulating in TWR ring will grow so long as all accumulated in SC energy will not pass completely in TWR. After this the return swapping of energy from TWR to SC will begin. The qualitative graph of the circulating in TWR wave average amplitude variations is shown on Fig. 2.

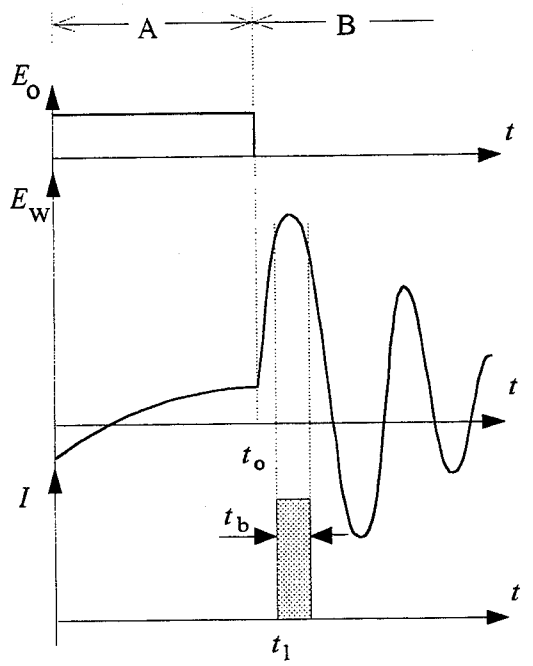

Fig. 2. The RF wave average amplitude variations in a system with a resonant load (E_o - generator wave amplitude; E_w - wave in TWR ring; I - beam current).

Theory

Traveling wave resonator is forming at the end of storage period (at moment t_0) by the switched coupler. RF generator is connected with an absorbing load and accelerating section output — with storing cavities. The wave, emitted from the SR, is added to a wave circling in the TWR. In this case the amplitude of a summarized wave at the

acceleration structure entrance during the energy use period is described by a following expression [4]:

$$E_w(t)=\begin{cases}(-\frac{2\beta}{1-\beta}(1-e^{-t/\tau})+1)E_0\ , & \text{for } 0\le t<t_0\\ \sum\limits_{n=0}^{N}E_{wn}(t)\ , & \text{for } t\ge t_0\end{cases} \quad (1)$$

where:

$$E_{wn}(t)=-\frac{2\beta}{1+\beta}E_0(1-e^{-\frac{t_0}{\tau}})e^{-n\alpha}e^{-\frac{t-t_0-T}{\tau}}F(-n,1,A)$$

$$F(-n,1,A)=\sum_{k=0}^{n}\frac{C_n^k}{k!}(-1)^nA^n\ ;A=\frac{2\beta}{1+\beta}\cdot\frac{t-t_0-nT}{\tau}$$

$N=[(t-t_0)/T]$ - number of wave revolutions in TWR, T - time duration of one turn-over of a wave in a TWR.

For function $F(-n, 1, A)$ evaluation one can use formula:

$$F(-(n+1),1,x)=\frac{2n+1-x}{n+1}F(-n,1,x)-\frac{n}{n+1}F(-(n-1),1,x)$$

where $F(0, 1, A) = 1$ and $F(-1, 1, A) = 1-A$.

The expression (1) describes microwave amplitude at accelerating section without current loading. Coupling factor β depends on the storing energy duration period t_0.

In case, when the current loading appears essential, it is necessary to take into account changes of wave amplitude falling on cavities. Using principle of independence of fields, it is possible to consider that two waves exist: one wave is connected with RF energy in SC, second — will be formed by electron beam. The expression for field amplitude of the beam radiation wave at any point of accelerating section with coordinate z, has a kind:

$$E_b(t)=\begin{cases}-IR(1-e^{-\alpha z})+\sum\limits_{n=0}^{N}E_{bn}(t-t_1-\frac{z}{v})e^{-\alpha z}, & \\ \qquad\qquad\qquad\qquad \text{for } t>t_1+T & (2)\\ -IR(1-e^{-\alpha vt}), \qquad \text{for } t-t_1\le T & \end{cases}$$

Where designations are used:

$$E_{bn}(t)=\frac{2\beta}{1+\beta}E_1e^{-(n-1)\alpha l}e^{-\frac{t-nT}{\tau}}\sum_{i=0}^{n-1}(1-\frac{2\beta}{1+\beta})^i\times$$

$$\times F(-(n-1-i),1,\frac{2\beta}{1+\beta}\frac{1-nT}{\tau})+(1-\frac{2\beta}{1+\beta})^nE_1e^{-(n-1)\alpha l}$$

$E_1=-IR(1-e^{-\alpha l})$, I - beam current, R - shunt impedance of accelerating section, v - group velocity of accelerated wave, t_1 - beam injection moment, l - accelerator structure length.

The resulting amplitude of a high-frequency wave at accelerating section input is determined by addition of two waves E_w (t) and E_b (t):

$$E(t)=E_w(t)+E_b(t) \quad (3)$$

Analytical expression of beam energy is enough difficult problem. For this reason the determination of beam energy of linear accelerator was carried out in numerical kind by using formula:

$$W_b(t)=\int_0^l(E_w(t-t_0-\frac{z}{v})+E_b(t-t_1-\frac{z}{v}))e^{-\alpha z}dz \quad (4)$$

ESC with resonant loading give increased amplitude RF wave on extent several turn-overs of a wave on TWR. So it can receive much longer pulses of an accelerated beam in comparison with other type compression systems. For example, we have obtained RF pulses with 15...17 dB multiplication factor and about 0.5 μs pulse duration for accelerating section filling time about 24...40 ns [4]. The electric field is considerably changed in time at accelerating section at one turn-over period. However, it does not result in increase of beam energy spectrum. It is possible to assume, that stored in traveling wave resonator energy is almost in accelerating section. So the beam energy is close to constant during one turn-over period.

Calculation results

Calculation was made for following parameters of ESC and accelerating section: power of the generator output P_0 = 10 MW, Q-factor Q_0= $90\cdot10^3$, shunt impedance of accelerating section R = 40 MOm/m, t_0 = 2.5 μs, power decrease per unit of acceleration section α = 0.04 and 0.08 m^{-1}, accelerator section feeling time T = 40 and 60 ns.

To achieve maximum beam energy it is need choice coupling factor β for an energy storage period t_0. Dependencies of maximum value E_w/E_0 and optimum coupling factor β are shown on Fig. 3.

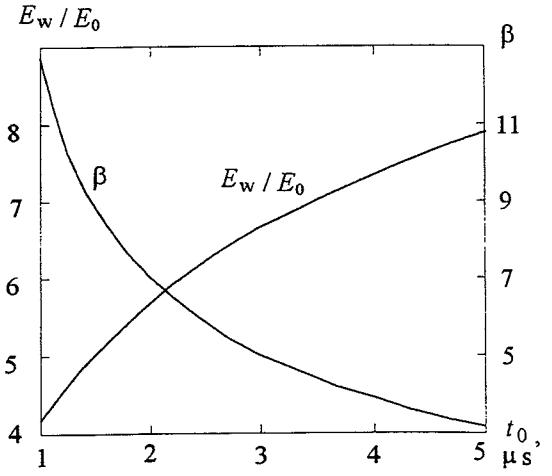

Fig. 3. Dependence of maximum averaged wave amplitude at an accelerating structure entrance E_w/E_0 and coupling factor β on an energy storage period t_0 (T=40 ns).

The accelerator beam energy W_b (normalized to W_0 - accelerator energy without any ECS) depend upon time t as shown at Fig. 4. Width electron energy spectrum remains practically constant ($\Delta W_1 \approx \Delta W_2$) for current values from 0 up to 1.5...2 A. At given current pulse of beam duration t_b the influence of a beam loading has an effect on average energy of particles. The maximum beam energy with minimum spectrum width can be achieved by appropriate choice of an

injection moment t_1. Spectrum width less then 3...5% can be obtained for current pulse about $t_b \leq 2.3T$ for pulse current values up to 2 A.

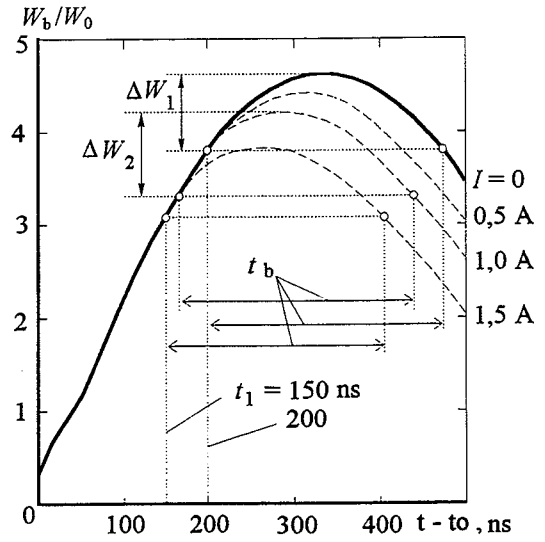

Fig. 4. Dependence of beam energy W/W_0 at output accelerating structure from time $t - t_0$ (T=60 ns).

The typical beam energy dependence from accelerating structure length l at output TWR accelerating section is shown in Fig. 5.

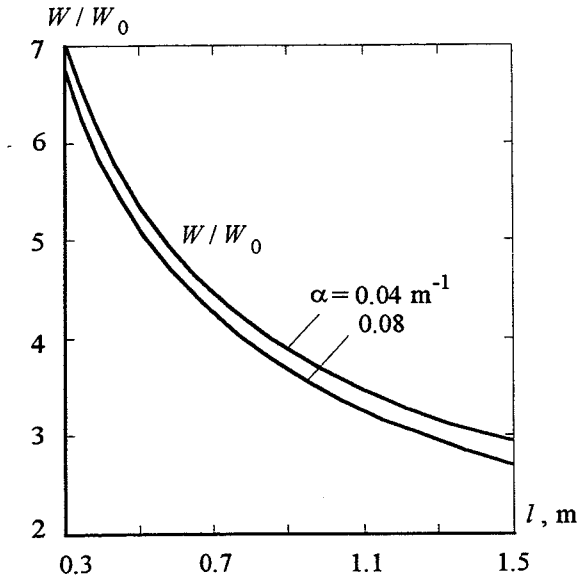

Fig. 5. Dependence of maximum accelerator energy from accelerating structure length l (T=40 ns).

The normalized energy W/W_0 of accelerated beam grows with reduction of length accelerating section (filling time of accelerating section is proportional to its length). Absolute value of beam energy appears higher for longer sections. Therefore to achieve higher energy long accelerating of section should be apply.

References

[1] Farkas Z.D., Hogg H.A., Loew G.A., Wilson P.B. SLED: A Method of Doubling SLAC's Energy, - Proc. of the 9th Int. Conf. on High Energy Accelerators, 1974, SLAC, pp.576-583.

[2] Bogdanovich B.Yu., Ignatyev A.P., Senyukov V.A. RF Pulses with Flat Output Generation in RF Power Upgrade Systems. - Particle Accelerators Conf. San Francisco, California, 6-9 May 1991.

[3] Shalnov A., Bogdanovich B., Senyukov V. RF-Energy Compression Systems for Electron Linacs. - Particle Accelerators Conf. (PAC'95) Dallas, USA, May 1-5, 1995. Bulletin of the American Physical Society, May 1995, Vol.40, **3**, p.1106.

[4] Shalnov A., Bogdanovich B., Ignatyev A., Senyukov V. RF-Energy Compression System with Resonant Loading. - Particle Accelerators Conf. (PAC'95) Dallas, USA, May 1-5, 1995. Bulletin of the American Physical Society, May 1995, Vol.40, **3**, p.1106.

RF-FIELD GENERATION IN WIDE FREQUENCY RANGE BY ELECTRON BEAM

B. Bogdanovich, A.Nesterovich, S.Minaev
MEPhI, Moscow, Russia

Abstract

A simple device for generating powerful RF oscillations in the frequency range of 100-250 MHz is considered. The two-gaps cavity is based on the quarter-wavelength coaxial line loaded by drift tubes. Frequency tuning is accomplished by using the movable shorting plunger. A permanent electron beam being modulated at the first gap return the energy at the second one. The additional tube with the permanent decelerating potential, introduced into the main drift tube, allows to decrease the drift tube length and keep the excitation conditions in frequency tuning. Both autogeneration and amplification modes are under consideration. RF-parameters of the cavity and experimental results are described.

At present there is a number of scientific and applied problems, for the decision of which it is necessary to have RF generator with power up to hundreds kW with smooth adjustment of frequency in a wide range. At the same time, made and used the powerful lamp generating devices are allowed rebuilding up to by several percents. As far as the frequency change in wider range requires agreed rebuilding of several resonant contours of amplification cascades. Conventional klystron and magnetron devices not allowed significant rebuilding owing to specific character of a volumetric resonators design. Generating devices on TWT base can not supply required exit power value.

To ensure a condition of beam resonance interaction with RF structure in a wide range of wave length it is possible by changing system period or electron speed. However, it is practically impossible to change RF structure space charge by virtue of the constructive reasons. On the other hand, it is required a relative electron beam with energy ~100 keV for high-power reception. The speed of one makes size ~0,5·c. The speed reduction, for example, in two times would result in this case in injection beam essential loss. Other the discussed scheme defect is a large RF system period length: at the electron energy 100 keV and wave length 2 m the period will make 1 m. That will cause to excessive general accelerator length growth and efficiency fall. Besides the injection energy change can ensure synchronism maintenance at frequency rebuilding only on an initial structure site.

That to minimize installation dimensions and to ensure electron beam resonant interaction with a resonator in wide range of wave length scheme with electrical adjustment of a structure effective length is offered. This scheme is based on system with drift tubes. Inside ones are coaxial located additional isolated tubes, those are under electrons slowing down (or accelerating) constant potential. Thus the electrons speed inside tubes can vary depending on value and sign of potential. It enables to support synchronism at frequency rebuilding and constant injection energy.

As the first section of a generating device based on these principles is developed double-gap buncher resonator with drift tubes. One capable to work as in a mode of self-excitation (that is independent generation) and as a buncher with independent excitation. In the self-excitation mode the electron beam receives modulation on energy in a first backlash, is grouped in drift tube and gives back energy (brake) in the second backlash. Distance between backlashes centers is 200 mm. Thus on frequency 150 MHz electrons with relative speed β=0,5 past first backlash in optimum group phase ($\varphi_1=-\pi/2$ in cosine readout) and fall in the second backlash in a phase $\varphi_2=-\pi/2+\pi$, that is close to the slowing down half-wave top. With frequency increasing the significance φ_2 is increased and for preservation of self-excitation optimum conditions it is necessary to submit breaking potential on internal tube or to reduce injection energy. Self-excitation conditions on high frequencies are possible also at multiple flight corners. For example, $5\pi/4$.

The developed resonator design is schematic submitted on fig. 1. Resonator contain vacuum jacet 1

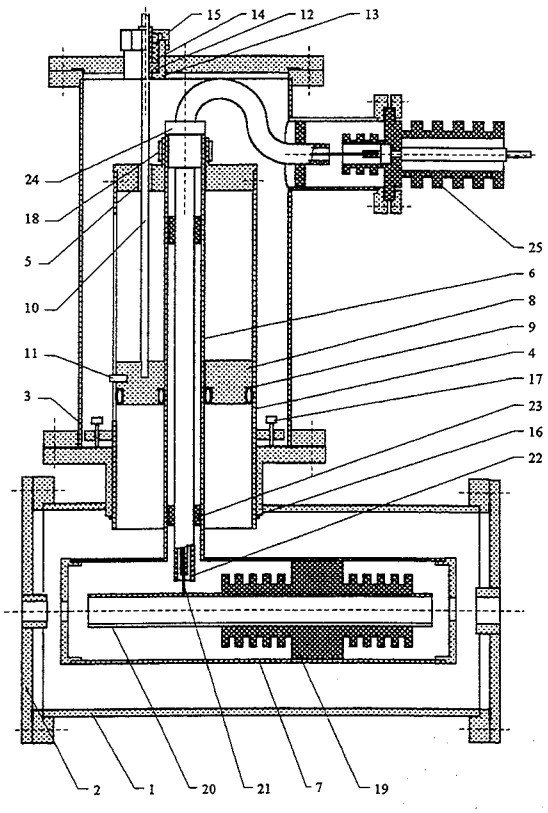

Fig.1. The resonator design scheme.

with face flange 2 and vacuum volume 3. In ones places own rebuilding resonator. It consists of a cylindrical screen 4 with face cover 5 and internal coaxial guide 6. On guide is fixed drift tube 7. In a resonator is present a mobile shorting piston 8 with sliding silvering contacts 9. The piston can be moved through coaxial at the help of the rod 10. For restriction of moving and azimuth turn prevent is stipulated restrictive pin 11, which moved in cylindrical RF screen longitudinal split. The design provides a piston moving without vacuum infringement through a traffic input device. Bush 12 is placed in a framework 13 and upsets by a rubber lining 14, the effort on which is created at the help of a device 15. The smooth surface of the rod permits to move the piston and save vacuum in systems at a level 10^{-5}-10^{-6} Torr. The cylindrical screen 4 RF contact with jacet 1 is provided by special copper ring compression 16, which is established in stipulated slot and key between a jacet and screen at screw 17 protracting. Thus, drift tube should be fixed in the resonator by the tightening ring 18 only after screws 17 protracting.

In drift tube 7 on isolator 19 coaxial fixed potential tube 20, on which constant voltage feeds. The copper guide is used for transmit voltage. High-voltage copper guide 21 placed in rigid ceramic tube. Ones, in turn, place in isolation tube. Isolation tube is fixed in internal coaxial at the help of bushes 23 and exit bushes 24. Further high-voltage guide is removed from vacuum chamber through isolator 25.

The made installation is represented reasonably simple and at the same time reliable for study powerful RF oscillations in a wide wave lengths range.

Maximum rebuilding range of resonator own frequency makes 117-235 MHz and is limited from below by coaxial line length. The top limit is connected to a significant drift tube length, which at close to it a shorting piston situation represents large part of a quarter wave line. Own resonator quality is weak drops with frequency decrease from 1300 up to 800. It is connected with two circumstances:

1. It is necessary to reduce magnetic field screening of pulsing focusing tube. So coil drift is executed from stainless steel and have become in comparison with copper coaxial much more resistance. At a piston approach to tube relatively more part of currents flow on tube, that results in quality decrease.

2. At high frequency the resistance of mobile contacts grows.

Separate problem is choice of connection factor with a making path value. By use of a resonator as a buncher with independent excitation optimum is the critical connection. If the resonator works in a selfexcitation mode, the choice is not obvious. On the one hand, at small connection conditions of selfexcitation are facilitated at small beam currents. From the other hand, connection should increase for effective generated power transfer to a load. Hence, for ground choice of a connection factor value in a selfexcitation mode and system power efficiency optimization it is necessary to carry out detailed numerical accounts and subsequent experimental research.

Other problem of a broadband generator is its coordination with a path in all frequencies range. In considered construction individual connection unit in a kind of a loop is used. Loop is located near to internal coaxial line guide in the field of junction with drift tube. On first stage the resonator was investigated in a independent excitation mode on frequency 148,72 MHz. Thus close to critical (ρ~1,2) connection value was supplied. The rebuilding in the low frequencies area results in connection reduction. In the area of higher frequencies connection, opposite, grows. It is stipulated as by shorting piston reactive impedance change, as its situation relatively shorting piston. Here in after, for preservation of coordination conditions, probably, expediently to use capacitor connection, as far as in this case the effect of reactivity change at frequency rebuilding can be compensated (completely or partially) by connection unit situation displacement relatively shorting.

The RF generator model research was conducted on a experimental stand, the block diagram of which is submitted on fig. 2. Stand contains following main elements:

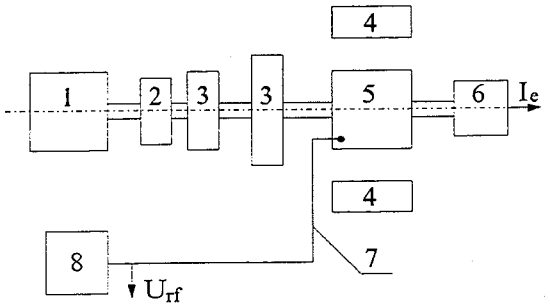

Fig.2. The experimental stand block diagram.

electron injector 1, electromagnetic lens 2, compressor coils 3, focusing solenoid 4, double-gaps buncher 5, electrons collector 6, external RF path 7 and load 8. The lens 2 and coils 3 formed a site cross compression of a electron beam in adiabatic increasing longitudinal magnetic field. The field value changes from significance 0,005 Ò on injector cathode up to 0,2 Ò on compressor output. The beam diameter decreases from 30 mm up to 8 mm. The compression site length is equal ~1 m.. The resonator placed inside the solenoid 4. One creates on the installation axis close to a similar magnetic field by size up to 0,25 Ò. The lens 2 feed scheme is operated in a continuous mode, but the coils 3 and solenoid 4 - in pulsing.

The described system of the electron beam formation permits to receive pulsing electrons beams with energy up to 100 keV and current up to 20 A at a pulses duration ~100 μs.

As far as for maintenance of the best electrons beam grouping it is desirable to have more electrons slowing down in potential tube, its potential should be approximate to injection potential up to value, determined by optimum current flow conditions. For experiments at a initial stage a settlement ratio of high-resistance divider shoulders resistance equals 0,85 was chosen. At high-voltage system tests on a idle running (without electron beam) the measured relation of potentials on tube U_t and injector U_i has appeared close to this significance. At the same time, at experiments with beam for the account of current load and hit electrons part on tube redistribution of potentials occurred. Therefore the significance U_t/U_i was increased and actually has

appeared close to 0,95. The generation was observed at injection voltage exceeding by 12 kW.

Experimental electron current oscillograms on collector is shown on fig.3. The form of the flat top of a electrons current pulse is close to sine with period ~10 ns.

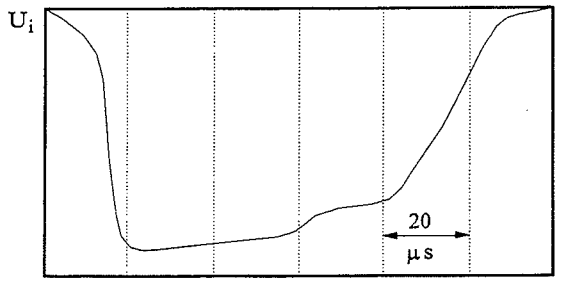

Fig.3. The electron current oscillograms on the collector.

The resonator excitation process is largely defined by the electrons beam geometrical characteristics, as far as the generation takes place only in a in comparison narrow range of electron injector magnetic field B value change. That is exists optimum significance Â in relation to electrons energy. We shall note, that at the increase U_i the optimum significance B also grows.

The RF oscillations occurrence in a resonator is accompanied by signal arising on detector in external RF path and eroding of the electron current pulse flat top on the collector (a dotted line on fig. 3, a continuous line shows the pulse form at generation absence). Availability of electron beam RF modulation in the sine form signal is well visible on oscillogram (fig.3). The modulation period within the limits of measurements error well coincides significance 0,67 ns, appropriate resonator working frequency equal to 148,72 MHz (the modulation frequency coincides resonator self-excitation frequency).

Dependences of constant I_b and of the first harmonic amplitude variable I_1 of a making electrons current signal on a collector from the value U_i are shown on fig.4.

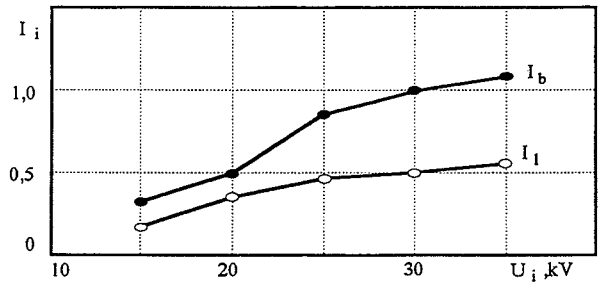

Fig.4. The dependences of I_b and I_1 from U_i.

Both signal are increased with the growth U_i. The relation I_1/I_b dependence from the significance U_i is submitted on fig.5. In accordance with the increase U_i the share of the first harmonic grows, reaches a maximum, and then decreases up to some significance, about constantly.

RF amplitude signal U dependence in external RF path from U_i is shown on fig.6. Availability of optimum significance U_i at which maximum U is reached is visible. It is connected as appear with selfexcitation optimum phase conditions (groped electron beam falls in the second backlash in close to a break phase). At the same time the pulse duration T RF signal continuously grows at the increase U_i (fig.7).

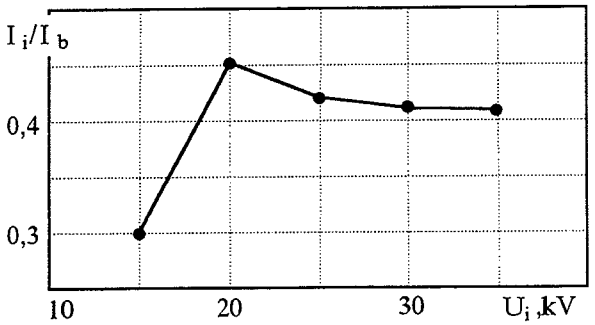

Fig.5. The dependence of I_b/I_1 from U_i.

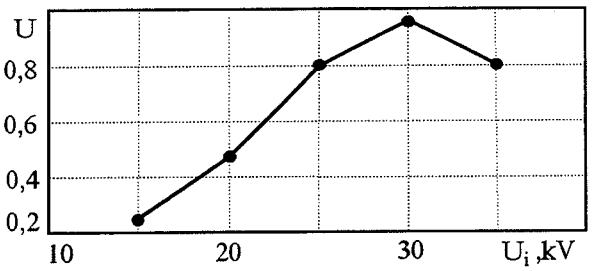

Fig.6. The dependence of U from U_i in external RF path.

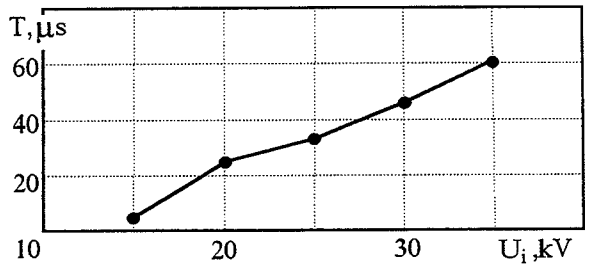

Fig.7. The dependence of T from U_i.

At a following stage resonator serviceability check was conducted at other significance of its own resonance frequency. For this purpose by shorting piston 8 moving (fig.1) the working frequency was biased in the lower frequencies area (piston was moved closer to input voltage unit on ~800 mm). The experiments results have appeared similar above described. The resonator selfexcitation frequency was measured with the help of a spectrum analyzer and has appeared equal 132 MHz.

Thus, is experimentally proven, that creation of waves lengths meter range generator with smooth frequency rebuilding in a wide range (in some times) is possible at enough large efficiency. For the entered power level increase and the maximum efficiency mode realization expediently work making on manufacturing and start of the RF structure second series. One can be based on the same principle of action, as described above.

RECENT STATUS OF FCI : PIC SIMULATION OF COUPLED-CAVITY STRUCTURE

Tsumoru Shintake
KEK, Tsukuba, 305 Japan

Abstract

New version of FCI(Field Charge Interaction)-code simulates beam dynamics of an electron beam running in a coupled-cavity structure, such as a multi-cell output structure in a klystron amplifier, a coupled cavity TWT amplifier, a bunching structure in an electron injector and also an rf-gun with multi-cell accelerating cavity. The particle-in-cell simulation takes into account the space charge field, the beam loading effect and energy exchange with an external circuit in a self-consistent manner.

Introduction

FCI-code is 2+1/2 dimensional particle-in-cell simulation code developed by the author in 1989[1], which has been used to analyze the beam dynamics in the klystron. FCI-code has contributed to develop many high-power klystrons at KEK and in industries[2]. The FCI is a name of a code group, which includes a cavity-field calculation routine, a magnetic-field routine, a main routine of beam simulation, and post-processors. Recent version is equipped with MOVIE-PLAYER to show an animation of beam profile.

In this paper, new version of FCI is described, which simulates beam dynamics in a multi-cell coupled-cavity structure. It can be applied to several electron beam devices such as

(1) Klystron with multi-cell output cavity.
(Traveling or standing wave).
(2) Electron Injector (sub-harmonic, pre-buncher, buncher).
(3) TWT amplifier.
(4) RF-gun(single-cell or multi-cell).

Modeling of RF-Field in Multi-Cell Structure

In FCI-code, the RF-field in a coupled-cavity structure is represented by a superposition of eigenmodes in each cell (here we call this as "cell-mode"). For example, the traveling wave in a disk-loaded structure is represented by a superposition of cell-modes, whose field intensity (cell-voltage) oscillates at the rf-frequency, but their phases are differed from cell-to-cell, resulting in a traveling wave as a group motion.

The electro-magnetic interaction between cells, which is so called "the coupling", is taken into account in a coupled-cavity circuit-model (see the next section).

The electric field of the cell-mode is represented by

$$E_z(r,z,t) = E_{z0}(r,z)\cdot\cos(\omega t+\phi), \qquad (1)$$

where $E_{z0}(r,z)$ is the electric field pattern at the maximum phase. In vacuum electron beam devices the dominant mode (TM01-mode) in a cylindrical cavity is usually used, whose electric field is uniform around the axis. Therefore, an azimuthal dependence was dropped in eq.(1). We define the cell-voltage by the line integral on the "frozen electric field" along the axis as follows.

$$V_{CF} = \int_{-\infty}^{\infty} E_{z0}(r=0,z)\cdot dz \qquad (2)$$

The subscript CF denotes "Cell-voltage on Frozen electric field". The shunt-impedance is given by

$$(R/Q)_{CF} = \frac{V_{CF}^2}{2\omega W} \qquad (3)$$

This definition does not include the transit-time factor. Note that this definition is different from the accelerator definition used in theory of the high energy accelerators, which includes the transit-time factor. The relation between them is

$$(R/Q)_{CF} = (R/Q)_{acc}/2T^2, \qquad (4)$$

where T is the transit time factor for a particle of speed of the light.

An electron beam running in the coupled-cavity structure interacts with cell-mode in each cell independently. The field excitation is taken into account into the equivalent circuit as an induced current given by

$$I_{ind} = \frac{\int J_b\cdot E_{z0}(r,z)\cdot d\mathbf{r}}{V_{CF}}. \qquad (5)$$

Modeling of Coupled Cavity Structure

Figure 1 shows an equivalent circuit model for a multi-cell coupled-cavity structure. The circuit equation for the n-th cell is given by

$$\bar{V}_n'' + (1-\delta_n)\frac{\bar{V}_n'}{Q_n} + (1-2\delta_n)\bar{V}_n = \frac{1}{2}(1-2\delta_n)\cdot\left(k_{n-1,n}\bar{V}_{n-1} + k_{n,n+1}\bar{V}_{n+1}\right) + \bar{I}_{ind}\ , \qquad (6)$$

where

$\bar{V}_n' = d\bar{V}_n/d\theta = d\bar{V}_n/\omega dt$, $\bar{V}_n'' = d^2\bar{V}_n/d\theta^2 = d^2\bar{V}_n/\omega^2 dt^2$

$k_{n-1,n}$, $k_{n,n+1}$: coupling constant.

$\delta_n = (\omega-\omega_n)/\omega_n$: detuning of cell from the rf-frequency.

ω_n : resonance frequency of n-th cell.

$\bar{V}_n$: cell voltage (peak) normalized by

$$\bar{V}_n = V_{CF.n}/[\omega_n(R/Q)_{CF.n}]^{1/2}$$

I_{ind} : beam induced current normalized by

$$\bar{I}_{ind} = [(R/Q)_{CF.n}/\omega_n]^{1/2} I_{ind}$$

Above normalization makes the stored energy in a simple form:

$$\langle W_{EM}\rangle = W_e^{max} = \frac{1}{2}C_n V_n^2 = \frac{1}{2}\bar{V}_n^2.$$

Here we introduce "the quasi-steady state approximation". Since in most applications, the time variation of the cell voltage and current is much slower than the sinusoidal oscillation at the rf-frequency, we can separate the time

variation into two parts: a slow change in voltage and phase and a fast sinusoidal oscillation at rf-frequency as follows.

$$\overline{\mathbf{V}}(t) = \overline{V}(t)\cdot\exp(j\omega t),\quad \overline{\mathbf{V}}'(t) = (\overline{V}' + j\overline{V})\cdot\exp(j\omega t)$$

$$\overline{\mathbf{V}}''(t) = (\overline{V}'' + 2j\overline{V}' - \overline{V})\cdot\exp(j\omega t) \qquad (7)$$

Using eq.(7) into eq.(6), we have the quasi-steady state circuit equation.

$$\overline{V}_n'' + (2j + \frac{1}{Q_n})\overline{V}_n' + (\frac{j}{Q_n} - 2\delta_n)\overline{V}_n$$

$$= \frac{1}{2}\left(k_{n-1,n}\overline{V}_{n-1} + k_{n,n+1}\overline{V}_{n+1}\right) + \bar{I}_{ind}' + j\bar{I}_{ind} \qquad (8)$$

In FCI-code, eq.(8) is solved by the finite difference method in time sequence.

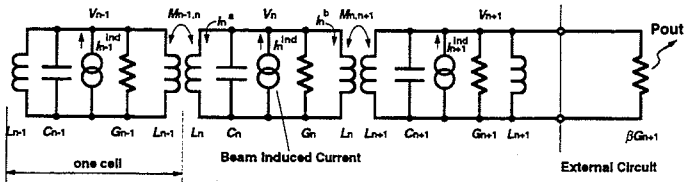

Fig. 1. Equivalent circuit model for a coupled cavity structure.

Particle-In-Cell Simulation

In FCI-code, an electron beam is simulated by a flow of macro-particles of ring shape (2D, circular symmetry). The space charge field is calculated by solving the wave-equations of the scalar and the vector potentials by the finite difference method. The particle motion is determined by integrating the relativistic equation of motion in 2+1/2 dimension: $(r, \dot{r}, z, \dot{z}, \dot{\theta})$, which takes into account the space charge field, the self-magnetic field, the external focusing magnetic-field and the rf fields in cavities. The details are described in references [1] and [2].

Traveling Wave Output Structure

As an example, a traveling wave output structure was simulated by FCI. A structure was designed as shown in Fig. 2 and attached to the 5045-tube[4] in place of the single-cell output cavity of original design. The coupling constant and the loaded-Q were determined as follows. The steady state circuit-equation of the coupled cavity is given by[3]

$$\left[j\left(\frac{\omega}{\omega_n} - \frac{\omega_n}{\omega}\right) + \frac{1}{Q_n}\right]\overline{V}_n$$

$$= -j\frac{\omega_n}{\omega}\frac{1}{2}\left(k_{n-1}\overline{V}_{n-1} + k_{n+1}\overline{V}_{n+1}\right) + \bar{I}_{ind} \qquad (9)$$

We use a traveling $\pi/2$-mode, which requests resonance frequencies of all cells being tuned to the rf-frequency : $\omega_1 = \omega_2 = \omega_3 = \omega$. Applying eq.(9) to all cells and neglecting the cavity loss ($1/Q_0 \rightarrow 0$), we have

$$\begin{bmatrix} 0 & jk_{12}/2 & 0 \\ jk_{12}/2 & 0 & jk_{23}/2 \\ 0 & jk_{23}/2 & 1/Q_{e3} \end{bmatrix}\begin{bmatrix}\overline{V}_1 \\ \overline{V}_2 \\ \overline{V}_3\end{bmatrix} = \begin{bmatrix}\bar{I}_{ind.1} \\ \bar{I}_{ind.2} \\ \bar{I}_{ind.3}\end{bmatrix} \qquad (10)$$

To smoothly extract the kinetic energy from the beam, we assume the same energy loss in each cell. Since we want to establish a traveling $\pi/2$-mode running with beam, the cell-to-cell distance was chosen at $\lambda/4$ wavelength on the beam, additionally the cell-voltage must be $\overline{V}_2 = -j\overline{V}_1$, $\overline{V}_3 = -\overline{V}_1$. Applying this relation into eq. (10), we get the optimum condition of the coupling constant and the loaded-Q as follows.

$$k_{12} = 2\left[(R/Q)_1(R/Q)_2\right]^{1/2}\frac{|I_{ind.1}|}{|V_2|} \qquad (11.a)$$

$$k_{23} = 2\left[(R/Q)_2(R/Q)_3\right]^{1/2}\frac{|I_{ind.2}|}{|V_3|} + k_{12} \qquad (11.b)$$

$$\frac{1}{Q_{e.3}} = (R/Q)_3\frac{|I_{ind.3}|}{|V_3|} + \frac{k_{23}}{2} \qquad (11.c)$$

We design the beam deceleration voltage close to the beam voltage of 350 kV. By taking into account the transit-time factor (~0.7), the required total cell-voltage becomes 500 kV. Thus, $|V_1| = |V_2| = |V_3| = 163\,kV$. On the other hand, the modulation rf-current on a beam is normally as high as 1.5 times of DC-current. It is 600 A in the present case. By considering the transit-time factor and de-bunching effect, we assume the beam induced current as 350, 300, 250 A in the 1st, 2nd and the 3rd cell, respectively. From eq. (11), we have the optimum coupling constants as listed in Table-1. Once, we execute a beam simulation, we get precise values of the beam induced currents, then we can refine the coupling constant using eq.(11), and execute the beam-simulation again. In actual design works, we need a few cycles of this iteration process to reach an optimum solution.

The cell-mode and shunt impedance were calculated by the DENKAI-code[5]. Figure 3 shows the electric field plots of the 1st, 2nd and the 3rd cell. In calculating each mode, the neighboring cavity was detuned by terminating the cavity wall by the "magnetic short". The cavity radius was determined to tune the resonance frequency at 2856.0 MHz.

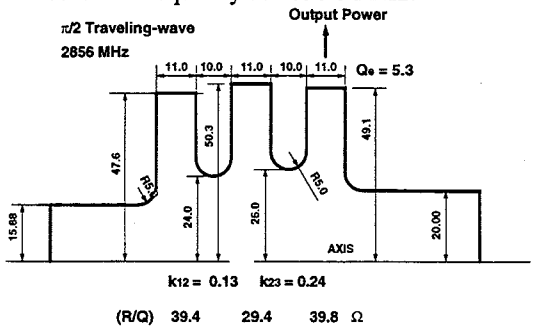

Fig. 2. Klystron output structure using traveling $\pi/2$-mode.

The simulation results are summarized in Table-1. At 150 W of the input power, simulation predicted the output power of 69.2 MW, and the power efficiency of 48.5 %. The simulated voltages are about 10 % higher than the expected one. This is due to a difference between the simulated beam induced-current to the assumed one. The maximum surface electric was reduced to 13.7 MV/m, which is 51 % of the field in the original single-cell cavity design.

Figure 4 shows a snap shot of the beam. The top is the beam profile on (z,r) plane. Since in a traveling wave structure the aperture can be designed much wider than a single cell cavity, we can keep a large clearance for a beam to the cavity wall. Additionally, the beam deceleration is smooth and the radial kick by the cavity field is much less, resulting

in a smooth profile in beam shape after the output structure. This is an important feature of the traveling-wave output-structure to eliminate collision of electrons in beam hallows on the cavity surface, and avoid accompanied rf-break-down in the output gap. The middle plot is the kinetic energy profile and bottom is the instantaneous beam current, where deceleration and de-bunching of beam in the output structure are clearly shown. The MOVIE-PLAYER shows animation of this plot on BIM-PC machine.

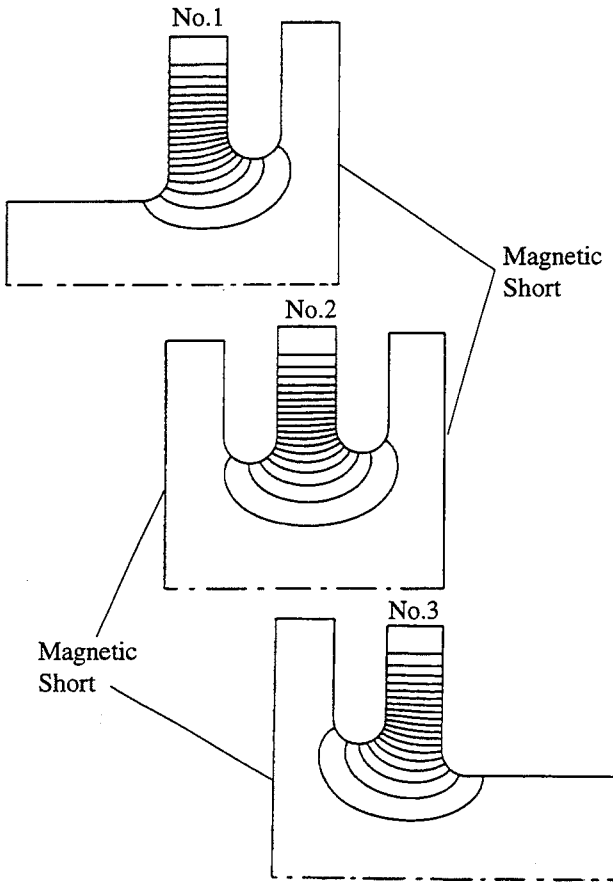

Fig. 3 Cell-modes in the 1st, 2nd and 3rd cell.

Discussions

In this paper, the rf-field in a multi-cell couple-cavity was approximated by the superposition of cell-modes, and whose voltages were calculated by the equivalent circuit model. In case of a small coupling, the energy transfer per one cycle along cell-to-cell is much smaller than the stored energy in one cell, therefore this approximation works very well. However, in a case of a large coupling, such as in a klystron output structure, we has to pay attention on errors in the approximation. In order to verify accuracy of the simulation, we are continuing studies, such as comparison of cell-mode model to standing wave modes in coupled cavity without beam, or direct finite-difference modeling of coupled-cavity structure with beam. The code is also under testing on several existing cases, such as X-band klystron having multi-cell output cavity, and an electron injector with traveling-wave buncher.

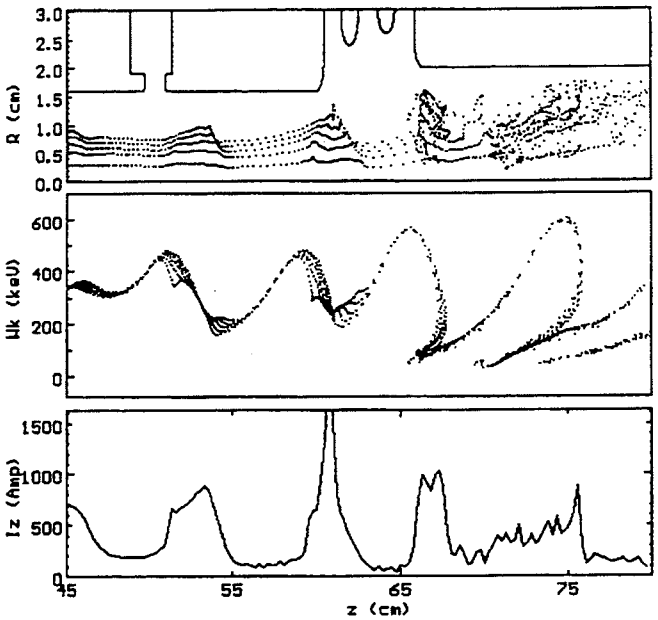

Fig. 4. Snap shot of simulated beam.

Table-1

Cavity parameter			
	fo	(R/Q)CF	QL
No.1	2856.0	39.4	2000
No.2	2856.0	29.4	2000
No.3	2856.0	39.8	5.3
k12	0.13		
k23	0.24		
Beam Parameter			
Beam Voltage	350	kV	
Beam Current	408	A	
Drive Power	150	W	
Simulation Results			
	Vc (kV)	Ic (A)	
No.1	177.6	345.2	
No.2	187.2	279.3	
No.3	170.9	167.8	
Surface Electric Field	13.7	MV/m	
Output Power	69.2	MW	
Power Efficiency	48.5	%	

References

[1] T. Shintake, "FCI field charge interaction program for high power klystron simulators", Proc. 1989 Particle Accelerator Conf., Accelerator Science and Technology, March 20-23, 1989, Chicago, USA

[2] T. Shintake, "Klystron simulation and design using the Field Charge Interaction (FCI) code", Nucl. Instrum. and Method in Physics Research A363 (1995) 83-89

[3] E. A. Knapp, B. C. Knapp and J. M. Potter, "Standing Wave High Energy Linear Accelerators", Review of Scientific Instruments, Vol. 39, No. 7, 1968, pp. 979-991

[4] T.G.Lee, et.al., "A Fifty Megawatt Klystron for the Stanford Linear Collider", SLAC-PUB-3214, Sep. 1983(A)

[5] T. Shintake, "User's guide to DENKAI", KEK Report 91-3, June 1991 A/D

C-BAND MAIN LINAC RF SYSTEM FOR e^+e^- LINEAR COLLIDER OF 0.5 TO 1.0 TeV C.M. ENERGY

T. Shintake, N. Akasaka, K. Kubo, H. Matsumoto, S. Matsumoto, Shigeru Takeda,
K. Oide and K. Yokoya : *KEK Tsukuba Japan,*
P. Pearce : *CERN, Geneva, Switzerland,* H.S. Lee and M.H.Cho : *PAL, Pohang Korea,*
K. Watanabe : *Tohoku University,* Osamu Takeda : *TOSHIBA Co.*, H. Baba : *NIHON KOSHUHA Co.*

Abstract

A hardware R&D for the C-band (5712 MHz) rf system for a linear collider started in 1996 at KEK. An accelerating gradient of 32 MV/m (including beam loading) will be generated by 50 MW C-band klystrons in combination with an rf-compression system. The klystron and its power supply can be fabricated by conventional technology. The straightness tolerance for the accelerating structures is 30 μm, which is also achievable with conventional fabrication processes. No critical new technology is required in a C-band system. Therefore, a reliable system can be constructed at low cost with a minimum of R&D studies. The first high-power test is scheduled for 1997.

Introduction

The e^+e^- linear collider is a large-scale machine. In the main linacs for two beams, we use more than 8000 accelerating structures, 4000 klystrons and pulse modulators. Therefore, the system must meet the followings demands:

(1) High reliability

To provide beams with reasonable availability, the system must be highly reliable; that is, the fault rate must be negligibly small and the lifetime of the key devices must be sufficiently long. To achieve this, we eliminate any critical parameter or excessive stress in the hardware components.

(2) Simple

For the same reason as (1), the system must be simple. This will also help to lower the construction cost and to make hardware maintenance easier.

(3) Lower construction cost

We should try to reduce the construction cost while not sacrificing the system performance and reliability.

(4) Reasonable power efficiency

We assume that the maximum limit on the whole wall-plug power in a site is 200 MW. To meet this requirement, the rf system must efficiently accelerate the beam. However, since an actual rf system needs auxiliary power in addition to the wall-plug power to generate rf, we must optimize the total system, not just the acceleration hardware.

(5) Easy to operate

The machine operation should be easy. In the actual machine operation, the system must have flexibility to accelerate various patterns of the beam current. The tuning procedure must also be simple and easy.

The above list provides a guide-line and boundary conditions to our design work. Among the system parameters, the choice of the drive rf frequency plays the most important role concerning the system performance as well as the hardware details. We proposed the C-band frequency as being the best choice to meet all of the demands listed above[1-4].

Overall Parameters

The overall parameters are listed in Table-I for 500-GeV and 1-TeV C.M. energy linear colliders. In the 500-GeV case, an accelerating gradient of 31.7 MV/m is generated by a 50-MW klystron in combination with rf pulse compression; thus, an active length of 7.3 + 7.3 km is sufficient to reach 500 GeV C.M. energy. A luminosity of 6.6 x $10^{33}/cm^2/sec$ can be obtained using a 150 MW wall-plug power. The details are described in ref.[3].

Table-I

CM Energy	TeV	0.5	1.0
Number of electrons per bunch	$x10^{10}$	1.1	1.4
Number of bunches per pulse		72	
Bunch separation	nsec	2.8	
Repetition frequency	Hz	100	50
Bunch length	mm	0.2	
------- RF-parameters -------			
RF frequency	GHz	5.712	
Peak input power at cavity	MW	83.0	165
Nominal accelerating gradient	MV/m	40.0	56.0
Effective accelerating gradient	MV/m	31.7	46.4
Wall-plug power for RF (2 linacs)	MW	150	133
------- Accelerating Structure -------			
Number of structures per beam		4080	5748
Total length of cavities per beam	km	7.3	10.3
Structure Type		CG with choke-mode	
Unit length of structure	m	1.80	
Iris radius/wavelength		0.13 - 0.17	
Shunt-impedance	MΩ/m	59.2 - 47.0	
------- Pulse-compressor -------			
Compression Scheme		multi-cell coupled cavity	
Pulse compression ratio		5	
Pulse compression efficiency	%	70	
------- Klystron -------			
Klystron peak power	MW	50.3	98.6
Efficiency	%	45	70
Number of klystrons per beam		2040	2874
RF pulse length	μsec	2.5	
------- Modulator -------			
Number of modulators per beam		2040	2874
Power efficiency from AC to pulse	%	75	
------- Beam Dynamics -------			
Injection energy	GeV	20	
Phase delay of rf-crest	deg	14.5	10.0
Structure straightness tolerance	μm	30	
------- Final focus -------			
Spot size at IP (horizontal)	nm	318	318
(vertical)	nm	4.3	3.0
Crossing angle (crab crossing)	mrad	8.0	8.0
Luminosity	$x10^{33}$	6.6	7.0

System Description

Figure 1 shows a schematic diagram of one unit in the main linac rf-system. Two 50 MW klystrons are driven by two high-voltage pulse modulators independently, followed by a 3dB hybrid power combiner and pulse compressor to generate 350 MW peak power, which drives four accelerating structures. The pulse-compression action is performed by rotating the phase of the input rf-signal in opposite directions in each klystron. By combining two powers at 3-dB hybrid, the phase modulation (PM) is converted to the amplitude modulation (AM) of the ramp-waveform, which compensates the beam loading effect in the accelerating structure. The energy-storage cavity consists of three coupled cavities using a low loss TE01n mode.

We use a standard rectangular waveguide: EIA187 (47.55 mm x 22.15 mm, 3.95-5.85 GHz), whose attenuation constant is 0.03 dB/m (5% loss/m).

Figure 2 shows the key points concerning the C-band, which make the system simple and reliable.

Klystron Power Supply & Pulse Transformer

The filling time of the accelerating structure scales as

$$t_F = \frac{2Q}{\omega}\tau \propto \omega^{-3/2}.$$

At the C-band, it becomes 280 nsec. Including the pulse-length of the beam and a compression factor of five in the rf-compression system, the rf-pulse at the klystron becomes 2.5 μsec. Including the rise- and fall-times, the pulse-length of the high-voltage applied to the electron-gun of the klystron becomes 3 μsec or longer, which is quite suitable to the conventional power-supply consisting of a Pulse Forming Network (PFN) and a step-up pulse-transformer. This type of power supply has been used in many linear accelerators, owing to its high reliability and good efficiency.

To charge high voltage into the PFN capacitors, we use an inverter power supply. Such a high-voltage power supply has been widely used to drive pulsed lasers for a long time. Modern technology for power-semiconductor devices (such as IGBT) has improved the power efficiency by better than 90%. Using this power supply, we can simplify our modulator design, making it modular according to the required functions: the inverter power supply (DC block), the PFN module (pulse forming block), and the pulse-transformer tank (matching block to a klystron). With this approach, it becomes easier to reduce the cost, improve the reliability and ease maintenance. In the case of a failure, we simply replace any broken block with a new one and send the old one to a factory for repair.

C-band Klystron

Since the klystron drift-tube diameter is proportional to the rf wavelength, we can use an electron beam with a larger diameter than higher frequency bands. It also makes it easier to design an electron gun with a larger cathode to extract a higher beam current. Therefore, we can design the beam voltage as low as 350 kV, which enables the PFN voltage to be as low as 43 kV. At this voltage level, it is easier to obtain suitable PFN-capacitors from existing ranges of various manufacturers.

RF Pulse Compressor

We use a three-cell coupled-cavity pulse-compressor instead of a delay-line type pulse-compressor. The cavity is compact, having a length of 1 m, and its diameter is 160 mm. Therefore, it will be easier to fabricate at lower cost. A computer-simulation code was made to simulate the time response of the coupled-cavity system, which has shown a maximum efficiency as high as 70%. The details are reported in ref. [5].

Accelerating Structure

We use a choke-mode cavity structure[6], in which all of the higher-order modes are heavily damped. Therefore, the multi-bunch wakefield and any associated instability will not harm the beam emittance. The only concern is the single-bunch emittance dilution due to the short-range wake-field, which is a strong function of the iris aperture. We use relatively large iris-aperture: average <2a>=16 mm. As a result, the straightness tolerance for one structure becomes 30 μm or larger. This is a controllable level in conventional fabrication techniques of the disk-loaded structure. To eliminate any stress and make the structure straighter, a low temperature brazing technique will be adopted[7]

To align the structure with beam, we use an RF-BPM attached to the structure. This type of RF-BPM was tested using the FFTB beam line at SLAC in December 1995[9]. It demonstrated a very high resolution of 44 nm for a single bunch. Three RF-BPM were assembled in one block, and the misalignment between them was measured with electron beam. It was only 3 μm. This is a quite promising result for a structure-alignment procedure.

The dark-current problem due to field-emission under the high accelerating gradient has been studied using computer simulations[10]. From which, no serious contributions to the background in the detector at IP is expected at C-band frequency.

Hardware R&D Program

In January, 1996, the hardware R&D has been started at KEK. In 1997-1998, we will construct one unit of rf-system. Since we use one klystron, the input rf will be directly amplitude modulated to demonstrate the flat-top output from the compressor. The first klystron tube will be available in 1997.

References

[1] JLC Group, "JLC-I", KEK Report 92 - 16, December 1992, A/H/M

[2] T. Shintake, *et al.*, "C-Band Linac RF-System for e^+e^- Linear Collider", Proc. 1995 Particle Accelerator Conf. and Int. Conf. on High-energy Accelerators, May, 1995, Dallas, Texas, U.S.A., KEK Preprint 95-49

[3] K. Yokoya, *et al.*, "C-band Linear Collider with C.M. Energy 500 GeV to 1 TeV", Proc. 5th European Particle Accelerator Conference (EPAC96), Sitges, Barcelona Spain, 10-14, June 1996, KEK Preprint 96-68, July 1996 A

[4] T. Shintake, et al., "C-band RF Main Linac System for e+e- Linear Colliders at 500 GeV to 1 TeV C.M. energy", Proc. 5th European Particle Accelerator Conference (EPAC96), Sitges,

Barcelona Spain, 10-14, June 1996, KEK Preprint 96-69, July 1996 A

[5] T. Shintake and N. Akasaka, "A New RF Pulse-Compressor using Multi-Cell Coupled-Cavity System", Proc. 5th European Particle Accelerator Conference (EPAC96), Sitges, Barcelona Spain, 10-14, June 1996, KEK Preprint 96-71, July 1996 A

[6] H. Matsumoto, et al., "C-band Choke-Mode Accelerating Structure for the Linear Collider", Proc. 5th European Particle Accelerator Conference (EPAC96), Sitges, Barcelona Spain, 10-14, June 1996, KEK Preprint 96-70, July 1996 A

T. Shintake, *et al.*, "HOM Free Linear Accelerating Structure for e+e- Linear Collider at C-band", Proc. 1995 Particle Accelerator Conf. and Int. Conf. on High-energy Accelerators, May, 1995, Dallas, Texas, U.S.A., KEK Preprint 95-48

T. Shintake, "The Choke Mode Cavity", Jpn. J. Appl. Phys. Vol.31, pp.L1567-L1570, Part2, No.11A 1992

[7] H. Matsumoto, *et al.*, "Low Temperature Brazing Technique for the Accelerators", Proc. 5th European Particle Accelerator Conference (EPAC96), Sitges, Barcelona Spain, 10-14, June 1996, KEK Preprint 96-67, July 1996 A

[8] K. Kubo, *et al.*, "Alignment Issue for C-band Linear Collider", Proc. 5th European Particle Accelerator Conference (EPAC96), Sitges, Barcelona Spain, 10-14, June 1996, KEK Preprint 96-66, July 1996 A

[9] The experimental results on RF-BPM will be published soon.

[10] N. Akasaka, "Dark Current Simulation in High Gradient Accelerating Structure", Proc. 5th European Particle Accelerator Conference (EPAC96), Sitges, Barcelona Spain, 10-14, June 1996, KEK Preprint 96-65, July 1996 A

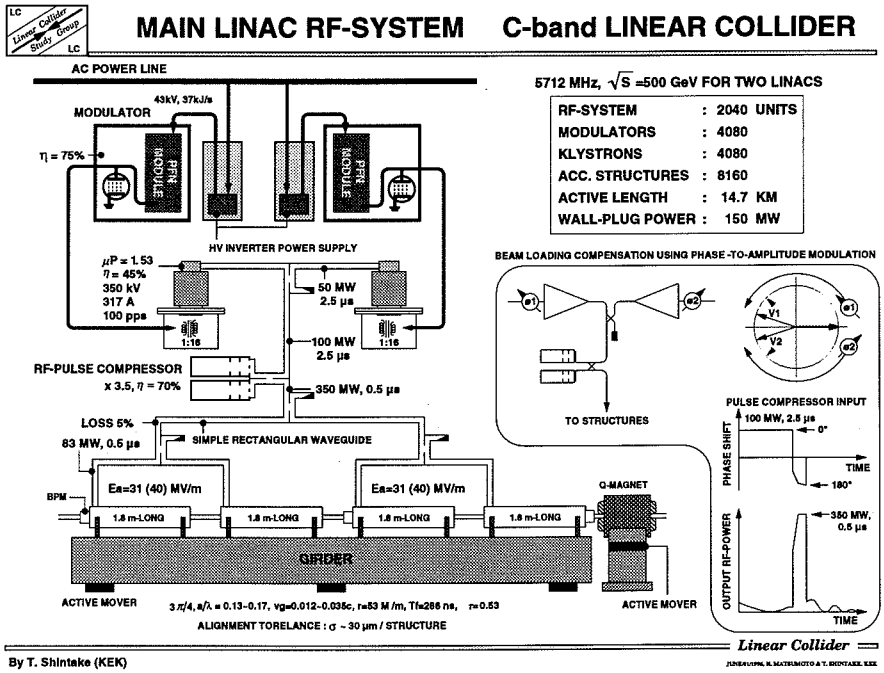

Fig. 1 One unit of the C-band RF system.

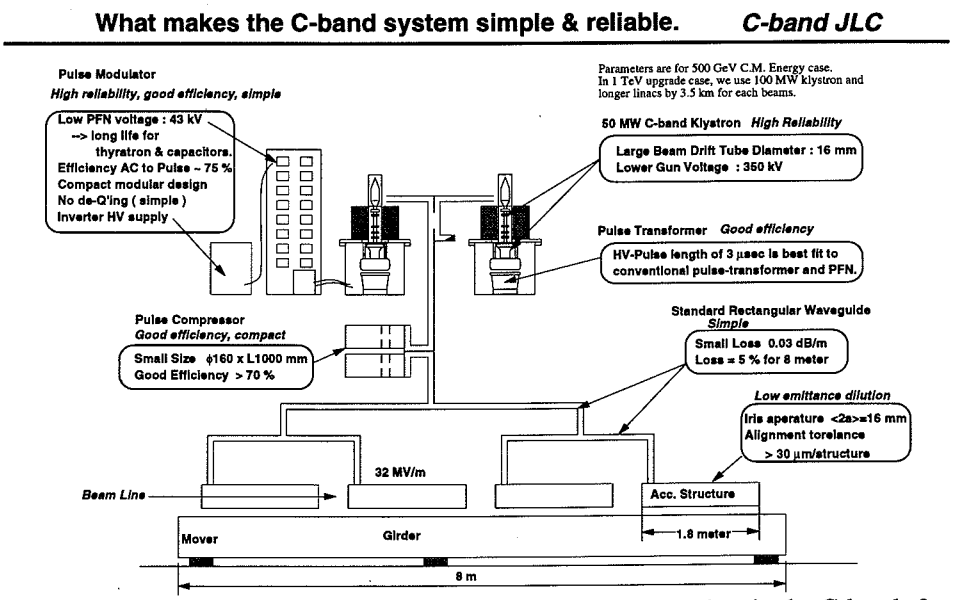

Fig. 2 What makes the C-band system simple and reliable. The key points in the C-band rf-system.

PERFORMANCE OF THE RF-SOURCE FOR THE KEKB LINAC

S. Fukuda, S. Michizono, Y. Saito, K. Nakao and S. Anami
National Laboratory for High Energy Physics (KEK)
1-1 Oho, Tsukuba, Ibaraki 305, Japan

Abstract

The KEKB project, which requires an energy upgrade of the KEK linac from 2.5 GeV to 8.0 GeV, started in 1994, and has been progressing. About fifty 50-MW high-power klystrons (including equivalent 40-MW tubes) have been produced and tested. Twenty-eight of them have already been installed in the klystron gallery. We also obtained more than 60-MW rf peak power with a reasonable efficiency from this 50-MW tube. The klystron assemblies, including the magnets and pulse transformers, have been operated with no problems. In order to operate the SLEDs, we have also developed a sub-booster klystron, a driver klystron which produces more than 60-kW peak power for 8 high-power klystrons. Two of them have been successfully operated in the klystron gallery. We have started SLED operation at 2 sectors (sectors #4 and #5) and are accumulating data concerning the SLED and accelerated beams. We now describe this performance of the rf-source for the KEKB linac.

Introduction

An upgrade of the PF linac in order to increase the acceleration energy from 2.5 to 8 GeV, by using a combination of 59 klystrons having an average output power of 41 MW (max. 46 MW) and SLAC-type rf compressors (SLED) is now in progress[1]. We have achieved progress concerning the sub-booster klystron, the driver klystron, and feeding to 8 high-power klystrons, since it is necessary to change the driving scheme (shown in Fig. 1) in order to use the SLED operation with proper timing. In this modification, more than 40 kW of output power is required from the sub-booster klystron by taking account of the transmission losses. We had manufactured 5 tubes, including a prototype; 2 tubes have already been set in the gallery in order to test the SLED operation. Installation of the high-power tubes is proceeding on schedule. Twenty-eight tubes have already installed to the gallery, and 12 tubes are being operated under the SLED mode. Those tubes are operated during an injection to the PF ring and AR (Accumulating ring) for the SOR experiment users. Some of the high-power tubes are being operated at 335 kV to 350 kV, and have succeeded in outputting more than 60 MW. They are expected to be used at the unit just after the positron target position, where high-gradient acceleration is desirable.

Sub-booster Klystron Development

For the KEKB energy upgrade project, new 50-MW klystrons have been developed. In order to feed a drive power to these 8 high-power tubes, which are operated with SLED cavities, a 60-kW sub-booster klystron (SBK) is required. Since there are no commercial tubes which satisfy our specifications, this tube has been designed at KEK, and manufactured under the collaboration of KEK and MHI (Mitsubishi Heavy Industry Co.)[2]. The specifications for the sub-booster klystron are

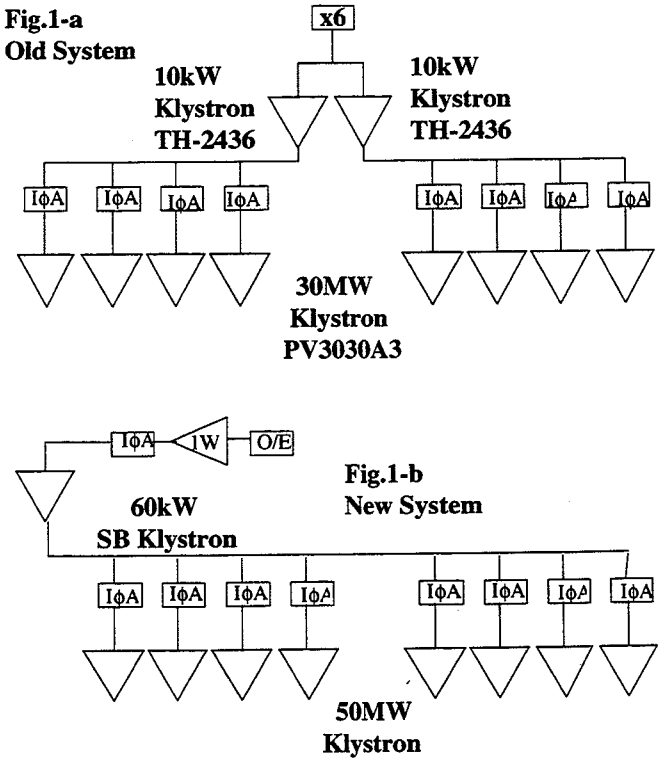

Fig. 1. Comparison between the old and new driving systems.

the collaboration of KEK and MHI (Mitsubishi Heavy Industry Co.)[2]. The specifications for the sub-booster klystron are given in the table 1.

We have been using two 10-kW tubes of Thomson CSF (TH2436) in parallel in each sector, as shown in Fig. 1a[3]. The different points between the old TH2436 tube and the new SBK-tube are as follows: (1) Electromagnet focusing has been adopted instead of permanent magnet focusing. (2) The tuning frequencies for the each klystron cavity are fixed, since our purpose of this tube is limited. The new tube has 6 cavities, while the old tube has 4. These modifications enable us to obtain a high gain. (3) The new tube has an integrated ion pump. (4) Water cooling is adopted in order to stabilize the operation performance. (5) The input power feeder is set vertically to make the inside bore diameter of the magnet small. (7) The output waveguide is a coaxial 39D-type waveguide and the output waveguide flange type is BFX-39D, which is popular in Japan (Old type is EIA-39D standard.) (8) An Ir-coated dispenser cathode of 1 inch diameter is adopted instead of the oxide cathode based on a life consideration. (6) Our tube configuration is partly based on the design of the SLAC sub-booster klystron, especially concerning item (5). [4]

The basic design of the tube is fulfilled in KEK and some manufacturing processes: for instance, as the cathode processing, baking-and-evacuation of the tube and pinching off

Table 1. Specification of SBK

item	unit	specification
Peak pulse voltage	kV	25.0
Peak pulse current	A	7.91
Microperv	$\mu A/V^{3/2}$	2.0
Pulse width(rf)	μsec	4.0
Pulse width(beam)	μsec	>6.0
Repetition	pps	50
Peak RF power	kW	>60
Average RF power	W	12
Efficiency	%	>30
Gain	dB	57
Input power	mW	120
Total length	mm	about 690
Electric gun	BI Cathode	
Focusing magnet	Electromagnet	
Cooling	Water cooling	
Ion Pump	1 *l* /sec integrated ion pump	
Cavity number	6	
Output Waveguide	39D Coaxial Waveguide	
Output Flange	BFX-39D standard	

were first demonstrated at KEK. A proto-type tube was manufactured in FY94. In FY95 it was tested and a 60-kW output power was obtained at a beam voltage of 25 kV, which was supplied by the newly developed SBK-modulator using a semiconductor switching device. In FY95 three tubes were ordered and two were tested. These tubes were installed at the klystron gallery in order to evaluate the SLED operations, and have operated satisfactorily. We need 8 sub-booster klystrons for KEKB-project. Up to now, we could achieve an output power of around 60 kW, while the efficiency is about 30%.

Status of High Power Klystron

Test and Installation in the Gallery

As previously reported[5, 6], we have been developing 2 types of high-power klystrons for this project: one is an improved type of an old 30-MW tube by enlarging the high-voltage ceramic-seal; the other is an improved one by using a larger cathode and larger high-voltage seal. PV3030A3 (MELCO; Mitsubishi Electric Company) and E3728 (Toshiba) are the former types of tubes and PV3050 (MELCO) and E3730 (Toshiba) are the latter types. Both types have abilities to produce more than 50 MW of output power at 310-kV applied voltage. The focusing electromagnet has compatibility between these two types with only a slight change at the gun region of the tube.

An output power of 50 MW and an efficiency of 45-46% were achieved on the average in the 50-MW tubes. The saturation point is located at 250-300 W at the input power on an average (a gain of around 53 dB is achieved). The typical performances of the 50-MW tubes are shown in Figs. 2 and 3. Our tubes have a single window and cooling structures are set on the upper and lower waveguides of the windows. The window material of our tube is high-density pure alumina of 99.7% (HA997: NGK) and has a very low tanδ value[7]. The evaluation after running in the gallery is satisfactory.

We have already purchased 50 tubes, including both types. Performance tests of 27 tubes have been finished and the tubes have been installed in the klystron gallery. During the first stage of tube development, some instabilities and arcing problems were observed in the Toshiba 50-MW tubes, which were completely solved by changing the cathode processing of the manufacturing process. Another type of instability and poor gain problems were observed in the MELCO tubes. These were solved by changing the structures inside the tube so as to prevent any distortion of the cavity during the manufacturing process.

60-MW test using the 50-MW klystron

Performances at an applied voltage higher than 310 kV have been of interest since the FCI[8] calculation predicted an output power of 70 MW at the 350-kV beam voltage. This test has been attempted using a prototype tube (PV3050#2) as a tentative low-duty test; a 64-MW output power was observed with an efficiency of about 42%; the performance has strongly depended on the magnetic-field distribution near to the output-cavity region, as predicted by FCI. Furthermore, the E3730 tube produced a 60-MW output power at 331 kV beam voltage and rf pulse width of 2 μs with an efficiency of 47% at a factory test. These output power level are highest when using single output windows. We have been planning that this tube operation mode will be used at the #2-1 unit, which is located just after the positron-conversion target, since high-gradient acceleration is required.

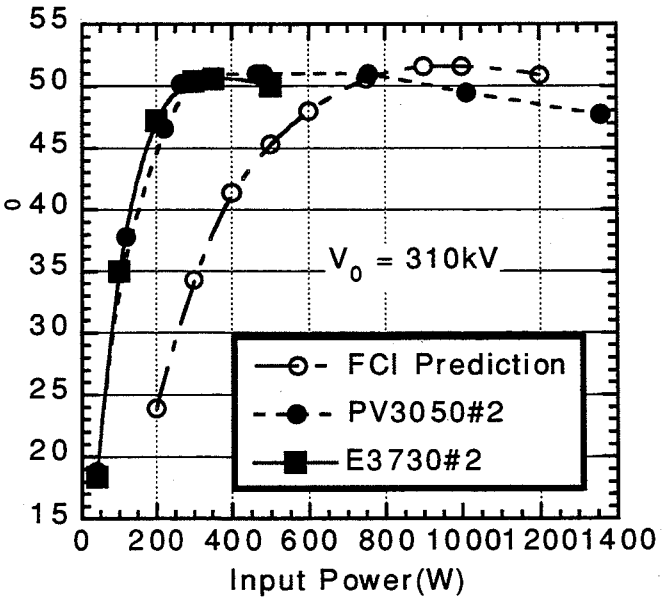

Fig. 2. Input -output power characteristics predicted by the FCI and those of two 50-MW tube performances.

Design and Status of the Socket Assembly

The final design of the pulse transformer is such that the step-up ratio has been changed to be 1 : 13.56; there are 7 primary turns and 95 secondary turns. This is an bifiller auto-winding type; a core reset bias is applied. More detail descriptions are given in reference [6]. We have newly

developed corrugated high-voltage insulators made from epoxy material to support the klystron heater transformer, which is at a high-voltage potential. The heater transformer has been redesigned, and the final thickness is half that of the old one. Owing to these design changes, we can continue using the same oil tanks and same configurations, including the waveguide ports. A feeder section inside of the tank comprises a knife-switch-type connector made by Multi-contact Co., which enables it to be easily disconnected. The capacitive divider, used as a voltage monitor, has been replaced from the Pearson-Inc. type to the Stangenes-Inc. type for higher voltage applications of up to 350 kV. Two small-size current transformers are set in a tank circuit instead of the old home-made one; one is used for the current monitor and the other for a dedicated application of an interlock signal. So far, we have experienced no troubles up to around 320 kV in full duty and 350 kV under in lower duty. For the 350-kV application it is necessary to use a pulse-transformer with a step-up ratio of 1:15; this approach is being prepared

Forty-nine electromagnets have been manufactured up to FY95, including 2 types of magnets. Both types can be easily changed from one type to another by replacing the iron skirts and coil part. Thirty-two pulse-transformer assemblies have been modified from the old type to a new type by rewinding the pulse-transformer windings and adding pulse-circuits components. Since machine operation has been continued during the construction periods, the reformation schedule for the pulse transformer is the most tightest part.

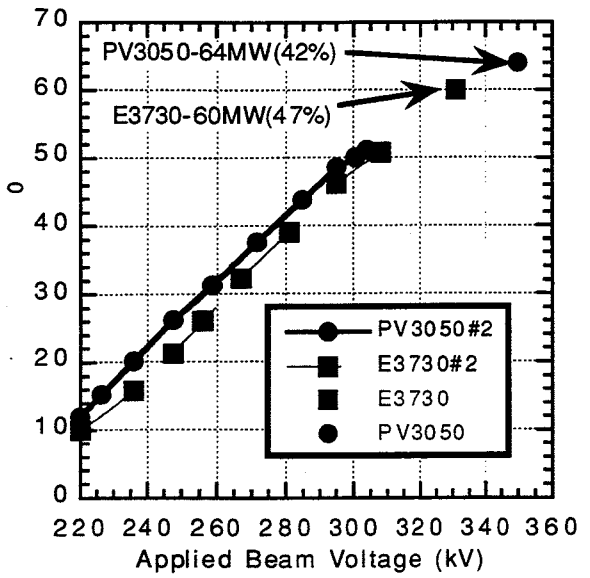

Fig. 3. Output-power characteristics as a function of the applied beam voltage

SLED Operation in the Gallery

Up to the FY95, 12 SLEDs have been installed in the gallery, and more 13 SLEDs are being installed during the summer shut-down period of 1996. Two sub-booster klystrons were installed in sectors #4 and #5; complete mode operation of the SLED has been carried out. In these sectors, conditioning of the upgraded high-power units is proceeding, and such processing data as discharging and the time dependence of the processing etc. have been analyzed. The averaged energy gain and energy-multiplication factor of the developed units in operation is 163 MeV/unit and 1.93, respectively[9].

The performances of the two sub-booster klystrons have so far been satisfactory. However, the tube efficiency is around the 30%, and the optimum focusing-magnetic field is quite different from the design field. It was found that a weak parasite oscillation exists under some conditions. It might be necessary to check the magnetic field, especially near to the cathode region. So far an output power of about 60 kW is sufficient for each high-power klystron to work at the saturation point, while 10 kW from the previous TH2436 tube was short for saturation-point operation for some poor-gain tubes. It is not clear that the some unstable operation of the SBK affects the SLED's operation or not.

A long processing time was necessary for some special unit up to the specified value. The main task for us will be to investigate what kind of the causes prevent full processing. This summer we will install another 2 sub-booster klystrons in the sectors #2 and #3, and we will also start operating in the SLED's mode there.

Conclusion

We are progressing satisfactorily regarding high-power klystron testing and installation in the klystron gallery. Purchasing the tubes and focusing electromagnets is on schedule. The final design of the pulse-transformer assembly has been fixed, and also continuously modified. The sub-booster klystrons, which are inevitable for our SLED's operation, are being developed and evaluated in the klystron gallery. Since FY95, the useful processing data have been accumulated by the SLED's operation of the sectors #5 and #4. These kinds of studies will be continued after this summer shut-down; roughly half of the construction will be completed.

References

[1] A. Enomoto et. al., "Upgrade of the 8 GeV Electron Linac for KEKB", 18th International Linac Conference, Geneva, Switzerland 26-30, August (1996)

[2] "Design Report on PF Injector Linac Upgrade for KEKB" (in Japanese) ed. by I. Sato et. al,. KEK Report 95-18, (1996)

[3] S. Anami et. al., "The RF Systems of the Photon Factory Injector Linac" Proc. of the 1981 Int. Linac Conference, Santa Fe, NM, USA, pp. 177-179 (1981)

[4] Private communication

[5] S. Fukuda et. al., "Development of the B-Factory Linac 50-MW Pulse Klystron", 17th International Linac Conference, Tsukuba, , Japan, pp.427-429 (1994) .

[6] S. Fukuda et al., "Design and evaluation of a compact 50 MW rf source of the PF linac for the KEKB project", Nucl. Instrum. and Method A368, pp.561-571 (1996)

[7] S. Michizono, Ph. D. Thesis, Tokyo University (1994).

[8] T. Shintake, "Klystron simulation and design using the Field Charge Interaction (FCI) code", Nucl. Instrum. and Method A363, pp. 83-89 (1995)

[9] H. Hanaki et al., " Test operation of the PF linac RF system upgrade for the KEKB injector", KEK Preprint 96-62, 5th European Particle Acc. Conf. (EPAC 96), Barcelona, Spain, June 10-14 (1996)

DESY LINAC-III UPGRADE STUDY

S.K.Esin, L.V.Kravchuk, V.A.Moiseev, P.N.Ostroumov, V.V.Paramonov
Institute for Nuclear Research, Moscow, 117312 Russia
W.Ebeling, N.Holtkamp, A.Febel, M.Nagl, J.Maidment
Deutsches Electronen-Synchrotron, DESY
Notkestraße 85, 22603 Hamburg, Germany

Abstract

In the frame of the HERA luminosity upgrade program, the present performance of the HERA preinjectors has been studied in detail. Upgrading the proton linac (Linac III) energy from 50 MeV to 160 MeV is one possibility currently under discussion to obtain higher luminosity. Taking into account the limited space between the existing setup and the injection beam line to the DESY III, DESY's proton synchrotron, an upgrade study of an 810 MHz linac has been carried out. The results are summarized in this paper and some aspects are discussed leading to the solution presented here.

Introduction

The present transport channel from Linac III to the synchrotron is long enough in order to use the straight beam line downstream of the last tank of the Drift Tube Linac (DTL) for installation of additional accelerating structures in order to upgrade the energy of the H^- linac. According to our study a frequency of 810.24 MHz should be used for the upgraded part. Using four times the frequency of the 50 MeV Alvarez linac allows to obtain a high accelerating gradient which accelerates the H^- beam up to 160 MeV over a distance of approximately 33 m. A higher injection energy could be a remedy against beam emittance blow-up in the DESY Synchrotron and finally would allow beams with higher brightness in HERA.

Using existing diagnostic equipment in the Linac, both the longitudinal and transverse emittances have been reconstructed by measuring the momentum spread and beam profiles [1,2,3]. In order to estimate the full emittance an elliptical symmetry for lines with constant density in phase space has been assumed. The final values of the measured emittances, which have been used for the design of the upgraded linac part as well as the main beam characteristics of the LINAC III are presented in the Table 1.

2 General Design

In the energy range to be considered which in this case is greater than 50 MeV no efficient accelerating structures other than DTL's existed so far. However recent studies carried out mainly at Los Alamos Laboratories resulted in the development of accelerating structures for intermediate energies of light ions between 20 to 100 MeV [4]. The structure is a combination of the Coupled Cell Structure (CCS) and DTL - CCDTL. Careful studies of the beam dynamics show that even for the 50 MeV beam with the characteristics listed in Table 1, an operating frequency for a CCDTL four times higher as compared to the Linac III frequency is appropriate. The use of a 810 MHz structure allows to achieve a high accelerating gain. In addition 810 MHz klystrons are available (e.g. supplied by LITTON) as with small modifications as compared to the 805 MHz klystrons which have been developed for the Fermilab linac upgrade [5]. Also the modulator system could be very similar to the Fermilab design [5] except for the average power which is 30 times smaller.

Table 1: Linac III beam parameters

Repetition rate, Hz	1
Pulse length, μs	30
Pulse current, mA	20
Energy, MeV	50
Emittance:	
Long. (φ-φ_S, $\Delta W/W$)	
α	0.0
β, deg./%	40.7
$\varepsilon_{l\ eff}$ deg·%, rms	1.55
90%	4.48
~100%	9.68
Horizontal&Vertical	
α_x	0.035
β_x, mm/mrad	5.59
ε_x, π·mm·mrad, rms	2.06
90%	9.6
~100%	33
α_y	0.885
β_y, mm/mrad	14.45
ε_y, π·mm·mrad, rms	1.81
90%	4.1
~100%	29

Providing a high accelerating gradient and the use of the fourth harmonic on the other hand results in some disadvantages which must be taken into account:

a) Smaller longitudinal acceptance with respect to the Linac III DTL;
b) High accelerating gradient causes a coupling of longitudinal and transverse motion which produce transverse emittance growth.

Both transverse and longitudinal motions of the particles require a transition region (TR) at the output of the present DTL. Using a 12 MW klystron the upgraded part of Linac must be divided into three parts. Each part is powered by a separate klystron. With one CCDTL part an energy gain of approximately 40 MeV can be achieved while the other two parts are based on a more conventional CCS. Considering in addition proper beam focusing results in 10 accelerating sections with constant phase velocity and 9 coupling bridges in the CCDTL part and 6 accelerating sections and 5 bridges in each CCS part. The quadrupole lenses are placed between the sections as well as the cavities to provide a FODO lattice. The design of the CCS has been made, taking into account that each accelerating section consists of 16 cells each.

Special attention has been given to the distance between the sections. It is obvious that this length must be as small as possible from the requirements determined by the

longitudinal beam motion. In practice this distance is chosen according to the design of the focusing lenses which are installed in between, as well as steering magnets and beam instrumentation required at these places. For linacs operating today which are based on the CCS, this space is an odd multiple of $\beta\lambda/2$ and the shortest length of $3\beta\lambda/2$ has been realized for example in the upgraded Fermilab linac. In the energy range between 50 to 100 MeV this value is not sufficient to fit the equipment mentioned before and we decided to choose the inter-section distance in the CCDTL cavity equal to $2\beta\lambda$ while for the CCL this distance is $3\beta\lambda/2$. Rectangular coupling bridges operating in a TE_{11n} mode are planned for coupling of accelerating sections in each part. This type of bridge has been successfully applied in the main part of INR linac [6]. The TE_{11n} bridge avoids mode mixing, provide the space needed for equipment and can provide either π or 2π phase shift between accelerating sections.

The Accelerating structure

The well known Side Coupled Structure (SCS) could be a good solution for the Linac Upgrade. However relatively large number of cells in the CCL sections (96) require strong coupling (> 5-7 %), which is more than typically used for the SCS. The use of a SCS in the CCDTL would result in even smaller coupling (~1%). On the other hand the Disk and Washer (DAW) structure can be used for this purpose. Nevertheless, for a comparativley short linac (272 accelerating gaps in total), the development and production cost for DAW structure is higher as compared to the CCSs. In addition a DAWDTL has not been studied in detail and preliminary studies show that more interfering modes exist. Methods to remove parasitic modes from the vicinity of the operating mode, which have been developed for standard DAW structures, are not evidently effective in DAWDTL and need more detailed analysis.

An On-axis Coupled Structure (OCS) was chosen in order to provide a larger coupling constant. In addition this structure is comparatively simple from the mechanical point of view and with the low repetition rate (heat load of the structure is only 60 W/m) it is not necessary to use internal cooling of the accelerating cells. A sketch of the OCS and OCSDTL is shown in Figure 1 and 2.

An OCS has been used already in many electron machines. For the upgrade we have studied and optimized the On-axis Coupled Structure for cells, which are used in the velocity range of $0.3<\beta<0.52$, with the 2D/3D MAFIA code [7].

A few key points have been taken into account:

- The maximum surface field is 1.35 of Kilpatrick limit (36.2 MV/m = 1.35×26.1 MV/m).
- The shape of the accelerating cells has been optimised using a 2D approximation, both for OCS and OCSDTL option.
- To reduce possible sparking rate during transients in the coupling cells the ratio of $E_{c,max}/\sqrt{W_c}$ has been limited. Here $E_{c,max}$ is a maximal electric field on the surface for the coupling mode for given value of the energy W_c stored in a coupling cell.

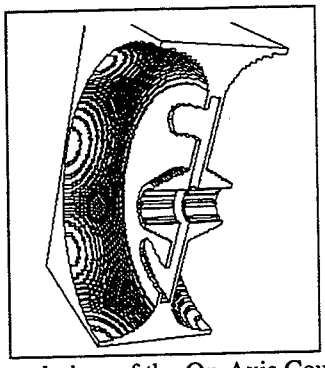

Fig. 1. The general view of the On-Axis Coupled Structure.

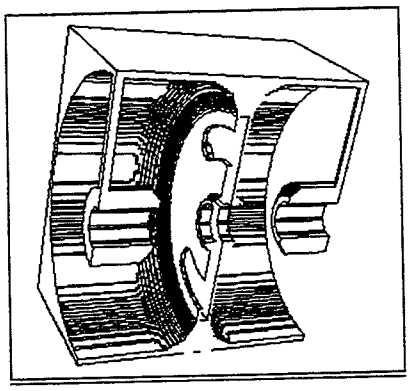

Fig. 2. The general view of the On-Axis Coupled Structure combined with the drift tubes.

- The coupling slots have been investigated and optimised. The axial length of the slot has been varied to achieve a coupling constant of 15% for OCS sections and 10% for OCSDTL sections.

The calculated values of ZT^2 , taking some degradation into account and E_0T for the finally chosen option of the OCSDTL and OCS are plotted in Figure 3.

Beam Dynamics

The accelerating structure geometry has been modeled using functions of the effective accelerating gradient E_0T, effective shunt resistance ZT^2 and the gap ratio a_g with respect to the relative beam velocity b, as being obtained from the MAFIA calculations. A general parameter list of the upgraded Linac is given in the Table 2.

Due to the different periodicity of the focusing structure in section 1 (16·bl) and section 2 (19·bl), matching of the transverse beam dimensions is necessary between these two sections. This is provided using four quadrupole lenses at the end of the cavity 1.

The main component of the transition region (TR) is a buncher cavity followed by a drift space in order to reduce the phase spread of the 202.56 MHz bunches from ±13° to ±4° as is required for the matching conditions at the entrance of the upgraded linac. The TR contains four quadrupoles to match the transverse phase space parameters.

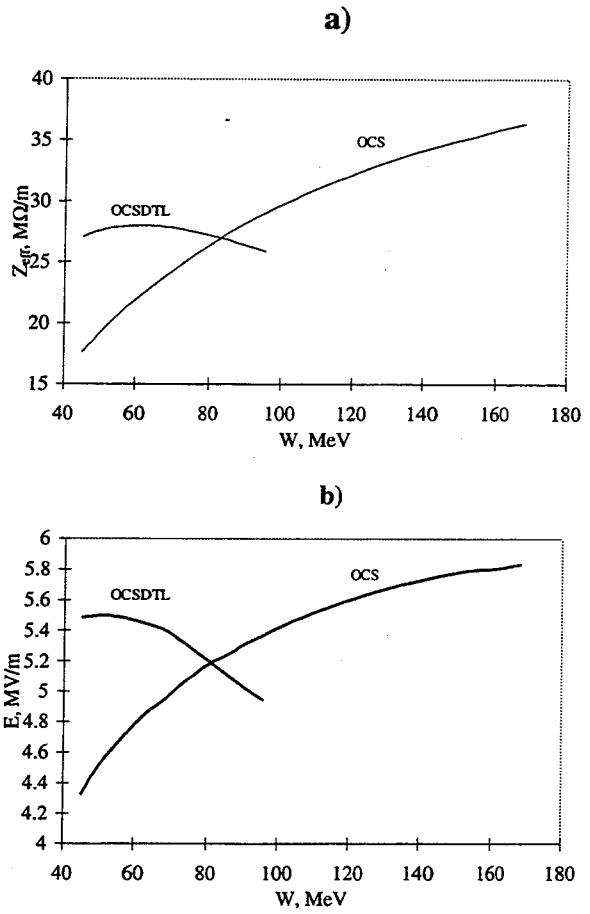

Fig. 3. Effective shunt impedance (a) and accelarating gradient (b) as a function of beam energy.

Table 2: General parameters of the upgraded linac

Parameter	Cavity 1	Cavity 2	Cavity 3
Initial kinetic energy, MeV	50	85.412	119.86
Final kinetic energy, MeV	85.412	119.86	159.75
Total length, m	10.630	9.112 m	10.084 m
Frequency, MHz	810.24	810.24	810.24
Synchronous phase	-35°	-35°	-35°
Number of sections	10	6	6
Number of cells per section	4	16	16
Type of structure	OCSDTL	OCS	OCS
Focusing structure	FODO	FODO	FODO
Section separation, bl	2	3/2	3/2
Section length, bl	6	8	8
Length of focus. period, bl	16	19	19
Cavity bore radius, cm	1.5	1.5	1.5
Power consumption, MW	9	8.5	9.0 MW
copper loss, MW	8.288	7.816	8.196
beam power, MW	0.708	0.689	0.798

In Figure 4 the beam envelopes (x-plane = solid line, y-plane = dashed line), the relative energy spread DW/W and the phase spread Dj of 90% of the particles are presented along the longitudinal coordinate for the upgraded part of the linac. The simulation has been performed for all 100% particles including a beam halo. The beam losses are less than 0.04%. An rms-emittance growth of 22 % in the transverse phase planes due to the rf defocusing has been calculated.

Several sources of accelerator imperfections and their effect on beam dynamics have been studied. The conventional random deviation of linac parameters from the design values produce a transverse rms-emittance growth of 20 % and a longitudinal rms emittance growth of 3 % with a probability of 90%. Two other sources of accelerating field distortions in a long CCS cavity are:

a) a natural drop of the rf power along the cavity containing a large number of coupled cells;
b) transient beam loading and compensation schemes. The first effect is negligible due to the high cell coupling.

The latter slightly increases the momentum spread of a 20 mA beam for a very short part of the beam pulse.

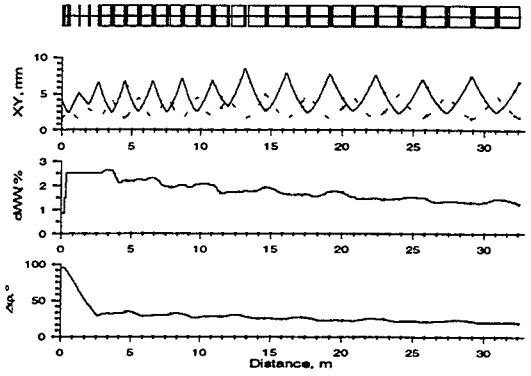

Fig. 4. Beam envelopes (90% of particles) along the linac.

References

[1] Linac III Group. Project study for the 50 MeV HERA LINAC as H^- injector for DESY III , DESY HERA 84 - 12, 1984.

[2] L.Criegee. The 50 MeV H^- Beam Transport Line. PLIN - Note 89-08, 1989.

[3]Yu.V.Bylinsky and P.N.Ostroumov. 50 MeV Linac Beam Parameters. DESY Report, February, 1996.

[4]J.H. Billen et al. A New rf Structure for Intermediate-Velocity Particles. Proc. of the 1994 Linac Conf., p. 341, 1994.

[5]Fermilab Linac Upgrade Conceptual Design Report, FNAL, November 1989.

[6] V.G. Andreev et al. The test results of the experimental module of the second part of the meson factory linac. Proc. RTI AS USSR, Moscow, No. 25, 1976.

[7] L.V.Kravchuk, V.V. Paramonov. The On-Axis Accelerating Structure for Proton Linacs with Moderate Heat Loading. This proceedings.

A THREE DIMENSIONAL BUNCH SHAPE MONITOR FOR THE CERN PROTON LINAC

S.K.Esin, V.A.Gaidash, A.V.Feschenko, A.V.Liiou, A.N.Mirzojan, A.A.Menshov, A.V.Novikov, P.N.Ostroumov
Institute for Nuclear Research, Moscow 117312, Russia
O.Dubois, H.Kugler, L.Soby, D.J.Williams
Division PS, CERN, CH-1211, Geneva 23

Abstract

The development, performance and test of the Three Dimensional Bunch Shape Monitor (3D-BSM) are presented. The principle of operation is based on the analysis of secondary electrons produced by a primary beam on a 0.1 mm tungsten wire to which a potential of -10 kV is applied. The horizontal particle distribution is provided by moving the wire across the primary beam. A horizontal slit located outside the primary beam area is moved vertically in order to analyse the secondary electron density distribution in the vertical direction. The longitudinal profile is measured as in the bunch length detector developed at INR earlier. The 3D-BSM has been installed and commissioned at the CERN proton linac.

Introduction

The distribution of charge in the real beam of linear accelerators is described by a three dimensional distribution function $I(x,y,z)$ or $I(x,y,\varphi)$. Conventional beam instrumentation devices provide projections of this function for just one of the co-ordinate axes or planes. Thus, widely used wire scanners and harps provide a one co-ordinate function. To measure the longitudinal distribution, bunch shape monitors are used [1-3]. There is also the method and device to measure two dimensional distribution in the transverse plane [4] as well as the proposal to obtain a two dimensional distribution with a combination of the longitudinal and one of the transverse planes [5].

The first idea to measure a real three dimensional distribution is described in [6]. This idea has been revised and implemented in the Three Dimensional Bunch Shape Monitor (3D-BSM) developed and built at INR for the CERN proton linac.

General Configuration and the Design

The general configuration of the 3D-BSM is presented in fig. 1. The beam under study crosses the target (1) (tungsten wire 0.1 mm diameter) and knocks out low energy secondary electrons. A HV negative potential (-10 kV) is applied to the target. Owing to the high strength of electric field near the target, the electrons move practically horizontally and their vertical co-ordinates at the plane of the horizontal slit (2) correspond to a short vertical section of the target wire determined by the position of the slit.. If the target has a horizontal co-ordinate X_0 and the slit a the vertical co-ordinate Y_0 then the intensity of the electron current downstream of the slit is proportional to the intensity of the primary beam at the point (X_0,Y_0) of the transverse plane and its temporal structure reproduces that of the proton beam. The temporal structure of the electron beam downstream of the slit is coherently transformed into a spatial one through transverse rf modulation in the deflector (3) combined with the electrostatic lens as in the conventional

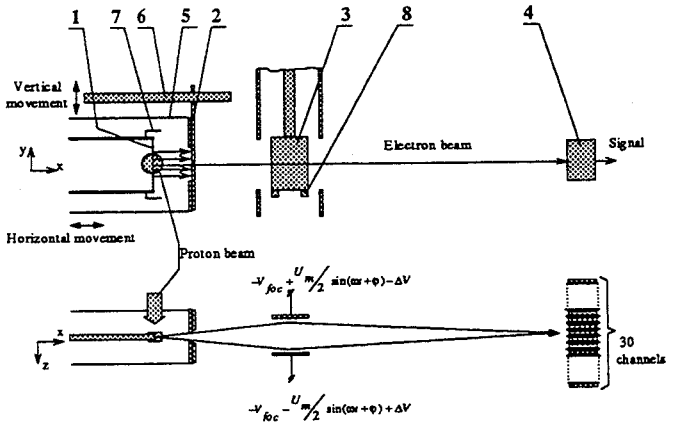

Fig. 1 General configuration of the 3D-BSM

bunch shape monitor. This spatial distribution is measured with the 30 channel electron collector (4). For a fixed position of the target and the slit, the signal from one channel of the collector is proportional to the intensity of the protons having the corresponding transverse and longitudinal co-ordinates. The signals from all the channels represent the longitudinal distribution of protons with the transverse co-ordinates (X_0,Y_0). By measuring the longitudinal distribution for different locations of the collimator one can get a two dimensional distribution $I(x_0,y,\varphi)$. A three dimensional function can be obtained if a horizontal movement of the target is added. If however, the target were displaced without the collimator and slit following it, the temporal structure and intensity of the electrons would change. To avoid these effects the target is surrounded by an electrostatic screen (5) which moves with the target. Since now the electrostatic field pattern in the target - collimator area remains constant, the temporal structure of the electrons is not modified. Similarly, the intensity of the electrons passing through the slit does not change. Variation of the drift distance from the slit to the

deflector entrance results in a systematic phase error which has however, been taken into account knowing the well defined velocity of the electrons. When the position of the target, along with the screen changes with respect to the deflector-lens, the size of the focused beam at the collector varies but the variation of phase resolution is negligible.

When the target and the electrostatic screen are moved, the collimator plate also moves, sliding along the guide (6). Vertical movement of the collimator is provided by the vertical displacement of the guide.

There are strict requirements for the vertical uniformity of the accelerating electric field in the target region and for the focusing field in the deflector-lens. Non-uniformity of the accelerating field leads to vertical displacement of the electron beam from the working area of the collector when the collimator is moved, thus resulting in loss of information. Non-uniformity of the focusing field is the main reason why the phase resolution is dependent on the collimator position. To avoid the first effect, the correcting elements (7) are installed on the target holders. The second effect is corrected with the help of the elements (8) installed on the plates of the deflector-lens. Use of these elements helped obtain a vertical operating range of ±10 mm. There are also requirements for the uniformity of the rf deflecting field but in our case this problem was negligible.

The assembly drawing of the detector is presented in fig. 2. The 3D-BSM includes the following main units: body

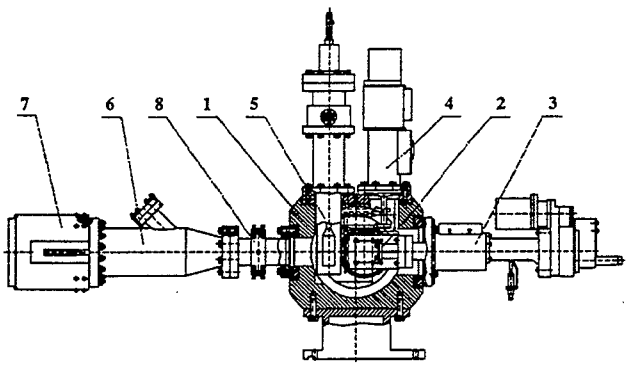

Fig. 2 Assembly drawing of the 3D-BSM

of the detector (1), target unit (2) with the screen and the collimator plate, target actuator (3), collimator actuator (4), rf deflector combined with electrostatic lens (5), registration unit (6) including multi-channel collector along with the viewing port and the mirror for visual observations of the thermal electrons during laboratory tests, signal preamplifier (7) and permanent adjustable magnet (8) to steer the electrons vertically.

Signal Detection and the Control System.

To detect the electron intensity a multi-channel electron collector, along with sensitive signal amplifiers are used. The 30 channel collector, developed for the 3D-BSM, is of a sandwich type consisting of collector, insulating and bias plates. The latter are used to limit the influence of secondary emission electrons from the collector plates.

The signals are amplified by fixed gain (30 mV/nA) preamplifiers followed by amplifiers with remotely controlled gains. The overall gain can be changed from 3 mV/nA to 1500 mV/nA in 10 steps. For normal operation of Linac-2 (peak current 130-140 mA) the gains of 50-100 mV/nA were used. A calibration mode with a 10 nA input signal has been incorporated. The response time of the amplifier chain is 2-3 μs and the rms noise level is about 0.5 pA/√Hz.

The 3D-BSM has an independent control system using an IBM PC and one VME crate. Special electronic modules (HV, rf, interface, stepper motor drivers) are housed in two additional CAMAC crates. Using five 8 channel STR755 digitizers gives the possibility of sampling all of the signals with 250 ns steps, thus providing information on the behaviour of the distribution in time and allowing a four dimensional function $I(x,y,\varphi,t)$ rather than the three dimensional distribution to be obtained.

The software includes three programs. The first one is used for signal observation, detector parameter adjustment and detector tuning. The measurements and the initial data processing are made with the help of the second program whilst the third gives visual presentations of the results.

Total measuring time depends on the number of points in the transverse plane. For example 20 points along the vertical and 20 points along the horizontal axis require 420 pulses of the accelerator = 504 sec. plus about 1 minute for setting up and 5 minutes for data processing.

Parameters of the 3D-BSM

To find the vertical resolution, a simulation of electron dynamics from the target to the collimator was made. The vertical size of the electron beam emitted from a fixed point on the target was calculated to be about 0.5 mm at the slit, therefore this is the best vertical resolution that can be obtained, however, a 1 mm slit was chosen rather than risk an inadequate signal intensity.

A value of phase resolution of less than 1° of rf phase can be achieved. However, to fully cover the 60° rf phase of the linac bunches with the 30 channel collector, the power in the deflector was decreased from 15 W to 1.5 W thus reducing the resolution from 1° to 3°.

The detector has the following main parameters:

Horizontal resolution	<0.1 mm
Vertical resolution	1 mm
Phase resolution	<1°
Horizontal range of measurements	±10 mm
Vertical range of measurements	±10 mm
Operating frequency	202.56 MHz
RF power consumption	1.5-15 W
Signal response	2-3 μsec

Detector Commissioning

Laboratory commissioning included testing of the hardware and tuning electron optics using thermal electrons produced by heating the target. Selection of the shape and size of the correcting elements has also been made from observation of thermal electrons. The spiral shape of the correcting elements (8) was chosen to minimise their influence on the resonant frequency.

After installation of the detector in the beam line, it was tuned with secondary electrons; the values of the focusing voltage (V_{foc}), the steering voltage (ΔV) and the rf voltage (U_m) (fig. 1) were optimised and the correspondence of the channel number to phase was determined. To find the latter, the dependencies of the channel output signals vs deflecting field phase for slow phase variations (from pulse to pulse) are measured. The functions obtained represent the same bunch shape but are shifted along the phase co-ordinate. This shift gives the function of channel to phase correspondence for given values ΔV and U_m.

The very first measurements proved the efficacy of the detector. However we encountered the following unexpected phenomenon. In a range of target positions from -9 mm to -3 mm the signals from all the channels increased abnormally. These signals appeared for beam currents above 50 mA, they increased with time, and after 50 μsecs considerably exceeded the signals obtained with normal beam current. Analysis of the observations enabled the following assumption to be made about the nature of the unexpected signals. On passing through the detector, the beam induces electromagnetic fields and moving the target unit with its electrostatic screen and collimator plate changes the resonant frequencies of the system. For the target positions mentioned above, resonant conditions are satisfied for high harmonics (presumed >1 GHz) of the bunch frequency. Electromagnetic fields penetrate into the deflector through its openings and initiate oscillations on the correcting elements (8) (fig. 1), initially made as spirals, and thereby cause a multipactor discharge in equipotential space between the turns. Owing to the HV focusing potential applied to the spirals, the space between the turns is equipotential and the electrons produced in the discharge are accelerated by the electrostatic field; a fraction of them reaches the collector producing the unexpected signals. This mechanism explains all the observed experimental effects.

The following improvements were made to avoid the unexpected signals: the spiral elements were replaced by plates, screening of the deflector cavity was improved and additional screening of the space between the collimator and the deflector exit was made. After the improvements the unexpected signals totally disappeared.

It was anticipated from the design calculations that the 3D-BSM target could overheat if the product of the beam current and its duration exceeded a certain value. Experimental testing of the thermal stability of the wire showed that neither thermal emission nor target destruction occurs for the maximum beam intensity during normal operation: current 140 mA and pulse duration 145 μsec.

Up to now we have no final conclusion about the influence of the beam fields on the detector operation and its parameters. Whilst increasing the target potential should decrease these effects, measurements with different target potentials have shown no change in the transverse parameters for target potentials of -7.5 kV and -10 kV.

The main results of the first experiments are presented in [7].

Conclusion

A fundamentally new beam instrumentation device for the CERN 50 MeV proton linac has been developed, built and successfully commissioned. The 3D-BSM enables proton density distribution to be measured in real three dimensional co-ordinate space and, moreover, shows its variation along the beam pulse. Commissioning and first measurements have confirmed the validity of the principal idea and the correct choice of elements for the realisation of this detector. The complexity of the detector and its application in an area of very intense proton beams resulted in some problems during its initial operation. Most of these seem to be solved successfully. A full understanding of the device's potential and limitations will, however, require machine development studies dedicated to the characterisation of the device itself. So far no degradation of quality has been observed in the PS-Booster beam when the 3D-BSM is being used.

References

[1] Feschenko A.V., Ostroumov P.N. Bunch Shape Measuring Technique and Its Application For an Ion Linac Tuning, Proc. of the 1986 Linear Accelerator Conference, Stanford, 2-6 June, 1986, pp. 323-327.

[2] Hurd J.W. and 11 coauthors, Bunch Shape Monitor for SSCL Linac. Proc of the 1993 Particle Acc. Conf., Washington, May 17-20, 1993, V.3, pp. 2426-2428.

[3] Bylinsky Yu.V. and 6 coauthors, Bunch Length and Velocity Detector and its Application in the CERN Heavy Ion Linac. Proc. of the EPAC-94, London, June 27-July 1, 1994, pp. 1702-1704.

[4] A.Tron. Secondary electron method of monitoring of beam distribution in transverse cross section. Proc. of the XIV Meeting on Particle Accelerators, V.2, Protvino, 1994, pp. 87-92 (in Russian).

[5] A.V.Feschenko, A.A.Menshov, P.N.Ostroumov. A Detector to Measure Longitudinal and Transverse Distributions of a Two Component Ion Beam. Proc of the EPAC-92, Berlin, 22-24 March, 1992. V.2, pp. 1073-1075.

[6] S.Esin, A.Feschenko. Detector of three dimensional charge density distribution function of linear accelerator beam. Proc. of the XIV Meeting on Particle Accelerators, V.2, Protvino, 1994, pp. 17-20 (in Russian)

[7] O. Dubois and 10 coauthors, Study of Beam Parameters of the CERN Proton LINAC Using a Three Dimensional Bunch Shape Monitor, Proc. of this Conf.

STUDY OF BEAM PARAMETERS OF THE CERN PROTON LINAC USING A THREE DIMENSIONAL BUNCH SHAPE MONITOR

A.V. Feschenko, A.V. Liiou, P.N. Ostroumov
Institute for Nuclear Research, Moscow 117312, Russia

O. Dubois, H. Haseroth, C. Hill, H. Kugler, A. Lombardi, F. Naito, E. Tanke, M. Vretenar.
CERN, CH-1211, Genève 23, Switzerland.

Abstract

A Three Dimensional Bunch Shape Monitor (3D-BSM) has been developed for the CERN Proton Linac 2. A new area for beam studies at high intensities has been opened by this detector. Bunch density distributions in all three dimensions and their variations along the beam pulse can be obtained. Changing field gradients in linac quadrupoles, emittance variation along the bunch has been calculated. Measurements of beam halos become possible thanks to the large dynamic range of the device. Beam parameters at various linac settings have been measured and analysed.

Introduction

The new detector [1] allows the measurement of the three dimensional density distribution I(x,y,z) of a bunch and its evolution along the beam pulse. For example, using this distribution the first and second moments and the beam profiles in each direction (x,y,z) have been obtained. The CERN Linac 2 is a high intensity accelerator consisting of an RFQ and three Alvarez tanks producing 140 mA of protons at 50 MeV [2]. As proven during the detector commissioning, the 100 μm tungsten wire can operate safely with pulse lengths up to 145 μs. The insertion of the target in the beam does not disturb injection into the downstream booster synchrotron. Therefore the 3D-BSM can be used as a non-destructive beam diagnostic tool during linac operation.

Bunch Shape Measurements of the 50 MeV Beam

In Fig.1 the evolution of the longitudinal profile along the beam pulse is presented. The analysis of the figure as well as of the evolution of other beam parameters along the bunch shows that beam-loading is well compensated in Linac 2. There is no variation either of the bunch centre or the bunch shape along the entire pulse length. It has been demonstrated that the bunch shape changes along the pulse if beam-loading is not sufficiently compensated. This can be seen in Fig. 2 where the RF field in tank 3 has been increased by 4% while keeping the maximum power to the tank constant.

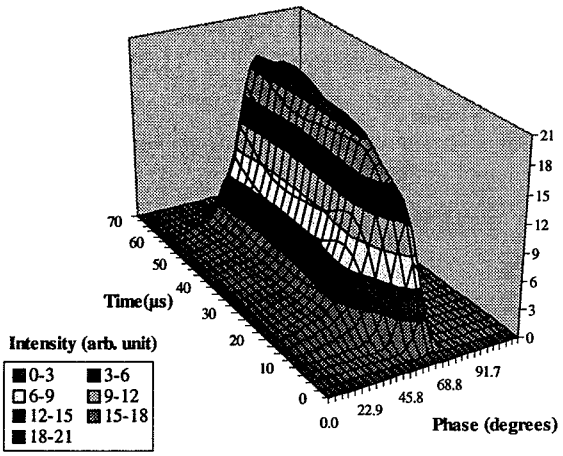

Fig. 1. Bunch shape evolution along the beam pulse for nominal settings. Linac RF frequency is 202.56 MHz.

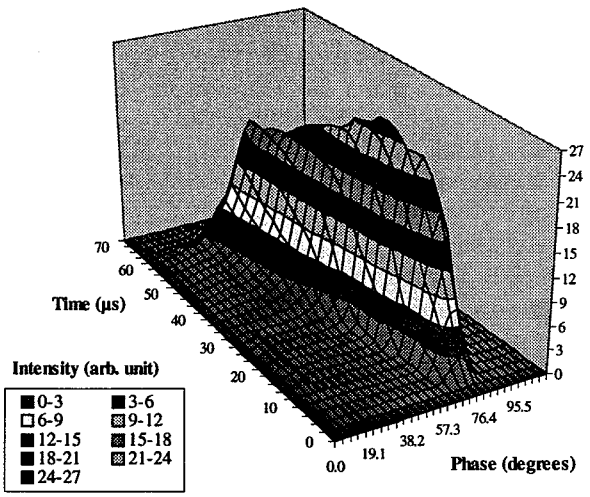

Fig. 2. Bunch shape evolution along beam pulse in case of insufficient beam loading compensation in tank 3.

When changing the phase of tank 3 in a 60° range, the bunch length varies between 13° and 30° (1 rms values) and the phase of the bunch centre (with respect to the phase of the reference line) varies by 130° (see Fig. 3). Deviation of the bunch centre phase is due to two main reasons: the energy change and the coherent oscillations in the longitudinal phase space.

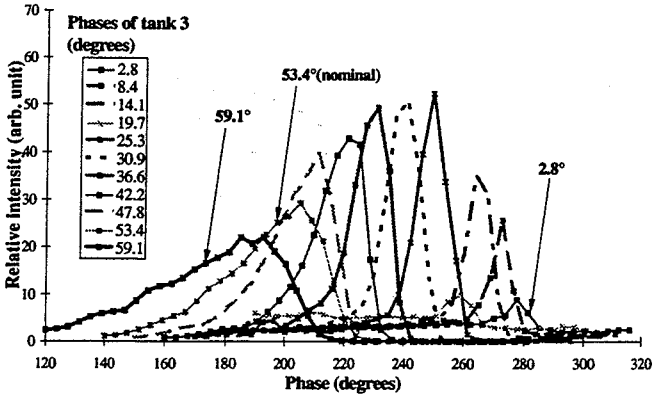

Fig. 3. Average (over entire bunch volume and whole pulse) bunch shapes for different tank 3 phases. Nominal phase of tank 3 corresponds to 53.4°.

Although the present phase setting of the last tank (53.4°) produces long bunches with a specific tail (see Fig. 3), it seems that the energy spread is moderate in that case, so that the beam is safely transported to the booster rings.

The high intensity beam dynamics for different phases of tank 3 have been simulated by the computer code LANA [3]. Simulations gave a bunch width about two times smaller than the observed one. The difference is mainly due to the tails. The central part of the bunch is well reproduced by LANA. The bunch centre variations with tank 3 phase are similar to simulations results (see Fig. 4). Some changes of the amplitude in tank 3 from the design values even improve the fitting.

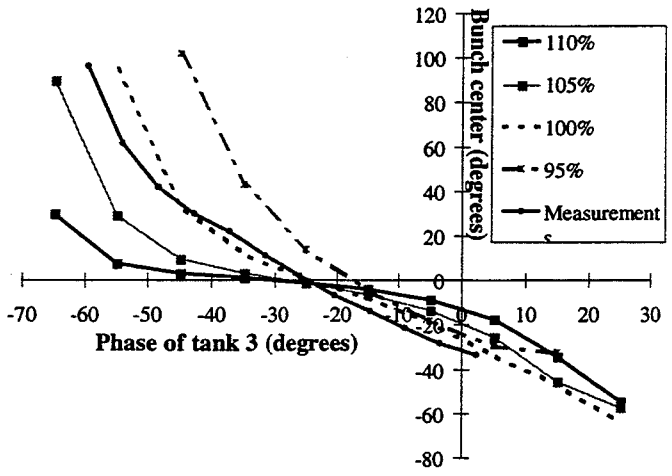

Fig. 4. Bunch centre as a function of protons arrival phase in tank 3. The experimental curve has been arbitrarily placed on this graph.

The bunch shapes have been measured for various rf field levels in the first and third tanks and different beam currents. All the measurements showed a strong dependence of the density distribution of the bunch on the parameters of the linac.

Study of Transverse Emittance Variation along the Bunch

From the measured data, the transverse rms size of the proton beam has been calculated for "slices" (in phase) through the bunch. The rms beam widths have been measured for three magnetic field gradient settings in upstream quadrupoles inside tank 3. Using these data the (rms) emittance as a function of phase along the bunch has been calculated (see Fig. 5). Due to limited time for all experiments, only the measurements enabling the derivation of horizontal emittance have been made. These studies were restricted to the central part of the bunch, where the signal level ensures a good precision. However, the beam transverse behaviour can also be studied in the bunch tails using a higher dynamic gain of the signal amplifiers of the 3D-BSM. There is a significant variation of the rms beam size with phase.

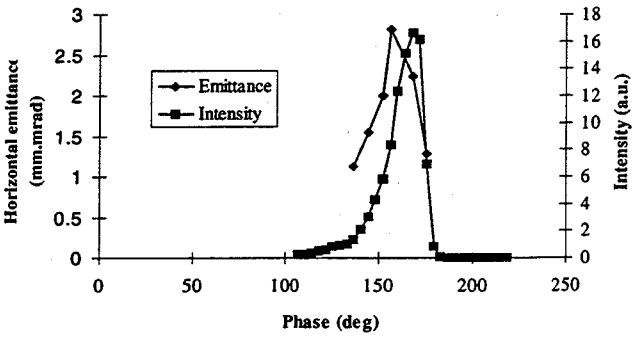

Fig. 5. Horizontal unnormalized rms emittance of beam and intensity versus phase.

The iterative use of TRACE and TRANPAR [4] allowed the derivation of horizontal transverse emittance taking into account space charge and acceleration in the last three gaps (between the quadrupoles used for the experiment) for different "slices" along the bunch (see Fig. 5 and 6). The use of the TRANPAR code alone to reconstruct emittances showed that neglecting space charge in this calculation process can induce an error of up to 50% on emittances.

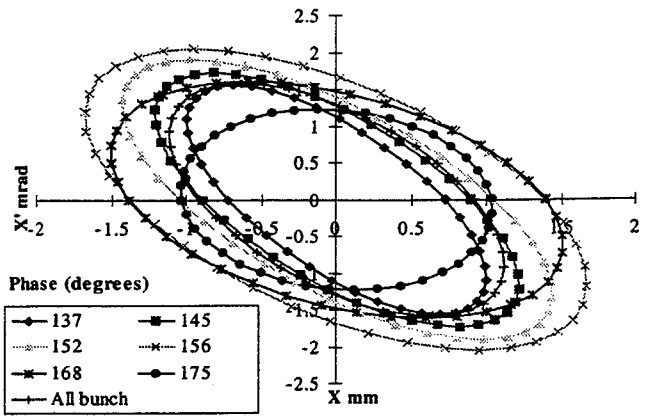

Fig.6. Evolution of the horizontal rms emittance. Only the central part of the pulse (20 to 65 μs in that case) has been taken into account.

The horizontal rms emittance averaged over the whole bunch and the whole pulse (0 to 75 μs) is 2.5 mm.mrad, which is consistent with the theoretical value from PARMILA (2.4 mm.mrad).

Measurement of the Transverse Density Distribution.

The 3D-BSM has a wide dynamic range: the signal gain can be varied by a factor 500. It can be used for the measurement of transverse cross-sections of the beam (see Fig. 7), including halo because these measurements do not require rf voltage on the deflector of the 3D_BSM [1].

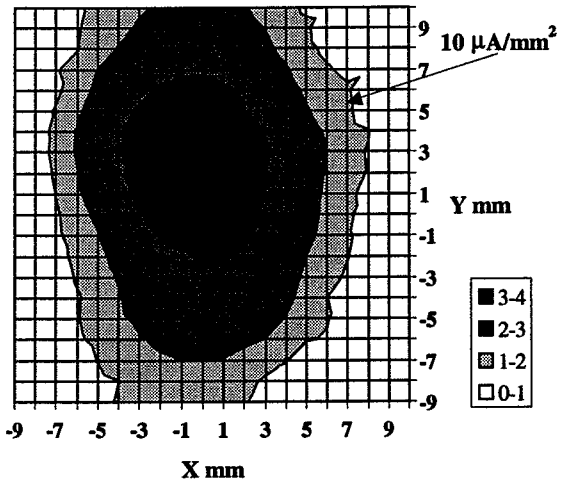

Fig. 7. Beam cross-section. This graph shows log(j) where j is the proton current density in μA/mm². The total current is 150 mA. The maximum current density is 3.95 mA/mm². The borders between shades represent 1000, 100 and 10 μA/mm². They contain respectively 69.0, 96.9 and 99.7% of the beam.

Bunch Distribution in φ-x Plane

The bunch length depends on the horizontal position (see Fig. 8a). The bunch length has a maximum for a horizontal position different from the mean. This effect could be due to the influence of the field created by the space charge of the proton bunch on the trajectory of the secondary electrons ejected from the tungsten wire[1]. However it is still unclear why this effect is smaller for shorter bunches, when the proton density is higher (see Fig. 8b). Therefore, it could be a real feature of the proton beam due to a misalignement of quadrupoles in the linac. It is possible to simulate such an asymmetry by arbitrarily misaligning quadrupoles in tank 1 with DYNAC [5], but large alignment errors are required. More theoretical and experimental work is required to explain this effect. For instance, the 3D-BSM will be studied by a computer model including the influence of the space charge of the bunch on secondary electrons.

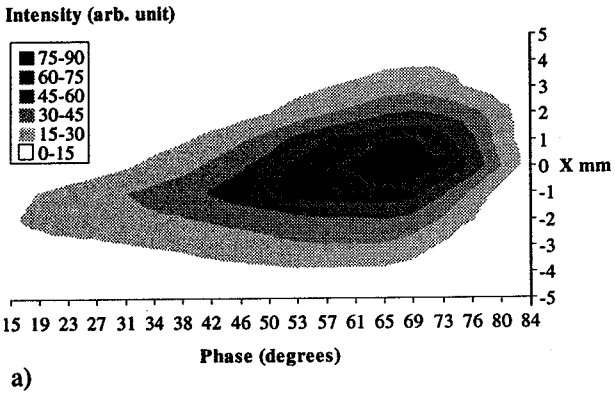

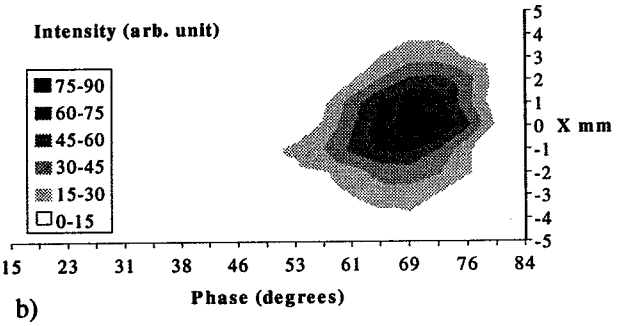

Fig. 8. Beam density distribution in φ-x plane for long (a) and short (b) bunch.

Conclusion

The study proved the effectiveness of the 3D-BSM in monitoring both transverse and longitudinal beam parameters. It has demonstrated that the bunch density distribution is very sensitive to the working parameters of Linac 2. The 3D-BSM will be an essential tool in future high intensity studies at currents greater than 180mA at the exit of the linac.

References

[1] O. Dubois, S.K. Esin, A.V. Feschenko, V.A. Gaidash, H. Kugler, A.V. Liiou, A.N. Mirzojan, A.A. Menshov, A.V. Novikov, P.N. Ostroumov, L. Soby, D. Williams, "A three dimensional bunch shape monitor for the CERN proton Linac." This conference.

[2] E. Boltezar, H. Haseroth, W. Pirkl, G. Plass, T. Sherwood, U. Tallgren, P. Têtu, D. Warner, M. Weiss, "The new CERN 50 MeV Linac". Proc. 1979 Linear Accelerator Conf., 10-14 September 1979, Montauk, New York, USA, p. 66-77.

[3] D.V. Gorelov, P.N. Ostroumov, "Application of the LANA code for design of ion Linac", EPAC 96, 10-14 June, Barcelona, Spain.

[4] I.N. Birukov, A.N. Mirzojan, P.N. Ostroumov, S.A. Petronevich, "Transverse beam parameter measurements at the INR proton linac". Proc. EPAC 92 Conf., Berlin, 24-28 March, V. 2, p. 1109-1111.

[5] P. Lapostolle, E. Tanke, S. Valero, "A new method in beam dynamics computations for electrons and ions in complex accelerating elements". Particle Accelerators, 1994, V. 44., p. 214-255.

THE STATUS OF DESY H⁻ – SOURCES

J. PETERS
Deutsches Elektronene-Synchroton DESY, Notkestrasse 85, 22607 Hamburg, Germany

Abstract

Two different types of H^- sources are operated at DESY, a magnetron source and an rf- driven volume source.
H^- sources for HERA have to run for long uninterrupted periods with a low duty factor and a high reliability.
Several necessary improvements are under construction for our rf - driven volume source.
The status of both our magnetron and our volume source will be discussed and the first LINAC III experiment with the rf-driven volume source will be presented.

Introduction

The H^- source is a component of LINAC III, the injector for DESY III. The H^- ions are converted to protons using a thin stripping foil. Multiturn injection then allows particle accumulation in the synchrotron, as described in Ref. [1].

At present an 18 kV magnetron source [2] is operated as the H^- source for LINAC III, with the matching of the source to the 750 kV RFQ (Radio Frequency Quadrupole) done by a LEBT (Low Energy Beam Transport) consisting of two solenoids.
A magnetron source has to be operated with cesium in order to reduce the work function for electrons.
The availability of the source is limited by the delay due to cesium [3].
A cesium free source became even more desirable for use on LINAC III when a glow discharge was seen in the four vane RFQ and multipactoring occurred in the first section of the Alvarez tank of LINAC III.
Although it was not possible to detect cesium in the RFQ or the Alvarez tank nevertheless measurements showed traces of cesium leaving the source [3].
A volume source can be operated without cesium. It has a lower emittance, but if uncesiated it produces a lower output current than a magnetron source.

Status of the magnetron source

The DESY magnetron has been operating since 1985. It is based on the design of FNAL [2] and was modified according to the DESY requirements [3]. Since 1993 the magnetron has been operated from one HERA maintenance period to the next for 152, 301 and 291 days without breaking the vacuum. There were only minutes of interruption due to failures of the electronics. Figure 1 shows the run periods since 1993. Until now the source has run in 1996 for 171 days.

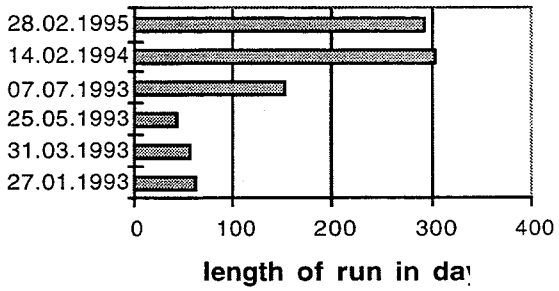

Fig. 1 Uninterrupted operation period of the magnetron vacuum unit.

Operation periods of more than 300 days are possible due to the low duty cycle of 75 µsec/6 sec = 12×10^{-6}.
Data from the magnetron source are summarized in Table 1.

Table 1: Data of the magnetron H^- source.

beam energy	18 keV
H^- beam current	60 mA
emittance	
$\varepsilon_{x\ rms.norm}$ ($\varepsilon_{x\ 90\%.norm}$) (35mA beam)	0.28(1.35) π mm mrad
$\varepsilon_{y\ rms.norm}$ ($\varepsilon_{y\ 90\%.norm}$) (35mA beam)	0.25(0.81) π mm mrad
arc voltage	140 V
arc current	47 A
arc pulse width	75 µsec
extraction repetition rate	1/6 Hz
magnetron repetition rate	1/6 Hz/ 6 Hz
cathode temperature	249 °C
anode temperature	147 °C
Cs boiler temperature	100 °C
Cs consumption 6 Hz magnetron repetition	3mg/day

The emittance in the vertical plane, is reduced due to aperture limitations of the magnet gap. A beam of up to 100 mA can be produced.

Status of the rf - driven volume source

The rf - driven volume source was originally built by AccSys [12] using plans from LBL [4]. The source was redesigned by DESY in order to gain a better reliability, higher currents and a beam energy of 35 keV.

A DESY designed piezo valve is now used which has successfully operated in the DESY magnetron source for many years. As the pulser of the piezo valve has to be rack mounted we had to build a new high voltage deck (see Fig. 2). The filament was replaced by a flash light which is directly mounted to the source bucket. It has a UV window Ref. [5].
The source is connected to a computer control system which delivers histograms and programmed diagrams of parameter dependencies.

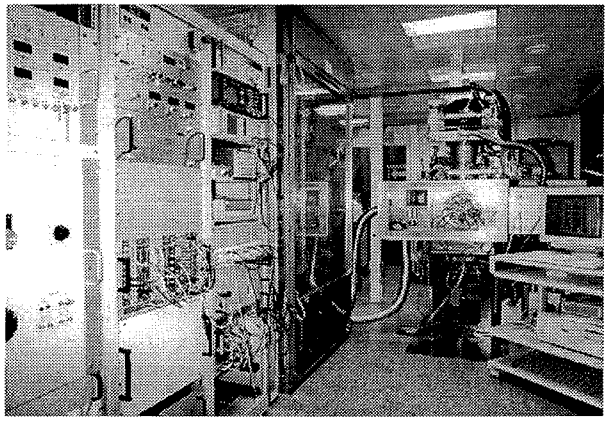

Fig. 2 rf driven volume source at DESY R&D laboratory.

A 2000 l/s vacuum pump and a water cooling system for the multi cusp bucket are necessary.

Figure 2 shows the rf driven volume source at DESY R&D laboratory with the new 35 kV box connected to the bucket.
The extraction system is an electrode with a 60 mm wide spectrometer similar to the LBL design [4].
An electron current of about 1A is dumped on a grooved graphite plate. The magnets are encapsulated in vacuum tight steel boxes in order to protect them against hydrogen (see Ref. [6]).
The beam position is corrected with a horizontal and vertical adjustable collar and plasma electrode.
The adjustments were measured with a multi faraday cup [6] which was inserted into the beam pipe. The beam current was measured in the 35 mm beam pipe with a current transformer. For several weeks it was possible to run the source above 23 kV with a current of 33 mA. Details are given in [9].
Measurements of the emittance are done after the beam is collimated by a 35 mm ∅ beam pipe which is more than 80 mm long.
The emittance was measured with a slit and grid system. Table 2 summarizes the data of this configuration.

LINAC 3 - DESY 3 test with the rf driven volume source

During January 1996 the magnetron source of LINAC 3 was replaced by the rf driven volume source.
The extraction system shown in Fig. 3 was connected to a LEBT consisting out of two solenoids.

Table 2: Data of the rf H^- source with a spectrometer.

beam energy	18–35 keV
beam current	16–33 mA
emittance	
$\varepsilon_{x\ rms,norm}$ ($\varepsilon_{x\ 90\%,norm}$) (16mA,18 keV beam)	0.18 (0.81) π mm mrad
$\varepsilon_{y\ rms,norm}$ ($\varepsilon_{y\ 90\%,norm}$) (16mA, 18 keV beam)	0.16 (0.72) π mm mrad
source voltage	–18 to –35 kV
extraction voltage	0 V
electron current	0.8–1.8 A
rf output power	25–45 kW
pulse width	100 µsec
repetition rate	1–6 Hz

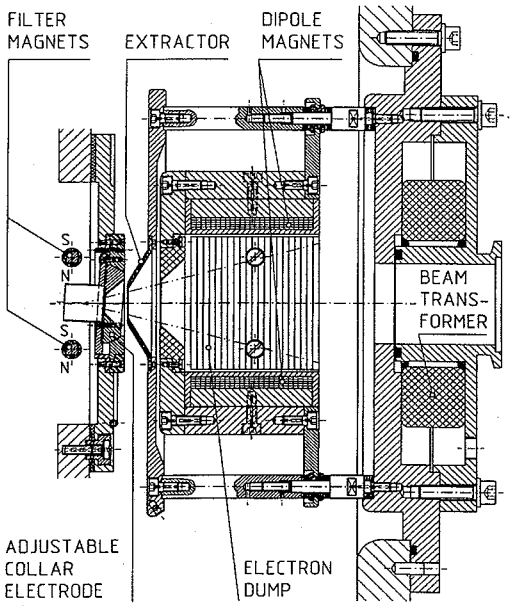

Fig. 3 rf driven volume source with a wide spectrometer and an adjustable collar electrode.

At the beginning the source delivered a 18 keV, 20 mA H^- current and about 39% of the beam was measured behind the RFQ.
Emittance measurements were made in the HEBT (High Energy Beam Transport) line. Table 3 summarizes the measurements with the magnetron and the volume source done at LINAC 3 [7].
There is almost no beam loss between tank 1 and tank 3 of the alvarez .
At DESY 3 after accumulation and acceleration to 7.5 GeV/c a proton current of 60–70 mA was measured [8].

Future source plans

The rf driven volume source of DESY has delivered a H^- beam of 15–33 mA for more than a year.

The long term experience shows that the graphite dump for the electron current deteriorates. It will be replaced by a multi faraday cup which makes it also possible to check the position of the electron beam.

Table 3: LINAC 3 measurements

	magnetron		volume source	
	current	trans-mission	current	transmission
source	60 mA		16.9 mA	
		0.33		.34 (.39)
RFQ	20 mA		5.8 mA	
		0.64		0.75
alvarez	14 mA	0.78	4.4 mA	0.9
HEBT	11 mA		4.3 mA	
$\varepsilon_{x\ rms.norm}$	0.68 π mm mrad		0.43π mm mrad	
$\varepsilon_{y\ rms.norm}$	0.6 π mm mrad		0.46 π mm mrad	

The reliability of the source depends very much on the quality of the antenna coating.
The H^- current will not only depend on the insulation of the antenna but also on sputtering of antenna insulation to critical parts of the bucket surface.
This insulation will limit the recombination of H^+ ions to H_2 and the production of excited H^*_2 on the walls.

Reliable tests were developed which make it possible to check the antenna insulation outside and inside of the source bucket. Before installation a power test in salt water detects even small defects in the coating.
After installation in the bucket the antenna insulation can be checked by applying HV during gas pulsing and measuring the antenna current. This makes a change of the driving circuitry necessary.
During operation of the source it was checked if critical parts of the antenna are not isolated by measuring the antenna bias voltage.
The transition during sparking damages the antenna significantly. Even with well designed HV circuitry it can not completely avoided. It happens mainly at the gap between extractor and plasma electrode.

Successful test were done with a small insulated plasma electrode. It is situated on the main plasma electrode opposite to the extraction electrode and is directly connected to the HV power supply.
If sparking occurs in the gap the current can flow directly to the HV supply.
Besides the insulation and sputter problem of the antenna there is also a limitation due to the different expansion of
the coating and the copper material in a source pulsed with 50 kW rf .

These problems can be easily solved by separating insulation and antenna. Al_2O_3 has similar sputtering coefficients to the Ti O_2 coating presently used .
With new methods [10] extremely smooth surfaces can be produced. The disadvantage is that only simple geometries can be improved.
Mafia calculations [11] show that rectangular antennas have similar fields to the present antenna. They can be built out of Al_2O_3 bends and straight pipes with a copper pipe inside.
A flat circular antenna behind a Al_2O_3 window has a different field but would be mechanically less complicated. Both antenna types are under production.

Conclusion

The magnetron source was successfully adapted to the HERA environment. Further test and development ofthe volume source is necessary to improve its reliability and performance.

Acknowledgment

The author is grateful for the contribution of the following colleagues at DESY:
N. Holtkamp, I. Hansen, H. Sahling and R. Subke.
I wish to thank the technical groups at DESY for their support, the students T. Butschkat (FHH) and O. Krücken (FHW), T. Warner (FHW) for their programming and J. Maidment of DESY for helpful suggestions to wording of the report. The support of the source groups of LBL, FNAL and BNL is gratefully acknowledged.

References

[1] LINAC3 collaboration, Rev.Sci.Instruments **62** (4), April 1991.
[2] Ch.W. Schmidt et al., IEEE Transaction on Nuc. Sci., NS-26 (1979) 4120.
[3] J.Peters, Rev.Sci. Instruments, **65** (4), April 1994, pp. 1237–1239.
[4] K.N. Leung, D.A. Bachman, and D.S. McDonald, AIP Conf. Proceedings No. 287, pp. 368–372.
[5] K.N. Leung, Rev. Sci. Instruments, **67** (3), March 1996, pp. 1302–1307.
[6] J. Peters, Rev. Sci. Instruments, **67** (3), March 1996, pp. 1046–1047.
[7] P.N. Ostroumov, Institute for Nuclear Research of the Russian Academy of Sciences, 117312 Moscow, Russia, private communication.
[8] W. Ebeling, DESY, private communication.
[9] J. Peters, DESY, to be published.
[10] Seilsdorfer GMBH & CO,D-83527 Haag-Winden.
[11] S. Wipf, DESY, private communication.
[12] AccSys, Pleasanton, California 94566.

SPACE-CHARGE NEUTRALIZATION EXPERIMENT WITH A LOW-ENERGY PROTON BEAM

P.Y. Beauvais, J.M. Lagniel. CEA-Saclay, DSM-GECA, LNS,
N. Pichoff, G. Haouat, P. Chaix, CEA/DRIF/DPTA, Bruyères-le-Châtel.

Abstract

The mechanism of space-charge neutralization of a low-energy proton beam is investigated both experimentally and theoretically. In the experiment, the transverse profile of a 500 keV proton beam delivered by a duoplasmatron source is accurately measured at the end of a 3 m long drift space. Profile measurements are performed by an imaging technique using a scintillating screen and an intensified CCD camera. Measurement results done with different beam intensities (between 0.5 and 15 mA) and various residual-gas pressures are described. They show that, at high beam current an increase of the gas pressure results in a reduction of the beam spot, which indicates an increase of the value of the neutralization coefficient. On the other hand, the behavior is the opposite at low beam current: the beam size increases with the gas pressure. An interpretation of these experimental results is proposed.

Introduction

Beam losses result from the existence of a diffuse halo which can extend far away from the dense beam core. Halo formation originates from different processes including space-charge effects [1] and Coulomb scattering on the residual gas [2]. In the first process, mismatch and misalignment in the transport of an intense beam in a long periodic channel, as well in a linac, are believed to be important sources of halo. To check these predictions, an experimental program has been initiated, aiming at the investigation of halo formation and development in the transport of an intense low-energy proton beam through a periodic focusing FODO channel [3]. Accurate measurements of beam emittance and brightness performed at the channel entrance indicate that the initial beam conditions are suitable for further halo development through the FODO channel [4].

The low-energy proton beam may however be partially neutralized in the residual gas of the transport channel, which would increase the tune depression and mismatch the beam to the FODO channel. Interpretation of the halo measurements would then be questionable.

Therefore, an experimental study of the space charge neutralization has been undertaken to provide compensation coefficients at various beam intensities for a low-energy proton beam. This study will be also useful for the design and simulation of the low energy part of a high-intensity linac such as the one studied for the TRISPAL project [5].

Experimental procedure

Space-charge neutralization measurements have been performed in the matching section between the proton source Amalthée and the FODO channel of our halo experimental set-up at Saclay.

Measurement method

The basic idea for measuring the space-charge neutralization rate is the following.

- A proton beam propagates freely in a residual gas toward a screen. We first measure its transverse size while the only force acting on it is the space-charge force.
- A pepper-pot is then placed on the beam path at the beginning of the drift space. The beamlets passing through the pepper-pot holes do not feel the full-beam space-charge force. The envelope of the beamlet spots corresponds to the full-beam transverse profile without space-charge effect. The pepper-pot can be replaced by a single-hole moved across the beam; a technique which yields more accurate beam profile measurement.
- The neutralization rate is recovered from a simulation which gives an equivalent beam current adjusted to reach the measured beam size.

Experimental set-up

The measurements are performed with a pulsed (500 μs, 1 Hz) proton beam at 500 keV with up to 50 mA peak current, delivered by the Amalthée duoplasmatron source. In the experiment (see **Fig. 1**), the beam is collimated by a ϕ10 mm diaphragm (D) located at the source exit. It propagates through a drift space toward a scintillating screen (S) 2.8 m downstream. The pepper-pot (PP) and single-hole (SH) plates are located very close to the diaphragm. The SH plate with a 0.2×0.2 mm^2 sampling hole is moved in the horizontal direction across the beam by a stepping motor (0.2 mm step). Both beam-profile and beamlet-spot images are observed with an intensified CCD camera.

Fast responses of both light intensifier and scintillator (a P46 phosphor (Y_3 (Al,Ga)$_5$ O_{12}; Ce) crystal powder deposited on a stainless-steel plate) allow to take beam-profile images during a 5 μs snapshot anywhere within the beam pulse. This good time resolution is very useful for analyzing the temporal evolution of the neutralization rate in the pulse.

Residual gas pressure and composition can be adjusted by modifying pumping conditions and injecting nitrogen gas at a given flow in the vacuum chamber.

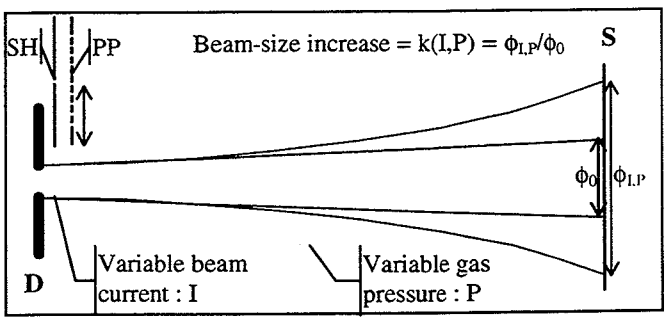

Fig. 1 : Schematic layout of the experimental set-up for space-charge neutralization measurement.

Measurement results

• In a first run, measurements were taken using the PP plate with a beam current of ~10 mA behind the diaphragm D. **Fig. 2** shows the beam profiles with and without the PP plate in the beam path.

Analysis of the experimental results shows that the "PP-in" beam size is systematically smaller than the "PP-out" beam size, whatever residual gas pressure (up to 5.10^{-5} hPa) and sampling instant in the pulse. This behavior indicates clearly that the proton beam is not totally space-charge compensated.

Nevertheless, these measurements are not entirely conclusive since the "PP-in" beam size is determined with up to 40% uncertainty due to large spacing of the PP holes.

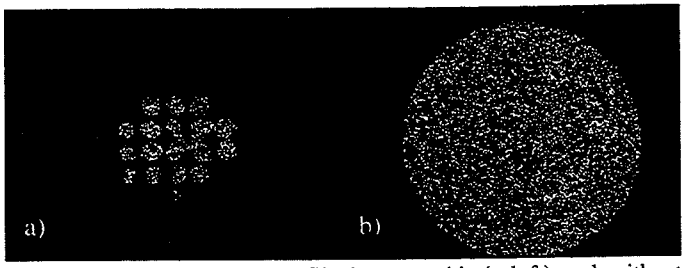

Fig. 2: Beam transverse-profile images with (a-left) and without (b-right) pepper-pot plate in the beam path.

• During a second run, the SH plate is used to accurately measure both beam size (ϕ_0) without space-charge and beam transverse emittance at the diaphragm location. Beam profiles (with and without SH plate) and emittances were measured for 8 beam currents ranging from 0.8 to 15.0 mA and four sets of residual gases and pressures, P_1 ($2\ 10^{-6}$ hPa H_2), P_2 ($1.2\ 10^{-5}$ hPa H_2), P_3 ($1.2\ 10^{-5}$ hPa H_2+ $2.6\ 10^{-5}$ hPa N_2) and P_4 ($1.2\ 10^{-5}$ hPa H_2+ $5.8\ 10^{-5}$ hPa N_2). Pressures given here are mean values on the drift space. All measurements were done 350 µs after the pulse start.

For each measurement, data processing consists in determining the beam-size growth k defined as the ratio of beam diameters with and without space-charge effect :

$$k(I,P) = \phi_{I,P}/\phi_0 ,$$

where I is the beam current, P the residual gas pressure, ϕ_0 the beam diameter on the screen without space charge and $\phi_{I,P}$ the beam diameter with space charge.

Analysis of the data shows that below 6 mA the beam size increases with the gas pressure, remains almost constant around 6 mA, and decreases at higher currents. This behavior is illustrated in **Fig. 3** where the curves for the two extreme pressure sets P_1 and P_4 are displayed. This indicates that at high-current the beam is more space-charge compensated in a high-pressure gas, as mentioned above. On the contrary, a low-current beam seems to be "undercompensated" when the pressure is high.

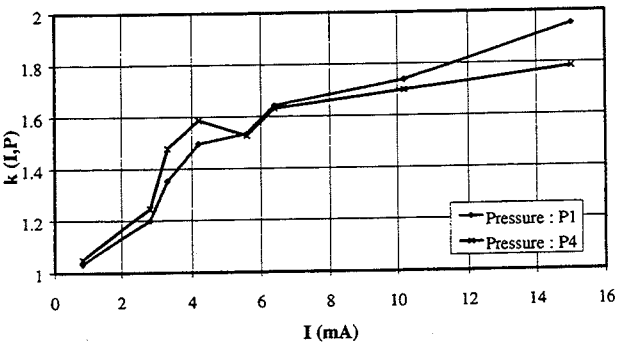

Fig. 3: Beam-size growth k as a function of beam current, for the pressure sets P_1 and P_4.

The rate of beam size growth with residual gas pressure is defined by :

$$\nu(I) = \langle dk(I,P)/dP \rangle ,$$

with I the beam current, P the residual gas pressure and <> is an average over the pressures.

The parameter ν has only a qualitative meaning since a precise determination of both gas pressure and composition along the drift is not possible. Nevertheless, **Fig. 4** shows a clear variation of this parameter with the beam current. A negative value of ν indicates that space-charge compensation increases with the pressure, since a positive ν indicates that the beam spread is larger than the one expected from the space-charge effect.

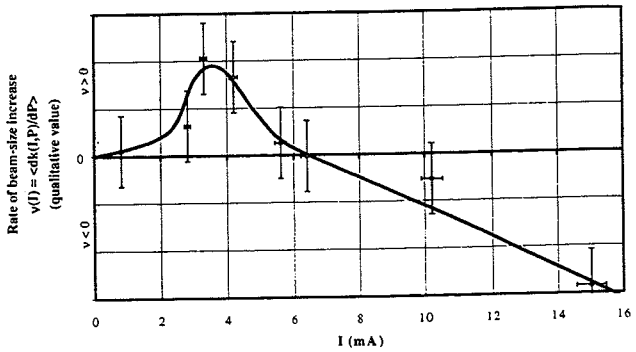

Fig. 4: Variation of the rate of beam size growth with residual gas pressure versus the beam current.

For each beam current, emittance measurements are processed to yield the beam-particle distribution in the phase